Thermo-fluid dynamics of falling film type vapour absorption process

流下液膜式冷媒吸収プロセスの熱流体力学的挙動に関する研究

February 2016

Waseda University

Graduate School of Fundamental Science and Engineering

Department of Applied Mechanics

Research on Dynamics and Control of Mechanical Systems

ジャンネッティ ニコロ

Niccolo GIANNETTI

Abstract

Absorption represents an opportunity towards clean and efficient energy conversion systems. However, the attempt to characterise heat and mass transfer performance of devices that make use of this process is still inadequate and has not led to generalised methods. On the other hand, the recent technical development of absorption chillers, heat pumps and heat transformers pushes towards increasingly complex plant configurations, and, in fact, seems to stand a step forward with respect to the theoretical background needed for an accurate performance prediction, optimisation and control. This work arises from the awareness of this discrepancy and constitutes an effort to get closer to a conclusive approach for absorption systems modelling and optimisation. The structure of this thesis reflects a convergent approach, originating from the development of a general model representing the thermodynamic silhouette of these systems in their interactions with the environment, pointing out the importance properly designed components and in particular of the absorber. Accordingly, a detailed numerical model of falling film absorbers is presented and used as the basis for a thermodynamic optimisation of the component with reference to the ultimate duty of the system in different application cases. Results suggest the importance to work at reduced mass flowrates with a thin uniform film to increase the system performance and/or reduce its size, but the surface partial wetting needs to be considered as a critical related issue. Therefore, a criterion for the film stability and, after the film breakage, a method to estimate the wet part of the exchange surface are defined by using the energy minimisation principle. The hysteresis phenomenon of the wetting behaviour for increasing and decreasing flowrates is highlighted and a first validation of the model is presented. In this way, the effect of these phenomena can be included in the absorption model to extend its validity and increase its accuracy. Experiments are performed to validate the absorption model in a wide range of operative conditions, and, lastly, the model is reduced to the analytical expression of heat and mass transfer coefficients, obtained from a closed solution of energy and species transport equations.

Keywords : Absorption, Falling film, Extended range, Partial wetting, Irreversibility, Analytical solution, Energy minimisation, Irreversibility, Contact angle, Wettability hysteresis

Preface

This thesis work is intended to embody an effort to contribute even minimally to a rich and fascinating field, effort which has utterly been compensated by the honour to have had the chance to behold the previous work of those giants I'm standing on the shoulders of. In fact, this work represents the results of a quest where I got lost and amused for a couple of years, both in a deep theoretical field and around the streets of an amusing metropolis, located in a remote country with its incredible culture. This circumstance uprooted most of my convictions, creating a continuous condition of general uncertainty, which indeed required me to be actively and constantly involved in some kind of Research.

The fundaments of heat and mass transfer are relatively well established, however, a comprehensive modelling of absorption systems encompasses moving and deformable interfaces involved in wettability issues and thermo-fluid dynamics of two-phase flow, making the subject complexity an order of magnitude higher than standard transfer problems. Metaphorically, absorption systems constitute the intersection of various leading and challenging research paths at the boundary of macroscopic physics. Nonetheless, given the interdisciplinary interest in these topics, and in view of their practical importance, in the last three decades substantial research efforts have been made to tackle the modelling of these phenomena with different approaches. Whether the research interest lies in fundamental physics, engineering or chemistry, as a manufacturer or a consumer of energy conversion systems, the matters converging in fundamental and technical absorption research constitute a challenging problem whose solution is believed to contain a potentially remarkable effect on the development of technical solution for an effective and environmentally friendly use of energy.

Acknowledgements

Special thanks to 齋藤先生、who has been my supervisors supporting me for this thesis and my actual survival necessities in a new fascinating and difficult environment, and to Proff. Andrea Rocchetti, Adriano Milazzo and Giuseppe Grazzini from the University of Florence, whom have aided my work at a considerable distance, providing me helpful information and active support with constant willingness. Thanks to proff. 勝田、武藤、天野 to have taken time from their busy schedule for the reviewing process. Thanks to all the other members of Saito Laboratory, especially Proff. 山口, 大野 and 井上 for their wise suggestions, and the organising staff of the Department of Applied Mechanics and Aerospace Engineering of Waseda University for their assistance.

Afterwards, I simply want to recognise my debt of thankfulness towards those precious people I've met, which is too important to be repaid anyhow. I can only heartily appreciate the possibilities that my family let me free to exploit, every moment spent with my friends and my girlfriend, and be grateful to all worthy people who taught me somewhat significant. Therefore, I'd like to recall all their names, respectively,

Tsu Ling, Gabry, Maria, Massimo, Andrea, Barby, Lorenzo, Lory, Chiara, Annamaria, Mario, Giacomo, Francesca, Nonna Rina, Maria, Giovanni, Gianni, Serena, Nonna Amalia, Loriana, Zia Laura, Marcello, Giulio, Navone, Nanni, Ghera, Marci, Monte, Guodo, Albi, Mari, James, Red, Andre, Coppi, Pippo, Monti, Ciccio, Giada, C.Mi, Sbam, George, Elisabeth, Frank, Saif, Arnas, Mirta, Hiroshi, Richard, Dane, Rianne, Mark, Ishii 先生, 大阪, ゆめ, Stefano, Cesare, Alberto, Elena, Leon, 野沢 and all people I've sincerely practised Judo with.

Last but not least, I appreciate the generosity of all those people who kindly donated me coffee beans for my espresso machine, without which, in fact, my modest research contribution could not have been completed or might have been immeasurably delayed.

Index

Nomenclature

a	Thermal diffusivity [m^2s^{-1}]
a, b	Power series coefficients
A	Cross-section Area [m^2]
A, B	Eigenfunction coefficients
b	Average rivulet Thickness [m]
B	Wetting ratio First tube distribution coefficient
Bi	Biot number
C	Tube bundle distribution coefficient of the wetting ratio/Integration constants
c^2	Dimensionless group
c_p	Specific heat [$J \cdot kg^{-1}K^{-1}$]/Isobaric molar heat [$J \cdot mol^{-1}K^{-1}$]
d^+	Dimensionless diameter
D	Mass diffusivity [m^2s^{-1}]
DA	Dimensionless absorption flux at the interface
DQ	Dimensionless heat flux at the wall
e	Specific energy per unit width [$J \cdot m^{-2}$]
E	Energy [J]
E, H	Single variable exponential functions
f	Hysteresis tension [$N \cdot m^{-1}$]
F, G	Eigenfunctions
g	Gravity [$m \cdot s^{-2}$]
G	Dimensionless cyclic entropy parameter
Ga	Galileo Number
G_v	Absorbed mass flux per unit area [$kg \cdot s^{-1}m^{-2}$]
h	Specific enthalpy [$J \cdot kg^{-1}$]/Molar enthalpy [$J \cdot mol^{-1}$]
H	Number of nodes in radial direction
i_{abs}	Specific absorption heat [$J \cdot kg^{-1}$]
i_v	Latent vaporization heat [$J \cdot kg^{-1}$]
K	Heat exchanger inventory [$W \cdot K^{-1}$]

k	Thermal conductivity [$W \cdot m^{-1}K^{-1}$]
L	Tube length [m]
L_c	Characteristic critical length [m]
Le	Lewis Number
m	Mass Flowrate [$kg \cdot s^{-1}$]
M	Molar mass [$kg \cdot mol^{-1}$]
mtc	Mass transfer coefficient [$m \cdot h^{-1}$]
n	Number of tubes
N	Number of nodes
Nu	Nusselt number
p	Pressure [Pa]
P	Tube pinch [m]
Pr	Prandtl number
q	Heat flux per tube unit length [$kW \cdot m^{-1}$]/ /Heat flux per unit area [$W \cdot m^{-2}$]
Q	Heat transfer rate [W]/ /Heat flux per unit length [$W \cdot m^{-1}$]
r	Outer tube radius [m]
R	Rivulet Radius [m]
Re	Reynolds Number
R_{gas}	Perfect gas constant [$J \cdot kg^{-1}K^{-1}$]
s	Specific entropy [$J \cdot kg^{-1}K^{-1}$]/Molar entropy [$J \cdot mol^{-1}K^{-1}$]
S	Volumetric entropy generation rate [$W \cdot m^{-3}K^{-1}$]/Entropy rate [$W \cdot K^{-1}$]
Sc	Schmidt number
Sh	Sherwood number
t	Temperature difference parameter/Time [s]
T	Temperature [K]
u	Stream-wise velocity [$m \cdot s^{-1}$]
U	Overall Heat Transfer Coefficient [$W \cdot m^{-2}K^{-1}$]
un	Uncertainty term
Un	Expanded uncertainty

v Radial velocity [$m \cdot s^{-1}$]

V Volume [m^3]

w Molar concentration [$mol \cdot m^{-3}$]

W Mechanical power

We Weber number

WR Wetting Ratio

WS Global surface wetting

x Local tangential position [m]

X Local wetting ratio

y Local normal position [m]

Y Potential specific energy [$J \cdot m^{-2}$]

z Transversal coordinate [m]

Z Straight line segment of the rivulet [m]/number of nodes in the transversal direction

Greek symbols

α Heat Transfer Coefficient [$W \cdot m^{-2} K^{-1}$]

β Stream-wise Angle [rad]/Surface Inclination Angle [rad]

χ Vapour quality

δ Film Thickness [m]

E Entropy generation rate per unit length [$W \cdot m^{-1} K^{-1}$]

ε Dimensionless tangential position

ϕ Heat conductance parameter

Φ General parameter identification

Γ Mass flow rate per unit length [$kg \cdot s^{-1} m^{-1}$]

γ Dimensionless concentration

η Dimensionless normal position

η_{Ca} Carnot efficiency

ι Heat exchanger effectiveness

φ Circulation ratio

ϑ Dimensionless temperature

κ Chemical activity

λ Surface Width/rivulet spacing [m]

Λ Normalized heat of absorption

μ Viscosity [Pa·s]

ν Kinematic viscosity [$m \cdot s^{-2}$]

Π Interface extension [m^2]

Θ Entropy parameter of the fluid

θ Rivulet transversal angle

θ_0 Contact angle

ρ Density [$kg \cdot m^{-3}$]

Σ Irreversibility rate [$W \cdot K^{-1}$]

σ Surface tension [$J \cdot m^{-2}$]

τ Shear stress tensor [Pa]

υ Specific volume [$m^3 \cdot kg^{-1}$]

ϖ Chemical potential [$J \cdot mol^{-1}$]

ω Lithium Bromide concentration

Ω Ratio of dimensionless position difference

Ξ Dimensionless sub-cooling parameter

ξ,ς Eigenvalues

Ψ Total Velocity [$m \cdot s^{-1}$]

ζ Molar flux [$mol \cdot m^{-2} s^{-1}$]

Υ Lagrangian function [$J \cdot m^{-2}$]

Subscripts

0	critical value
*	standard value
∞	stable Configuration
A	absorber/advancing
av	average
b	break-up
β	local angle value
c	cooling water/internal to the tube
C	condenser
CH	chiller
d	Diffusion
D	Dry
e	Equilibrium
E	evaporator
f	Friction
F	fluid
g	Global
G	generator
h	convection
H	high
H_2O	water
HP	heat pump
HT	heat transformer
i,j	Node indexes
if	Interface
in	inlet
k	Tube axial mesh index

K	related to kinetic energy
L	low
l	liquid
LiBr	lithium bromide
n, m	Eigenvalue/Eigenfunction indexes
M	intermediate
max	maximum
min	minimum
o	outlet
p	pump
θ	related to Θ parameter
R	refrigerant/receding
riv	rivulet
RM	Refrigerating machine
s	solid
S	solution
σ	related to surface tension
sat	phases equilibrium
t	related to K parameter/ thermal
TM	Thermal machine
u	uniform film
v	vapour
w	wall
Wet	wet
x	stream-wise direction
Y	Young's value

Superscripts

+	dimensionless
‘	first derivative
‘‘	second derivative

Chapter 1, Introduction

1.1. Research background

Nowadays the awareness of the environmental issues of the planet steers towards clean and efficient energy conversion systems. Absorption chillers, heat pumps and heat transformers represent an opportunity in this direction.

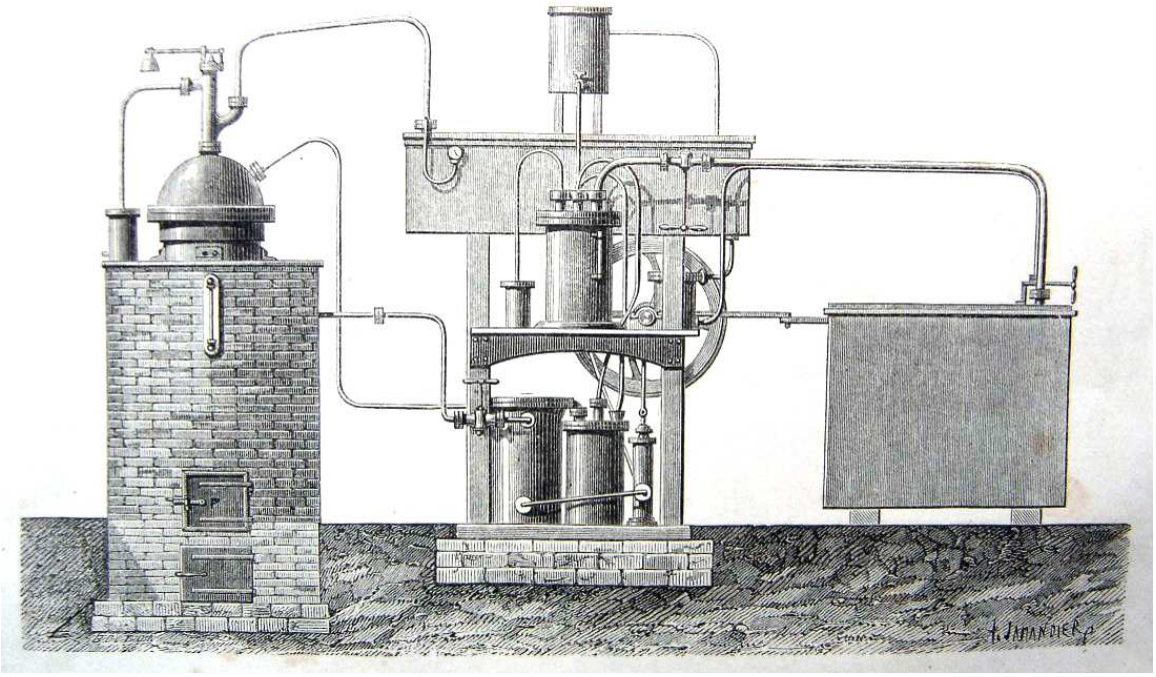

Fig. 1.1 Ferdinand Carré's ice-making device [Grand appareil de Ferdinand Carré pour fabriquer de la glace Illustration tirée du livre "L'eau" de Gaston Tissandier 4e édition (1878) - Librairie Hachette Chargé par Gérard Janot][1)]

The use of the vapour absorption cycle for heat driven energy systems was originally among the first popular and widely used methods of refrigeration. Before the advent of the first absorption refrigerating machine attributed to Ferdinand Carré (1859), the history of refrigeration technology can be led back to Michele Faraday in 1824. At that time, Faraday conducted a series of experiments to liquefy some stabilised gases, which, even though not directly used for refrigeration purposes, are considered a prelude for the refrigeration science proximately following to that time. Before the first absorption refrigerating machine, in1851 John Gorrie[2)] patented a refrigeration system for the production of artificial ice to treat patients affected by yellow fever. This system was using air as the refrigerant. Ferdinand Carré's ice-making machine featured ammonia as the refrigerant and water as the absorbent, but the original design used a solution of water and sulphuric acid[3)]. However, both these named technology were soon superseded by the use of carbon dioxide systems, and successively by the dominant vapour compression systems. Absorption machines were firstly commercially released only in the late 1923 by the company *ABArctic*, which was then incorporated by *Electrolux* in 1925. Albert Einstein and Leo` Szilard, in 1926, designed an alternative configuration of an absorption refrigerator operating with no moving parts and operating at constant pressure, known as “Einstein refrigerator” (Fig. 1.2)[4)].

Even though the development of vapour compression cycles has limited the implementation field of vapour absorption systems, the main benefits of absorption cycle are still evident: first, since a negligible amount of electricity is needed, waste heat can be used as the main energy source and higher reliability can be ascribed to the reduced number of moving parts. Accordingly, absorption plants exhibit long lifetimes and excellent part-load operability. In

addition, typically used refrigerant (water or ammonia) are not responsible of ozone depletion effect. These characteristics allow a safe and environmentally friendly use of energy, which can be portrayed by application cases like trigeneration, heat temperature boosting and renewable plants. The large renewed interest in vapour absorption cycles gives the way to a number of unexplored solutions, high margins of improvement and pushes forward active research towards new ideas for an advanced design of energy conversion systems; providing, along these lines, optimistic future prospective originating from an "antique" technology.

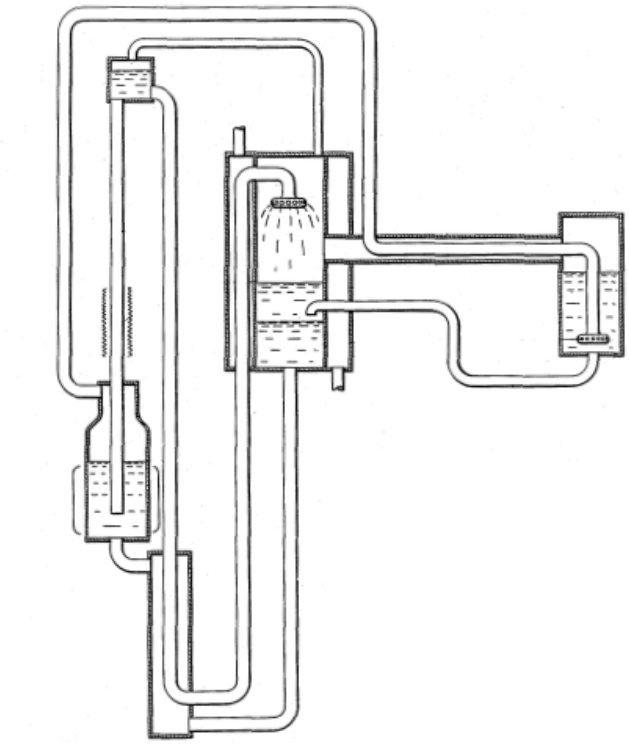

Einstein Refrigerator

Patent number US1781541 -- November 11, 1930

Albert Einstein

Leo Szilard

Fig. 1.2 Einstein's and Szilard's patent application[4)]

Absorption cycles are similar to vapour compression cycles in featuring an evaporator, a condenser and an expansion valve connecting different pressure levels. The method used to convert low-pressure vapour into high-pressure vapour, and to maintain steady operability between the evaporator and the condenser, constitutes the main difference that distinguishes the operative principle of these two systems. As opposed to the mechanical compressor required in a vapour compression system, an absorption system consist of two additional heat reservoirs, an absorber and a generator, enabling the system to use thermal power as the driving source. As already pointed out, this main feature constitutes a critical advantage for heat recovery and renewable sources application possibilities, multiplying the options for different plant configurations and for an optimised design with respect to the ultimate duty required to the system.

Broadly speaking, the absorption/desorption process consists in the partial separation/recombination of a volatile working fluid (the refrigerant) from the carrier solution, which require heat rejection/input to maintain the solution far from thermodynamic equilibrium and assure steady cyclic operability of the system. The two most widely used

absorption pairs are: water-lithium bromide (LiBr), and ammonia-water. The first being limited to application cases where the minimum refrigerant temperature is higher than the melting point of ice (0^oC) and the minimum solution temperature to be kept safely above the crystallisation point of the aqueous LiBr at given pressure-concentration conditions. On the other hand, ammonia-water plants demands special care to be properly designed accounting for the refrigerant toxicity and flammability. Additionally, the vapour-pressure curve of ammonia forces the system to operate at relatively high pressure, whereas LiBr-water plants run under partial vacuum that constitutes a safety point in favour of the latter operation mode. Besides being thermally driven, according to J.M. Gordon and K.C. Ng (2000)[5], there are other four major ways in which absorption systems differ from their mechanical counterparts. First, there are three/four heat reservoirs rather than two. Second, the absorber is a distinct critical additional component. Third, if the total heat rejection is constrained, one additional control variable is given by the partition of the heat rejection between the absorber and the condenser. Finally, a significant part of the total internal dissipation can be ascribed to mass-transfer processes intrinsic to the absorption cycle and regenerative heat exchangers, when these are employed. The main limitations of absorption machines are restricted temperature ranges and rather high initial investment cost. The COP of an absorption machine is also evidently lower than that of a corresponding mechanical system. However, their second law efficiencies are comparable. Multiple-stage cycles are conceived to overcome some of these main limitations of the basic cycle. Commercial and experimental plants range in size from small domestic units to large industrial system with cooling rates in the order of megawatts. As a rule, three different fundamental configurations, associated to different useful effects, results from absorption systems: absorption chiller, extracting heat at the evaporator (eq. 1.1), absorption heat pump, rejecting heat at the condenser and the absorber (eq. 1.2), and heat transformer, delivering heat from the absorber to the heating load at a higher temperature than that of the heat source (eq. 1.3). The performance of the system is conventionally evaluated in terms of COP, as the useful effect for a given input power unit. Namely,

$$COP_{CH} = \frac{Heat \quad extracted \quad at \quad the \quad evaporator}{Heat \quad input \quad at \quad the \quad generator} \tag{1.1}$$

$$COP_{HP} = \frac{Heat \quad rejected \quad at \quad condenser \quad and \quad absorber}{Heat \quad input \quad at \quad the \quad generator} \tag{1.2}$$

$$COP_{HT} = \frac{Heat \quad rejected \quad at \quad the \quad absorber}{Heat \quad input \quad at \quad evaporator \quad and \quad generator} \tag{1.3}$$

In order to overcome the constitutive limitations of the basic absorption cycle, different configurations, hybrid cycles and multiple stage plants are envisaged and realised in a number of application cases [6-22]. The number of stages refers to the number of heat recovery units (generators). These can be arranged either in series or in parallel configurations, depending on the method used to deliver the solution leaving the absorber. This short introduction gives a simple outline of the long history and the recent technical development of absorption systems.

Even though the fundaments of heat and mass transfer constitutes rather solid pillars, however, an exhaustive modelling procedure of absorption systems covers multi-components fluid in multiphase conditions, where moving and deformable interfaces play a major role for the process thermo-fluid dynamics, exchange surface extension and flow wetting ability. Therefore, the subject complexity is made orders of magnitude higher than standard transfer problems. Nonetheless, given the interdisciplinary interest in these topics, and in view of their practical importance, substantial research efforts have been made in the last three decades to tackle the modelling of these phenomena with different approaches [23-29].

Whether the research interest lies in fundamental physics, engineering or chemistry, as a manufacturer or a consumer of energy conversion systems, the matters converging in fundamental and technical absorption research constitute stimulating problems whose clarification is believed to convey potentially remarkable results for the technical progress,

solution of the maim environmental issues and for the refinement of the fundamental understanding of the originating fields.

1.2. Research purposes

As mentioned, the recent technical development of absorption chillers, heat pumps and heat transformers pushes towards increasingly complex plant configurations, and, in fact, seems to stand a step forward with respect to the theoretical background needed for an accurate performance prediction, optimisation and control of these systems. This work arises from the awareness of this discrepancy, and constitutes an effort to get closer to a conclusive approach for absorption systems modelling.

The fundamental heat and mass-transfer processes constituting the absorption cycle are realised inside specific heat exchangers, whose characteristics have decisive impact on the overall system efficiency, on its dimensions and on its cost. In particular, recent literature concerning absorption-based systems suggests that their heat and mass transfer performances are drastically affected by several hydrodynamic aspects responsible for determining the solution distribution along the exchange surface.

Conventionally, falling film heat exchangers are employed for their high transfer performances and low pressure drops. However, the attempt to model and optimise the complex heat and mass-transfer mechanism occurring inside these devices is still incomplete and has not leaded to conclusive approaches. In this configuration, the film thickness constitutes the main heat transfer resistance with the cooling water circulating inside the tube and simulations theoretically indicate that working with reduced solution mass flowrates could improve the system performance. Consequently, operability at reduced Reynolds number is attractive for absorption plants, but the partial wetting of the tube surface needs to be considered as a critical related issue.

This work aims at the inclusion of partial wetting phenomena in absorption heat and mass transfer modelling. On the way to this goal, an improvement of the fundamental understanding of the absorption process, and results useful for other technical applications can be obtained as a parallel.

1.3. Thesis outline

The structure of this thesis reflects a converging and focusing approach (Fig. 1.3):

The first chapter, closing with this outline, has broadly presented the research background, a statement of purpose and possible positive revenues of the results, thusly, creating the basis and pointing at a research direction.

The second chapter develops and presents a general model for absorption systems representing their thermodynamic silhouette in its interactions with the environment. By combining first and second principle, this approach provides the guidelines for designing optimised systems, as well as a criterion for performing existing plants' diagnostics and improving their performance. The importance of properly designed components and in particular of the absorber is discussed and pointed out.

In the third chapter the attention is concentrated towards the component. A detailed numerical model of falling film absorbers is presented and used as the basis for the development of a thermodynamic optimisation criterion of this heat exchanger with reference to the ultimate duty of the system in different application cases. Results suggest the importance to work at reduced mass flowrates with a thin uniform film to increase the system performance, and/or reduce its size.

Chapter four faces the problem of the surface partial wetting at low Reynolds numbers. A criterion for the film stability and, after the film breakage, a method to estimate the wet part of the exchange surface are defined by using the energy minimisation principle, for increasingly complex problem geometry. Hysteresis phenomena of the contact angle and the wetting behaviour for increasing and decreasing mass flowrates are highlighted, then, a practical application and a first validation of the model are presented.

In the fifth chapter the effect of partial wetting phenomena is included in the numerical model of falling film absorption to extend its validity and increase its accuracy in the low Reynolds region.

A sixth chapter is dedicated to consistently simplify the energy and species transport equations and lead to the analytical expression of heat and mass transfer coefficients in a closed form solution.

Lastly, chapter seven describes the experimental equipment and data collection method used as a closing point to qualitatively and quantitatively validate the theoretical model.

The eighth chapter is intended to summarise the results obtained in order to draw significant conclusions and future prospects. On the other hand, the conclusions of this research effort bring the attention back to the starting point (presented in chapters 2 and 3), namely system and component optimisation for real plant design and operability.

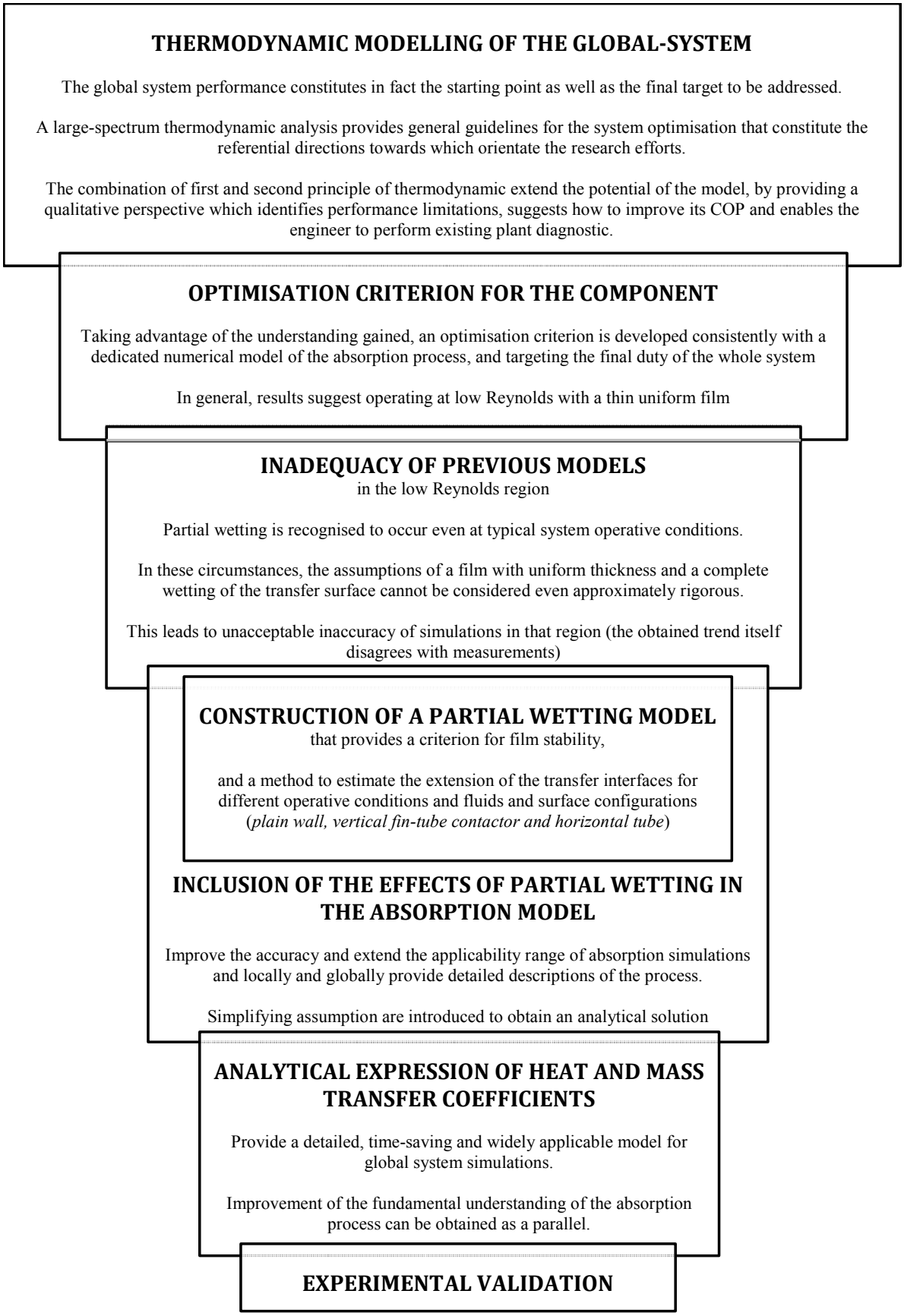

Fig. 1.3 Flow-diagram of the thesis outline

Chapter 1,
Introduction

Chapter 2, Thermodynamic analysis of irreversible absorption systems

The purpose of thermodynamic optimisation methods deals with identifying features and physical circumstances by which the system fulfils its functions while performing at the highest thermodynamic level possible [30]. As long as designed products are necessarily imperfect, efforts are made to achieve the least irreversible operability, spreading the imperfection through the system in the best possible way, in order to achieve a wide range of efficient working conditions. An optimal distribution of imperfection is the principle that generates topology (construction, configuration) in flow systems (engineered and naturally occurring ones) [31]. As an instance, in the field of refrigeration the purpose of a machine is to maintain a cold space cold, "forcing" the heat current to flow in an unnatural direction. Since this requires work, the general objective is to reach the goal with least power expenditure and minimum energy degradation [32], given the boundary conditions which define the outer environment interacting with the system and providing the required driving-energy.

In this preliminary chapter absorption systems are considered as rather indefinite multi-temperature-level thermodynamic entities, focusing on their similarities regardless their technical differences in detail. To this aim, the constitutive physical processes of the absorption cycle are treated as irreversible thermodynamic transformations facing finite thermal capacity heat sources through the fundamental heat exchangers. Dimensionless parameters which characterise the transformations followed by internal and external fluids are introduced, and their influence on the cycle efficiency is investigated. First and second principles are combined to express the system performance. This approach identifies the limitations imposed to the physical processes by accounting for the inevitable dissipation due to their constrained duration and intensity, and is used to define a general thermodynamic criterion for the characterisation and optimisation of three-thermal irreversible systems. Dependence on the main factors is highlighted in a way that shows how to change them in order to improve the overall efficiency. Under this point of view, the analysis evaluates COP improvements and can be used to perform plant diagnostics, besides predicting the system performance. The use of this criterion is exemplified for absorption chiller and heat transformers application cases.

2.1. Multi-temperature-level systems

Multi-temperature-level systems enlarge the prospects and degrees of freedom for an efficient design and an environmentally friendly use of energy. In general, the development of technical solution for an effective use of energy is guided by the formulation of optimisation criteria based on the fundamental thermodynamic principles. If the sole aim is to ascertain COP, efficiency or energy expenditure and cooling/heating capacity at given operative conditions, in fact, the use of the first principle of thermodynamics will suffice. On the other hand, since every real process occurring as part of an energy conversion system is associated to an unavoidable degradation of the earliest amount of energy, a thermodynamic analysis should provide a qualitative description, properly identify the limitations imposed to the physical processes, point out the most relevant parameters and how to change them in order to improve the performance of that process. In this way, the study is intent upon evaluating COP improvements and performing plant diagnostics, not only predicting the system performance. To this objective, an accurate evaluation of irreversibility (or entropy generation), namely the use of the second principle of thermodynamics, becomes essential.

Multi-temperature-level systems actually increase the number of possible plant configurations for an optimised and environment-friendly use of energy; however, as a counterpart, the increased complexity of these plants is often prohibitive with regards to a comprehensive modelling of all the details at play, making the calculation very difficult or impossible, and the physical content obscure. An absorption system, in its simplest arrangement, transfers heat between three temperature levels, but more often between four thermal sources with finite heat capacity [32-33]. Albeit the vast development of vapour compression cycles has narrowed down the implementation field of vapour absorption systems, the absorption cycle still pave the way to sustainable and reliable perspectives. However, given the complexity of the heat and mass transfer phenomena occurring inside absorption systems, and the number of possible choices for different

cycle configurations or combinations with other technologies, their optimisation is still incomplete and has not led to conclusive approaches. Originally, a three-thermal refrigeration cycle has been thermodynamically conceived as the combination cycle of an endo-reversible thermal engine driving an endo-reversible two-heat sources refrigerator [34], whereas the influence of finite rate heat transfer towards the surroundings has been considered in a second paper [35]. In addition, Chua H.T. et al. (1993)[36] use entropy production analysis with an analytical irreversible thermodynamic model. By focusing on the thermodynamics of absorption chillers, Ng K.C. et al. (1998) [37] have shown the necessity of accounting for internal dissipation, and defined the concept of Process Average Temperature (PAT). As for two thermal sources irreversible refrigerators, Grazzini G. and Rocchetti A. (2014) [38] use a general irreversible thermodynamic model to obtain an expression of the coefficient of performance accounting for the second principle in a way useful to produce maps of efficiency in terms of meaningful dimensionless parameters. A similar approach can be applied to increasingly complex thermodynamic entities like multi-temperature-level systems, and this model is developed in the following paragraph.

2.2. Absorption chillers

This chapter is conceived as a characterisation of a three-thermal sources inverse thermodynamic cycle that includes the influence of the irreversibilities on the cycle efficiency. Considering a three-thermal inverse-absorption cycle (Fig. 2.1), the use of this method is firstly exemplified for a chiller application case. The analysis is generalised to include both heat and mass transfer phenomena. Since absorption chiller, heat pumps or heat transformers are thermodynamically similar units, except for different temperature ranges and useful effects, this approach can be directly applied to other system configurations.

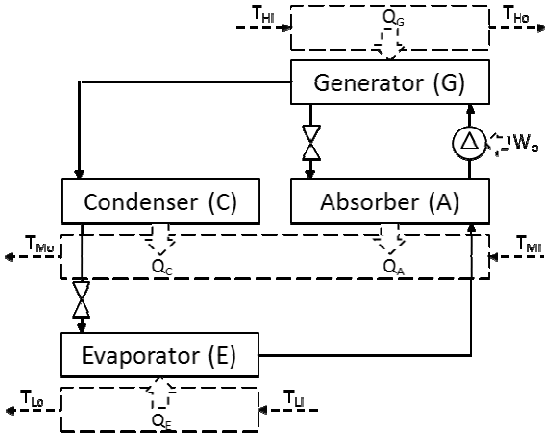

Fig. 2.1 Schematic of an absorption chiller

Steady cyclic-operability is assumed neglecting the effects of potential and kinetic energy of the refrigerant and the absorptive solution. Since the circulation pump processes saturated liquid solution, its electrical power consumption is disregarded. Furthermore, considering heat leaks to the surrounding to be ineffective, the Coefficient of Performance COP is defined as in eq. 2.1.

$$COP = \frac{Q_E}{Q_G} \tag{2.1}$$

The first law states,

$$Q_G + Q_E = Q_A + Q_C \tag{2.2}$$

Since the refrigerant and the solution perform a closed cycle, and since entropy is defined as a state function, its cyclic variation is null. Thus, if other thermal exchanges are overlooked, internal irreversibilities (eq. 2.3) are transferred outside the cycle to the surroundings through the heat exchangers. This directly influences the real operability of the system and its ultimate performance.

$$\Delta S_F = \Delta S_{RC} + \left(\Delta S_{RA} + \Delta S_{SA}\right) - \left(\Delta S_{RG} + \Delta S_{SG}\right) - \Delta S_{RE} \tag{2.3}$$

The entropy variation ascribable to those transformations involving the pure refrigerant is given in a general form by eq. 2.4.

$$\Delta S_R = m_R \Delta s = m_R \left(\int_i^o \frac{dh}{T} - \int_i^o \left(\frac{\partial \upsilon}{\partial T} \right)_p dp \right) \tag{2.4}$$

Where in general,

$$\int_i^o \left(\frac{\partial \upsilon}{\partial T} \right)_p dp = l \Delta p \tag{2.5}$$

As a rule, $l=\upsilon \cdot dln(V)/dT$ for a liquid, and $l=R_g/p$ for a perfect gas [39]. This term accounts for internal irreversibility related to pressure change and includes pressure drops contributions.

Differently, inside the generator and the absorber, entropy variation terms related to the absorptive solution are evaluated with eq. 2.6 [40],

$$\Delta S_S = m_S \Delta s = m_S \left\{ \int_{T_i}^{T_o} \frac{1}{T} \left(\frac{\partial h}{\partial T} \right)_{p,\omega} dT - \int_{p_i}^{p_o} \left(\frac{\partial v}{\partial T} \right)_{p,\omega} dp + R_{gas} \left[\int_{\omega_i}^{\omega_o} \frac{\ln \kappa_{H2O} - \ln \kappa_{LiBr}}{M_S} d\omega \right] \right\} \tag{2.6}$$

To characterise the amount of steadily circulating refrigerant extracted from the absorptive solution, the circulation ratio φ is introduced according to eq. 2.7.

$$\varphi = \frac{m_R}{m_S} \tag{2.7}$$

Were the refrigerant mass is related to the amount of circulating solution and the average concentration difference between strong and weak solution, as in eq. 2.8.

$$m_R = \frac{\left(\omega_H - \omega_L\right) m_S}{\omega_H} \tag{2.8}$$

Accordingly, the circulation ratio φ can be directly related to the concentration difference experienced in the absorber and generator at steady cyclic functioning (eq. 2.9).

$$\varphi = \frac{\left(\omega_H - \omega_L\right)}{\omega_H} \tag{2.9}$$

Combining equations 2.3 and 2.7 with eq. 2.10, which expresses the thermal power exchanged by the fluid streams of the heat exchangers, and neglecting pressure losses eq. 2.11 is obtained.

$$Q = m\Delta h \tag{2.10}$$

$$\Delta S_F = \left(Q_C + Q_A\right)\frac{\left[f\Delta s_{RC} + \left(f\Delta s_{RA} - \Delta s_{SA}\right)\right]}{\left[f\Delta h_{RC} + \left(f\Delta h_{RA} - \Delta h_{SA}\right)\right]} - Q_G\frac{\left(f\Delta s_{RG} - \Delta s_{SG}\right)}{\left(f\Delta h_{RG} - \Delta h_{SG}\right)} - Q_E\frac{\Delta s_{RE}}{\Delta h_{RE}} \tag{2.11}$$

Entropy variation terms are evaluated referring to the physiognomies of the heat exchangers and the physical state of the refrigerant and the solution.

In a previous paper, R. Tozer et al. (2005) [41] have presented the use of T-s diagram for aqueous LiBr absorption cycles. The supplementary saturation curves referred to different solution concentrations extend the depiction to include both the refrigerant (water) and the solution behaviours inside the cycle. Temperature-entropy diagrams are appropriate to characterise thermodynamic transformations in terms of both the first and second laws.

Considering an approximate T-s diagram of a single stage absorption refrigeration cycle (the black lines in Fig 2.2), where condenser and absorber temperature are close enough to be considered facing the same heat sink, the vapour generation/absorption processes are split into a constant concentration transformation, embodying temperature changes to reach the equilibrium temperature, a constant temperature one representing the release/absorption of the heat of absorption, and an isobaric segment to cool down to its saturation temperature the separated superheated vapour.

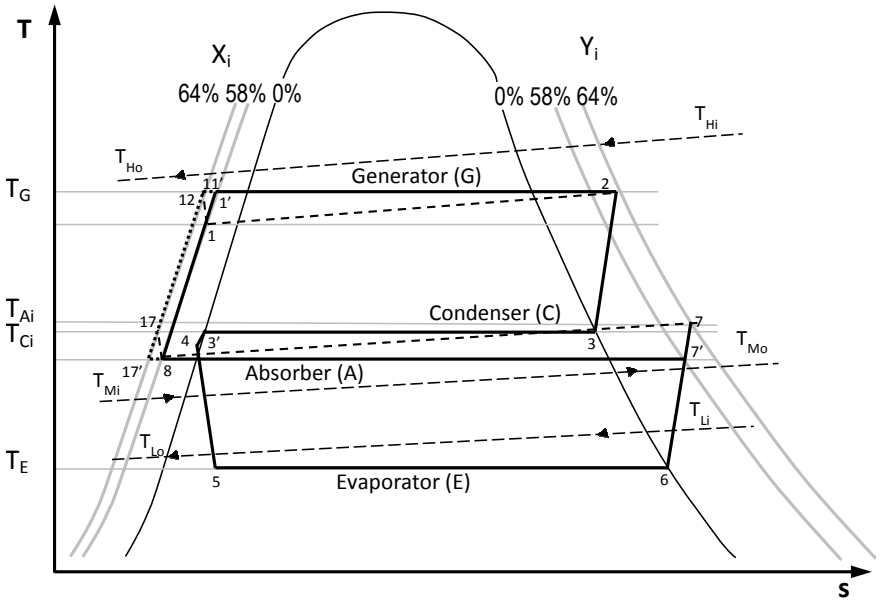

Fig. 2.2 T-s Diagram of an absorption chiller

As already pointed out, in a first approach, pressure losses are neglected.

$$\Delta S_F = \frac{\left(Q_C + Q_A\right)}{T_{Ai}}\Theta_{AC} - \frac{Q_G}{T_{Gi}}\Theta_G - \frac{Q_E}{T_{Ei}}\Theta_E \tag{2.12}$$

Where,

$$\Theta_{AC} = \frac{T_{Ai}\left[\varphi\Delta s_{RC} + \left(\varphi\Delta s_{RA} + \Delta s_{SA}\right)\right]}{\left[\varphi\Delta h_{RC} + \left(\varphi\Delta h_{RA} + \Delta h_{SA}\right)\right]}$$
$$\Theta_{G} = \frac{T_{Gi}\left(\varphi\Delta s_{RG} + \Delta s_{SG}\right)}{\left(\varphi\Delta h_{RG} + \Delta h_{SG}\right)} \tag{2.13}$$
$$\Theta_{E} = \frac{T_{Ei}\Delta s_{RE}}{\Delta h_{RE}}$$

These dimensionless parameters depend on concentration, temperature and thermodynamic properties of both the refrigerant and the solution within the heat exchangers. Considering the entropy and enthalpy variation terms singularly related to the transformations constituting the cycle (also observable in eq. 2.11), their analytical expressions is presented as follows. In particular, entropy and enthalpy variations of the vapour generation process from the refrigerant point of view (1-1'-2 in Fig 2.2) are calculated, respectively, as in eq.s 2.14 and 2.15.

$$\Delta s_{RG} = c_{pl}\ln\frac{T_G}{T_1} + \frac{i_{abs,G}}{T_G} \tag{2.14}$$

$$\Delta h_{RG} = c_{pl}\left(T_G - T_1\right) + i_{abs,G} \tag{2.15}$$

While, from the solution point of view, the desorption process (1-11'-12) is modelled with reference to eq. 2.16.

$$\Delta s_{SG} = c_{pS(p1,\omega1)}\ln\frac{T_G}{T_1} + R_{gas}\left[\int_{\omega_1}^{\omega_2}\frac{\ln\kappa_{H2O} - \ln\kappa_{LiBr}}{M_{S(p1,\omega1)}}d\omega\right] \tag{2.16}$$

Where the activities of water κ_{H2O} and lithium bromide κ_{LiBr} are estimated by means of the calculation procedure by R. Palacho-Bereche et al. (2010) [42]. The calculation technique for the specific enthalpy variations of the solution refers as well to Palacho-Bereche et al. (2010) [42], in which the molar enthalpy of pure water and lithium bromide are combined considering the enthalpy excess as described by D.S. Kim (2006) [43]. From the refrigerant point of view, entropy and enthalpy variations of the vapour absorption process (7-7'-8) are calculated, respectively, as in eq.s 2.17 and 2.18.

$$\Delta s_{RA} = c_{pv}\ln\frac{T_{Ai}}{T_{7'}} + \frac{i_{abs,A}}{T_{7'}} \tag{2.17}$$

$$\Delta h_{RA} = c_{pv}\left(T_{Ai} - T_{7'}\right) + i_{abs,A} \tag{2.18}$$

Terms attributed to condensation (2-3-4) and evaporation (5-6-7) of the refrigerant are embodied by eq.s 2.19-2.22.

$$\Delta s_{RC} = \frac{i_{vRC}}{T_{Ci}} + c_{pl}\ln\frac{T_{Ci}}{T_4} \tag{2.19}$$

$$\Delta h_{RC} = i_{vRC} + c_{pl}\left(T_{Ci} - T_4\right) \tag{2.20}$$

$$\Delta s_{RE} = \frac{(1-\chi_5) i_{vRE}}{T_E} \tag{2.21}$$

$$\Delta h_{RE} = (1-\chi_5) i_{vRE} \tag{2.22}$$

As a consequence, the dimensionless groups defined in eq. 2.13 can be developed and calculated, once temperature, concentration and thermodynamic properties of the refrigerant and the solution are established throughout the cycle. Introducing the definition of heat exchangers effectiveness ι by W. Kays and A.I. London (1954) [44],

$$\begin{aligned} Q_{AC} &= \iota_{AC} \left(mc_p\right)_{AC\min} \left(T_{Ai} - T_{Mi}\right) = K_{AC} \left(T_{Ai} - T_{Mi}\right) = K_{AC} \Delta T_M \\ Q_G &= \iota_G \left(mc_p\right)_{G\min} \left(T_{Hi} - T_{Gi}\right) = K_G \left(T_{Hi} - T_{Gi}\right) = K_G \Delta T_H \\ Q_E &= \iota_E \left(mc_p\right)_{E\min} \left(T_{Li} - T_{Ei}\right) = K_E \left(T_{Li} - T_{Ei}\right) = K_E \Delta T_L \end{aligned} \tag{2.23}$$

Accordingly, the expression of the internal irreversibilitiy becomes,

$$\Delta S_F = \frac{K_{AC} \Delta T_M \Theta_{AC}}{T_{Ai}} - \frac{K_G \Delta T_H \Theta_G}{T_{Gi}} - \frac{K_E \Delta T_L \Theta_E}{T_{Ei}} \tag{2.24}$$

Temperature difference parameters at the constitutive heat exchangers, t_H, t_M and t_L, are defined in a dimensionless form (eq. 2.25) suitable to represent the interaction of the system with the external heat sources.

$$\begin{aligned} t_H &= \frac{\Delta T_H}{T_{Hi}} \rightarrow \frac{\Delta T_H}{T_{Gi}} = \frac{\Delta T_H}{T_{Hi}} \frac{T_{Hi}}{T_{Hi} - \Delta T_H} = \frac{t_H}{1-t_H} \\ t_M &= \frac{\Delta T_M}{T_{Mi}} \rightarrow \frac{\Delta T_M}{T_{Ai}} = \frac{\Delta T_m}{T_{Mi}} \frac{T_{Mi}}{T_{Mi} + \Delta T_M} = \frac{t_M}{1+t_M} \\ t_L &= \frac{\Delta T_L}{T_{Li}} \rightarrow \frac{\Delta T_L}{T_{Ei}} = \frac{\Delta T_L}{T_{Li}} \frac{T_{Li}}{T_{Li} - \Delta T_L} = \frac{t_L}{1-t_L} \end{aligned} \tag{2.25}$$

Going back to the system irreversibility, a dimensionless expression can be obtained (eq. 2.26).

$$G = \frac{t_M}{1+t_M} \phi_{\theta'} - \frac{t_H}{1-t_H} \phi_{\theta''} - \frac{t_L}{1-t_L} \tag{2.26}$$

Where,

$$\begin{aligned} G &= \frac{\Delta S_F}{K_E \Theta_E} \\ \phi_{\theta'} &= \frac{K_{AC} \Theta_{AC}}{K_E \Theta_E} \\ \phi_{\theta''} &= \frac{K_G \Theta_G}{K_E \Theta_E} \end{aligned} \tag{2.27}$$

The simple observation that entropy and heat exchangers' heat conductance have the same physical dimensions (see for example eq. 2.27) gives an idea about the importance of properly design these components by taking into account the related heat transfer irreversibilities. In parallel, the dimensionless parameters defined above can be used to express the COP of the system.

$$\frac{1}{COP}=\frac{|Q_G|}{|Q_E|}=\frac{Q_A+Q_C-Q_E}{|Q_E|}=\phi_t\frac{t_M}{t_L}-1 \tag{2.28}$$

$$\phi_t=\frac{K_{AC}T_{Mi}}{K_E T_{Li}} \tag{2.29}$$

Finally, using the dimensionless expression of the global entropy variation G, it is possible to generalise the absorption chiller efficiency as a function of either t_H and t_M (eq. 2.30) or t_H and t_L (eq. 2.31).

$$\frac{1}{COP}=\phi_t\frac{t_M\left[(1-G)(1+t_M)(1-t_H)+t_M\phi_{\theta'}(1-t_H)-t_H\phi_{\theta''}(1+t_M)\right]}{t_M\phi_{\theta'}(1-t_H)-t_H\phi_{\theta''}(1+t_M)-G(1-t_H)(1+t_M)}-1 \tag{2.30}$$

$$\frac{1}{COP}=\phi_t\frac{G(1-t_H)(1-t_L)+t_H\phi_{\theta''}(1-t_L)+t_L(1-t_H)}{t_L\left[(\phi_{\theta'}-G)(1-t_H)(1-t_L)-t_H\phi_{\theta''}(1-t_L)-t_L(1-t_H)\right]}-1 \tag{2.31}$$

2.3. Results and discussion

The following analysis is based on input experimental data and operative parameters referred to previous literature, and it is intended to explore results, potentiality and feasibility of the present thermodynamic approach.

Table 2.1 Operative parameters from literature experimental data

Parameter		[41]	[36]
T_{Hi}	K	388.25	390.85
T_{Gi}	K	366.83	359.31
T_{Go}	K	377.75	/
T_{Mi}	K	302.15	302.55
T_{Ci}	K	321.45	317.45
T_{Co}	K	311.85	313.85
T_{Ai}	K	325.71	330.04
T_{Ao}	K	316.54	314.58
T_{Li}	K	285.25	284.95
T_{Ei}	K	278.25	278.75
T_{Eo}	K	278.25	278.75
K_G	kW/K	82.58	63.40
K_{CA}	kW/K	140.07	103.00
K_E	kW/K	203.56	86.60
ω_H		0.64	0.66
ω_L		0.60	0.58
COP		0.68	0.63

Table 2.2 Dimensionless parameters calculated from literature data

	Θ_E	Θ_{AC}	Θ_G	t_H	t_M	t_L	ϕ_t	$\phi_{\theta'}$	$\phi_{\theta''}$	G	COP
[41]	1.00	0.78	0.56	0.05	0.08	0.02	0.73	0.54	0.23	0.001	0.741
[36]	1.00	0.69	0.22	0.08	0.09	0.02	0.56	0.36	0.06	0.003	0.738

Table 2.2 makes evidence that the present analysis method tends to slightly overestimate the cycle COP. This could be mainly related to the significance of heat loss and the assumption of negligible work of the circulation pump in the particularly selected system.

Since the analytical interpretation of eq.s 2.30 and 2.31 is complex and could result to be obscure in its content, a graphical approach is more convenient and understandable. Figures 2.3 and 2.4 represent COP curves as a function of either t_L or t_M, respectively, for different values of t_H and ϕ_t, being other parameters set constant as the values calculated from R. Tozer et al. (2005) [41] in Table 2.2. These graphs make evidence of the occurrence of a maximal COP, signifying the possibility to optimise the system operability when the system has already been designed and all the operative parameters, except either t_L or t_M, are set at their nominal value. This means that, given a certain system, by acting on the inlet temperatures of either the absorber/condenser or the evaporator it is possible to operate at highest system efficiency. Dashed lines are obtained for the literature value of the secondary variable, and the markers represent the operative condition of the real plant from R. Tozer et al. (2005) [41]. The comparison between actual and maximum efficiency conditions points out that there is room for system improvement. In this way, it is possible to perform system diagnostic and show how to improve the overall system efficiency.

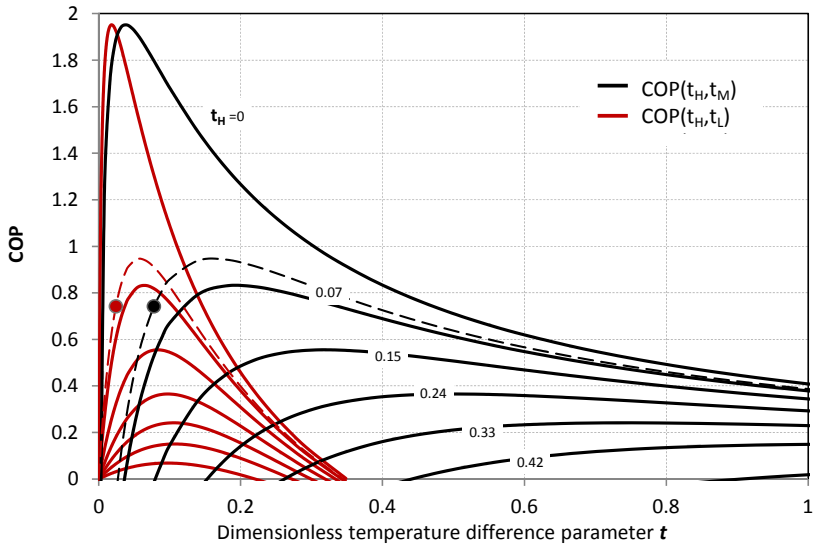

Fig. 2.3 COP curves as a function of either t_L and t_M for different values of t_H

Fig. 2.4 shows how the values of the temperature difference parameters maximising the system COP are independent of ϕ_t, but the maximal COP increases with lower values of this dimensionless parameter.

This effect can be expounded by considering the definition of ϕ_t and its physical meaning; from a technical point of view, lower values of this parameter resemble smaller absorbers and condenser for the same cooling effect (which requires the same amount of steadily absorbed/desorbed refrigerant) and temperature levels, i.e. higher local transfer rates; these, in principle, could be obtained operating at lower solution flowrates if film breaking is avoided, employing liquid surfactants or surface enhanced tubes (or a proper combination of these possibilities). Alternatively, the same beneficial effect could be achieved with the same components, by achieving the same absorption rate at a lower absorber temperature.

Given the discrepancy between the experimental values of the temperature difference parameters in the absorption chiller plant of R. Tozer et al. (2005) [41], and the optimal values suggested by the analysis, a higher temperature difference at the low and intermediate temperature heat exchangers for the same high temperature conditions, or, ceteris paribus, a lower temperature difference at the generator, will bring the system closer to the maximum first law efficiency.

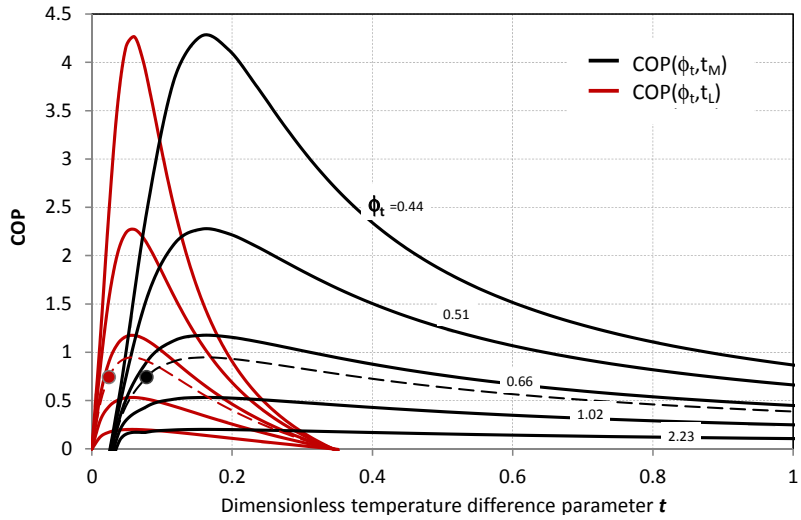

Fig. 2.4 COP curves as a function of either t_L and t_M for different values of ϕ_t

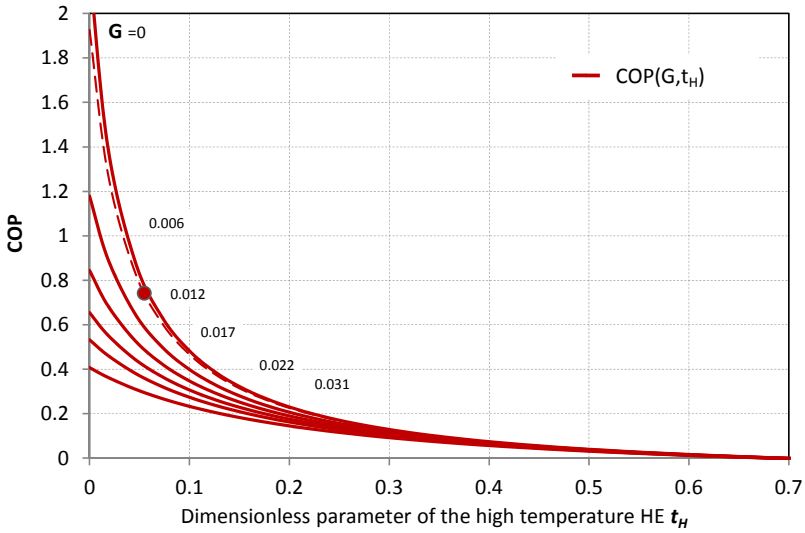

Fig. 2.5 COP curves as a function of t_H for different values of G

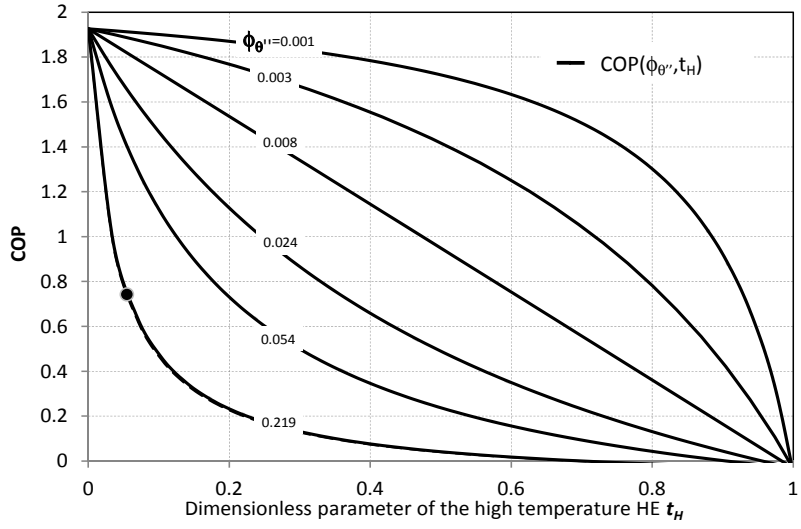

Fig. 2.6 COP curves as a function of t_H for different values of $\phi_{\theta''}$

In case the dimensionless parameter representing the cyclic irreversibility G and the temperature parameter defined for the high temperature thermal source t_H are used as variables, when those are increased the COP shows a relentlessly decreasing trend (Fig. 2.5).

The same statement is valid with reference to $\phi_{\theta''}$ and t_H (Fig. 2.6), while the opposite trend is shown with respect to $\phi_{\theta'}$ (Fig. 2.7). Thus, referring to the definition of this latter parameter (eq. 2.27), in general, an extension of the heat conductance associated to the absorber and the condenser could be beneficial for the overall system performance.

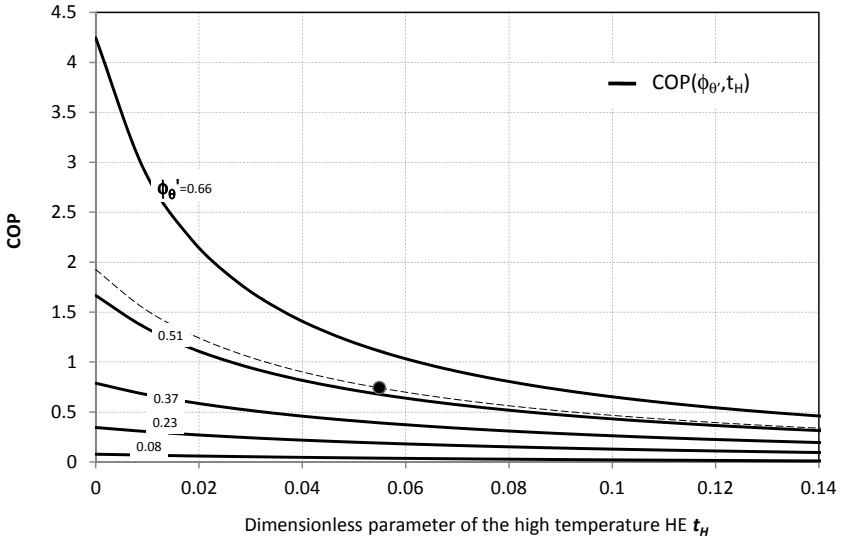

Fig. 2.7 COP curves as a function of t_H for different values of $\phi_{\theta'}$

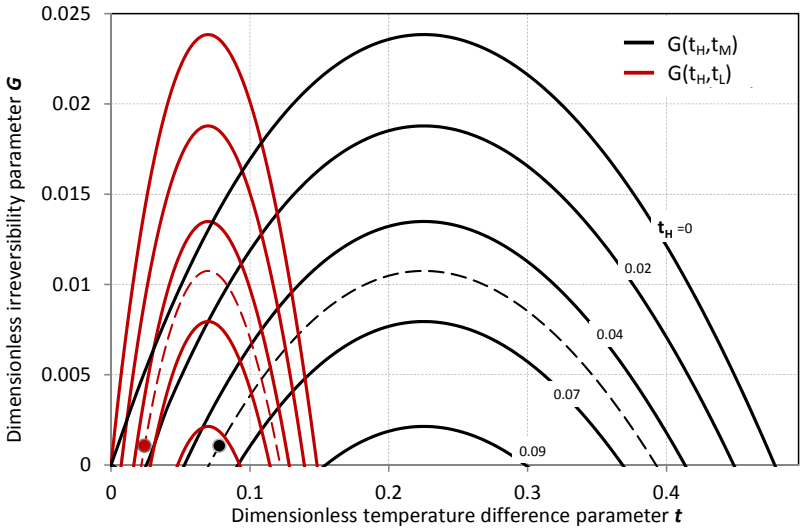

Fig. 2.8 G curves as a function of either t_L and t_M for different values of t_H

Furthermore, if the COP value is preliminarily fixed or defined as an objective parameter at its value of interest, the main dimensionless parameters for the system design can be related as follows.

$$G = \frac{t_H \phi_{\theta''}\left(t_L - 1\right) + t_L\left(t_H - 1\right)}{\left(1 - t_H\right)\left(1 - t_L\right)} + \frac{\phi_{\theta'} t_L \left(1 + COP\right)}{t_L\left(1 + COP\right) + COP\phi_t} \tag{2.32}$$

$$G = \frac{t_M \phi_{\theta'}\left(1-t_H\right) - t_H \phi_{\theta''}\left(1+t_M\right)}{\left(1-t_H\right)\left(1+t_M\right)} - \frac{t_M COP \phi_t}{\left(1+COP\right) - t_M COP \phi_t} \tag{2.33}$$

Figures 2.8 and 2.9 portray the influence of some among the main dimensionless parameters on the dimensionless irreversibility function G at constant COP (fixed at the reference value from [41] calculated in table 2.2), as analytically expressed in eq. 2.32 and eq. 2.33. Given the fact that G is a dimensionless form of entropy variation which combines first and second principles of thermodynamics over a cyclic steady functioning of the system, its value symbolizes the global operative irreversibilities transferred outside through heat exchangers and, hence, it's required to be positive. By observing Fig. 2.8, the dimensionless parameter G outlines a range limitation of the dimensionless temperature parameters t_L and t_M for a fixed value of the system COP. These practicable ranges narrow down for higher t_H. Moreover, with respect to the same parameters, a maximum value of G can always be associated to defined values of t_L and t_M, and those values depends on the dimensionless heat conductance parameter ϕ_t (Fig. 2.9), but not on t_H (Fig. 2.8).

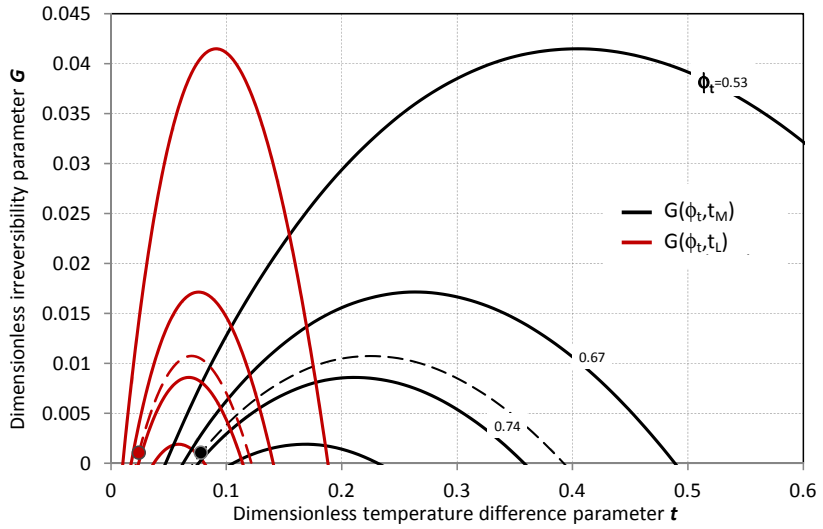

Fig. 2.9 G curves as a function of either t_L and t_M for different values of ϕ_t

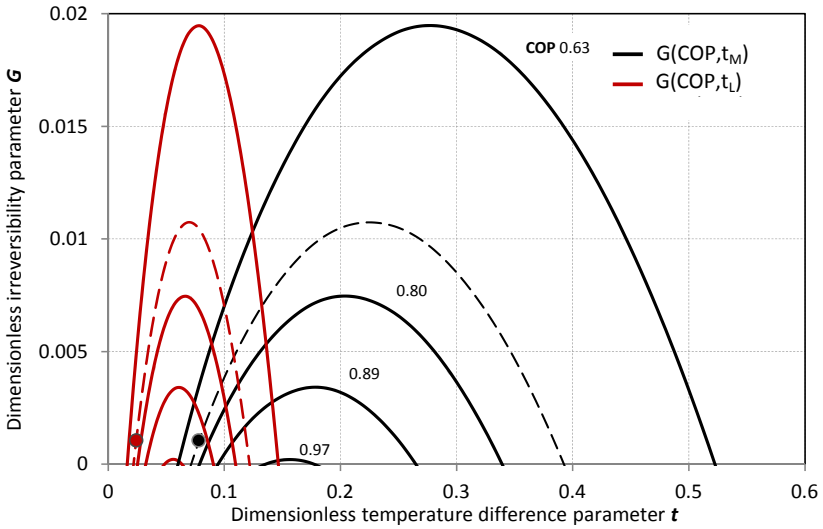

Fig. 2.10 G curves as a function of either t_L and t_M for different values of COP

This practicable range narrows down for higher t_H. Also, for each defined value of the system COP, the positive range of G defines a maximum value of t_H, above which the system cannot reach that objective value of the COP. Moreover, with respect to the same parameters, a maximum value of G can always be associated to defined values of t_L and t_M, and those values depends on the dimensionless heat conductance parameter ϕ_t (Fig. 2.9), but not on t_H (Fig. 2.8). Figure 2.9 highlights that the value of ϕ_t is also limited by a maximum value. It can be stressed once again the importance of the parameters related to the characteristics of the absorber; in particular, higher heat conductance of the absorber (higher ϕ_t) are associated to considerably lower irreversibility G. The operative condition of the real system described by R. Tozer et al. (2005) [41] is plotted in figures 2.8, 2.9 and 2.10, where it is obvious that the system is designed for low irreversibility operability.

Figure 2.10 displays how the operative range of the temperature parameters t_L and t_M narrows down for increasing target COP, showing as well how COP is limited to a maximum endoreversible value for given operative condition of the system.

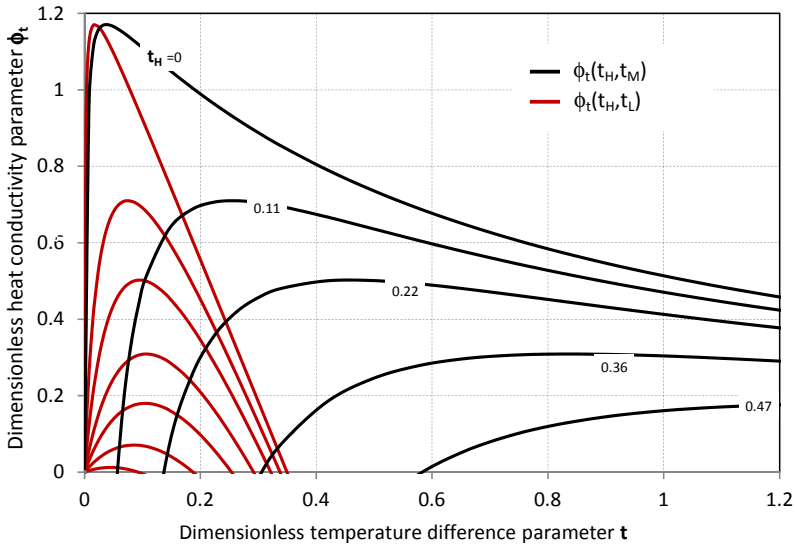

Fig. 2.11 ϕ_t curves as a function of either t_L and t_M for different values of t_H

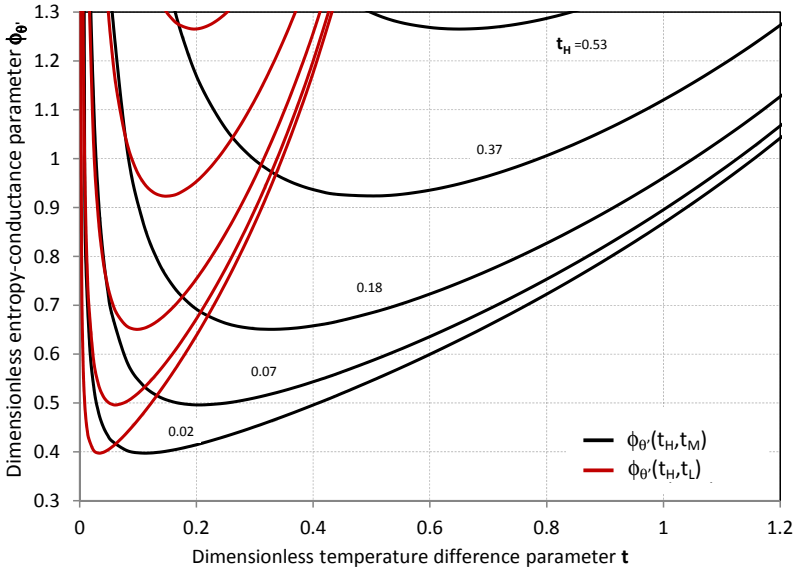

Fig. 2.12 $\phi_{\theta'}$ curves as a function of either t_L and t_M for different values of t_H

When the dimensionless heat conductance parameter ϕ_t is studied as an independent function, figure 2.11 makes evidence of the analogy between this parameter and the COP trend with respect to the same independent parameters. Once again this stresses the importance of properly allocate the transfer area of the fundamental heat exchangers (absorber and evaporator in particular) to design optimised systems.

To conclude the parametric analysis of this exemplifying case, the dimensionless entropy-conductance parameters $\phi_{\theta'}$ and $\phi_{\theta''}$ are studied as dependent function of the fundamental temperature parameters. Precisely, $\phi_{\theta'}$ is a monotonically increasing function of t_H, whereas a local minimum can always be identified for a specific value of both t_L and t_M, where position and value moves higher for increasing t_H (Fig. 2.12). Conversely, is monotonically decreasing with t_H, and is characterised by a local maximum associated to a particular value of t_L and t_M, which are independent on t_H. Additionally, the operative ranges of t_L and t_M are not dependent on t_H (Fig. 2.13).

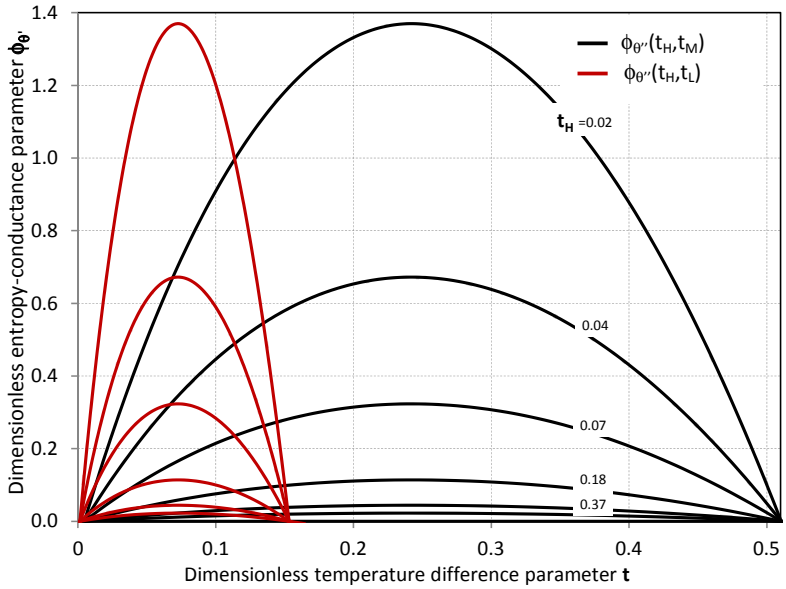

Fig. 2.13 $\phi_{\theta''}$ curves as a function of either t_L and t_M for different values of t_H

Summing up, based on an approximated analytical thermodynamic model of the absorption cycle (eq.s 2.14-2.22), this approach presents significant solutions of the key cycle performance by considering the influence of internal irreversibilities due to temperature and concentration variations of the refrigerant and the absorptive solution. Namely, neglecting pressure losses inside the heat exchangers, Q_{AC}, Q_G and Q_E can be calculated once concentration, temperatures and thermodynamic properties of the fluids are available. The dimensionless parameter G stands for the effect of internal irreversibility of the cycle and shows critical impact on the overall performance. When other thermal exchanges are overlooked, refrigerant and absorptive solution irreversibilities of the system steady cycle are transferred outside to the finite heat capacity sources through the heat exchangers. In capturing the fundamental physical phenomena involved and overcoming the limit of the endo-reversible cycle, also leaving flexibility in generalising results to other absorption devices, this model provides a useful predictive and diagnostic tool. The dimensionless parameters defined are suitable for an overall system optimisation, and by investigating their influence on best cycle efficiency a first screening of the parameters relevant for the system design and control has been performed. In particular, by relating cycle efficiency and entropy variation rates through specifically defined dimensionless parameters it is possible to design optimised systems and enhance the performance of existing ones. By acting on the heat exchangers temperature differences, represented by the corresponding parameters t_L, t_M and t_H, it is possible to maximise the COP of the system. Comparing experimental data from literature with the optimal performance suggested by this analysis, possible improvement of the system thermodynamic efficiency can be attained. Furthermore, the

absorption refrigeration cycle model and the thermodynamic analysis can be readily extended to heat pump and heat transformer application cases.

2.4. Heat transformers

Absorption heat transformers distinguish themselves to other energy conversion systems with a unique characteristic, which is to thermally deliver part of the earliest amount of heat input from the generator and evaporator temperature level to a higher temperature, requiring a minimal amount of input work or electricity expenditure.

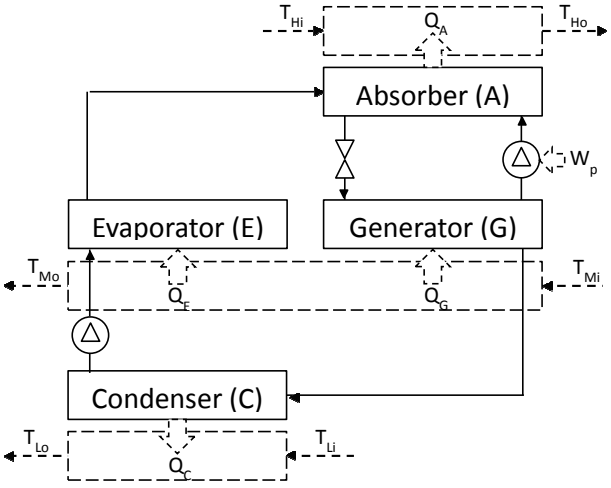

Fig. 2.14 Schematic of an absorption heat transformer

These systems are being increasingly utilised to generate steam from medium temperature waste heat, so that the latter can be reintroduced in the production/utilisation process and reused. Furthermore, these systems are promisingly being designed to meet the requirements of plants conceived for many different renewable sources application cases. A considerable amount of literature has been published about theoretical and experimental studies on different configurations and applications [7) 9) 46-48)].

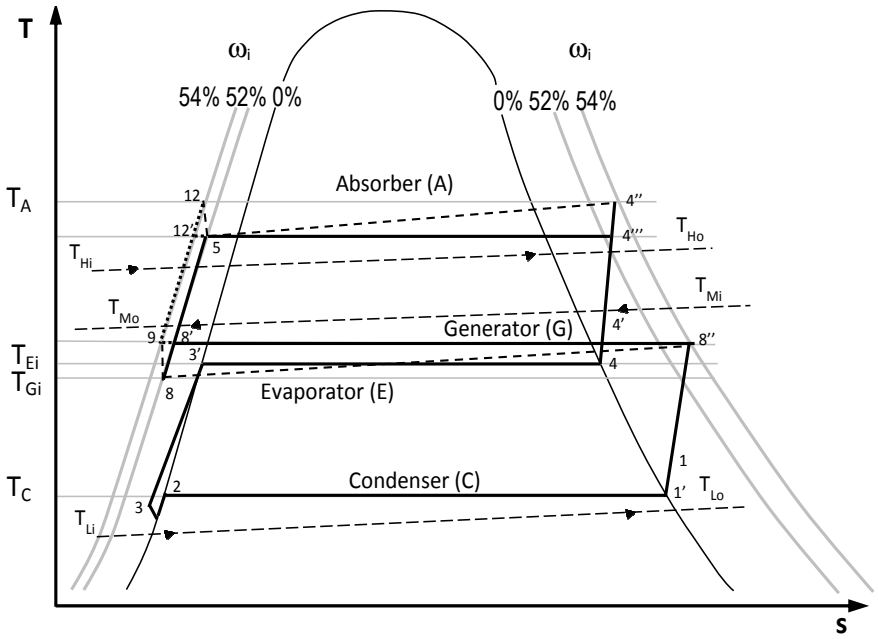

Fig. 2.15 T-s Diagram of an absorption heat transformer

Considering an absorption heat transformer application case (Schematically illustrated in Fig. 2.14), under the assumptions stated in the previous section, the COP of the system is defined as the ratio of the power released at the absorber to the total heat input at the generator and evaporator. In this application case, eq. 2.11 is rearranged to represent the entropy variation occurring at the three temperature levels of a single-stage heat transformer (eq. 2.34).

$$\Delta S_F = Q_A \frac{\left(\varphi\Delta s_{RA} + \Delta s_{SA}\right)}{\left(\varphi\Delta h_{RA} + \Delta h_{SA}\right)} - \left(Q_G + Q_E\right)\frac{\left[\varphi\Delta s_{RE} + \left(\varphi\Delta s_{RG} + \Delta s_{SG}\right)\right]}{\left[\varphi\Delta h_{RE} + \left(\varphi\Delta h_{RG} + \Delta h_{SG}\right)\right]} + Q_C \frac{\Delta s_{RC}}{\Delta h_{RC}} \tag{2.34}$$

An approximate cycle of the system is represented by the black lines in figure 2.15, where generator and evaporator temperatures are assumed to be close enough to be embedded in a single thermodynamic component (representing the two real heat exchangers), and, consistently with the previously presented analysis, the vapour generation/absorption processes are split into traceable transformations; a constant concentration part where temperature changes to reach the equilibrium temperature at the generator/absorber, an isothermal transformation representing the release/absorption of the heat of absorption, and an isobaric segment to cool down to its saturation temperature the superheated vapour once separated from the solution at its equilibrium.

By defining apposite dimensionless parameters characterising the transformations followed by the refrigerant and the liquid solution in this configuration, eq. 2.35 can be written.

$$\Delta S_F = -\frac{\left(Q_G + Q_E\right)}{T_{Ei}}\Theta_{GE} + \frac{Q_A}{T_{Ai}}\Theta_A + \frac{Q_C}{T_{Ci}}\Theta_C \tag{2.35}$$

Where,

$$\begin{aligned}
\Theta_{GE} &= \frac{T_{Ei}\left[\varphi\Delta s_{RE} + \left(\varphi\Delta s_{RG} + \Delta s_{SG}\right)\right]}{\left[\varphi\Delta h_{RE} + \left(\varphi\Delta h_{RG} + \Delta h_{SG}\right)\right]} \\
\Theta_A &= \frac{T_{Ai}\left(\varphi\Delta s_{RA} + \Delta s_{SA}\right)}{\left(\varphi\Delta h_{RA} + \Delta h_{SA}\right)} \\
\Theta_C &= \frac{T_{Ci}\Delta s_{RC}}{\Delta h_{RC}}
\end{aligned} \tag{2.36}$$

Further adapting the definition of heat exchangers effectiveness (eq. 2.23) and dimensionless parameters t_H, t_M and t_L, eq. 2.37 can be applied.

$$\begin{aligned}
\frac{\Delta T_H}{T_{Ai}} &= \frac{\Delta T_H}{T_{Hi}}\frac{T_{Hi}}{T_{Hi} + \Delta T_H} = \frac{t_H}{1 + t_H} \\
\frac{\Delta T_M}{T_{Ei}} &= \frac{\Delta T_m}{T_{Mi}}\frac{T_{Mi}}{T_{Mi} - \Delta T_M} = \frac{t_M}{1 - t_M} \\
\frac{\Delta T_L}{T_{Ci}} &= \frac{\Delta T_L}{T_{Li}}\frac{T_{Li}}{T_{Li} + \Delta T_L} = \frac{t_L}{1 + t_L}
\end{aligned} \tag{2.37}$$

A specific dimensionless expression of the cyclic irreversibility is consistently obtained.

$$G = \frac{t_H}{1+t_H}\phi_{\theta''} - \frac{t_M}{1-t_M}\phi_{\theta'} + \frac{t_L}{1+t_L} \tag{2.38}$$

Where, the dimensionless parameters appearing are defined according to eq. 2.39.

$$\begin{aligned} G &= \frac{\Delta S_F}{K_C \Theta_C} \\ \phi_{\theta'} &= \frac{K_{GE}\Theta_{GE}}{K_C \Theta_C} \\ \phi_{\theta''} &= \frac{K_A \Theta_A}{K_C \Theta_C} \end{aligned} \tag{2.39}$$

And the COP of the system can be expressed as a function of the dimensionless temperature parameters defined above and ϕ_t.

$$COP = \frac{|Q_A|}{|Q_G + Q_E|} = \frac{Q_G + Q_E - Q_C}{|Q_G + Q_E|} = 1 - \phi_t \frac{t_L}{t_M} \tag{2.40}$$

$$\phi_t = \frac{K_C T_{Li}}{K_{GE} T_{Mi}} \tag{2.41}$$

Using the dimensionless expression of the cycle entropy variation G, it is possible to generalise the heat transformer efficiency as a function of either t_H and t_M (eq. 2.42) or t_H and t_L (eq. 2.43).

$$COP = 1 - \phi_t \frac{-t_M \phi_{\theta'}(1+t_H) + t_H \phi_{\theta''}(1-t_M) - G(1+t_H)(1-t_M)}{t_M\left[(1-G)(1-t_M)(1+t_H) + t_M \phi_{\theta'}(1+t_H) - t_H \phi_{\theta''}(1-t_M)\right]} \tag{2.42}$$

$$COP = 1 - \phi_t \frac{t_L\left[(\phi_{\theta'} - G)(1+t_H)(1+t_L) + t_H \phi_{\theta''}(1+t_L) + t_L(1+t_H)\right]}{-G(1+t_H)(1+t_L) + t_H \phi_{\theta''}(1+t_L) + t_L(1+t_H)} \tag{2.43}$$

2.5. Results and discussion

To extend the results and analyse the potentiality of this thermodynamic approach, the following study is also based on input experimental data from literature.

Table 2.3 contains measured values of the working parameters from an operative single stage heat transformer [49]. Table 2.4 shows the values of the dimensionless parameters previously defined. Correspondingly to the previous exemplifying case, the present analysis method tends to slightly overestimate the cycle COP (Table 2.4). This could be mainly related to the relatively important impact of heat loss and the assumption of negligible work of the circulation pump. Since, again, the analytical interpretation of eq.s 2.42 and 2.43 could be obscure, a graphical approach is more convenient and understandable.

Figure 2.16 exhibits constantly increasing COP curves as a function of either t_H (red lines) and t_M (black lines), for different values of t_L, being other parameters set constant as calculated from W. Rivera et al. (2011) [49] in Table 2.4. The opposite trend is shown with respect to t_L. Dashed lines are obtained for the literature value of the secondary variable considered in each graph and the markers represent the operative condition of the real system from W. Rivera et al.

(2011) [49] (Table 2.4). In this case as well, by comparing the measured efficiency with the performance maps obtained, it is possible to perform system diagnostic and show how to improve the overall system efficiency.

Table 2.3 Operative parameters of a single-stage heat transformer from literature experimental data

Parameter		Test1 [49]	Test2 [49]
T_{Hi}	[K]	359.75	359.25
T_{Gi}	[K]	347.93	352.53
T_{Go}	[K]	351.00	355.60
T_{Mi}	[K]	359.75	359.25
T_{Ci}	[K]	318.19	322.76
T_{Co}	[K]	297.85	296.35
T_{Ai}	[K]	381.14	382.22
T_{Ao}	[K]	377.90	378.99
T_{Li}	[K]	294.65	292.85
T_{Ei}	[K]	344.76	346.26
T_{Eo}	[K]	353.25	352.45
K_A	[kW·K^{-1}]	0.03	0.03
K_{GE}	[kW·K^{-1}]	0.03	0.03
K_C [	[kW·K^{-1}]	0.03	0.02
ω_H	[-]	0.54	0.54
ω_L	[-]	0.52	0.52
COP	[-]	0.27	0.32

Looking at the data from W. Rivera et al. (2011) [49], increasing the temperature difference at the high and intermediate temperature heat exchangers, for the same low temperature value, or, ceteris paribus, decreasing the temperature difference at the condenser (higher t_L), will increase the first law efficiency of the system.

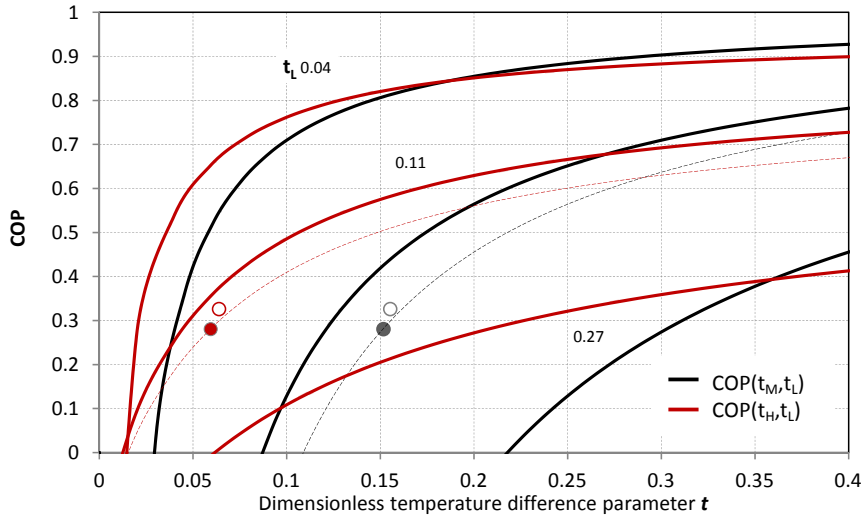

Fig. 2.16 COP curves as a function of either t_H (red lines) or t_M (black lines) for different values of t_L

Table 2.4 Dimensionless parameters for a single-stage heat transformer calculated from literature data

	Θ_C	Θ_{GE}	Θ_A	t_H	t_M	t_L	ϕ_t	$\phi_{\theta'}$	$\phi_{\theta''}$	G	COP
Test1 [49]	0.88	0.84	1.05	0.06	0.15	0.13	0.81	0.96	1.31	0.021	0.280
Test2 [49]	0.89	0.83	1.05	0.06	0.16	0.16	0.64	1.19	1.47	0.010	0.326

Figure 2.16 exemplifies the performance of the same system operating in two different conditions, respectively test1 (filled markers) and test2 (empty markers) from W. Rivera et al. (2011) [49], showing that an increase of the temperature difference at either the generator/evaporator or at the absorber increases the overall efficiency. However, to maintain a correct system operability the values of the temperature parameters are required to be positive and, since G stands for the total irreveribilities, limited to those giving positive values of this parameter.

COP curves as a function of either t_L (red lines) and t_M (black lines) for different values of ϕ_t or t_H are displayed, respectively, in figures 2.17 (a) and (b) show. It can be stated that decreasing either t_L or t_M is advantageous for the system when t_H and ϕ_t, and accordingly G, are fixed.

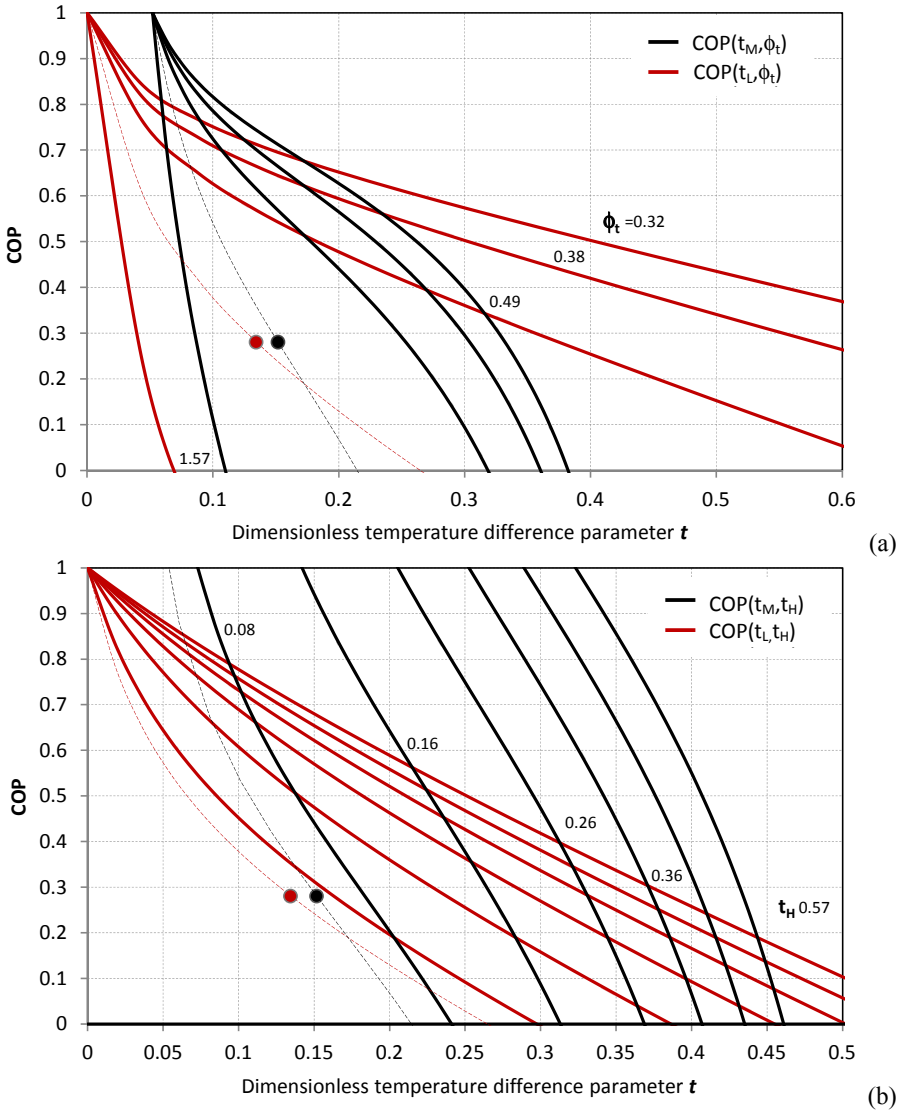

Fig. 2.17 COP curves as a function of either t_L or t_M for different values of ϕ_t (a) and (b) t_H

Figures 2.18 (a) and (b) consider COP curves as a function of either ϕ_θ (red lines) or $\phi_{\theta'}$ (black lines), respectively, for different values of t_H or t_M. It can be observed that, when G is fixed, either by increasing $\phi_{\theta'}$ or decreasing ϕ_θ is beneficial for the system performance. This observation implies that a higher fraction of exchange surface allocated to the absorber will increase significantly the COP of a heat transformer, once the size of the system and the proportion of internal irreversibility are constrained. However, the corresponding change of the thermodynamic transformations responsible for determining the values of the main dimensionless parameters, might actually conflict with the result of

this analysis, which consider constant values of other parameters when the variables are changed. Thus, careful attention should be directed to this circumstance when the performance maps represented by the obtained graphs are analysed.

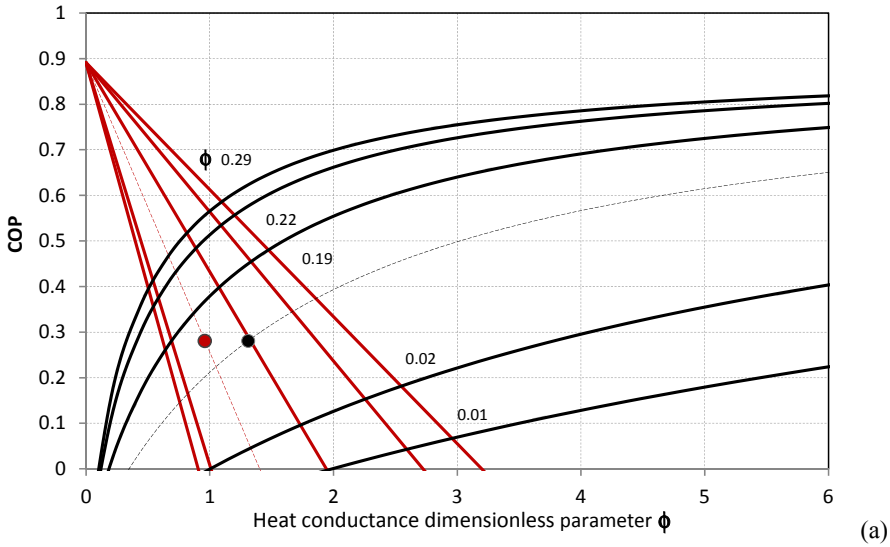

(a)

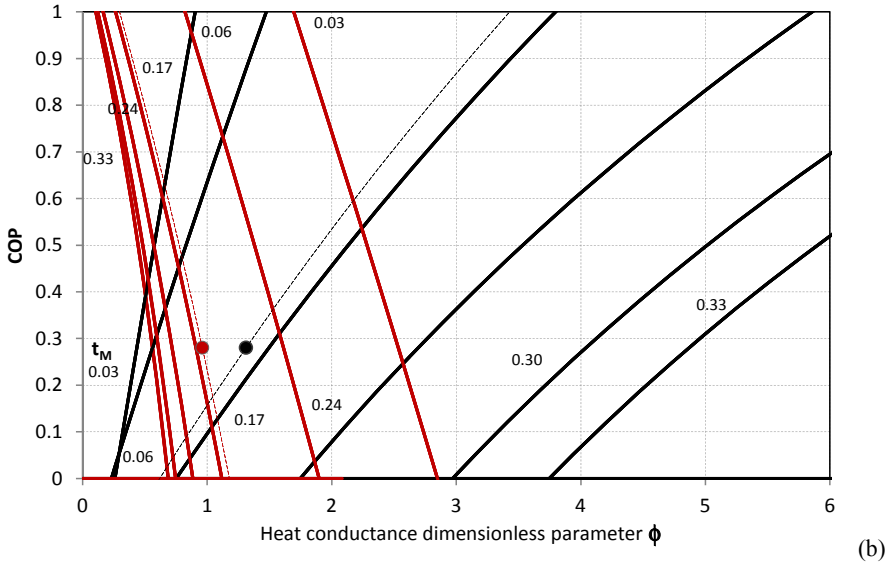

(b)

Fig. 2.18 *COP* curves as a function of $\phi_{\theta'}$ (red lines) *or* $\phi_{\theta''}$ (black lines) for different values of t_H (a) or t_M (b)

When t_H (the temperature parameter defined for the high temperature thermal source) and the dimensionless parameter representing the irreversibility of the cycle G are used as variables, when t_H is increased the system COP results in a relentlessly decreasing trend, whereas the opposite tendency is shown with respect to the first (Fig. 2.19).

With the same approach used for a chiller application, the COP can be set as a target factor and the main dimensionless parameters for system design can be related as follows.

$$G=\frac{t_H\phi_{\theta''}\left(1-t_M\right)-t_M\phi_{\theta'}\left(1+t_H\right)}{\left(1+t_H\right)\left(1-t_M\right)}-\frac{\left(COP-1\right)t_M}{\phi_t-\left(COP-1\right)t_M} \tag{2.44}$$

$$G = \frac{t_H \phi_{\theta''}\left(1+t_L\right)+t_L\left(1+t_H\right)}{\left(1+t_H\right)\left(1+t_L\right)} - \frac{\phi_{\theta'}\phi_t t_L}{1-COP-\phi_t t_L} \tag{2.45}$$

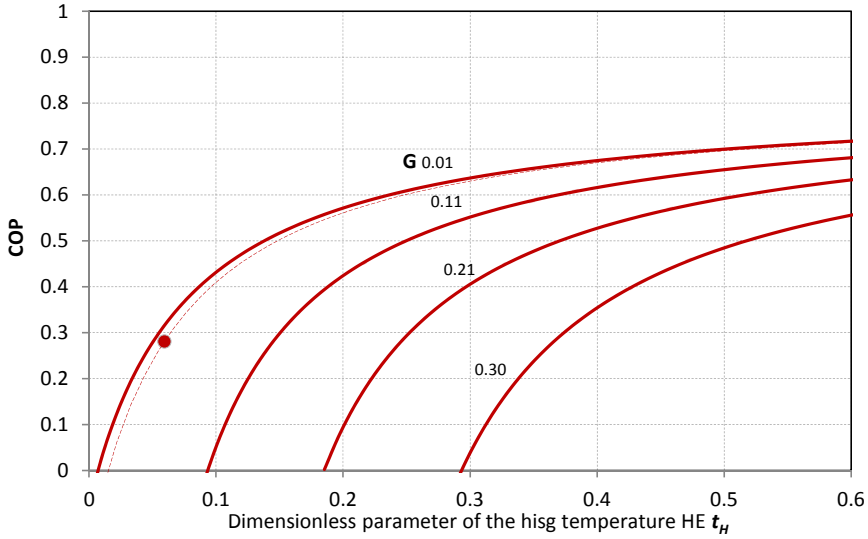

Fig. 2.19 *COP* curves as a function of t_H for different values of G

The influence of the main dimensionless parameters on the dimensionless function G at constant COP (set at value calculated in Table 2.4 from the data used as a reference W. Rivera et al. (2011) [49]) is demonstrated in figures 2.20, 2.21 and 2.22 as analytically stated in eq. 2.44 and eq. 2.45.

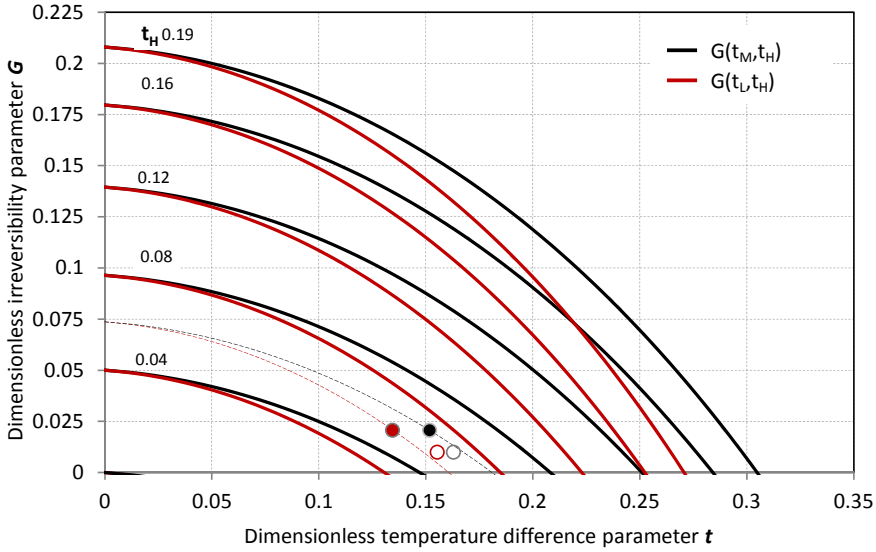

Fig. 2.20 G curves as a function of t_L (red lines) and t_M (black lines) for different values of t_H

By observing figure 2.20, the dimensionless parameter G, which combines first and second principles of thermodynamics, outlines a range limitation of the temperature difference parameters t_L and t_M for a given value of t_H, ϕ_t and system COP. These feasibility ranges narrow down at lower t_H. G is maximum when t_L and t_M are zero, and is constantly decreasing with respect to the same parameters. Moreover, a maximum value of G can always be associated to defined values of t_L and t_M, and those values depends on the dimensionless heat conductance parameter ϕ_t (Fig. 2.17),

and on COP (Fig. 2.18), but not on the value of t_H. The operative conditions of the real system described by [14] are plotted in figure 2.20, where it is evident that the system has been designed for low irreversibility operability, and that test2 brings the system to a less irreversible condition and to a higher COP (Fig. 2.16).

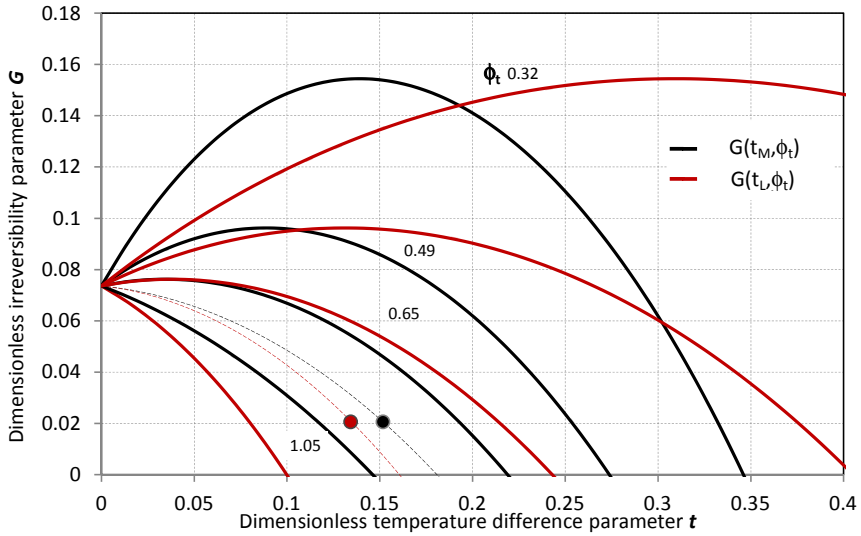

Fig. 2.21 G curves as a function of either t_L (red lines) and t_M (black lines) for different values of ϕ_t

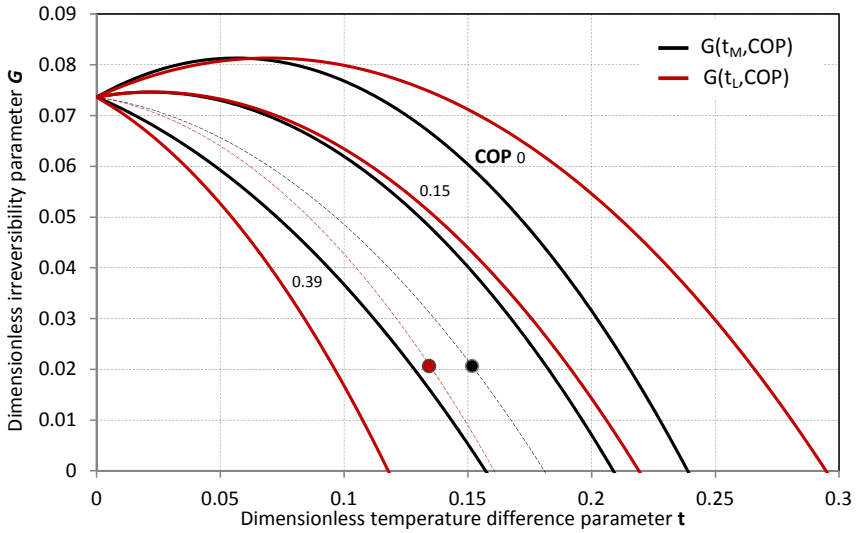

Fig. 2.22 G curves as a function of either t_L (red lines) and t_M (black lines) for different values of COP

2.6 Summary

This approach constitutes a general thermodynamic criterion for the performance investigation and optimisation of three-thermal irreversible systems.

Based on a general thermodynamic model of three-thermal cycles with finite thermal capacity of the heat sources and on an analytic thermodynamic approach for the transformation internal to the absorption cycle, significant solutions of the performance of heat transformer and absorption chiller configurations have been globally studied by considering the impact of the internal irreversibility of the refrigerant and the absorptive solution on the system key performance. Contributions due to temperature and solution concentration variations are included in the analytical expression of the system efficiency through the values of the fundamental parameters defined. The use of this criterion has been

exemplified for specific data of a heat transformer and an absorption chiller from previous literature. Dimensionless parameters for an overall system optimisation and control are defined, and a first parametric analysis is performed to clarify their influence. Dependence on the main elements is highlighted in a way that suggests how to change them in order to enhance the system COP. By acting on the heat exchangers temperature differences, represented by the corresponding parameters t_L, t_M and t_H, it is possible to increase the COP of existing systems. Comparing experimental data from literature with the performance suggested by this analysis possible improvement of the system thermodynamic efficiency are pointed out. Under this point of view, the analysis evaluates overall performance improvements and can be used to perform existing plant diagnostics, besides constituting a preliminary tool for systems' design. The dimensionless parameter G stands for the effect of internal irreversibility of the cycle and shows significant impact on the global performance and helps identifying the limitations imposed to the physical processes constituting the cycle. Specifically, parameters involving the performance of the absorber show critical impact and appear to be the leading design pillars to carefully act on for the construction of a solid and efficiently operating system.

Chapter 2,
Thermodynamic analysis of irreversible absorption systems

Chapter 3, Falling film absorbers optimisation criterion

The thermodynamic analysis presented in the previous chapter and prior literature concerning absorption systems recognise the absorber as the component which affect the plant cost, size and performance the most. This chapter focuses on the details of falling film absorption; however, even though local details could have a minor effect at a small scale, these phenomena might play a major role on the global performance of the process and their inclusion may have a leading impact on the plant operability. On the other hand, not to lose sight of the final objective and how the component characteristics will affect the whole system is crucial for a proper design and control procedure. Under these two main viewpoints, associated to different characteristic scales, local results regarding the process are to be summed up to the higher scale (the component), and used globally to optimise the transfer performance of the absorber, as well as its design features and operational regime, with reference to the final duty of the system. The fundamental model adopted to investigate falling film absorption is centred on the numerical analysis of the fundamental equations of water vapour absorption in a laminar, gravity driven, viscous, incompressible liquid film of aqueous lithium-bromide solution, flowing over a horizontal and internally-cooled tube.

A local entropy irreversibility analysis can be performed referring to velocity, temperature and concentration fields, to characterise qualitatively and in detail the transfer performance of the thermodynamic process. From a general expression of the volumetric entropy generation, a suitable form for representing falling film absorption is obtained and different irreversibility sources are distinguished and analysed. The impact of each term (fluid friction, heat transfer, mass transfer and their coupling effects) is locally examined with respect to the main operative and geometrical parameters; specifically, results are explored for different tube radii, wall temperatures and operative conditions (representing both chiller and heat transformer configurations), in order to characterise the process from a second law point of view and, eventually, to establish the basis of a criterion for the optimisation of the absorber. A least irreversible solution mass flowrate can always be identified and studied in its dependence on the main geometrical and operative conditions of this component. Based on this local thermodynamic approach, this analysis aims at the definition of proper dimensionless parameters for the optimisation of this component regarding the ultimate objective of the system. A simple and general thermodynamic analysis of a refrigerating machine and a heat boosting (heat transformer) applications makes evidence of dimensionless groups that separates the weight of the irreversibilities and transfer performance related to the absorber. These suggest a way to the definition of an optimisation criterion applied to the absorber to designate the condition that will maximise the whole system efficiency. Both thermodynamic equilibrium and sub-cooling conditions of the solution at the inlet are considered for typical temperature and concentration of refrigerators' and heat transformers' absorbers. Also, it is highlighted that the two parameters defined with reference to the dimensionless groups highlighted in the general expression of the system efficiency can be maximised by specific values of the tube radius, operative Reynolds number, solution sub-cooling and temperature difference between the wall and the inlet solution. As a general recurrent conclusion, results suggest the importance to work at reduced solution flowrates with a thin and uniform film.

3.1. Second law analyses

The second law of thermodynamics provides a qualitative description critical to identify the limitations imposed to a process, and its significance is not confined to physics and engineering. Every real process occurring as a part of an energy conversion system is accompanied by an unavoidable degradation of the earliest amount of energy. Regarding this general design-issue, thermal system design and basic thermodynamics are to be employed together with the purpose of identifying the optimum operating regime, topology or size of a certain system, where by "optimum" the least energy decaying (or exergy destroying) condition which can still assure the fundamental engineering function, is intended. Among the number of possible scenarios, entropy generation minimisation can be used to characterise the quality of energy-conversion processes, and develop consistent criteria for the optimisation and control of the system.

From this perspective, the enhancement of efficiency describing the achieved technological progress could be interpreted as a secondary result of an optimal irreversibility distribution and entropy generation minimisation [50].

As for global systems, authors in [32] and [51] have presented a literature review of finite-time thermodynamics optimisation of absorption systems and investigated different possible objective functions. In general, in order to consider the temperature level of the various heat fluxes involved in the energy conversion process, a second law approach is particularly significant for the characterisation of the performance of heat-driven systems. Exergy-based analyses of absorption refrigeration systems, in both their single [52] and multiple effect configurations [53], and heat transformers [54], have been performed to evaluate performance, and exergy loss of the system and its components. As a rule, M. Kilic and C. Kaynakli (2013) [52], S.C. Kaushik and A. Arora (2007) [53], P. Donnellan et al. (2013) [54] and O. Kaynakli (2008) [55] have emphasised that the maximum exergy destruction occurs in the absorber and the analysis and optimisation of this device is crucial for absorption systems operating both in refrigerator or heat transformer applications. In the conventional case of falling film heat exchangers, high transfer coefficients and low pressure drops can be obtained. However, the attempt to theoretically describe and experimentally quantify the complex heat and mass-transfer phenomena occurring inside these devices is still incomplete and has not led to conclusive modelling approaches.

Concerning modelling efforts, A. Yigit (1999) [56], J.W. Andberg and G.C. Vliet (1987) [57], V.D. Papaefthimiou et al. (2012) [58], K. Banasiak and J. Kaziot (2009) [59] and F. Babadi and B. Farhenieh (2005) [60] have discussed simplified models for falling film absorption of water vapour over a horizontal tube. These problem solutions are carried out with a finite difference method to approximate the fundamental differential equations governing heat and mass transfer, and the effects of different parameters on these processes are described.

Entropy generation minimisation has been widely accepted as a method for heat exchangers' design and optimisation [39) 61-67]. This method has been also applied to design counter-flow heat exchangers [39) 50] and combined heat and mass transfer devices [68-70] or desiccant systems [64) 71-72]. Yet, few studies [50) 73-74] have performed local second law analyses of the absorption process itself. In particular, I. Chermiti et al. (2011) [73] and N Hidouri et al. (2013) [74] report an irreversibility analysis based on an analytical study of gas absorption into a laminar, incompressible, gravity-driven, isothermal liquid film flowing over a vertical wall. The main conclusion states that entropy generation is mostly ruled by the simultaneous effects between heat and mass transfer in proximity of the vapour-liquid interface and by viscous irreversibility near the solid wall. However, heat transfer and the tube wall geometry were not comprised in the problem formulation. In fact, simultaneous cooling and absorption allow the process to be maintained far from the thermodynamic equilibrium at which absorption won't occur any longer. Thus, an effective analysis should encompass these features and operative circumstances, which are typical of real absorbers in existing plants.

The main directions and purposes of this chapter stem from a detailed qualitative description of falling film absorption and a proper expression of the local entropy generation rate representing real LiBr-H_2O absorptive films. Thermal, velocity and concentration gradients inside the absorptive film yields a non-equilibrium state, responsible of entropy generation (better defined as entropy variation due to irreversibility). Entropy can be used to evaluate the irreversibility introduced, characterise the quality of energy-conversion, and eventually, develop consistent criteria for the optimisation and control of a component or the system. Besides, entropy constitutes a critical variable especially when the analysis scale is contracted to the order at which macroscopic and microscopic physics come to a shared limit of validity. The question arising is whether, and to what extent, the details of microscopic mechanics influences mechanics at a macroscopic scale. This extremely problematic and not completely resolved threshold, in proximity of which these two "shifted descriptions" of "contemporary universes" ruled by different laws start clashing, is close enough to the scale of the processes involved in transport phenomena in general and absorption in particular.

Conversely, for systems involving intrinsically irreversible transformations the optimisation target should be defined carefully. This is the case of non-equilibrium thermodynamic in general, and vapour absorption in particular; as an instance, mixing and sub-cooling of the absorptive solution increase absorption heat and mass transfer, but these are unavoidably connected to high and incrasing irreversibility. Accordingly, the solution of energy and species transport

equations of falling film absorption around a cooled horizontal tube and the local numerical analysis of the related entropy generation are used as the basis to define suitable objective parameters for the improvement of the whole system performance by means of the optimisation of the absorber.

3.2. Numerical model

The system to be modelled is showed schematically in figure 3.1. A single horizontal tube is considered and the LiBr-H_2O solution flows down over it as a laminar incompressible liquid driven by gravity, while vapour mass transfer occurs at the film interface, and the heat of absorption is rejected to the cooling water circulating inside the tube.

Heat and mass transfer characteristics of this thermodynamic system are studied by solving numerically mass and energy transport equations in a two-dimensional domain defined in the radial and stream-wise directions, under the following main assumptions:

1. The flow is steady, laminar and without interfacial waves.
2. Thermodynamic equilibrium of the solution with the vapour at the film interface.
3. There is no shear force between the liquid film and the vapour.
4. Physical properties are function of the inlet concentration and temperature, but remain constant while the solution is flowing on a single tube.
5. Heat transfer to the vapour phase is negligible.
6. The temperature of the outer tube surface of the tube is constant and directly related to the coolant temperature.
7. Disturbances at the edges of the system are neglected and body fitted coordinates (*x* along the tube surface and *y* normal to it at any point) are used because the film thickness is orders of magnitude lower than the tube circumference [73].

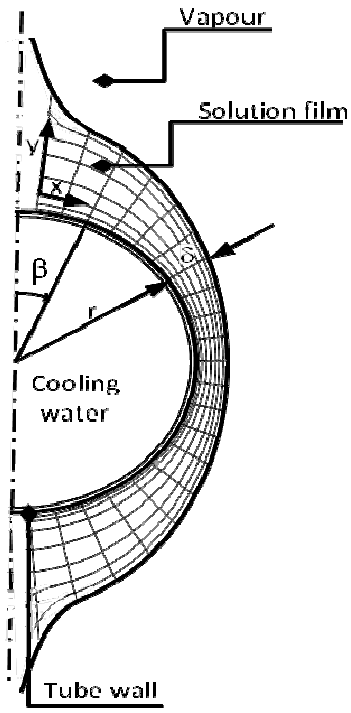

Fig. 3.1 Local coordinate system of the falling absorptive film

The hydrodynamic description is established by the solution of the stream-wise momentum and continuity equations under the assumptions of Nusselt integral theory. The tangential (eq. 3.2) and normal (eq. 3.4) velocity components are then used for the numerical solution of energy (eq. 3.9) and species (eq. 3.10) transport equations, once the general boundary conditions are fixed properly.

The boundary conditions and the simplified momentum equation representing the falling film flowing around the horizontal tube are presented by eq. 3.1.

$$\mu \frac{\partial^2 u}{\partial y^2} = -\rho g \sin\beta \ ; \text{At } y=0;\ u=0 \text{ At } y=\delta;\ \frac{\partial u}{\partial y} = 0 \tag{3.1}$$

Where $\beta=x/r$ and r is the outer tube radius. Eq. 3.1 is solved for the component of velocity u in the body fitted tangential direction x, resulting in the following distribution:

$$u = \frac{\rho g}{\mu} \sin\beta \left(\delta y - \frac{1}{2} y^2 \right) \tag{3.2}$$

The component of the velocity distribution v in the radial direction y can be obtained from the integration of the continuity equation (eq. 3.3), along with the boundary condition at the wall ($y=0$), $v=0$.

$$\frac{\partial u}{\partial x} + \frac{\partial v}{\partial y} = 0 \tag{3.3}$$

Finally obtaining [60]:

$$v = -\frac{\rho g y^2}{2\mu} \left[\frac{d\delta}{dx} \sin\beta + \frac{1}{r} \left(\delta - \frac{y}{3} \right) \cos\beta \right] \tag{3.4}$$

Once the flowing film mass flowrate per unit length is determined in its value and tangential velocity component in its distribution, eq. 3.5 can be written.

$$\Gamma = \int_0^\delta \rho u(y) dy = \frac{1}{3} \frac{\rho^2 g \sin\beta}{\mu} \delta^3 \tag{3.5}$$

Accordingly, eq. 3.6 expresses the film thickness as a function of film mass flowrate, fluid properties and angular position.

$$\delta = \left(\frac{3\mu\Gamma}{\rho^2 g \sin\beta} \right)^{1/3} \tag{3.6}$$

Using this solution for an extended range of conditions would indeed be questionable, due to effects having the upper hand on the film hydrodynamics (i.e. inertia, viscosity or surface tension forces) and actually producing a deviation from the symmetrical distribution predicted by Nusselt equation. Film thickness deviation due to inertia (principally the convective terms in the streamwise direction) can be overwhelming in the second half of the tube, but this deviation is reduced at sufficiently low flowrates (as the range of conditions at which the present analysis is directed) [75].

To proceed towards a solution, the problem formulation needs to be consistently closed by proper boundary conditions.

At $x=0$ and $0<y<\delta$; $T=T_{in}$, $\omega=\omega_{in}$

Along the tube surface the boundary conditions set a constant value of temperature and null diffusion.

At y=0; T=T_w, $\frac{\partial \omega}{\partial y} = 0$

At the interface, temperature is related to interface concentration and the heat exchanger pressure by the thermodynamic equilibrium condition of the absorptive liquid mixture. The correct choice of the boundary condition at a phase interface is still an unresolved subject [76]. Assuming interfacial equilibrium of the solution, constant pressure and neglecting heat transfer and shear forces with the vapour leads to neglect the interfacial resistance to absorption; namely, the entropy jump characterising the microscale resolution of the phase transition interface. This approach is guided by the final purpose of this work, which deals with the overall component optimisation at a macroscopic scale, and this local phenomenon is presently overlooked.

At y=δ, T=T_{sat}(ω_{if},p), ω=ω_{if}

Fick's law of diffusion relates the interface concentration to the interfacial mass flux and to the interdiffusion inside the film (eq. 3.7).

$$G_v = -\frac{\rho D}{\omega_{if}} \frac{\partial \omega}{\partial y} \tag{3.7}$$

And the heat generated by the exothermic property of the absorption process is transported through the film towards the tube surface by conductive heat transfer. This effect can be modelled by Fourier's law of heat conduction (eq. 3.8), once the heat of absorption i_{abs} is known:

$$G_v i_{abs} = k \frac{\partial T}{\partial y} \tag{3.8}$$

Heat and mass transfer characteristics of a steady flow with constant properties, without internal heat generation, where viscous dissipation and diffusion terms in the direction tangential to the flow, are estimated by solving the two-dimensional form of energy and species transport equations (eq.s 3.9 and 3.10).

$$u \frac{\partial T}{\partial x} + v \frac{\partial T}{\partial y} = a \frac{\partial^2 T}{\partial y^2} \tag{3.9}$$

$$u \frac{\partial \omega}{\partial x} + v \frac{\partial \omega}{\partial y} = D \frac{\partial^2 \omega}{\partial y^2} \tag{3.10}$$

The solution method to obtain temperature and concentration fields introduces a dimensionless rectangular coordinate transformation (eq.s 3.11 (a) and (b)) matching that of S.K. Choudhury et al. (1993) [77].

$$\varepsilon = \frac{x}{\pi r} = \frac{\beta}{\pi} \text{ (a)} \qquad \eta = \frac{y}{\delta} \text{ (b)} \tag{3.11}$$

To make the grid finer where steeper gradients are expected to occur, explicitly, at the film interface and near the tube wall, a cosine type grid is employed in the η direction as in L. Harikrishnan et al. (2011) [78]. Furthermore, this grid construction method reduces numerical instabilities.

The coordinates of *N*x*H* points(Fig. 3.2), respectively in circumferential and radial directions, are allocated as follows:

For *j*=1 to *H*; $$\eta_j = \frac{1}{2}\left[1-\cos\left(\frac{j-1}{H-1}\pi\right)\right] \tag{3.12}$$

For *i*=1 to *N*-1; $$\varepsilon_i = \frac{i}{N} \tag{3.13}$$

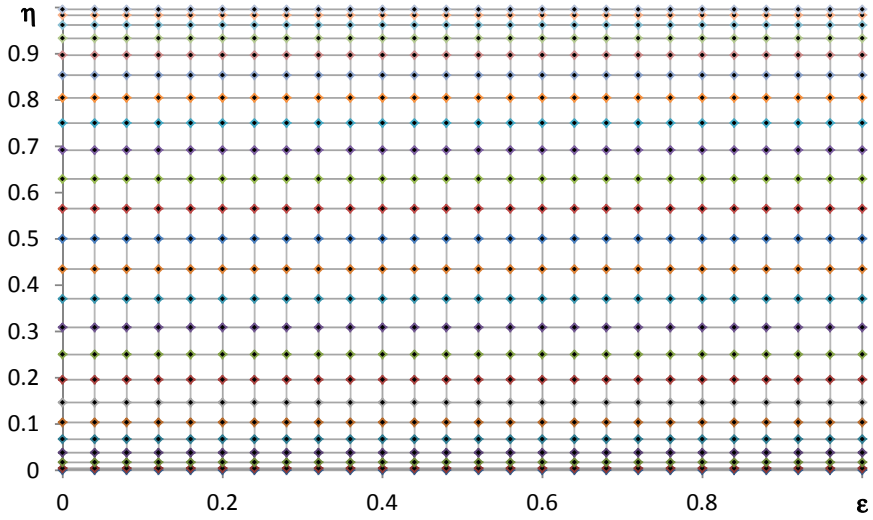

Fig. 3.2 Schematic of the cosine type calculation grid

The convective terms in the ε direction of both energy and species transport equations are approximated by a first order backward finite difference (eq. 3.14).

$$\left.\frac{\partial \Phi}{\partial \varepsilon}\right|_{i,j} = \frac{\Phi_{i,j} - \Phi_{i-1,j}}{d\varepsilon} \tag{3.14}$$

Where Φ is the generic parameter considered. This scheme results in an explicit form of the solution method in the stream wise direction, enabling to solve sequentially each angle steps and to reduce the computational time required for the convergence to a solution; Since no substantial change was highlighted between the resulting solution and that obtained in correspondent conditions with a fully implicit method, where the equations applied at all the nodes of the calculation domain are solved contemporarily, the first method is hereby adopted.

First and the second derivatives in the η direction, respectively embodying convective and diffusive terms, are approximated by second order central difference schemes, and written as in eq.s 3.15 and 3.16, where finite differences are adjusted in their expressions to account for the non-homogeneity of the calculation grid with respect to this coordinate.

$$\left.\frac{\partial \Phi}{\partial \eta}\right|_{i,j} = \frac{-\Omega^2 \Phi_{i,j-1} - (1-\Omega^2)\Phi_{i,j} + \Phi_{i,j+1}}{d\eta_j (1+\Omega)} \tag{3.15}$$

$$\left.\frac{\partial^2 \Phi}{\partial \eta^2}\right|_{i,j} = \frac{2\Omega\left[\Omega\Phi_{i,j-1} - (1+\Omega)\Phi_{i,j} + \Phi_{i,j+1}\right]}{d\eta_j^2 (1+\Omega)} \tag{3.16}$$

Where, $d\eta_j = \eta_j - \eta_{j-1}$ is the local grid spacing and $\Omega = d\eta_{j+1}/d\eta_j$ is the ratio of the local grid spacing. For the boundary conditions at the interface and at the wall, respectively, second order backward differences and second order forward differences are used to approximate first order derivatives in the radial direction η.

$$\left.\frac{\partial \Phi}{\partial \eta}\right|_{i,j+1} = \frac{\Omega^2 \Phi_{i,j-1} - (1+2\Omega+\Omega^2)\Phi_{i,j} + (1+2\Omega)\Phi_{i,j+1}}{d\eta_j (1+\Omega)} \tag{3.17}$$

$$\left.\frac{\partial \Phi}{\partial \eta}\right|_{i,j-1} = \frac{-\Omega(2+\Omega)\Phi_{i,j-1} + (1+2\Omega+\Omega^2)\Phi_{i,j} - \Phi_{i,j+1}}{d\eta_j (1+\Omega)} \tag{3.18}$$

The sinusoidal term in β at the denominator of the expression of the film tangential velocity distribution (eq. 3.6) limits the calculation to be performed between $\beta = \pi/N$ ($\varepsilon = 1/N$) and $\beta = \pi(N-1)/N$ ($\varepsilon = N-1/N$). Reference results of local velocity, concentration and temperature fields are shown in figures 3.3 and 3.4 for typical conditions of a single absorber tube with outer radius r=9mm, working with inlet coolant temperature of 32°C and absorber vapour pressure of 1.0kPa. The boundary conditions at the inlet ($\varepsilon = 1/N$) are set at the equilibrium for 60% solution concentration solution. As stated among the main assumptions, the variation of mass flowrate due to water vapour absorption is considered to be negligible. This assumption is valid for mass-flow rates higher than 0.001 kg $m^{-1}s^{-1}$ [78] and, accordingly, the analysis presented herein is performed in a consistent range.

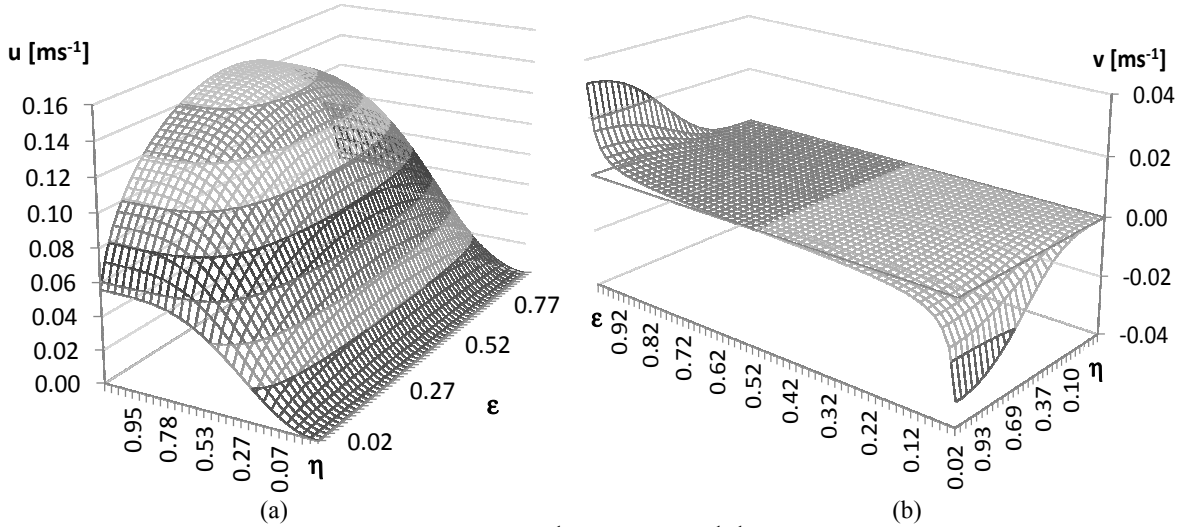

Fig. 3.3 Tangential (a) and normal (b) velocity fields [m·s^{-1}]; m=0.045kgm^{-1}s^{-1}, ω_{in}=60%, T_{in}=46.6℃, p=1.0 kPa, T_w=32.0℃, r=9.0mm

In figure 3.3 the parabolic tangential velocity component (eq. 3.2) is observed increasing along the circumference from ε~0 up to ε=0.5, where it reaches its maximum, and decreases moving further along the stream-wise direction towards higher ε. Likewise, the maximum value of normal velocity occurs at the film interface (η=1), but at two

different angular positions (ε=1/N and ε=(N-1)/N). In general, the magnitude of the maxima of this velocity component is nearly one order lower than the tangential one. Further, the direction of normal velocity, negative between $0<\beta<90^{o}$ and positive in the second half of the tube surface, is related to the local film acceleration and thickness variation.

Temperature and concentration fields (Fig. 3.4 (a) and (b)) are determined by the combination of effects related to the heat flux at the wall to the coolant, the absorption rate at the film boundary facing the vapour side, and velocity distribution inside the domain, that is the result of heat, mass and momentum transfer.

As a reference for a general analysis, the inlet temperature condition is fixed at the solution equilibrium temperature $T_{in}=T_e(p,\omega_{in})$ at the inlet concentration for constant vapour pressure of the absorber (see Fig. 3.4 (a) and (b)). Thus, absorption begins at a delayed position ($\varepsilon>\varepsilon_{in}$), where the temperature gradient originated from the cooling water reaches the film interface reducing its value and promoting vapour absorption.

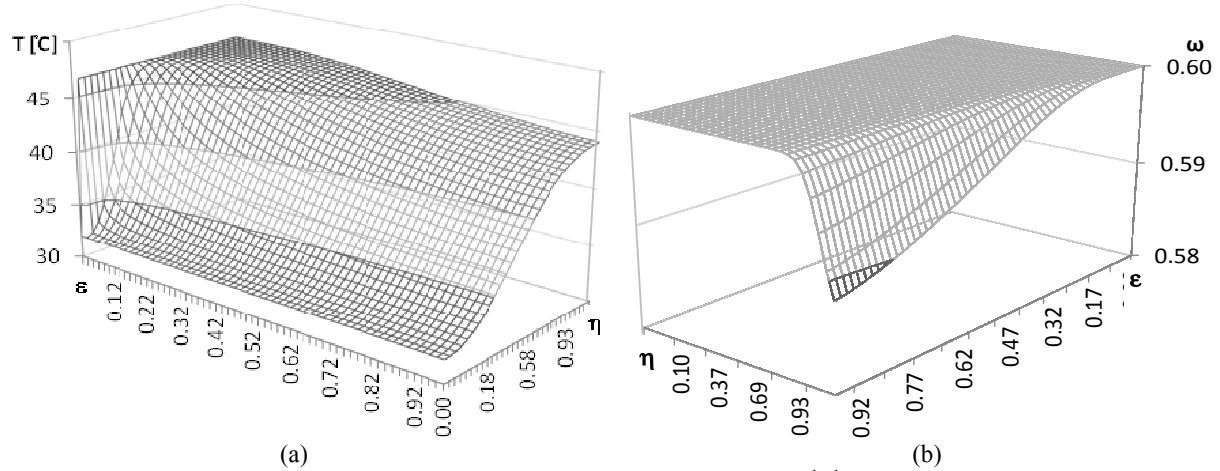

(a) (b)

Fig. 3.4 Temperature [^{o}C] (a) and concentration (b) distribution; m=0.045kgm^{-1}s^{-1}, ω_{in}=60%, T_{in}=46.6℃, p=1.0kPa, T_w=32.0℃, r=9.0mm

3.3. Mathematical formulation of the volumetric entropy generation rate

Heat, mass and momentum transfer, namely the presence of thermal, concentration and velocity gradients in the computational field representing the absorptive film yields a non-equilibrium state, which is responsible of internal irreversibility (entropy generation).

A local analysis is preliminarily performed by the identification of different entropy generation sources. The study is based on velocity, temperature and concentration fields, obtained, respectively, from Nusselt simplified solution of momentum equation, and the numerical solution of energy and species transport equations presented in the previous paragraph. Owing to the coupled heat and mass transfer, four key irreversibility sources, respectively related to fluid friction, heat transfer, coupled effects between heat and mass transfer by convection and coupled transfer effects by diffusion, can be recognised and mathematically distinguished.

Supplementary assumptions required for an apposite mathematical formulation of entropy generation for a single horizontal tube inside a falling film absorber include:

1. Physical absorption (no chemical reactions).
2. Gravity driven-flow of an incompressible, Newtonian, liquid, laminar film (LiBr-H_2O).
3. Absorbed water vapour is considered as a perfect gas.
4. Constant pressure of the absorber vessel.

According to problem formulation and introduced assumptions, the rate of volumetric entropy generation S_g of a viscous system subject to combined heat and mass transfer phenomena is expressed in a general way by eq. 3.19.

$$S_g = \vec{q} \cdot \vec{\nabla}\left(\frac{1}{T}\right) + \frac{\overline{\overline{\tau}} : \overline{\overline{\nabla}}(\vec{\Psi})}{T} - \frac{1}{T}\overrightarrow{\zeta_v} \cdot \vec{\nabla}(\varpi_v) \tag{3.19}$$

The three terms included in this general expression can be related, separately, to heat transfer, fluid friction and mass transfer irreversibilities. The heat flux q includes a term given by the Fourier Law of heat conduction and the enthalpy flux due to species diffusion.

$$\vec{q} = -k_S \vec{\nabla}(T) - h_v \overrightarrow{\zeta_v} \tag{3.20}$$

Therefore, a rearrangement of the expression yields to eq. 3.21.

$$S_g = \frac{1}{T^2} k_S \vec{\nabla}(T)^2 + \frac{1}{T^2} h_v \overrightarrow{\zeta_v} \cdot \vec{\nabla}(T) + \frac{\overline{\overline{\tau}} : \vec{\nabla}(\vec{\Psi})}{T} - \frac{1}{T}\overrightarrow{\zeta_v} \cdot \vec{\nabla}(\varpi_v) \tag{3.21}$$

Considering the absorbed vapour as an ideal gas and to be the only diffusing species through the liquid solution, its molar concentration w_v can be directly derived from the LiBr mass concentration field (ω) resulting from the solution of governing transport equations.

$$w_{v,ij} = \frac{\rho_S}{M_{H_2 0}}(1-\omega_{ij}) - \frac{\rho_S}{M_{H_2 0}}(1-\omega_{in}) \tag{3.22}$$

The molar chemical potential of the vapour can be calculated by eq. 3.23 [79].

$$\varpi_v(T, p_*) = c_{p,v}(T - T_*) - Tc_{p,v} \ln\left(\frac{T}{T_*}\right) + h_{v,*}(T_*, p_*) - Ts_{v,*}(T_*, p_*) \tag{3.23}$$

Where p_* and T_* are the standard values of pressure and temperature, respectively, 1 atm and 298 K. Standard enthalpy and entropy are calculated at the corresponding thermodynamic state. Vapour molar enthalpy and entropy, respectively, are given by eq.s 3.24 and 3.25.

$$h_v = c_{p,v}(T - T_*) + h_{v,*} \tag{3.24}$$

$$s_v = c_{p,v} \ln\left(\frac{T}{T_*}\right) + s_{v,*} \tag{3.25}$$

The shear stress tensor is reduced to a single component of interest specified by eq. 3.26.

$$\tau = \mu_S\left(\frac{\partial u}{\partial y} + \frac{\partial v}{\partial x}\right) \tag{3.26}$$

Hence, the local rate of volumetric entropy generation is articulated as,

$$S_g = \frac{k_S}{T^2}\left[\left(\frac{\partial T}{\partial x}\right)^2 + \left(\frac{\partial T}{\partial y}\right)^2\right] + \frac{\mu_S}{T}\left\{2\left[\left(\frac{\partial u}{\partial x}\right)^2 + \left(\frac{\partial v}{\partial y}\right)^2\right] + \left[\left(\frac{\partial u}{\partial y}\right) + \left(\frac{\partial v}{\partial x}\right)\right]^2\right\} + \\ + \frac{h_v}{T^2}\left[\zeta_{v,x}\left(\frac{\partial T}{\partial x}\right) + \zeta_{v,y}\left(\frac{\partial T}{\partial y}\right)\right] - \frac{1}{T}\left[\zeta_{v,x}\left(\frac{\partial \gamma_v}{\partial x}\right) + \zeta_{v,y}\left(\frac{\partial \gamma_v}{\partial y}\right)\right] \tag{3.27}$$

Transverse and axial molar fluxes are, in turn, given by,

$$\zeta_{v,x} = w_v u - D_{vS}\frac{\partial w_v}{\partial x} \tag{3.28}$$

$$\zeta_{v,y} = w_v v - D_{vS}\frac{\partial w_v}{\partial y} \tag{3.29}$$

By calculating the derivatives of the molar chemical potential, and by substituting mass fluxes and enthalpy terms, eq. 3.27 can be reorganised for representing the case of falling film absorption.

$$S_g = \frac{k_S}{T^2}\left[\left(\frac{\partial T}{\partial x}\right)^2 + \left(\frac{\partial T}{\partial y}\right)^2\right] + \frac{\mu_S}{T}\left\{2\left[\left(\frac{\partial u}{\partial x}\right)^2 + \left(\frac{\partial v}{\partial y}\right)^2\right] + \left[\left(\frac{\partial u}{\partial y}\right) + \left(\frac{\partial v}{\partial x}\right)\right]^2\right\} + \\ \left[c_{p,v}(T - T_*) + h_{v,*} + T\left(c_{p,v}\ln\left(\frac{T}{T_*}\right) + s_{v,*}\right)\right]\left[\frac{w_v}{T^2}\left(v\frac{\partial T}{\partial y} + u\frac{\partial T}{\partial x}\right) - \frac{D_{vS}}{T^2}\left(\frac{\partial w_v}{\partial y}\frac{\partial T}{\partial y} + \frac{\partial w_v}{\partial x}\frac{\partial T}{\partial x}\right)\right] \tag{3.30}$$

Different terms, related to different irreversibility sources, can be distinguished. The first group (eq. 3.31) on the right-hand side of eq. 3.30 is related to thermal irreversibility S_t.

$$S_t = \frac{k_S}{T^2}\left[\left(\frac{\partial T}{\partial x}\right)^2 + \left(\frac{\partial T}{\partial y}\right)^2\right] \tag{3.31}$$

The second term stands for the volumetric entropy generation rate due fluid friction.

$$S_f = \frac{\mu_S}{T}\left\{2\left[\left(\frac{\partial u}{\partial x}\right)^2 + \left(\frac{\partial v}{\partial y}\right)^2\right] + \left[\left(\frac{\partial u}{\partial y}\right) + \left(\frac{\partial v}{\partial x}\right)\right]^2\right\} \tag{3.32}$$

A third and a fourth term can be associated to the coupled properties of heat and mass transfer, respectively, by convection and diffusion.

$$S_h = \left[c_{p,v}(T - T_*) + h_{v,*} + T\left(c_{p,v}\ln\left(\frac{T}{T_*}\right) + s_{v,*}\right)\right]\left[\frac{w_v}{T^2}\left(v\frac{\partial T}{\partial y} + u\frac{\partial T}{\partial x}\right)\right] \tag{3.33}$$

$$S_d = -\left[c_{p,v}(T - T_*) + h_{v,*} + T\left(c_{p,v}\ln\left(\frac{T}{T_*}\right) + s_{v,*}\right)\right]\left[\frac{D_{vS}}{T^2}\left(\frac{\partial w_v}{\partial y}\frac{\partial T}{\partial y} + \frac{\partial w_v}{\partial x}\frac{\partial T}{\partial x}\right)\right] \tag{3.34}$$

3.4. Local Irreversibility analysis

From the calculated temperature, velocity and concentration fields, a local irreversibility analysis of the total volumetric entropy generation S_g, and each specific group (S_t, S_h, S_d and S_f), is performed for typical conditions of a single absorber tube working with inlet coolant temperature of 32 ℃ and vapour pressure of the absorber 1.0 kPa. Since Nusselt integral solution for velocity distribution is not defined at the inlet (ε=0) and outlet (ε=1) positions, and owing to the boundary conditions, the temperature and concentration gradients at the inlet can be significantly affected by the mesh dimensions. To reduce numerical errors related to this effect and, meanwhile, calculating on a thin grid, the entropy generation groups are evaluated between ε=2/N and ε=N-2/N, inside the whole film thickness. The solution properties are established for the inlet values of temperature, pressure and concentration, with reference to ASHRAE Trans. (1990) [80].

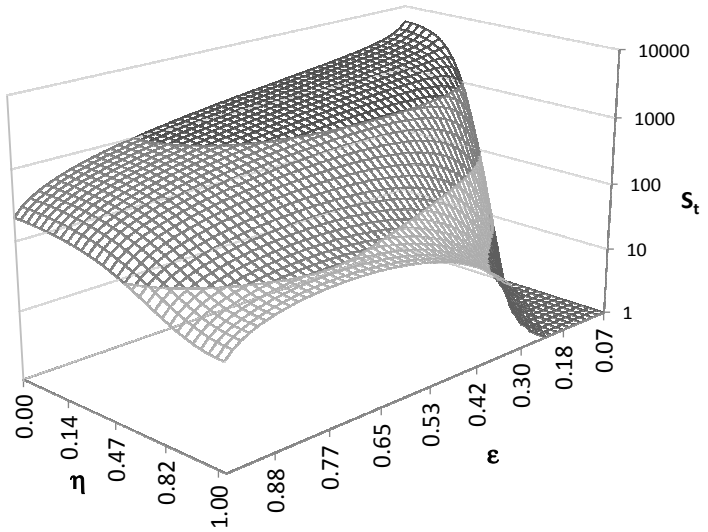

Fig. 3.5 Local thermal entropy generation rate [kW·m^{-3}K^{-1}]; I=0.045 kg·m^{-1}s^{-1}, ω_{in}=60% , T_{in}=46.6 ℃, p=1.0 kPa, T_w=32.0 ℃, flowing over a tube with outer radius r=9.0mm

Thermal entropy generation (Fig. 3.5, logarithmic scale) makes evidence of heat transfer effects at the tube solid surface and at the interface between liquid and vapour. Hereby, a relative maximum can be highlighted; its position corresponds to the point at which the absorbed flux maximises the temperature gradient for a given solution equilibrium temperature. In the condition considered (no sub-cooling of the inlet solution), the impact of the heat transfer occurring at the tube wall is much higher than that of the release of absorption heat at the liquid-vapour interface.

Even though temperature and concentration, as well as entropy generation fields, obtained and presented in their dimensionless form, don't illustrate film thickness variation alongside the stream-wise direction, the radial component of temperature and concentration gradients are also dependent on the film thickness distribution. In general, a reduction of δ increases both heat transfer and the rate of absorption. Conversely, the thickening of the film brings the opposite effect [60) 78)].

The resolution of energy and species transfer equations inside the domain is strongly related to the solution inlet and boundary conditions, as well as to the operative pressure, owing to the equilibrium hypothesis at the film interface. Since an inlet temperature of 46.6 ℃ is the equilibrium value for 60% LiBr solution concentration, mass transfer starts as soon as the thermal gradient reaches the interface, and the position at which this occurs depends primarily on the solution mass flowrate, the tube radius and the coolant temperature (Fig. 3.6). A reciprocal behaviour can be highlighted in figures 3.5, 3.6 and 3.7.

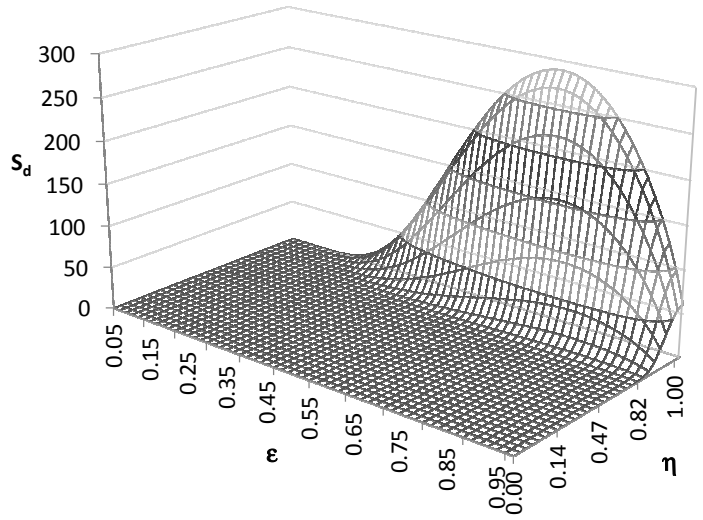

Fig. 3.6 Local diffusion related entropy generation rate [kW·m^{-3}K^{-1}]; I=0.045 kg·m^{-1}s^{-1}, ω_{in}=60% , T_{in}=46.6℃, p=1.0 kPa, T_w=32.0℃, flowing over a tube with outer radius r=9.0mm

At the vapour-liquid interface, where absorption takes place, the entropy generation group due to the coupled effect of convective heat and mass transfer S_h (Fig. 3.7) is always at its maximum absolute value.

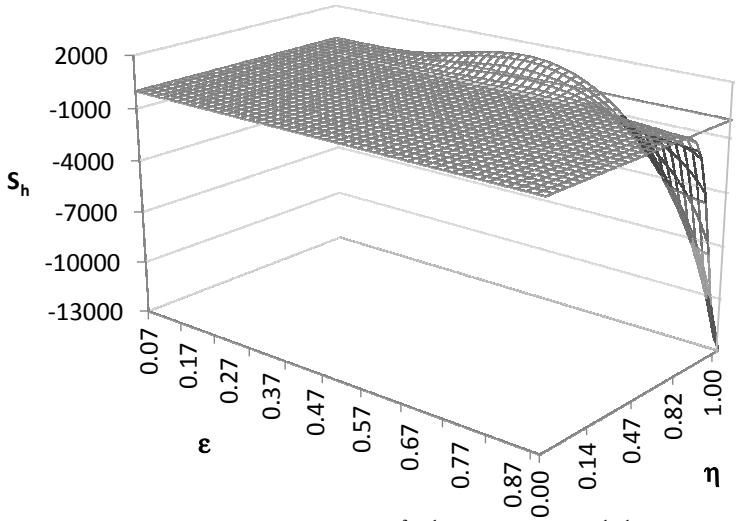

Fig. 3.7 Local convection related entropy generation rate [kW·m^{-3}K^{-1}]; I=0.045 kg·m^{-1}s^{-1}, ω_{in}=60% , T_{in}=46.6℃, p=1.0 kPa, T_w=32.0℃, flowing over a tube with outer radius r=9.0mm

A local maximum can be identified and can be related to the conflicting effects of absorbed mass-flux and velocity field (eq. 3.33). The boundary condition for the concentration gradient at the tube wall requires this entropy generation group to be constantly zero at that position. In the second half of the tube surface this group assumes negative values: this behaviour can be explained considering that the radial component of velocity v is positive (the tangential component u is decelerating) in that region and the local temperature decreases in the stream-wise direction and vapour concentration w_v increases in that region (eq. 3.33, where the term $w_v u/T^2 \cdot \partial T/\partial x$ becomes dominant).

Friction related irreversibility (Fig. 3.8) decreases regularly from the wall to the interface and reaches its maximum value in the vertical part of the tube, where the velocity field gradient is maximum, since the tangential velocity assumes its highest value and the film thickness is at its lowest. This irreversibility group shows generally a magnitude order largely lower than those of the other entropy groups.

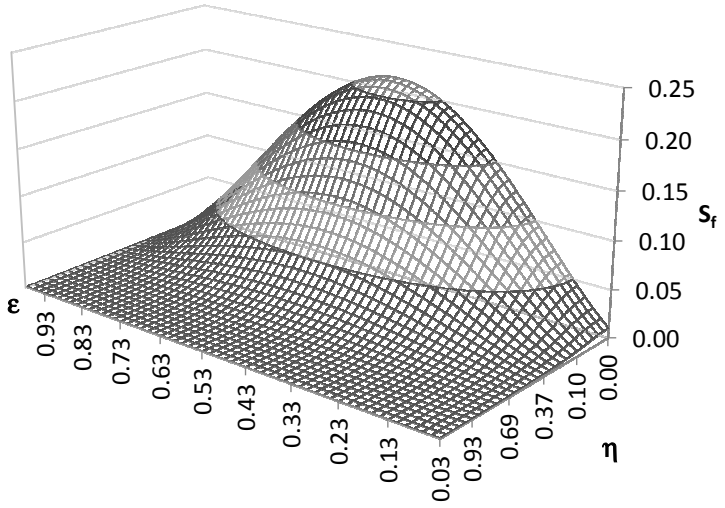

Fig. 3.8 Local friction related entropy generation rate [kW·m^{-3}K^{-1}]; Γ=0.045 kg·m^{-1}s^{-1}, ω_{in}=60% , T_{in}=46.6℃, p=1.0 kPa, T_w=32.0℃, flowing over a tube with outer radius r=9mm

The global rate of volumetric entropy generation inside an absorptive LiBr-H_2O thin film, flowing on a chilled horizontal tube S_g is illustrated in figure 3.9 in its two dimensions as the superimposition of the different groups previously identified. It can be highlighted that S_g always shows a local minimum in the radial direction except in the first and the last parts of the tube angular position, where the total rate of entropy generation is relentlessly decreasing. The local minimum is determined by the contemporaneity of wall heat transfer and simultaneous heat and mass transfer at the liquid-vapour interface, friction effects, and it is indicatively located at the penetration distance of the absorbed vapour diffusing inside the film.

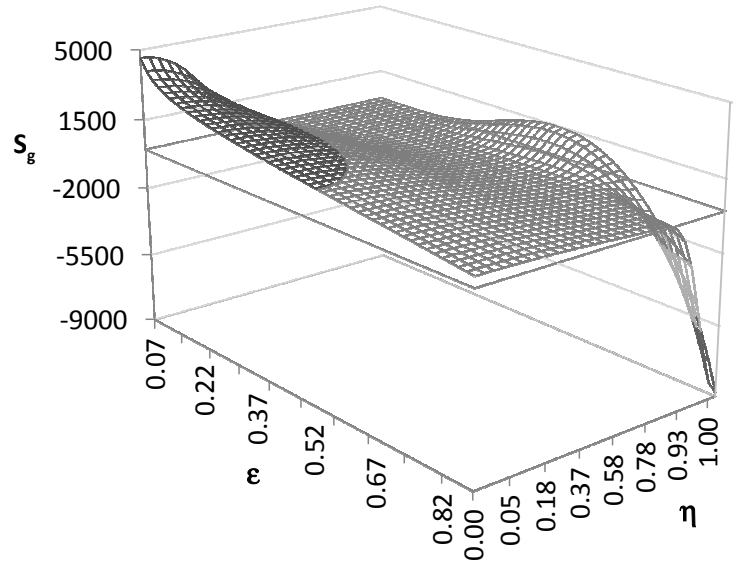

Fig. 3.9 Total local volumetric entropy generation rate [kW·m^{-3}K^{-1}]; Γ=0.045 kg·m^{-1}s^{-1}, ω_{in}=60% , T_{in}=46.6℃, p=1.0 kPa, T_w=32.0℃, flowing over a tube with outer radius r=9mm

The fact that the global results show that at the final part of the tube is characterised by negative values factually points out that the hydrodynamic description of the falling film might be not consistent and thermodynamically not justified in that part for this mass flowrate. Otherwise, this could be related to the fact that this model doesn't include

surface tension effect at the interface and mixing convective phenomena (which are renown to be an additional irreversibility source and highly beneficial for the transfer performance of the process). This suggests a rather definite direction for possible refinements of the model.

Figure 3.10 shows the distribution of various entropy generation groups in the stream-wise direction and the way they are combined together to get the global rate of volumetric entropy generation S_g. For the sake of the diagram readability, the entropy generation group related to friction refers to the secondary axes. The value associated at each position ε is obtained from the integral in the dimensionless radial direction η, and accordingly corresponds to the average value over the film thickness at that specific position. It can be highlighted that each entropy generation group is characterised by a local maximum value along the tube surface and the global irreversibility is maximum at a position close to the vertical part of the tube, where, due to the combined effects of temperature, concentration and velocity fields, gradients are at the highest value. Furthermore, for typical conditions of falling film heat exchangers the friction related entropy generation group appears to have the smallest impact on the global irreversibility.

The effect of geometrical parameters and operative conditions is analysed locally, in order to obtain a detailed and wide characterisation of each entropy generation groups involved in the absorption process of a falling film heat exchanger.

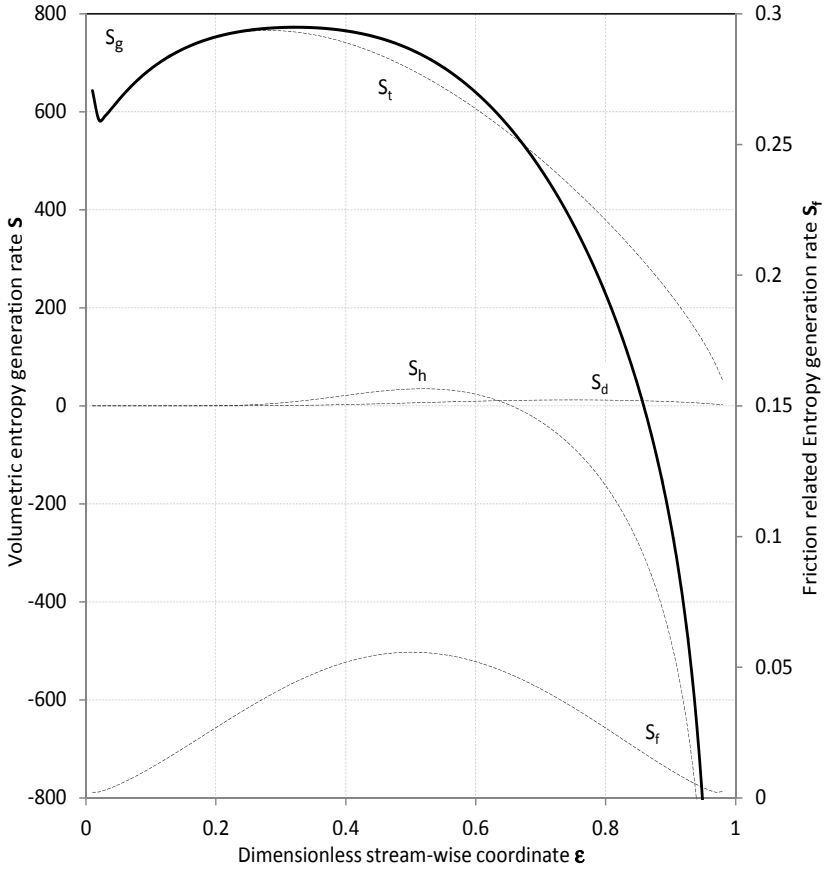

Fig. 3.10 Distribution of different entropy generation groups [kW·m^{-3}K^{-1}] in the stream-wise direction for Γ=0.045kgm^{-1}s^{-1}, ω_{in}=60%, T_{in}=46.6°C, p=1.0 kPa, r=9.0 mm, T_w=32.0°C

In particular, when the tube radius is reduced, the entropy generation groups S_t, S_h and S_f are increased at each position ε (Fig. 3.11a) and so does the global entropy generation S_g. In contrast, the entropy generation group related to the coupled effects of heat transfer and vapour diffusion S_d shows an opposite trend. This can be explained accounting for the increase in the vapour-liquid interface extension related to a bigger tube.

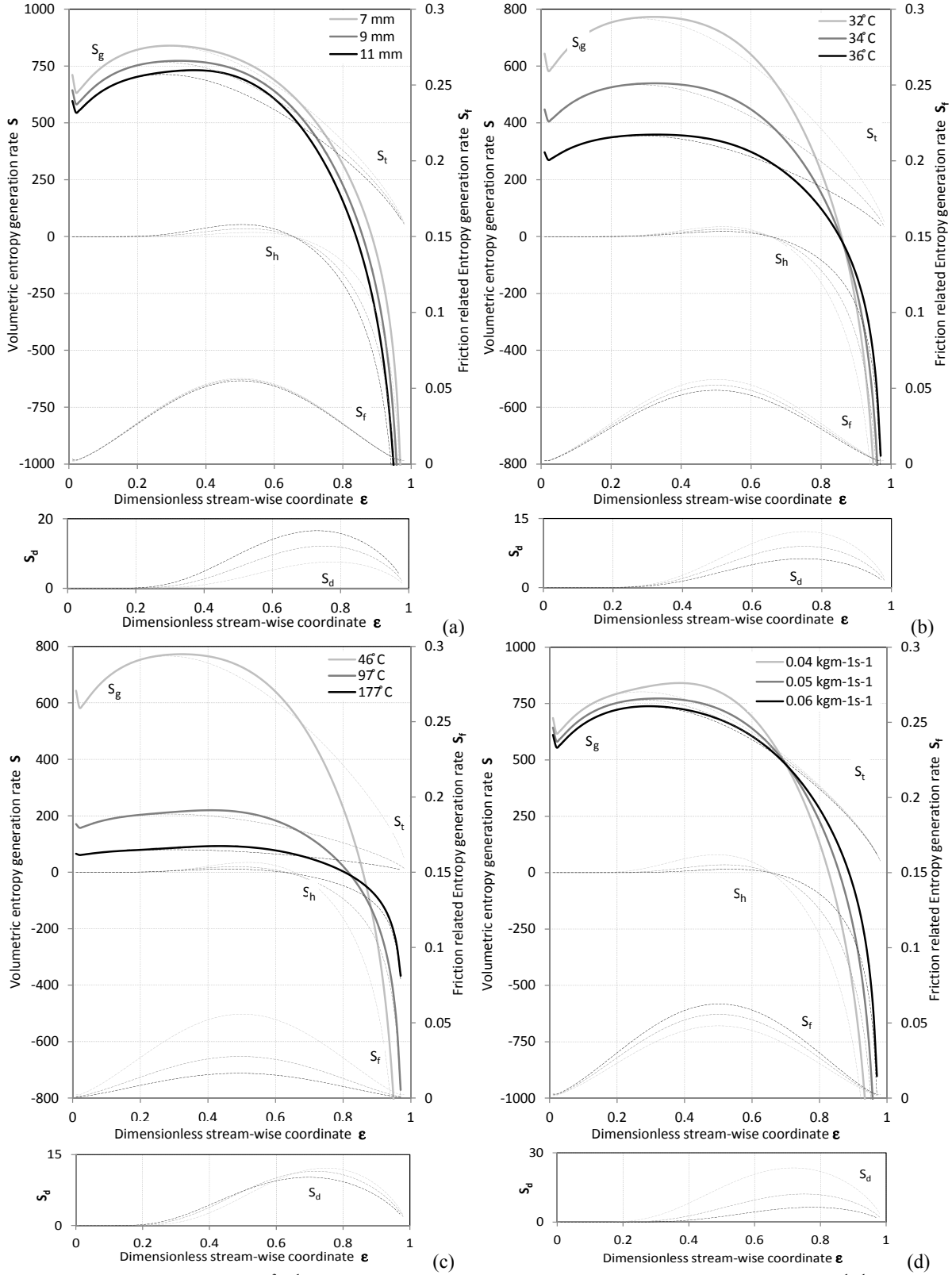

Fig. 3.11 Entropy groups [kW·m^{-3}K^{-1}] in the stream-wise direction for different (a) tube radii; Γ=0.045 kg·m^{-1}s^{-1}, ω_{in}=60%, T_{in}=46.6°C, p=1kPa, T_w=32°C, (b) wall temperatures; Γ=0.045 kg·m^{-1}s^{-1}, ω_{in}=60%, T_{in}=46.6°C, p=1kPa, r=9.0mm (c) inlet conditions; Γ=0.045kg·m^{-1}s^{-1}, r=9.0mm, lines labelled as 46°C (ω_{in}=60%, T_w=32°C, p=1kPa), 97°C (ω_{in}=60%, T_w=83°C, p=12.5kPa), 177°C (ω_{in}=63%, T_w=163°C, p=149kPa), (d) mass flowrates; ω_{in}=60%, T_{in}=46.6°C, p=1kPa, T_w=32°C, r=9.0mm

It can also be highlighted (Fig. 3.11a) that the position of the maximum global entropy generation S_g move streamwards when the tube radius is increased. Contrarily, the maxima of the maximum thermal related irreversibility S_t, the diffusion related S_d and coupled diffusion convection related S_h groups move backwards. Owing to increased intensity of heat and mass transfer and a lower average temperature, when the temperature of the coolant inside the tube is lowered, each entropy generation group increases in its absolute value (Fig. 3.11b). The relative maximum of each entropy generation group maintains its position ε along the tube surface. Furthermore, in order to extend the analysis to conditions typical of different applications, the local behaviour of the various entropy generation groups is studied when different concentration and absorber pressure (and, due to the equilibrium hypothesis at the inlet, different inlet temperatures) are selected. In particular, inlet solution temperatures of 46, 97 and 177°C are chosen to represent absorbers operating, respectively, in a chiller plant, single and multiple lift heat transformers.

In general, higher temperature applications have lower entropy generation rates (Fig. 3.11c). Each group is reduced by the leading impact of a higher solution temperature (eq.s 3.31-3.34), and the entropy generation group S_f is additionally lowered by the reduced value of the solution viscosity. Conversely, the entropy generation group related to vapour diffusion experiences the conflicting effect of an increased diffusivity, which brings to higher irreversibility in the first half of the tube. Figure 3.11d highlights the local effect of a different solution mass flowrate. Thermal and diffusion related entropy generation groups are increased at lower solution flowrates, representing enhanced local heat and mass transfer coefficients. The opposite behaviour is shown by S_h and S_f. As a consequence, the effect on S_g requires to be evaluated from a global point of view, suggesting the occurrence of a least irreversible flowrate.

3.5 Global irreversibility analysis

The fundamental design approach adopted in this paragraph is to thermodynamically determine the optimum operating regime of a thermodynamic system. However, the "optimal" condition for a system or a component can be defined in different ways depending on their main purpose. As previously stated, when by "optimum" the least irreversible operating condition for a specified objective is meant, the most desirable trade-off between competing irreversibilities should be sought for [50] to identify first and second law optima for a particular heat and mass transfer system, where an increased number of competing irreversibilities is involved. As a consequence, the basic problem of heat transfer can be reduced to a particular case of this general analysis of higher complexity.

The following parametric analysis makes evidence that a solution flowrate responsible to minimise entropy generation of falling film absorbers can always be identified in terms of Reynolds number (eq. 3.35).

$$\mathrm{Re} = \frac{4\Gamma}{\mu} \tag{3.35}$$

Firstly, the general trends of different irreversibility groups and the global rate of volumetric entropy generation are examined (Fig. 3.12). The value associated to a defined Reynolds number is obtained from the double integral in the dimensionless radial η and tangential ε directions, and, accordingly, corresponds to the weighted average value over the whole transversal section of the film. In the target range of operative conditions, increasing Reynolds determine increasing friction and decreasing absorption rates, consequently, their respective entropy generation groups show consistent trends. The thermal related irreversibilities show a maximum value, established by the conflicting effects of increasing extension of the entrance region, increasing film thickness and decreasing overall absorption heat release. Finally, the entropy generation group related to the coupled effects of mass convection and heat transfer shows a minimum value, which can be explained considering that, increasing Reynolds number, convection is amplified while absorption heat release is reduced.

As a result, the global entropy generation rate, obtained by the superimposition of all these phenomena, shows both a local minimum and a local maximum in the considered range of operative condition (Fig. 3.12). After the local maximum S_G starts decreasing again because the solution at the film interface flows too fast and absorption process

does not have enough time to occur, while the effect of friction is still small. If an extended Reynolds range is considered, after a certain value of this parameter, friction related irreversibilities would have a relative importance strong enough to cause the global entropy generation to increase relentlessly. Nonetheless, due to the assumption of a laminar film and with reference to the operative conditions-range of interest, the following analysis is carried out for a set of solution mass flowrates compatible with absorption technical applications.

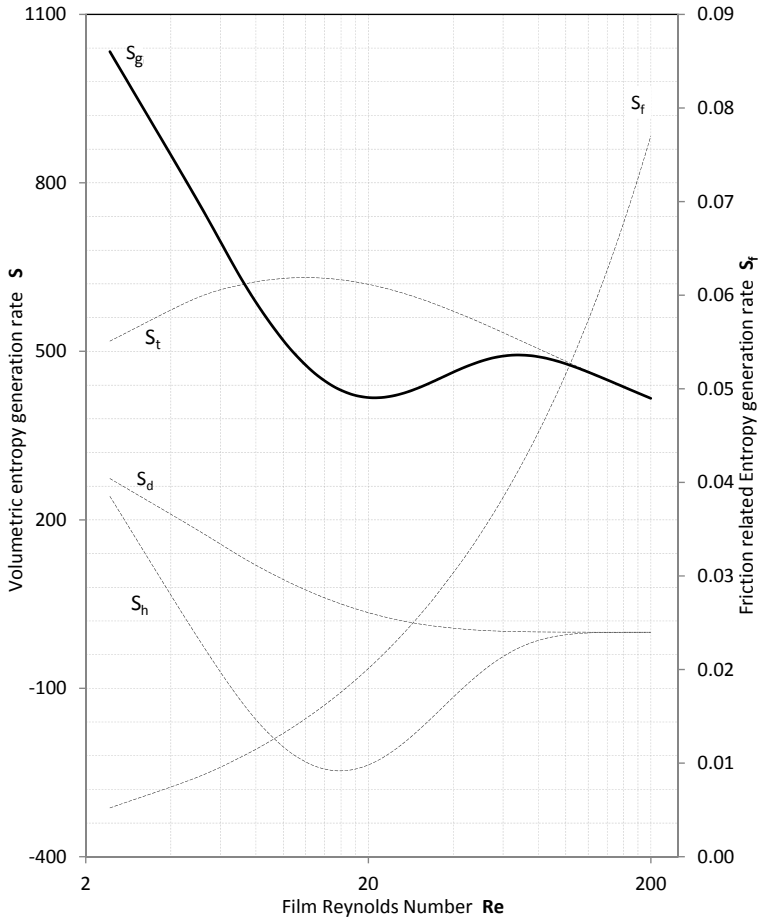

Fig. 3.12 Different groups of global volumetric entropy generation rate [$kW \cdot m^{-3}K^{-1}$] as a function of film Reynolds number (abscissa in logarithmic scale); ω_{in}=60% , T_{in}=46.6℃, p=1.0 kPa, T_w=32.0℃, flowing over a tube with outer radius r=9.0mm.

Figures 3.13(a)-(d) show the effect of tube radii as a parameter on each entropy generation group. The effect of a different radius can be primarily related to the change in intensity of the radial velocity field (eq. 3.4), which directly influences S_h, S_d, S_f (eq.s 3.32-3.34) and indirectly S_t through the released heat of absorption. A smaller radius increases thermal irreversibility S_t (Fig. 3.13a) and moves the position of its maximum to a lower Reynolds. A longer flowing time (time of residence in the calculation domain) of the solution over a tube with bigger radius can explain higher values of the entropy generation group related to vapour diffusion inside the film thickness S_d (Fig. 3.13b). When the tube radius is reduced, curves representing S_h (Fig. 3.13c) are shifted to lower entropy generation rates and the general trend corresponds to lower Reynolds numbers. Nevertheless, this behaviour is reversed at high Reynolds numbers, where operating with a lower radius causes higher S_h. Finally, friction related irreversibilities S_f (Fig. 3.13d) are slightly affected by the external tube radius.

In Figure 3.14, the influence of the tube radius on the global entropy generation for fixed inlet and boundary conditions is presented.

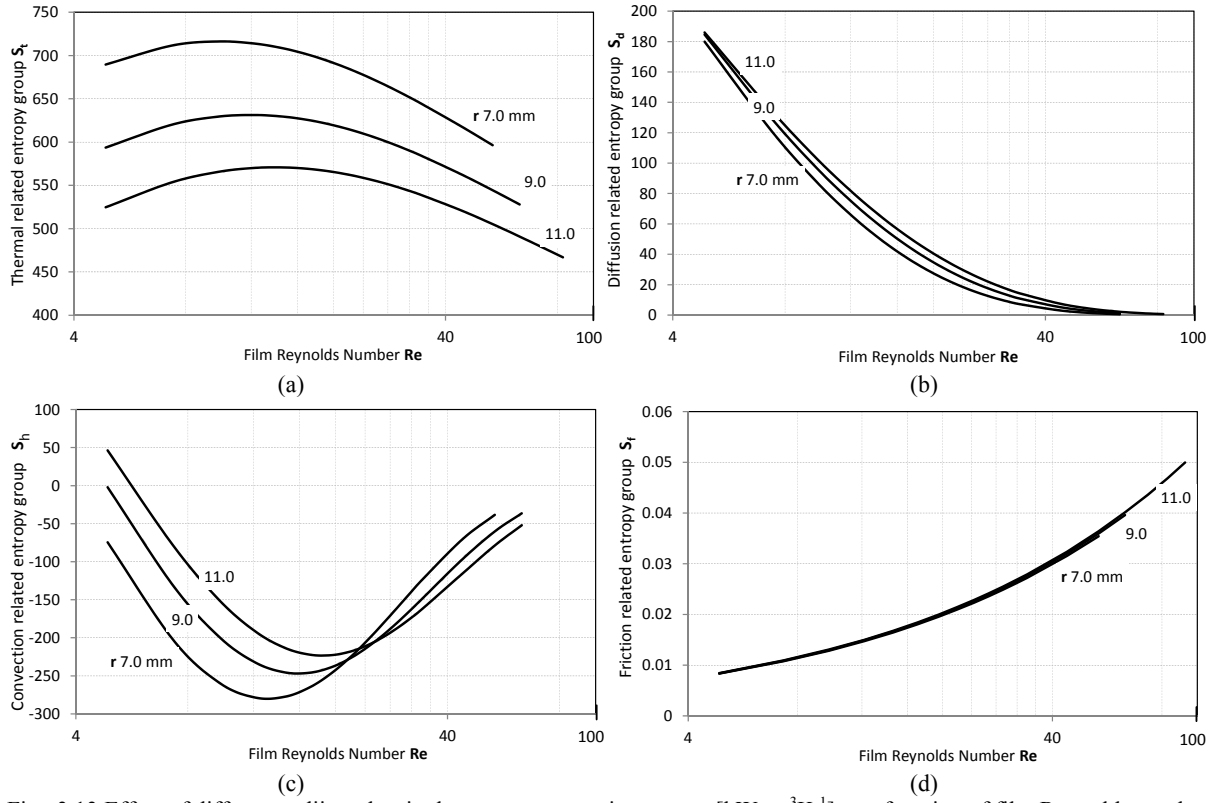

Fig. 3.13 Effect of different radii on the single entropy generation groups [kW·m^{-3}K^{-1}] as a function of film Reynolds number (abscissa in logarithmic scale) ω_{in}=60% , T_{in}=46.6℃, p=1.0 kPa, T_w=32.0℃.

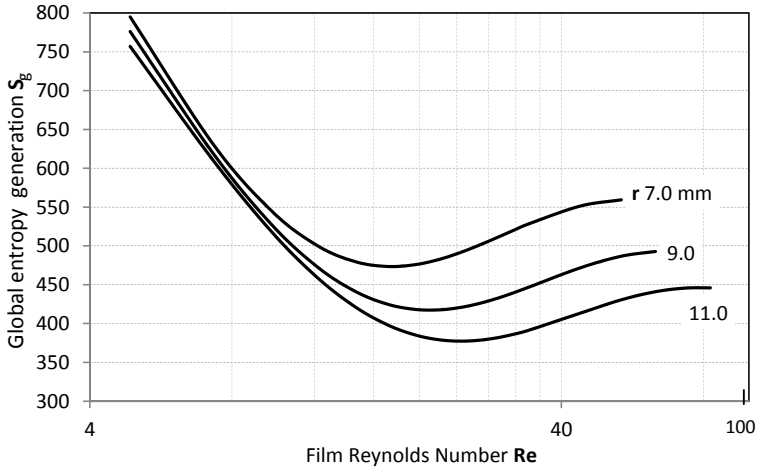

Fig. 3.14 Volumetric entropy generation for different outer tube radii [kW·m^{-3}K^{-1}] as a function of film Reynolds number (abscissa in logarithmic scale) ω_{in}=60% , T_{in}=46.6℃, p=1.0 kPa, T_w=32.0℃

As a rule, the lower the tube radius the higher the rate of volumetric entropy generation S_g (Fig. 3.14). The trend of the average volumetric rate S_g shows a decreasing behaviour in the low Reynolds region, where the effect of the film thickness is preponderant, and a subsequent increasing one at high Reynolds, where the effect of the velocity field dominates the heat and mass transfer process, increasing local gradients and related irreversibilities. The compromise between these conflicting effects establishes the position of the minimum value of the volumetric entropy generation rate, which occurs at lower Reynolds number when the tube radius decreases.

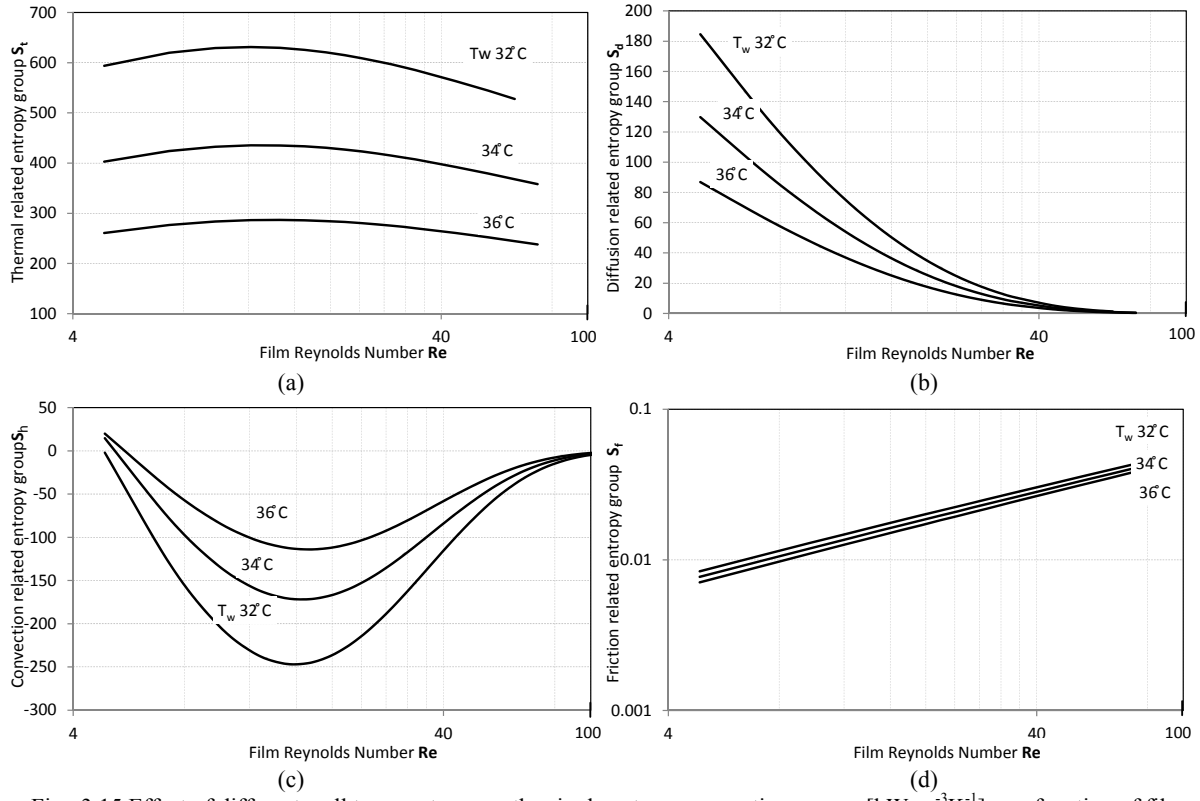

Fig. 3.15 Effect of different wall temperatures on the single entropy generation groups [$kW \cdot m^{-3}K^{-1}$] as a function of film Reynolds number (abscissa in logarithmic scale) ω_{in}=60% , T_{in}=46.6℃, p=1.0 kPa, r=9.0mm.

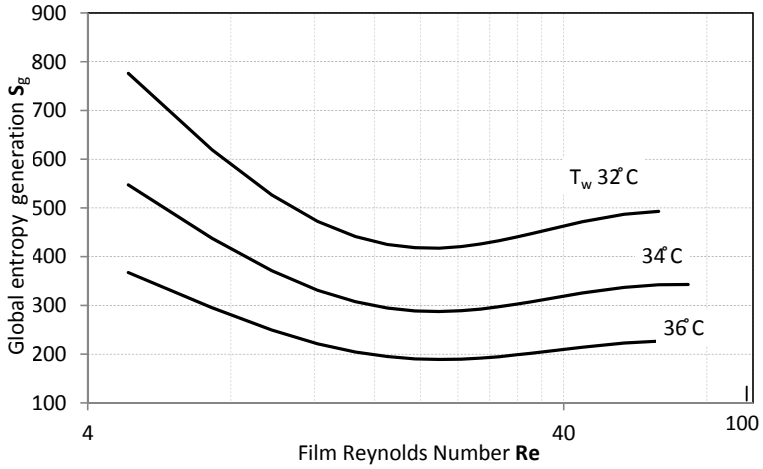

Fig. 3.16 Volumetric entropy generation for different values of the tube wall temperature [$kW \cdot m^{-3}K^{-1}$] as a function of film Reynolds number (abscissa in logarithmic scale) ω_{in}=60%, T_{in}=46.6℃, p=1.0kPa, r=9.0mm.

Figures 3.15(a)-(d) describe the outcomes obtained with different tube wall temperatures. In general, they make evidence of the fact that a lower wall temperature increases temperature gradients and, once the temperature gradient reach the interface, also concentration gradients (Fig. 3.15b). The trend of the thermal related entropy generation group is shifted to lower values and the maximum slightly moves to higher Reynolds when the temperature of the coolant is increased (Fig. 3.15a). Similar behaviour is shown by the absolute value of the entropy generation group S_h (Fig. 3.15c). Friction related irreversibilities (Fig. 3.15d, logarithmic scale) are increased by a lower value of the solution temperature T inside the film thickness (eq. 3.32).

Broadly speaking, a lower tube wall temperature increases both heat transfer and, increasing the driving force for vapour absorption, mass transfer at the interface. Accordingly, figure 3.16 makes evidence of a higher global entropy generation when tube wall temperature is decreased. Instead, the optimal Reynolds is weakly dependent on this parameter.

When different inlet temperatures, and, due to the inlet equilibrium hypothesis, different concentration and absorber pressure, are used, figures 3.17(a)-(d) describe this effect on each entropy generation group. This parameter has a substantial impact on the properties of the solution and, in general, when its value is increased, the trend of each irreversibility group is maintained, but moved to a higher Reynolds range. Thermal irreversibility S_t (Fig. 3.17a) decreases because of higher values of the solution temperature inside the calculation domain, even if the thermal conductance is also increased (eq. 3.31). Similarly, the group related to the coupled effects of mass convection and heat transfer S_h (Fig. 3.17c) is mainly scaled by the value of the solution temperature T (eq. 3.33). Friction irreversibility S_f (Fig. 3.17d) decreases with higher inlet temperatures also because of a lower viscosity (eq. 3.32).

On the other hand, the entropy generation group related to vapour diffusion inside the film thickness S_d (Fig. 3.17b) is dominated by an increased diffusivity of water vapour at higher solution temperatures.

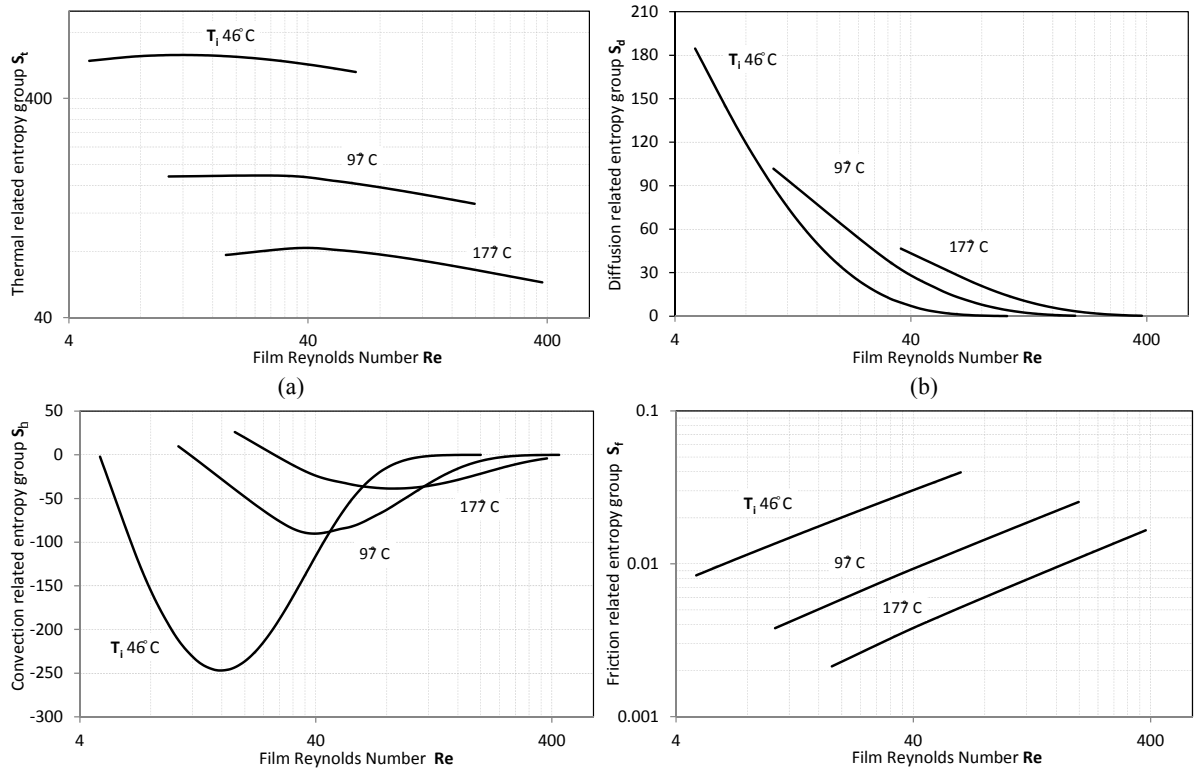

Fig. 3.17 Effect of different inlet solution temperatures on the single entropy generation groups [$kW \cdot m^{-3}K^{-1}$] as a function of film Reynolds number (abscissa in logarithmic scale) (b), (c) (abscissa in logarithmic scale) (a), (d) (logarithmic axes); r=9.0mm lines labelled as 46℃ (ω_{in}=60% , T_w=32.0℃, p=1.0 kPa), lines labelled as 97.0℃ (ω_{in}=60%, T_w=83.0℃, p=12.5 kPa) and lines labelled as 177℃ (ω_{in}=63% , T_w=163℃, p=149kPa).

Higher temperature applications (i.e. representing absorbers operating inside heat transformers) have lower global entropy generation and cope with higher solution Reynolds (Fig. 3.18). The thermodynamic optimum Reynolds, for fixed operative conditions, increases for higher temperature applications, such as heat transformer absorbers. Optimal Reynolds numbers of 22, 73 and 127 are obtained, respectively, for inlet solution temperatures of 46, 97 and 177℃ (correspondingly, 60%, 60% and 63% lithium bromide concentration). These values have been obtained as an ideal target condition which doesn't consider partial wetting of the solid surface, but typically (especially at lower

temperature operability), they correspond to solution mass flowrates which are not able to assure complete wetting, unless tension-active surfactants are added to the LiBr-H_2O solution.

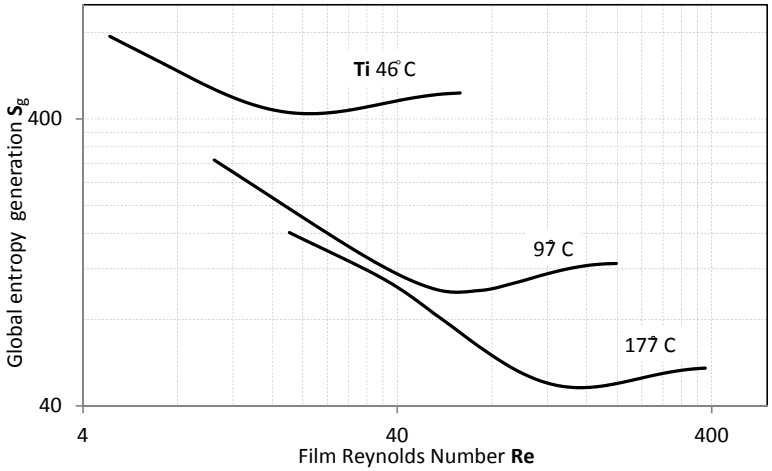

Fig. 3.18 Volumetric entropy generation [$kW \cdot m^{-3}K^{-1}$] as a function of Reynolds number for different operative conditions (logarithmic axes); r=9.0mm, lines labelled as 46℃ (ω_{in}=60% , T_w=32.0℃, p=1.0 kPa), lines labelled as 97.0℃ (ω_{in}=60%, T_w=83.0℃, p=12.5kPa) and lines labelled as 177℃ (ω_{in}=63% , T_w=163℃, p=149kPa).

Relaxing the equilibrium hypothesis at the inlet of the calculation domain, when the inlet concentration of the solution is increased the solution enters the calculation domain as a sub-cooled film. Figures 3.21(a)-(d) make evidence of a similar effects of higher inlet solution concentration and higher absorber pressure on each entropy generation group. In general, the higher the concentration the higher the optimal Reynolds number (Fig. 3.19). According to the global entropy generation distribution presented in figure 3.19, the lines crossing point appearing at Reynolds equal to 15 shows that, for higher Reynolds numbers, operating in closer proximity to thermodynamic equilibrium results to be thermodynamically advantageous.

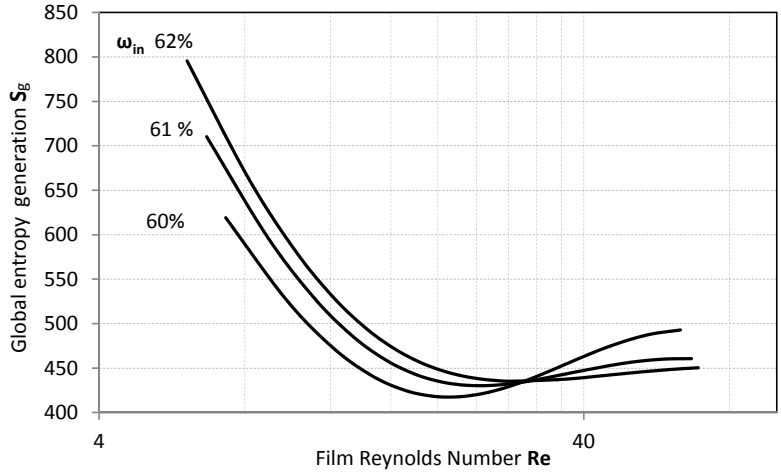

Fig. 3.19 Volumetric entropy generation [$kW \cdot m^{-3}K^{-1}$] as a function of Reynolds number for different inlet concentrations (abscissa in logarithmic scale); T_w=32.0℃, p=1.0 kPa, r=9.0mm, T_{in}=46.6℃.

Figure 3.20 highlights that increasing the absorber pressure also entropy generation increases. This response can be explained considering that a higher vapour pressure directly determines higher absorption rates and, indirectly, higher heat transfer rates at the tube wall. As a rule, increasing the absorber pressure or the inlet solution concentration, for the same value of the others parameters, increases the absorbed vapour mass flux (Fig. 3.21a-d). On the other hand, the

effect of an increased absorber pressure is stronger than a higher solution concentration, the irreversibility related to friction S_f decreases for increasing absorption pressures due to the higher heat released for the absorption of water vapour, while increases for higher concentration, pointing out that the influence of an increased viscosity is higher than that of heat of absorption on the temperature field.

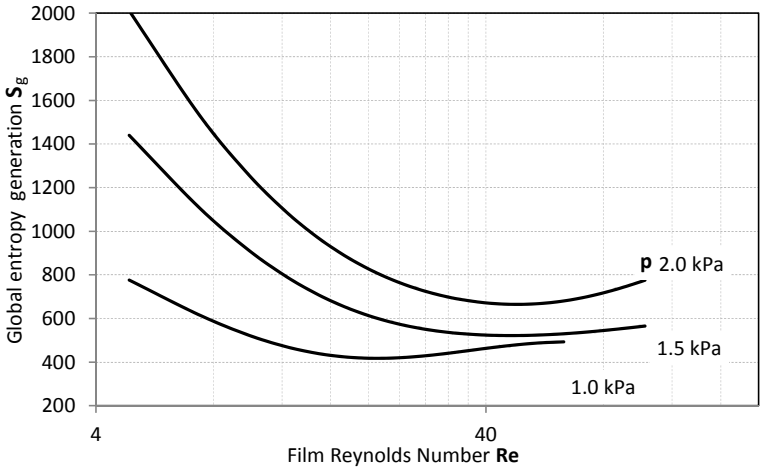

Fig. 3.20 Volumetric entropy generation [$kW \cdot m^{-3}K^{-1}$] as a function of Reynolds number for different absorber pressure (abscissa in logarithmic scale); ω_{in}=60%, T_w=32℃, p=1kPa, r=9mm, T_{in}=46.6℃.

Referring to the LiBr-H_2O concentration and temperature distributions that have been obtained from the numerical solution of the coupled species and energy transport equations inside the laminar falling film, where the velocity field was established according to Nusselt integral solution, gradients and fluxes of these variables can be estimated. As a result, the local volumetric entropy generation of the absorptive film flowing over a cooled horizontal tube can be integrated up to the component level.

Maintaining a distinction between the various entropy generation groups, related to different entropy variations sources, these have been globally discussed and analysed. The parametric analysis performed has made evidence of a minimum of the global entropy generation which can be always identified in terms of solution Reynolds number, and how the key operative parameters affect this optimal thermodynamic condition. The behaviour of each entropy generation group has been described and the importance of the group related to the coupled effect of heat and convective mass transfer on this strategic thermodynamic condition has been stressed. As a rule, lower tube radius, inlet temperature, inlet concentration and absorber pressure correspond to lower values of the optimal Reynolds number for the absorber, while the tube wall temperature shows a weak influence on that condition.

This analysis characterises the irreversibility of the process occurring in real absorbers and has been used to identify the least irreversible value of the solution flowrate for various operating conditions. These results make evidence of the importance to work at reduced values of this parameter with a thin uniform film. As a consequence, tension-active substances might be critical to realise this condition.

Also, it can be observed that changes in parameters' values (such as lower tube radii, lower coolant temperature or lower mass flowrates), which, in general, bring about an enhancement in the absorber performance, are associated to higher irreversibilities.

Nonetheless, the component internal irreversibilities have direct impact on the overall system performance being transferred outside the cycle through the heat exchangers and affecting the potential of these process that constitute the operative cycle. This observation suggests that the attempt to optimise the functionality of this device with respect to the sole second principle could also not be recognised as the best technical solution.

As a consequence, the internal process irreversibilities should be related to the performance improvement for the final technical target of the system to identify an optimal condition for the absorber and define a criterion for its thermodynamic optimisation.

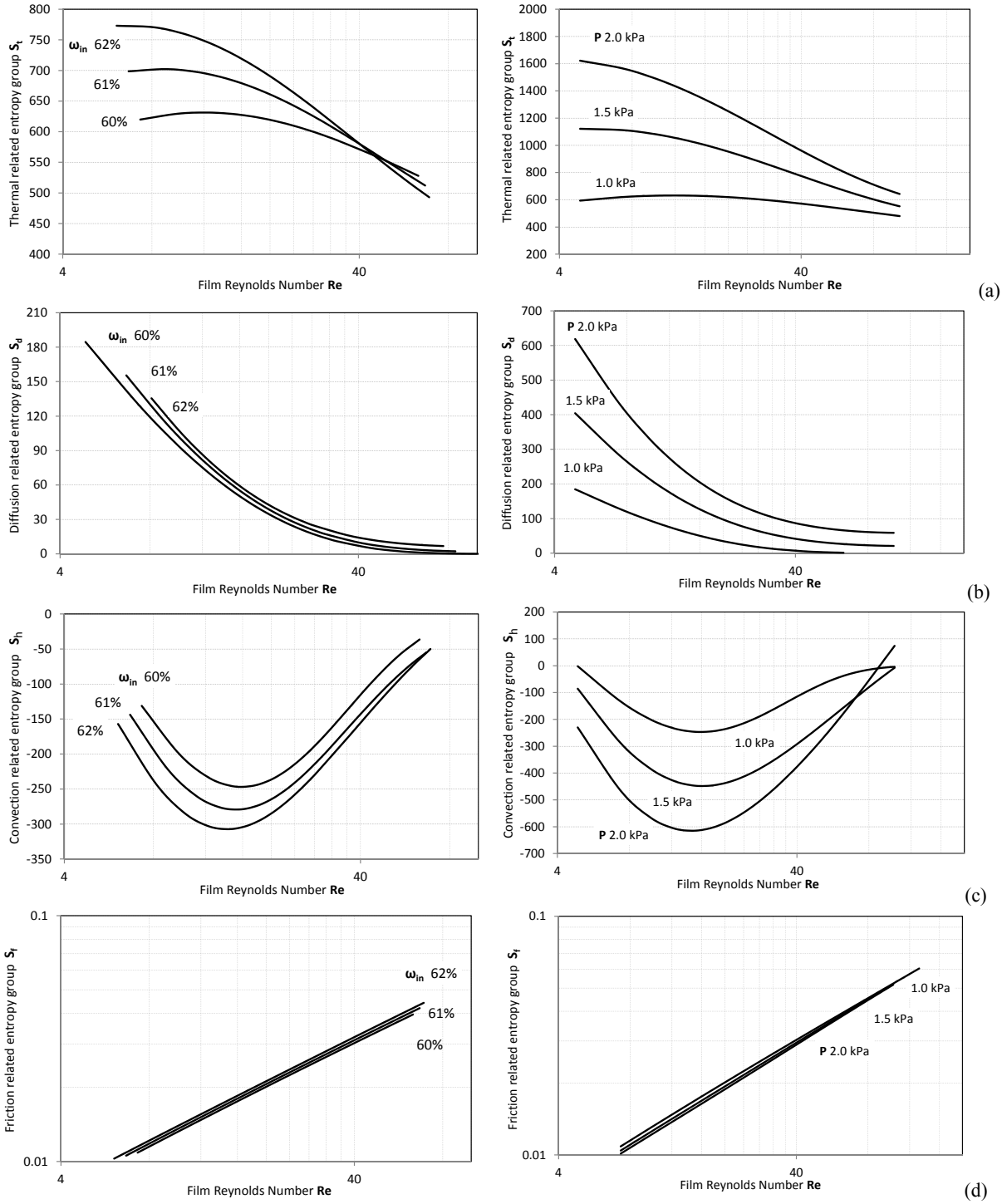

Fig. 3.21 Effects of different inlet concentration (left side) and absorber pressure [kPa] (right side) on the single entropy generation groups [$kW \cdot m^{-3}K^{-1}$] (a), (b), (c) (abscissa in logarithmic scale) (d) (logarithmic axes); T_w=32℃, T_{in}=46.6℃, r=9.0mm.

3.6 Optimisation parameters

In order to consider the final technical duty of the whole plant in which the absorber is operating, a general thermodynamic analysis is carried out for a chiller and a heat transformer, and it is used to underline the effect of the component irreversibility on the system COP. The inlet conditions of the LiBr-H_2O solution film are set at typical conditions of real absorbers, specifically at the equilibrium temperature for a 60% concentration solution at the absorber vapour pressure.

The total rate of entropy generation per unit volume S_g for an absorptive LiBr-H_2O liquid film flowing over a cooled horizontal tube is illustrated in figure 3.9. Nevertheless, in order to compare the performance of the system with the actual amount of irreversibility produced, the local volumetric entropy generation rate is integrated over the film physical domain. Considering film thickness and the circumference of the tube, the entropy generation rate per unit length of the tube E is defined by eq. 3.36.

$$\mathrm{E} = 2\int_0^{\pi r}\int_0^{\delta} S dy dx \tag{3.36}$$

The parametric analysis performed ascertains that, in terms of the film Reynolds number (eq. 3.35), it is always possible to identify a minimum E_g. This establishes the most desirable trade-off between two or more competing irreversibilities or the least irreversible thermodynamic condition of the specific process.

A parametric study is performed similarly to the one presented in paragraph 3.5, evaluating the influence on the entropy generation rate E of design and operability parameters, namely tube radius, coolant inlet temperature and inlet solution temperature, as function of the film Reynolds number. Figure 3.22 shows the effect of different tube radii on each entropy generation group.

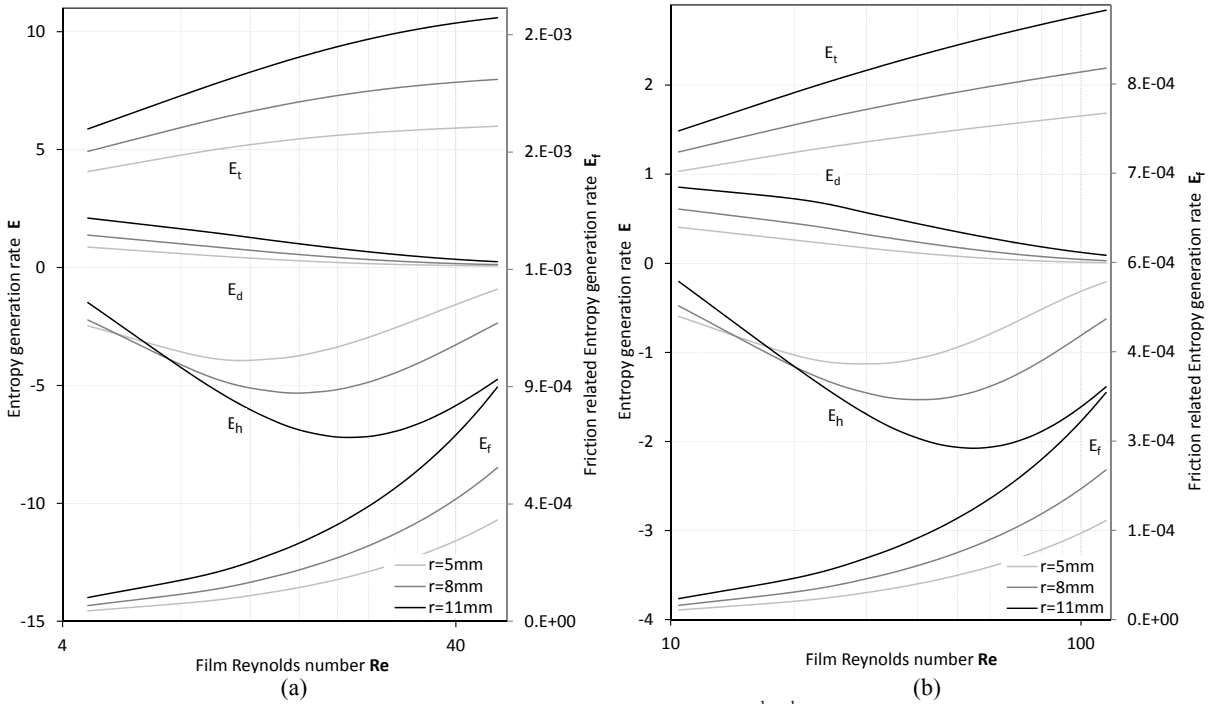

Fig. 3.22 Various entropy generation groups per unit length of the tube [$W \cdot m^{-1}K^{-1}$] as a function of film Reynolds number for different tube radii; (a) T_w=32.0℃, ω_{in}=60%, T_{in}=46.6℃, p=1.0 kPa, (b) T_w=83.0℃, ω_{in}=60%, T_{in}=97.1℃, p=12.5kPa

A bigger tube radius increases the absolute value of every entropy generation rate group integrated with reference to eq. 3.36. The group related to the coupled effects of mass convection and heat transfer E_h has a critical influence on the

global trend of the entropy generation rate per unit length E_g and, as already pointed out, it shows a minimum. A greater outer radius moves the minimum to higher Re and to lower values of E_h. Finally, the greater the tube radius the higher the friction related irreversibility E_f. Comparing chiller and heat transformer applications, as a rule, the latter highlights a greater impact of the diffusion related irreversibility, has lower entropy generation values and cope with higher solution Reynolds. Higher Reynolds numbers determine increasing friction and decreasing absorption rates, thus their respective entropy generation groups (E_f and E_d) show consistent trends. The combined effects of increasing extension of the entrance region, increasing film thickness and decreasing absorption heat release, globally establish increasing thermal related irreversibilities E_t. The minimum of the entropy generation group related to the coupled effects of mass convection and heat transfer E_h can be clarified considering that when Reynolds number is increased convection is amplified although absorption heat release is reduced, and this group assumes negative values.

The influence of the radius on the global entropy generation is presented in figure 3.23. As a rule, lower tube radii present lower entropy generation rates per unit length of the tube and match with lower solution Reynolds values. The trend of the global entropy generation shows a minimum value and the corresponding Reynolds number can actually be considered as the least irreversible operative condition for the specific technical configuration of horizontal tube falling film absorbers. For the chiller application case (Fig. 3.23a), least irreversibility Reynolds numbers of 10, 14 and 23 are obtained, respectively, for tube radii of 5, 8 and 11mm. For the same values of tube radii, but for an absorber operating at reference conditions for a heat transformer, respectively, 31, 42 and 52 (Fig. 3.23b) are the least irreversible Reynolds numbers. Again, careful attention should be paid to the fact that these values are extracted without considering partial wetting of the exchange surface, even though, in general, they correspond to solution mass flowrates which are not able to assure complete wetting, unless tension-active surfactants are added to the solution.

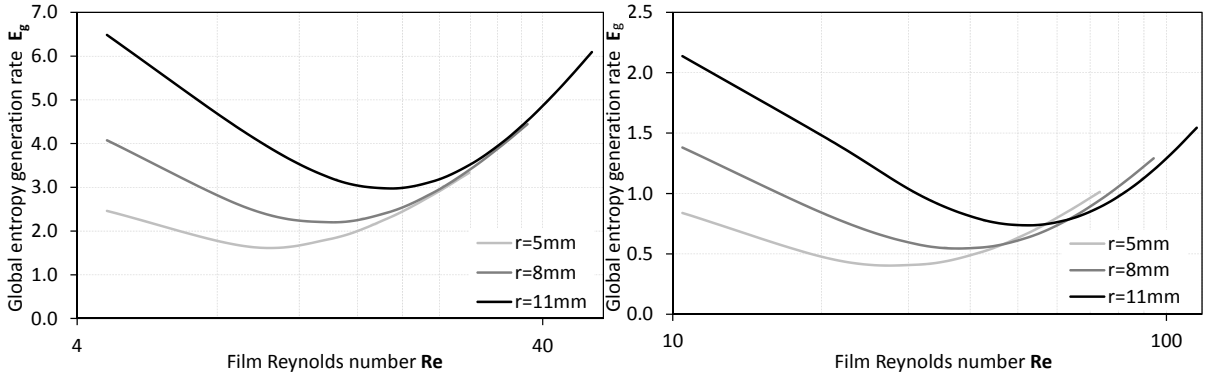

Fig. 3.23 Global entropy generation per unit length of the tube [$W \cdot m^{-1}K^{-1}$] as a function of film Reynolds number for different tube radii; (a) T_w=32.0℃, ω_{in}=60%, T_{in}=46.6℃, p=1.0 kPa, (b) T_w=83.0℃, ω_{in}=60%, T_{in}=97.1℃, p=12.5kPa

Figure 3.24 describes the effect of different tube wall temperatures on the various entropy generation groups. A lower wall temperature increases temperature gradients and, once the temperature gradient reaches the interface, also concentration gradients. Accordingly, figure 3.25 makes evidence of a higher entropy generation rate when the wall temperature is decreased, while the least irreversible Reynolds is weakly dependent on this parameter.

Also, friction related irreversibilities E_f (eq. 3.32) are indirectly affected by a different wall temperature which determines a different temperature field.

Given the low Reynolds operability typical of these systems, the overall significance of friction on the falling film absorption process on a horizontal smooth tube appears to be 4 orders of magnitude less important when compared to the other groups and phenomena involved.

Furthermore, the trend of the average rate of volumetric entropy generation S_g and the global rate per unit tube length E_g can be compared, observing different positions of the minima and reversed effect of the radius as a parameter.

Figures 3.23a-b, as well as 3.25a-b and 3.26a-b, if compared with the corresponding trends obtained for S_g, make evidence of the influence of the film thickness on the global entropy generation rate per unit tube length. This can be summarised as causing the increasing trend at high flowrates to be steeper and the decreasing trend at low flowrates to be less pronounced.

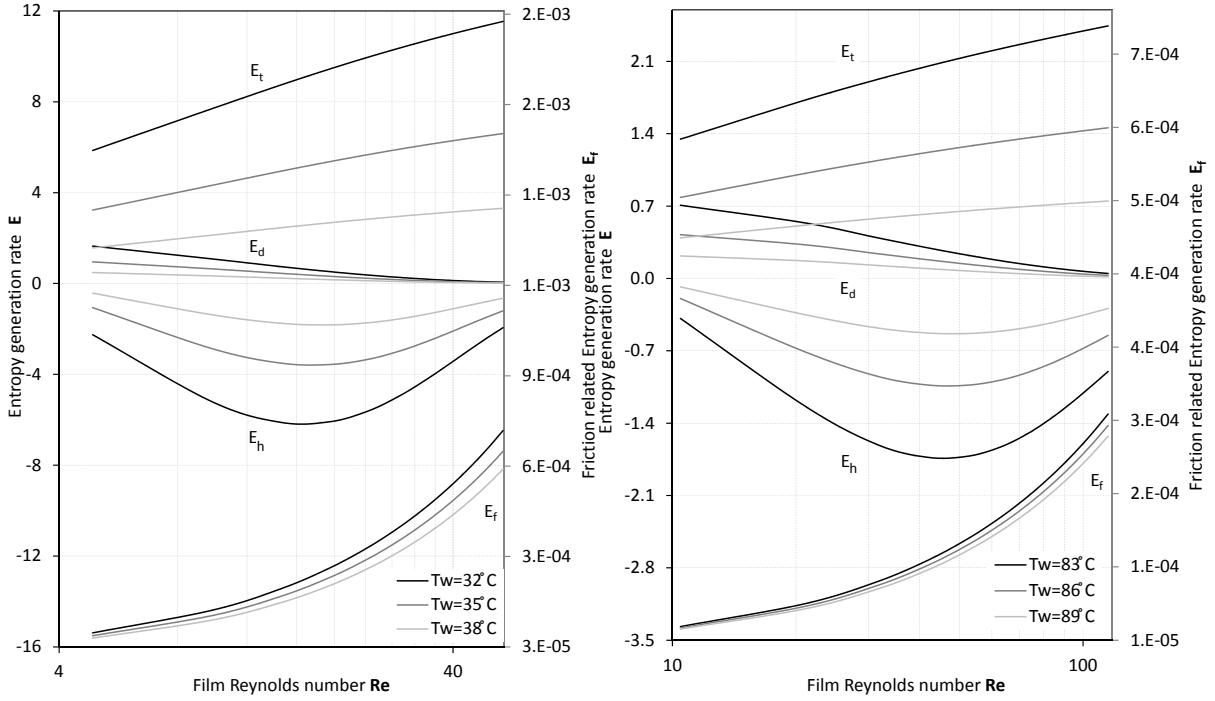

Fig. 3.24 Various entropy generation groups per unit length of the tube [$W \cdot m^{-1}K^{-1}$] as a function of film Reynolds number for different wall temperatures; (a) r=8.0mm, ω_{in}=60%, T_{in}=46.6℃, p=1.0 kPa, (b) r=8.0mm, ω_{in}=60%, T_{in}=97.1℃, p=12.5kPa

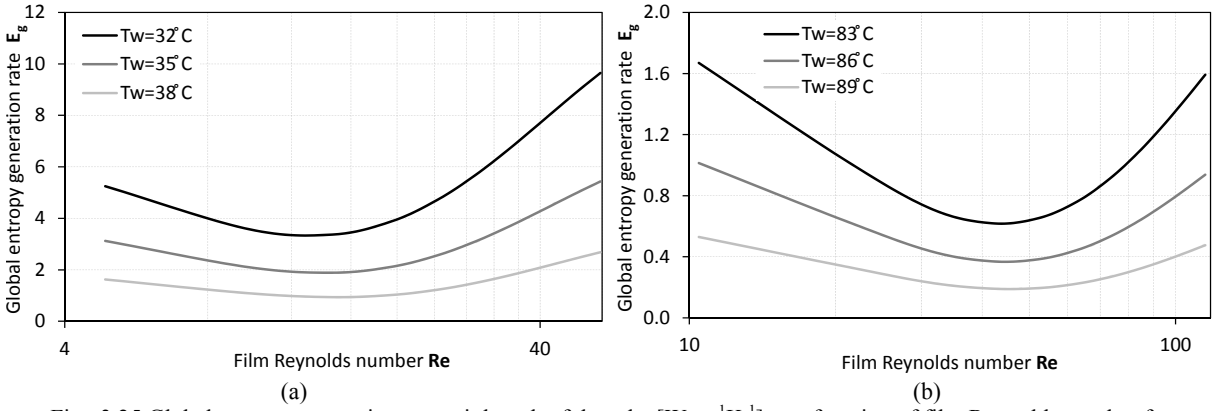

Fig. 3.25 Global entropy generation per unit length of the tube [$W \cdot m^{-1}K^{-1}$] as a function of film Reynolds number for different wall temperatures; (a) r=8.0mm, ω_{in}=60%, T_{in}=46.6℃, p=1.0 kPa, (b) r=8.0mm, ω_{in}=60%, T_{in}=97.1℃, p=12.5kPa

The effect of a different inlet temperature at the interface (and, a different absorber pressure due to the inlet equilibrium hypothesis) is revealed in figure 3.26 for both chiller and heat transformer applications. Since the tube wall temperature is maintained constant, it is possible to observe how different inlet temperatures have a similar effect to that of different wall temperatures for a fixed inlet condition. However, for the same temperature difference T_{in}-T_w, a change in the inlet temperature value brings about a smaller entropy generation than that correspondingly obtained by changing

the wall temperature. Also, lower the inlet temperatures are associated to slightly lower Reynolds corresponding to the least irreversible condition.

Acting again on the temperature difference T_{in}-T_w, inlet solution temperature variations have similar effects to those of a different wall temperature on each entropy generation group, thus the corresponding graph can be omitted, and the description of the influence of this parameter can be referred to figures 3.24a-b.

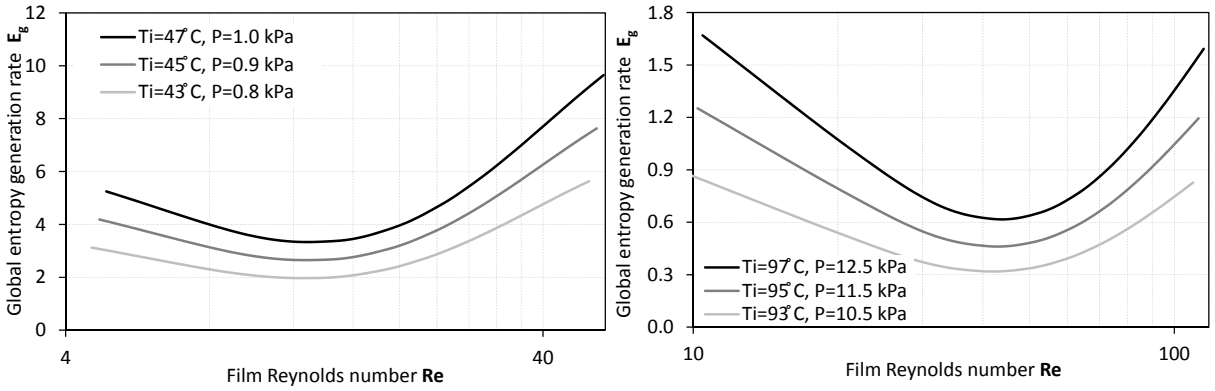

Fig. 3.26 Entropy generation per unit length [W·m^{-1}K^{-1}] as a function of Reynolds number for different inlet temperatures; (a) r=8.0mm, ω_{in}=60%, T_w=32.0℃, (b) r=8.0mm, ω_{in}=60%, T_w=83.0℃

As a rule, the formulation of thermodynamic optimisation criteria has always accompanied the technical development of energy systems in order to improve their performance. Since the development of finite-time thermodynamics, the attention has been moved towards the concept of non-equilibrium processes and their related irreversibility sources. Since the use of absorption systems has attracted a remarkable attention and has demonstrated a great potential in the utilisation of low-grade heat sources (as additional examples [81-84]), a comprehensive literature production have generally analysed both chiller and heat transformer configurations [6-22) 46-48) 53) 85-90)].

Based on the previous irreversibility analysis in a falling film configuration of the absorber, this chapter aims at the definition of proper dimensionless parameters for the optimisation of this component with reference to the ultimate duty of the whole system. In general, an absorption refrigeration machine is supposed to extract heat at a lower temperature than those of the external ambient and the driving-fluid delivering heat at the generator. The cooling effect is realised by the evaporation of the condensed refrigerant, which is then absorbed by the solution inside the absorber, in order to be effectively pumped at the generator pressure level and repeat the cycle steadily. A heat transformer is a system which aims at delivering heat at a higher temperature than the given temperature of the heat source. The component of the plant which actuates this final heat transfer process is, in fact, the absorber. Accordingly, the best operative condition of the absorber in different application cases may correspond to different circumstances.

For the first principle of thermodynamics, the COP of an absorption system can be expressed in a general way by eq. 3.37 for a refrigeration application and eq. 3.38 in case of heat temperature boosting one.

$$COP_{CH} = \frac{Q_E}{W}\frac{W}{Q_G} = \frac{Q_E}{Q_C - Q_E}\frac{Q_G - Q_A}{Q_G} = \frac{Q_E}{T_C\left(\frac{Q_C}{T_C} - \frac{Q_E}{T_C}\right)}\frac{T_A\left(\frac{Q_G}{T_A} - \frac{Q_A}{T_A}\right)}{Q_G} \tag{3.37}$$

$$COP_{HT} = \frac{Q_A}{W}\frac{W}{Q_G} = \frac{Q_A}{Q_A - Q_E}\frac{Q_G - Q_C}{Q_G} = \frac{Q_A}{T_E\left(\frac{Q_A}{T_E} - \frac{Q_E}{T_E}\right)}\frac{T_C\left(\frac{Q_G}{T_C} - \frac{Q_C}{T_C}\right)}{Q_G} \tag{3.38}$$

Introducing the second principle of thermodynamics, applied to irreversible cycles where isothermal heat transfer without any temperature difference at the heat exchange occurs, is possible to state,

$$\frac{Q_C}{T_C} = \frac{Q_E}{T_E} + \Sigma_{EC} \quad , \quad \frac{Q_A}{T_A} = \frac{Q_G}{T_G} + \Sigma_{GA} \tag{3.39}$$

$$\frac{Q_A}{T_A} = \frac{Q_E}{T_E} + \Sigma_{EA} \rightarrow \frac{Q_E}{T_E} = \frac{Q_A}{T_A} - \Sigma_{EA} \quad , \quad \frac{Q_C}{T_C} = \frac{Q_G}{T_G} + \Sigma_{GC} \tag{3.40}$$

Accordingly, the expression of the system performance, in terms of COP, can be rearranged highlighting the influence of components irreversibilities. These simplified expressions (eq.s 3.41 and 3.42) describe the system performance in a chiller and heat transformer configuration as a function of the main temperature levels of heat sources and sinks involved, the Carnot efficiencies of an engine, a refrigeration machine and a heat pump operating between these main temperature levels heat transfer and irreversibilities of the fundamental heat exchangers.

$$COP_{CH} = \frac{Q_E}{T_C\left(\frac{Q_E}{T_E} + \Sigma_{EC} - \frac{Q_E}{T_C}\right)}\frac{T_A\left(\frac{Q_G}{T_A} - \frac{Q_G}{T_G} - \Sigma_{GA}\right)}{Q_G} = \frac{1 - \frac{T_A}{T_G} - \frac{\Sigma_{GA}T_A}{Q_G}}{\frac{T_C}{T_E} - 1 + \frac{\Sigma_{EC}T_C}{Q_E}} = \frac{\eta_{CaTM-GA} - \frac{\Sigma_{GA}T_A}{Q_G}}{\frac{1}{\eta_{CaRM-EC}} + \frac{\Sigma_{EC}T_C}{Q_E}} \tag{3.41}$$

$$COP_{HT} = \frac{Q_A}{T_E\left(\frac{Q_A}{T_E} - \frac{Q_A}{T_A} + \Sigma_{EA}\right)}\frac{T_C\left(\frac{Q_G}{T_C} - \frac{Q_G}{T_G} - \Sigma_{GC}\right)}{Q_G} = \frac{1 - \frac{T_C}{T_G} - \frac{\Sigma_{GC}T_C}{Q_G}}{1 - \frac{T_E}{T_A} + \frac{\Sigma_{EA}T_E}{Q_A}} = \frac{\eta_{CaTM-GC} - \frac{\Sigma_{GC}T_C}{Q_G}}{\frac{1}{\eta_{CaHP-EA}} + \frac{\Sigma_{EA}T_E}{Q_A}} \tag{3.42}$$

Broadly speaking, when a comprehensive point of view is adopted, chiller and heat transformer application cases, eq. 3.41 and 3.42 emphasise the effect of irreversibility on the system COP. More precisely, making evidence of the importance to minimise components irreversibilities, they state that by maximising the dimensionless groups "$Q/\Sigma T$" the efficiency of the system is improved. Even though the expressions obtained for the system performance are based on a simplified approach, indicate a way to improve the system efficiency by acting also on single devices irreversibilities (in this case the absorber).

In a chiller (but this observation is also valid for a heat pump application case), the optimal performance can be identified by the condition at which the absorber operates at the maximum absorption rate with the least thermal power to be rejected. On the other hand, for a heat transformer, the best operative condition corresponds to the maximum thermal power supplied at high temperature for the least power supplied at the generator. Under this approach, based on the previous dimensionless group, two different dimensionless parameters are introduced. Eq. 3.43 defines the parameter used to maximise heat transfer at the absorber tube wall with regards to the irreversibility introduced, useful in order to enhance the efficiency of the whole system in a heat transformer application.

$$DQ = \frac{q_w}{\mathrm{E}_g T_w} \tag{3.43}$$

Namely, by maximising DQ the heat flux per unit tube length is maximised for a certain irreversibilitiy production inside the absorber. From an alternative standpoint, at maximum DQ, the product $E_g T_w$ of the total irreversibility per unit length of the tube and the tube temperature is minimised for a certain thermal power per unit length q_w to be extracted by the cooling water. This product embodies the thermal flux associated to the entropy variation of the whole process, in case this would be generated by heat transfer at constant temperature T_w and represents the loss of the available thermal power ascribed to the process irreversibility.

Similarly, eq. 3.44 defines the dimensionless group used to maximise absorption at the film interface with regards to the irreversibility introduced, in order to eventually enhance the efficiency of a chiller configuration.

$$DA = \frac{G_{vg} i_{abs}}{\mathrm{E}_g T_e} \tag{3.44}$$

T_e is defined as the equilibrium temperature of the solution at the inlet concentration ω_{in} (under the assumption of thermodynamic equilibrium at the inlet $T_e=T_{in}$), as a result, its physical significance corresponds to the temperature that would be reached if the equilibrium could be obtained without changes in concentration. DA is the ratio between the entropy generation rate that would be produced by the heat transfer of the thermal power per unit length related to the release of the heat of absorption by the absorbed vapour at the film interface (at fixed temperature T_e) and the global entropy generation rate per unit length E_g. Defined in this way, DA is proportional to the $Q/\Sigma T$ group appearing in eq. 3.41. As a result, by maximising this parameter the absorption flux per unit tube length G_{vg} (and consequently $Q_E=nLG_{vg}(h_{Eout}-h_{Ein})$) is maximised for a certain irreversibility generation inside the film and the absorber. Otherwise, at the maximum DA, the group $E_g T_e \cdot i_{abs}^{-1}$ is minimised for a certain vapour flux per unit length of the tube. This group represents the absorbed vapour flux per unit length of the tube associated to the entropy variation of the whole process, in case this would be generated by the release of the heat of absorption i_{abs} at constant temperature T_e.

The operability of the absorber can be investigated and then optimised with respect to these dimensionless parameters for both the absorption chiller and the heat transformer application cases under analysis.

3.7 Chiller operability optimisation

By performing simulation in the extended range of the parameters of interest, it can be observed that a specific value of the film Reynolds number maximising the dimensionless parameter proportional to the group $Q/\Sigma T$ (DA for the chiller application, DQ for the heat transformer application) can always be identified. It can be stated that these values of film Reynolds (referred to as optimal Reynolds in the following) are mainly dependent on the specific on the application case (i.e chiller or heat transformer operability) and on the outer tube radius, while a weak influence of the temperature difference between the inlet solution and the wall temperature is shown (Fig. 3.27, 3.28, 3.31 and 3.32).

In general, the maximum value of DA is approximately constant and the film Reynolds that maximise mass transfer, with regard to DA, increases continuously when the tube radius is increased (Fig. 3.27).

Indeed, according to the results presented in figure 3.27, it can also be stated that, for any fixed Reynolds there is an optimal value of the tube radius, whose value increases with Reynolds, but more steeply at low than high values. Accordingly it is possible to identify an asymptotic maximum value of the radius, above which is not convenient to operate with any flowrate.

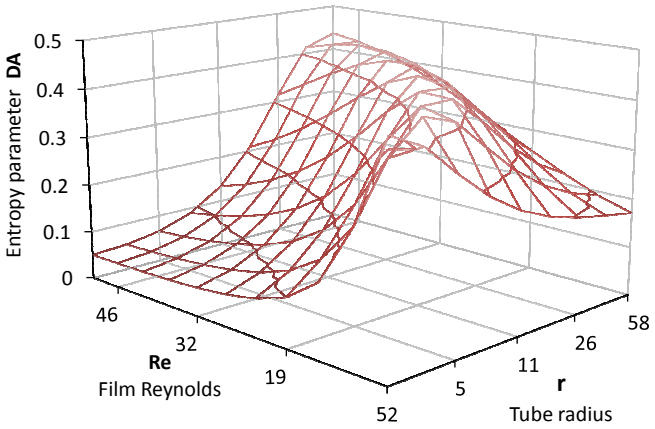

Fig. 3.27 Dimensionless parameters *DA* as a function of film Reynolds number and tube outer radius *r* [mm] at chiller representative conditions; ω_{in}=60%, T_{in}=46.6℃, T_w=32.0℃, p=1.0 kPa (T_e=46.6℃)

On the other hand, when the difference between tube wall and inlet temperature is decreased (Fig. 3.28), for a fixed Reynolds, the dimensionless group *DA* shows a persistently increasing trend. This behaviour can be explained considering the fact that, provided the increase of heat transfer (and indirectly mass transfer) for a lower temperature of the tube wall, the irreversibility associated to the absorption process increases at a higher rate than heat and mass transfer. In any case, an optimal condition in terms of film Reynolds number can always be recognised and the corresponding value increases when the inlet temperature of the solution is increased.

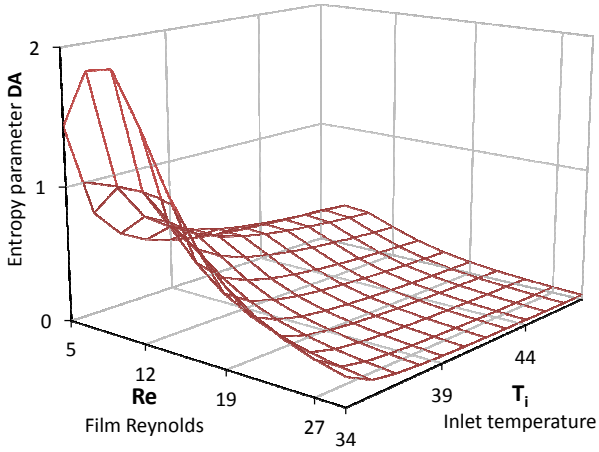

Fig. 3.28 Dimensionless parameters *DA* as a function of film Reynolds number and inlet solution temperatures T_{in} [°C] at chiller representative conditions; r=8mm, ω_{in}=60%, T_w=32.0℃

The previous calculation results have been attained under the assumption of thermodynamic equilibrium of the inlet solution with the vapour at the absorber pressure. This condition, which appears to be suitable for a general analysis, doesn't correspond to the typical operability of the absorber in actual plants [58) 60)]. Accordingly, relaxing this hypothesis, the analysis is extended to include sub-cooled conditions of the inlet solution. To this aim, the dimensionless parameter Ξ is defined according to eq. 3.44. The latter expresses the boundary and initial temperature conditions in a dimensionless form, linking solution sub-cooling to the temperature difference between the wall and the equilibrium temperature of the inlet solution with the vapour.

$$\Xi = \frac{T_e - T_{in}}{T_{in} - T_w} \tag{3.44}$$

As a first screening attempt, by introducing 2°C sub-cooling of the solution (Fig. 3.29) and keeping it constant the maximum values of *DA* move to higher Reynolds. The obtained trend of the objective function *DA* with respect to Reynolds and the tube outer radius in this case is qualitatively and quantitatively similar to the case of an inlet solution at thermodynamic equilibrium with the vapour in the absorber (Fig. 3.27), and will be hence omitted.

In order to directly investigate the influence of the sub-cooling, it is then possible to change the Ξ value keeping fixed T_w and T_e (Fig. 3.30).

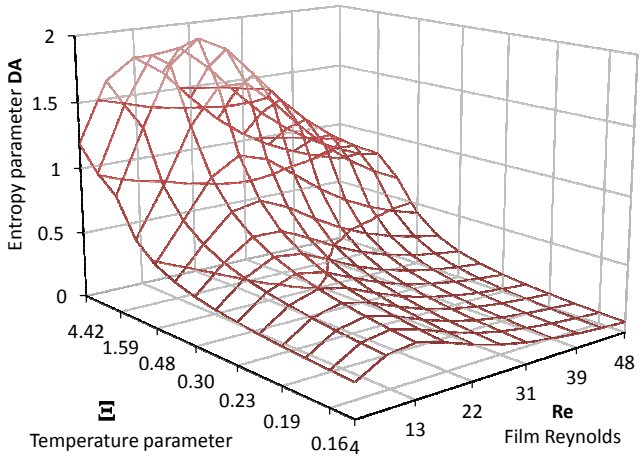

Fig. 3.29 Dimensionless parameters *DA* as a function of film Reynolds number and inlet temperature T_{in} [°C] at chiller representative conditions, 2°C sub-cooling inlet solution, r=8mm, ω_{in}=60%, T_w=32.0℃, p=1.0 kPa

Higher values of the sub-cooling at the inlet move the maximum to higher Reynolds.

Assuming a different optimisation standpoint in a chiller absorption system, it can be stated that a best value of the solution sub-cooling can be identified and furthermore, for a fixed value of Ξ, an optimal Reynolds can always be identified. What is more, when the absorber works with an inlet solution characterised by the optimal value of the sub-cooling, the corresponding optimal Reynolds (Re=17) is at its highest value.

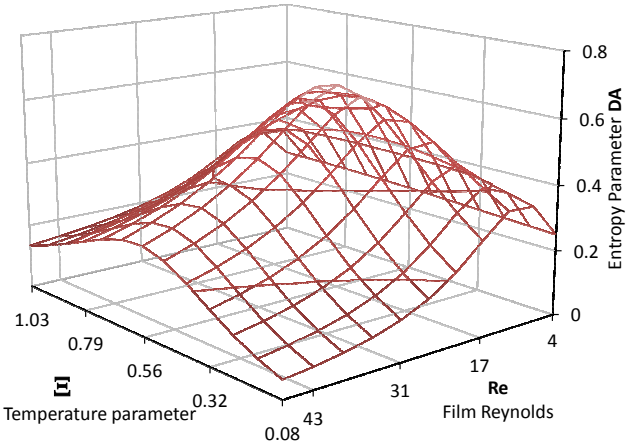

Fig. 3.30 Dimensionless parameters *DA* as a function of film Reynolds number by changing solution sub-cooling at chiller representative conditions, r=8mm, ω_{in}=60%, T_w=32.0℃, T_e=46.6℃, p=1.0 kPa

These results suggest once more operating at low solution mass flowrates and with a small temperature difference between the inlet solution and the cooling water. The latter requirement can be achieved by properly managing the

design of the solution heat exchanger. These findings are consistent with global simulation [91] results and empirically guided technical development.

In the specific case of falling film absorbers, the film thickness constitutes the main heat transfer resistance with the cooling water circulating inside the tube and it has been theoretically and experimentally recognised that working with reduced solution mass flow rate can improve the system performance. As a result, operability at reduced Reynolds number is attractive for absorption plants, but the tube partial wetting at low solution flow rate needs to be considered as a critical related issue. Regarding the temperature difference between the inlet solution and the tube wall temperature a low value of this parameter reduces the irreversibility of the process. However, under this point of view in a specific application case the size-constraint of the system is also expected to be decisive.

Both figures 3.29 and 3.30 show a maximum of the *DA* value. By considering the physical meaning of this parameter from a system point of view, the chiller operates at the maximum absorption rate with the least irreversibility introduced by the absorber, and, bearing in mind eq. 3.41, this is beneficial to the whole system COP.

3.8 Heat transformer operability optimisation

Similarly to the absorption chiller case, the dimensionless parameter *DQ* defined by eq. 3.45 gives a way to optimise the absorber of a heat transformer plant. When thermodynamic equilibrium is assumed, figure 3.31 shows that, similarly to *DA*, the optimal Reynolds increases for higher tube radii, but the maximal value of *DQ* is roughly constant. According to this criterion, for the heat transformer application case, Reynolds number of 30, 40 and 55 maximise heat transfer in the absorber (or minimise the process irreversibility for a given useful effect), respectively, for tube radii equal to 5mm, 8mm and 11mm.

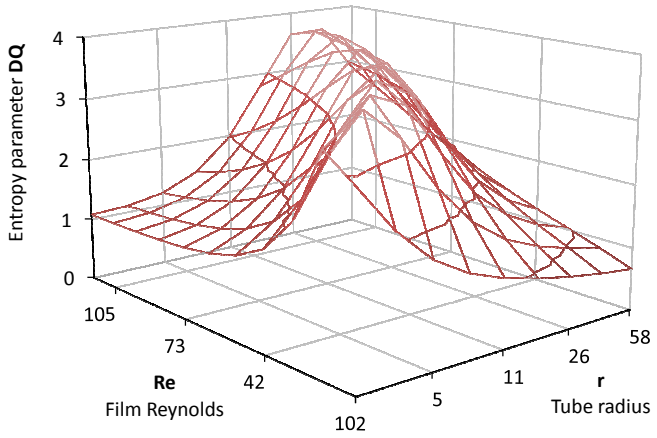

Fig. 3.31 Dimensionless parameters *DQ* as a function of film Reynolds number and tube outer radius *r* [mm] at heat transformer representative conditions, T_w=83.0℃, ω_{in}=60%, T_{in}=97.1℃, p=12.5kPa

DQ increases relentlessly when the wall temperature is augmented for a fixed Reynolds number (Fig. 3.32).

When the assumption of thermodynamic equilibrium of the inlet solution is relaxed (Fig. 3.33) and a 2°C sub-cooling is introduced (consistently with the calculation performed for the chiller application), the maxima move to slightly higher Reynolds. Also, the influence of the tube wall temperature is intensified and higher T_w are associated to increasing Reynolds. More significantly, an optimal *DQ* condition can be shown with respect to T_w and Reynolds for the heat transformer; corresponding to a solution flowrate of 0.035kg·m^{-1}s^{-1}, and a cooling water temperature bringing the tube surface at T_w=92 °C (Fig. 3.33). In this circumstance the optimal wall temperature is at its minimum and the optimal Reynolds (Re=71) is maximised.

The behaviour of the previously defined objective function *DQ* with respect to Reynolds and the tube outer radius for a sub-cooled solution marginally differs from the case of an inlet solution at thermodynamic equilibrium with the vapour in the absorber; therefore, is not represented herein.

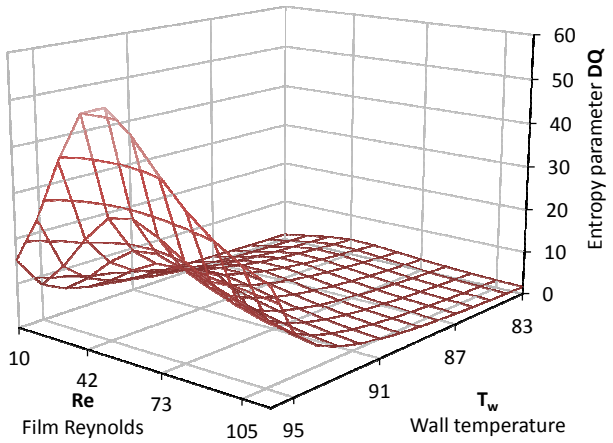

Fig. 3.32 Dimensionless parameters *DQ* as a function of film Reynolds number and tube wall temperature T_w [°C] at heat transformer representative conditions, r=8.0mm, ω_{in}=60%, T_{in}=97.1℃, p=12.5kPa

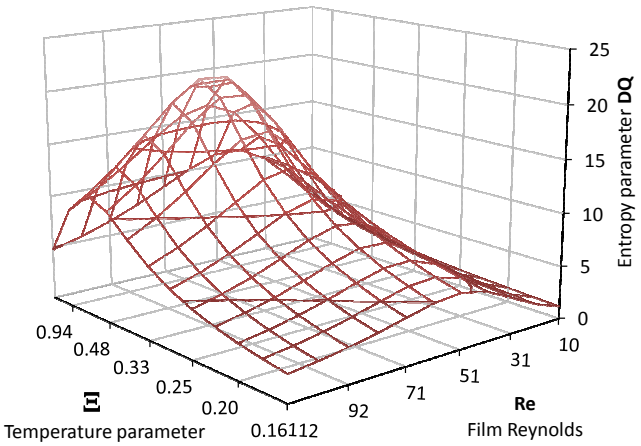

Fig. 3.33 Dimensionless parameters *DQ* as a function of film Reynolds number changing tube wall temperature T_w [°C] at heat transformer representative conditions, 2°C sub-cooling inlet solution, r=8.0mm, ω_{in}=60%, T_{in}=95.1℃, p=12.5kPa

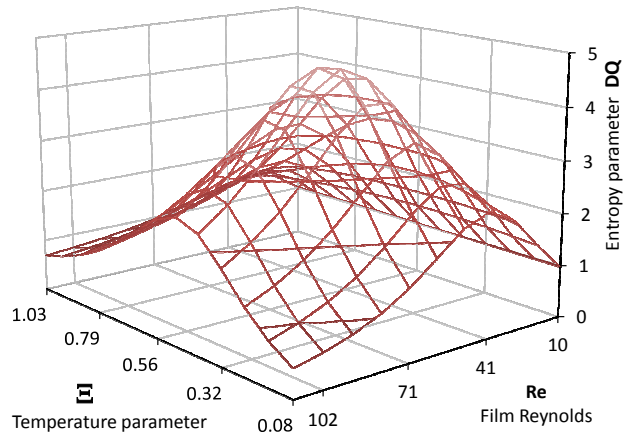

Fig. 3.34 Dimensionless parameters *DQ* as a function of film Reynolds number and solution sub-cooling at heat transformer representative conditions, r=8.0mm, ω_{in}=60%, T_w=83.0℃, T_e=97.1℃, p=12.5kPa

When both T_w and T_e are fixed and the sub-cooling of the inlet solution becomes a parameter, a best value of the latter (i.e. Ξ) can be identified (Fig. 3.34). Up to that value, higher sub-cooling at the inlet move the optimal condition to lower wall temperatures and higher Reynolds. By referring to the physical meaning of this parameter, while maximising

DQ, ceteris paribus for the operative conditions of the other components, the whole systems operate at its highest COP and best thermodynamic state. This condition corresponds to the maximum thermal power delivered by the heat transformer at high temperature for the least irreversibility generated at the absorber.

3.9 Summary

Summarising, LiBr concentration and temperature distribution inside the laminar falling film have been obtained from the numerical solution of the coupled system of species and energy transport equations. Velocity, temperature and concentration field, in turn, allow estimating gradients and fluxes of these variables and, finally, the local volumetric entropy generation of an absorptive film flowing over a cooled horizontal tube. Various entropy generation groups, distinguished with regard to different entropy variations sources, have been discussed and locally analysed with reference to the effects of different tube radii, tube wall temperature, inlet solution temperatures and concentrations. This analysis characterises the irreversibility of the process in this specific heat exchanger configuration and can be related to absorption occurring inside real absorbers operating inside chillers, heat pumps or heat transformers. As a result, the local volumetric entropy generation of the absorptive film flowing over a cooled horizontal tube can be integrated up to the component level. Maintaining a distinction between the various entropy generation groups, related to different entropy variations sources, these have been globally discussed and analysed. The parametric analysis performed has made evidence of a minimum of the global entropy generation which can be always identified in terms of solution Reynolds number, and how the key operative parameters affect this optimal thermodynamic condition. The behaviour of each entropy generation group has been described and the importance of the group related to the coupled effect of heat and convective mass transfer on this strategic thermodynamic condition has been stressed. As a rule, lower tube radius, inlet temperature, inlet concentration and absorber pressure correspond to lower values of the optimal Reynolds number for the absorber, while the tube wall temperature shows a weak influence on that condition.

This analysis characterises the least irreversible value of the solution flowrate for various operating conditions. These results make evidence of the importance to work at reduced values of this parameter with a thin uniform film. As a consequence, tension-active substances might be critical to realise this condition.

Also, it can be observed that changes in parameters values (such as lower coolant temperature, lower tube radii or lower flowrates), which generally bring an enhancement in the absorber performance, are at the meantime associated to higher local and global irreversibilities. This observation suggests that the attempt to optimise the functionality of this device with respect to the sole second principle could also not be recognised as the best technical solution. As a consequence, the related increase of irreversibility needs to be compared to the performance improvement related to the effect of these variations to identify the optimal thermodynamic condition for the absorber, and this model can been used to define a criterion for the thermodynamic optimisation of the absorber.

From the local volumetric entropy generation rate of an absorptive film flowing over a cooled horizontal tube the global entropy generation rate E has been estimated and investigated with respect to the critical parameters at play. The global analysis characterises the irreversibility of the process occurring in real absorbers and has been used to identify the least irreversible value of the solution flowrate for a chiller and a heat transformer application cases. In addition, the entropy generation rate at heat transformer operative conditions is lower than that of the chiller and, although the overall trend is conserved, the minima occur at higher Reynolds and a higher impact of the diffusion related irreversibility can be highlighted.

As a rule, a bigger tube radius increases the absolute value of every entropy generation group. The group related to the coupled effects of mass convection and heat transfer E_h has a critical effect on the global trend of the entropy generation rate per unit length E_g and shows a local minimum. The bigger the tube radius the higher the amount of friction related irreversibilities E_f are produced in the absorber. A higher difference between the solution inlet and tube wall temperatures increases the entropy generation rate, while the optimal Reynolds is weakly dependent on this parameter. Finally, a bigger diameter of the tube moves the minimum to higher Re and to lower values of E_h.

Moreover, a simplified and general thermodynamic analysis of the whole system performance has been proposed in order to highlight the important role of irreversibilities Σ on the overall performance of the system. This analysis brings back to the point made in the previous chapter and makes evidence of a dimensionless ratio "$Q/\Sigma T$" that separates the weight of the irreversibilities. Meanwhile, it is clarified how by maximising this term the system efficiency can be enhanced. Since the functioning duty of the absorber is different in refrigeration system and in a heat boosting application, two different dimensionless parameters, *DQ* and *DA*, have been defined by comparing, respectively, thermal flux at the tube wall and absorption at the interface with entropy generation rate related to the process. The following main conclusion can be accordingly stated:

- When the inlet solution is at thermodynamic equilibrium with the vapour pressure in the absorber, *DQ* and *DA* can be maximised by a defined value of film Reynolds number.
- The sub-cooling of the solution moves the occurrence of the maxima to higher Reynolds. Contrarily to the case of thermodynamic equilibrium, *DQ* and *DA* can be maximised also with respect to the temperature difference between the inlet and the wall temperatures and higher values of the sub-cooling move the maximum to higher temperature differences.
- Furthermore, by considering the physical meaning of each parameter and the different operability of the absorber in the two application cases considered, it can be observed that the optimal value of *DA*, at which the absorber operates at the maximum absorption rate with the least thermal power to be rejected, corresponds to the most suitable condition for a chiller or a heat pump, while by maximising *DQ* in the absorber the maximum thermal power is supplied at high temperature and the heat transformer performance is increased.

In conclusion, *DQ* and *DA* practically allow the user to realise a thermodynamic optimisation of the absorber performance with respect to Reynolds, tube radius and cooling water temperature, by taking into account entropy generation and the technical duty of the system. Also, their positive influence on the overall system performance has been suggested. Again results suggest operating the absorber at low solution flowrates with a thin and uniform film.

Chapter 3,
Falling film absorbers optimisation criterion

Chapter 4, Falling film stability and wetting behaviour

The thermodynamic analysis presented in the previous chapter and recent literature concerning falling film absorbers suggest that heat and mass transfer performances of falling film heat exchangers are drastically affected by various hydrodynamic aspects which are responsible for determining the distribution of the solution along and over the tube bundle. More precisely, the results of the previous analysis suggest the importance to work at reduced mass flowrates with a thin uniform film to increase the system performance and/or reduce its size.

At these operative conditions, specifically at low Reynolds and high Weber numbers, the assumptions of a film with uniform thickness and a complete wetting of the transfer surface can't be considered, even approximately, rigorous and leads to unacceptable inaccuracy of simulations results in that operative region. Furthermore, partial wetting is recognised to occur even at typical operative conditions of absorption systems. Accordingly, the inadequacy of previous theoretical models of the absorptions process in falling film heat exchangers can be ascribed to a major issue correlated to this particular phenomenon.

Partial wetting of the exchange surface as the solution flowrate is reduced brings about a reduction of the area of the interfaces contributing to heat and mass transfer. The circumstances under which the film breaks down and the extension of the resulting dry spots are of critical importance to predict the performance of these devices and of the system they belong to. Both a criterion of film stability, to identify the minimum wetting rate able to ensure a complete wetting of the solid surface, and, after the film breakage, a method to estimate the wet part of the solid surface and the extension of the vapour-liquid interface are demanded for an accurate description of these processes. To this aim, the principle of minimising the energy of a given stream-wise section of the film is applied in order to model and investigate the film stability and the local wetting behaviour. This approach is extended to include hysteresis behaviour of the contact angle (considering advancing and receding contact angles) and wettability hysteresis when increasing or decreasing mass flowrates are delivered. An application case on a vertical fin-tube contactor is studied and compared with experiments for a first validation. Afterwards, a semi-empirical model suitable for a horizontal tube bundle is developed to match the characteristics of real absorbers. In this way, the effect of these phenomena can be included in the absorption model to extend its validity and increase its accuracy. Nonetheless, to reach the highest technical performance of this component, new materials and surface characteristics for an improved wettability of the film along the tube bundle should be investigated in parallel with theoretical studies and modelling efforts.

4.1 Falling film hydrodynamics

The chaotic behaviour characterising falling film dynamics even at low Reynolds number constitutes a fascinating phenomenon frequently occurring in nature and being recurrent in technical applications. This complexity stems from the combination of a number of aspects, challenging and pushing forward an active research effort towards interdisciplinary issues that have not been comprehensively resolved as of yet. Concerning heat and mass transfer application cases at low specific mass flowrates, apart from the extended contact area and small thermal resistance, convection effects stimulated by surface tension gradients (or Marangoni effect) brings a drastic enhancement of interfacial and internal transport phenomena. As a rule, these devices require conditions which avoid thin liquid films to break into a number of rivulets, exposing the solid heat transfer surface partly uncovered and/or lowering the extension of the liquid-vapour interface, where mass transfer occurs. As a consequence, thin liquid films are attractive to increase the performance of heat and mass transfer devices and reduce their overall size, but the drop of the contact area due to the occurrence of partial wetting must be considered as a related issue.

Extensive literature and experimental data have been published about wetting phenomena [92-99] and properties involved in these mechanisms (especially, regarding the contact angle characterising the interaction between the coexisting three phases [100-103]), emphasising their complexity and the active interest about them. Unfortunately, a shared agreement on the specific reasons of film break-down has not been reached and the amount of data concerning a variety of parameters such as temperature level, surface inclination and geometry, mode of liquid distribution, physical

properties, etc., which have a significant role in preserving fully wetted surfaces, are incomplete [92-93] and characterised by large deviation. Nevertheless, the role of the film wetting ability in determining the efficiency of the absorption process has been recognised as a critical factor [6) 104-107].

Considering the main features at the characteristic scale of falling film absorption, the influences of inertia (in the specific case of interest directly caused by gravity) and surface tension dominate the film hydrodynamic behaviour. In particular, once the solid surface geometry is defined, their conflicting effects (gravity forcing towards flowing configurations and iso-potential flat interfaces, whereas surface tension tends to create stationary spherical phase boundaries) establish stability limitations which, in certain operative conditions, define metastable hysteresis phenomena. These, in turn, reflects importantly on a proper design and control of systems in which heat and mass transfer processes are performed by means of thin liquid films, two phase flows, spreading droplets or rivulets. Thus, the stability and the wettability of a uniform film are reduced to the identification of energetically stable configurations characterised by a minimum of its mechanical energy, which accounts for kinetic and surface tension energy. The delineation of a concurrent broken configuration (rivulet) can be used to describe the liquid partial wetting behaviour.

Going back to the main target of this study, absorption cycles include three fundamental heat and mass-transfer processes that are realised inside specific typologies of heat exchangers: evaporator/condenser, absorber and regenerator. Heat exchangers characteristics have decisive effects on the overall system efficiency, its dimensions and cost. However, the attempt to experimentally and theoretically describe their heat and mass transfer performance, in order to optimise these devices, is still incomplete and has not led to conclusive approaches.

Horizontal tube falling film heat exchangers are usually employed for their capability of realising high heat and mass transfer rate with reduced dimensions and low pressure losses. The state of the art reviewed by J. Killion and S. Garimella (2003) [105] (2001) [104] regarding falling-film heat exchangers calls attention to how their transfer performances may be drastically affected by various hydrodynamic aspects (unsteadiness of the flow, due to waves or turbulence, film thickness variation along the surface, flow contraction-increase along the tube bundle, flow mode between adjacent tubes and/or film breakdown causing dry patches formation), which, in turn, influence the distribution of the working fluid over the tube bundle. In this configuration, the film thickness constitutes the main heat transfer resistance with the cooling water circulating inside the tube and simulations theoretically recognise that working with low solution mass flowrates improve the system performance. As a result, operability at reduced Reynolds number is attractive for real absorption plants, but the tube partial wetting needs to be considered as a conflicting phenomenon and a critical issue.

Due to a smaller phase interface, incomplete tube wetting, which directly means a lower heat transfer area, leads to a strong reduction of the achievable heat extraction. Accordingly, a closed thin film structure is sought-after in order to realise heat and mass transfer processes effectively.

Reasons for tube wet surface reduction can be of various types: first of all, surface drying can arise when the film thickness falls below its minimal stable value, or can be caused by an asymmetric film distribution, by impurities causing bad wetting or by the occurrence of a combination of these stated phenomena. In addition, during absorption, the thermo-capillary force, which is related to the surface tension variation due to both the surface temperature and concentration gradients [107], brings about the departure of liquid away from the thinnest location in the layer (also called the Marangoni effect).

Excluding few exceptions [108-109] among the previously developed models, the effect of the amount of wetted surface has not been assessed or has been merely assumed as a fixed value imposed to the calculation [106) 110]. Moreover, related experimental data and visual description by digital image processing are also very limited both in the number of works which report them and in the condition range covered [26] Nevertheless, the role of the tube wetting has been recognised as a critical factor in determining the efficiency of the absorption process.

Among the various methods to predict the stability of a thin film [94], such as small perturbation approach [95] or the forces' balance at the upstream stagnation point of a dry patch [96-97], the principle of minimising the energy contained in a specified stream wise span of the falling film has been applied [98] in order to develop a stability criterion of the

uniform film. In order to obtain an expression of the rivulet wetting behaviour from the minimisation of its mechanical energy, the rivulet cross-section shape has been assumed to be a segment of a circle (as in J. Mikielewicz and J. R. Moszynski (1976) [99]). This research work reflects the purpose of practically characterise the wetting ability of a liquid interacting with a solid surface in a gaseous environment in a generalised way, and presents a first experimental validation. Film wetting behaviour and contact angle hysteresis phenomena are included under a sole energy-based theoretical approach based on the knowledge of the fluid properties, the solid surface features and geometry, to clarify the relation between wettability and solution mass flowrate. Additionally, direct flow visualisation data and wetted area measurements are obtained, in turn, by image acquisition and processing on an experimental test section when decreasing and increasing solution mass flowrates are delivered. The model is hence compared with the experimental data acquired and is expected to constitute a useful tool to include partial wetting phenomena in comprehensive system modelling for a number of technical applications. Finally, since an established method to predict the wetting behaviour of horizontal tube-falling film heat exchangers is not available at present, a semi-empirical model suitable for a horizontal tube bundle is developed to match the characteristics of real absorbers. This work eventually aims at modelling and evaluate of the direct inferences of thin films break-down on the transfer characteristics of falling film absorbers at low solution flowrates, which will elaborated in chapter 5 and chapter 6.

4.2 Critical condition of a uniform falling film over a plain wall

For the sake of the purpose stated above, the method adopted requires preliminarily delineating the geometry of the broken configuration to be compared with a uniform film to define its stability. Even though T. Hobler et al. (1964) [98] does explain the influence of the contact angle, on the other hand offers no information about the geometry or rivulet spacing. Afterwards, in a successive work J. Mikielewicz and J. R. Moszynski (1976) [99] have enlarged Hobler's formulation by considering the film to collapse into streams of a circular segment cross section-shape with amplitude of two times the contact angle in order to obtain an expression of the stable rivulet wetting behaviour from the minimisation of its mechanical energy. The method enables estimating the transversal extension of the rivulet in its stable configuration.

A. Doniec (1991) (1988) [111-112] observes that the assumption of a circle-shaped rivulet requires the contact angle to change with changing rivulet dimensions. Furthermore, and more specifically, when a circular segment cross-section of the rivulet is assumed, the width of the plain surface (or the distance between adjacent rivulets) can't be set as a geometrical parameter of the problem, but it's a result of the calculation. Within the bounds of the same approach, A. Doniec (1984) [113] uses the variational calculus to determine the rivulet shape, once set the minimum total energy. The solution for the symmetric half of the rivulet is composed of a segment of a straight line and an integral curve which cuts the solid surface with an angle corresponding to the contact angle.

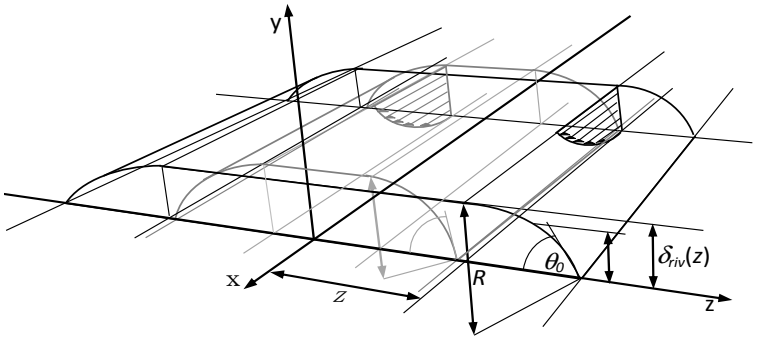

Fig. 4.1 Schematic of the composed cross-section shape of the rivulet

In the followings, an energy based criterion for the film stability is re-established for a generic inclination of a solid surface with given transversal width. Consistently with a composed cross-section shape of the rivulet, an additional

geometrical degree of freedom is added to the problem. Accordingly, the width of the surface is used as a parameter. Moreover, since an established method to predict the local transient wetting behaviour of thin films over plain inclined surfaces is not available at present, this work aims also at characterising the transition from uniform film to the steady rivulet configuration.

The problem considered is presented schematically in figure 4.1. A homogeneous liquid film of uniform thickness, with uniform surface tension (Marangoni effect is neglected), is considered to flow, waveless, down over a solid wall of width λ, with generic inclination β, only driven by gravity g.

- Steady state is postulated and each parameter changes quasi-statically;
- The contact angle θ_0 is initially assumed to be a constant property of the gas-liquid-solid set;
- The laminar flow is supposed to be fully developed;

To use the energy minimisation principle, and establish the stable extension of the rivulet, its total mechanical energy (kinetic energy E_K plus surface energy E_σ, as in eq. 4.1) must be computed, minimised with respect to the geometrical parameter responsible for the rivulet extension, and lastly compared to that calculated consistently for the uniform film configuration.

$$E = E_k + E_\sigma = \int_A \frac{1}{2}\rho u^2 dA + \int_\Pi \sigma d\Pi = \int_A \frac{1}{2}\rho u^2 dA + \int_{\Pi lv} \sigma_{lv} d\Pi + \int_{\Pi ls} \sigma_{ls} d\Pi + \int_{\Pi sv} \sigma_{sv} d\Pi \tag{4.1}$$

Furthermore, under the same assumptions of Nusselt integral solution for an isothermal plate (gravity g is the only external force active on the film, liquid properties are constant, the vapour at the film interface does not cause drag, heat transfer is neglected) the velocity profile and the corresponding film thickness are expressed as in the previous chapter by eq. 3.2 and 3.6.

The composed cross-section shape of the rivulet assumed in the followings is suitable for the local characterisation of the transition from uniform film to the steady rivulet configuration [112], as well as the analysis of the rivulet behaviour for increasing/decreasing flowrates, and consistent with that calculated by A. Doniec (1984) [113]. The rivulet profile $\delta(z)$ expressed by eq. 4.2 is a symmetrical and continuous combination of a straight segment of line and a circular segment, cutting the solid surface with an angle equivalent to the contact angle (Fig. 4.2).

$$\delta_{riv}(z) = \begin{cases} R(\cos\theta - \cos\theta_0), & z \in \langle Z, Z + 2R\sin\theta_0 \rangle \\ R(1 - \cos\theta_0), & z \in \langle 0, Z \rangle \end{cases} \tag{4.2}$$

Considering the rivulet cross-section identified on a plane section adjacent to the tube axis z, and dividing it into thin bands dz of height $\delta(z)$, the velocity distribution $u(y)$ in such a band is supposed to match the velocity profile in a film of uniform thickness δ_u equal to $\delta(z)$.

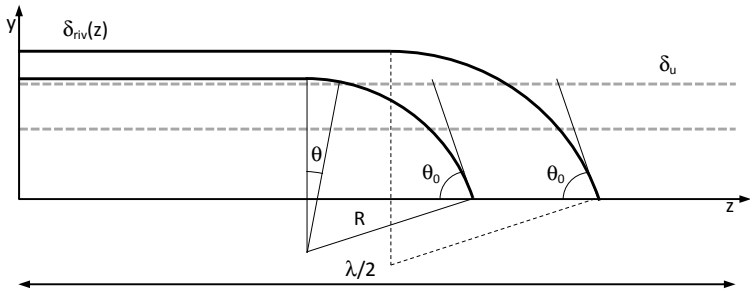

Fig. 4.2 Transversal cross-sections of rivulet and uniform film configurations

Therefore, the total energy per unit length is expressed, respectively, for the rivulet and uniform film configurations by eq. 4.3 and 4.4.

$$e_{riv} = 2\frac{\rho}{\lambda}\int_{Z}^{Z+R\sin\theta_0}\int_{0}^{\delta_{riv}} u^2(y)dzdy + 2\rho\frac{Z}{\lambda}\int_{0}^{\delta_{riv}} u^2(y)dy + \sigma_{sv}(1-X) + \sigma_{sl}X + \frac{\sigma_{lv}}{\lambda}(2R\theta_0 + 2Z) \quad (4.3)$$

$$e_u = \rho\frac{Z}{\lambda}\int_{0}^{\delta_u} u^2(y)dy + \sigma_{sl} + \sigma_{lv} \quad (4.4)$$

Considering the hydrodynamics of the system, the total energy per unit width and unit length in the stream-wise direction of the uniform film configuration can be expressed as,

$$e_u = \frac{1}{15}\frac{\rho^3 g^2 \sin^2\beta}{\mu^2}\delta_u{}^5 + \sigma_{sl} + \sigma_{lv} \quad (4.5)$$

And the corresponding mass flowrate per unit length is given by eq. 3.5 in the previous chapter. When the film breaks up into rivulets (Fig. 4.2), the basic parameter to compute the wet part of the tube surface X (eq. 4.6) is the ratio of the rivulet chord at its base to the corresponding width of the uniform film.

$$X = \frac{2R\sin\theta_0 + 2Z}{\lambda} \quad (4.6)$$

The mass flowrate per unit length for the rivulet configuration is given by eq. 4.7.

$$\begin{aligned}\Gamma_{riv} &= 2\left[\frac{\rho}{\lambda}\int_{Z}^{Z+R\sin\theta_0}\int_{0}^{\delta_{riv}} u(y)dzdy + \rho\frac{Z}{\lambda}\int_{0}^{\delta_{riv}} u(y)dy\right] = \\ &\frac{2}{3}\frac{\rho^2 g\sin\beta}{\lambda\mu}R^4\int_{0}^{\theta_0}(\cos\theta-\cos\theta_0)^3\cos\theta d\theta + \frac{2}{3}\frac{\rho^2 g\sin\beta}{\mu}\frac{Z}{\lambda}R^3(1-\cos\theta_0)^3 = \\ &\frac{2}{3}\frac{\rho^2 g\sin\beta}{\lambda\mu}R^4 f(\theta_0) + \frac{2}{3}\frac{\rho^2 g\sin\beta}{\mu}\frac{Z}{\lambda}R^3(1-\cos\theta_0)^3\end{aligned} \quad (4.7)$$

Where,

$$f(\theta_0) = \int_{0}^{\theta_0}(\cos\theta-\cos\theta_0)^3\cos\theta d\theta = -\frac{1}{4}\cos^3\theta_0\sin\theta_0 - \frac{13}{8}\cos\theta_0\sin\theta_0 - \frac{3}{2}\theta_0\sin^2\theta_0 + \frac{15}{8}\theta_0 \quad (4.8)$$

The mass balance between the two configurations (eq. 4.9) and the definition of the wetting ratio (eq. 4.6) yield a relationship (eq. 4.9) concerning the rivulets radius R, the uniform film thickness δ_u and X, which assures continuity. The surface tension forces' equilibrium at the point of contact of the three phases is imposed by the Young-Dupree equation (eq. 4.10).

$$\left(\frac{\delta_u}{R}\right)^3 = 2\frac{Rf(\theta_0)}{\lambda} + \left(X - \frac{2R\sin\theta_0}{\lambda}\right)(1-\cos\theta_0)^3 \quad (4.9)$$

$$\sigma_{sv} = \sigma_{sl} + \sigma_{lv}\cos\theta_0 \tag{4.10}$$

Accordingly, the energy contents of the rivulet configuration can be assessed as a function of the rivulet radius (eq. 4.11).

$$\begin{aligned} e_{riv} &= \frac{2}{15}\frac{\rho^3 g^2 \sin^2\beta}{\lambda\mu^2} R^6 \int_0^{\theta_0} (\cos\theta - \cos\theta_0)^5 \cos\theta d\theta + \\ &\frac{1}{15}\frac{\rho^3 g^2 \sin^2\beta}{\lambda\mu^2}\left(X - \frac{2R\sin\theta_0}{\lambda}\right) R^5 (1-\cos\theta_0)^5 + \\ &\sigma_{sv}(1-X) + \sigma_{sl}X + \frac{\sigma_{lv}}{\lambda}(2R\theta_0 + X\lambda - 2R\sin\theta_0) \\ &= \frac{1}{15}\frac{\rho^3 g^2 \sin^2\beta}{\mu^2} R^5 \left\{ 2\frac{R}{\lambda}\psi(\theta_0) + \left[\left(\frac{\delta_u}{R}\right)^3 - \frac{2Rf(\theta_0)}{\lambda}\right] R^5 (1-\cos\theta_0)^2 \right\} + \sigma_{sl} + \\ &\sigma_{lv}\left\{ \left[\frac{\lambda\delta_u{}^3 - 2R^4 f(\theta_0)}{R^3\lambda(1-\cos\theta_0)^3} + \frac{2R\sin\theta_0}{\lambda}\right](1-\cos\theta_0) + \cos\theta_0 + \frac{2}{\lambda}R(\theta_0 - \sin\theta_0)\right\} \end{aligned} \tag{4.11}$$

Where,

$$\begin{aligned} &\psi(\theta_0) = \int_0^{\theta_0} (\cos\theta - \cos\theta_0)^5 \cos\theta d\theta \\ &= \theta_0\left(\frac{5}{16} + \frac{15}{4}\cos^2\theta_0 + \frac{5}{2}\cos^4\theta_0\right) - \sin\theta_0\left(\frac{113}{48}\cos\theta_0 + \frac{97}{24}\cos^3\theta_0 + \frac{1}{6}\cos^5\theta_0\right) \end{aligned} \tag{4.12}$$

The rivulet will be stable if its total energy shows a local minimum with respect to the rivulet radius R (which determines the wetting ratio X for a certain flowrate and contact angle, see eq. 4.9), when $X<1$. Contrarily, if the broken configuration shows no minimum with respect to X, or if the uniform film configuration has a lower value of total energy, the uniform film is the stable and energetically advantageous configuration. Hence, differentiating eq. 4.11 with regard to R, and solving for R once equated to zero (eq. 4.13), it is made possible to establish the extension of the rivulet in the previously stated condition.

$$\begin{aligned} &\frac{\rho^3 g^2 \sin^2\beta}{\mu^2}\left[\frac{4}{5}\frac{R^5}{\lambda}\psi(\theta_0) + \frac{2}{15}\delta_u{}^3 R(1-\cos\theta_0)^2 - \frac{4}{5}\frac{R^5}{\lambda}f(\theta_0)(1-\cos\theta_0)^2\right] + \\ &+\sigma_{lv}\left\{\left[-\frac{3\delta_u{}^3}{R^4}\frac{1}{(1-\cos\theta_0)^3} - \frac{2f(\theta_0)}{\lambda(1-\cos\theta_0)^3} + \frac{2\sin\theta_0}{\lambda}\right](1-\cos\theta_0) + \frac{2}{\lambda}(\theta_0 - \sin\theta_0)\right\} = 0 \end{aligned} \tag{4.13}$$

From the knowledge of the value of the rivulet radius R, the equality of mass flowrates (eq. 4.9) yields the wetting ratio X and, finally, the extension of the straight line of the rivulet Z can be calculated from the definition of the wetting ratio (eq. 4.6).

The critical condition at which the uniform film breaks into rivulets can be identified by a minimum value of film thickness δ_0 as a function of solution properties, contact angle, width λ and inclination β of the plain surface. The system of eq. 4.13 and 4.14 is obtained by combining the minimisation of the rivulet energy and equating the energies

of the two configurations (eq.s 4.5 and 4.11). Its solution gives the critical condition for the uniform film and requires to be solved iteratively with respect to R and δ_0.

$$\frac{1}{15}\frac{\rho^3 g^2 \sin^2\beta}{\mu^2}\left\langle \delta_0^{\,5} - R^5\left\{2\frac{R}{\lambda}\psi(\theta_0)+\left[\left(\frac{\delta_0}{R}\right)^3-\frac{2Rf(\theta_0)}{\lambda}\right]R^5(1-\cos\theta_0)^2\right\}\right\rangle = \sigma_{lv}\left\langle\left\{\left[\frac{\lambda\delta_0^{\,3}-2R^4 f(\theta_0)}{R^3\lambda(1-\cos\theta_0)^3}+\frac{2R\sin\theta_0}{\lambda}\right](1-\cos\theta_0)+\cos\theta_0+\frac{2}{\lambda}R(\theta_0-\sin\theta_0)\right\}-1\right\rangle \tag{4.14}$$

As a result, when the thickness of the uniform film is lower than the minimum critical thickness ($\delta_u \leq \delta_0$), the film is assumed to be broken and the local wetting ratio X_0 is given by eq.s 4.9 and 4.11.

Table 4.1 Calculation results

	δ_0 [m]	θ_0[rad]	X_0	R[m]	$e_{riv,0}$[J·m^{-2}]
Mikielewicz and Moszynski (1976) [99]	0.000379	0.785398	0.402568	0.002351	0.104128
Present work	0.000449	0.785398	0.746554	0.001735	0.108431

Calculation results for the present model are characterised by higher values of both the critical thickness δ_0 and the stable rivulet wetting ratio X_0. This directly means that the break-up of the film would occur at a higher Reynolds, but at that condition the rivulet would cover about 75% of the plain wall width λ.

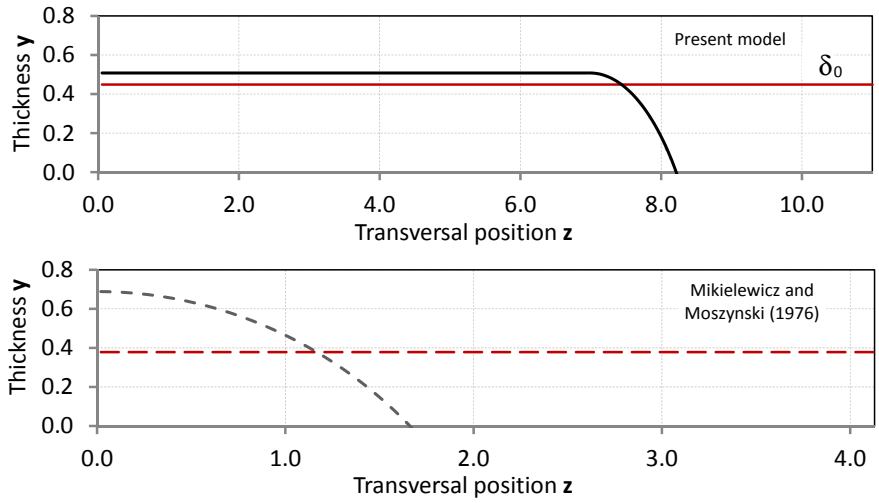

Fig. 4.3 Critical condition [mm] for a uniform film (a) present model (b) [99] model

Figure 4.4 illustrates the specific energy of the two configurations (quantified up to the value of σ_{ls}, which has been assumed to be constant and, as a result, not influent for the comparison) and makes evidence of the critical condition for the uniform film as the crossing point at which the rivulet energy becomes lower than the uniform configuration. The specific energy of the rivulet increases linearly with Reynolds number, whereas the uniform film shows a higher order dependence on the same parameter (5/3).

When the wetting ratio X is taken as the primary independent parameter, figure 4.5 highlights that the rivulet configuration is a stable condition characterised by a minimum energy. The path identified by all these minima constitutes the set of states defining the respective line e_{riv} in figure 4.4.

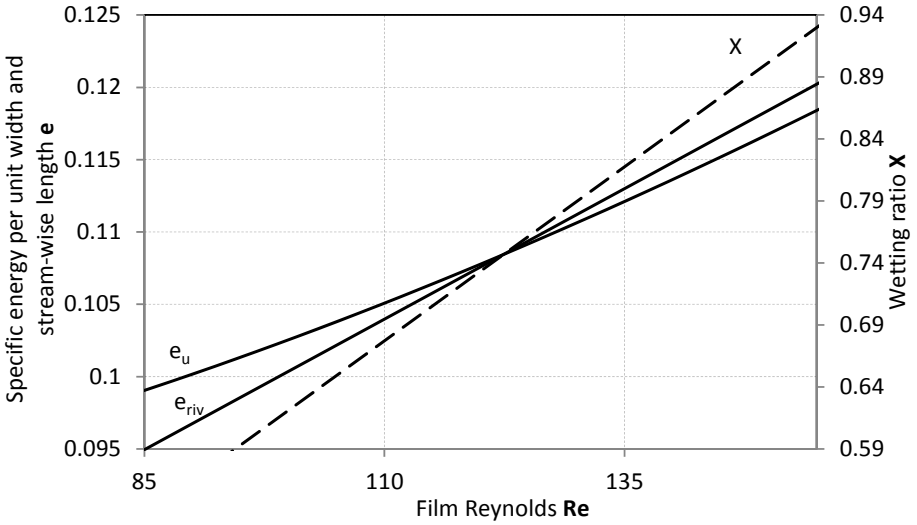

Fig. 4.4 Specific energy [J·m^{-2}] and wetting ratio as a function of film Reynolds diagram for LiBr/H_2O at 25°C and 60% concentration

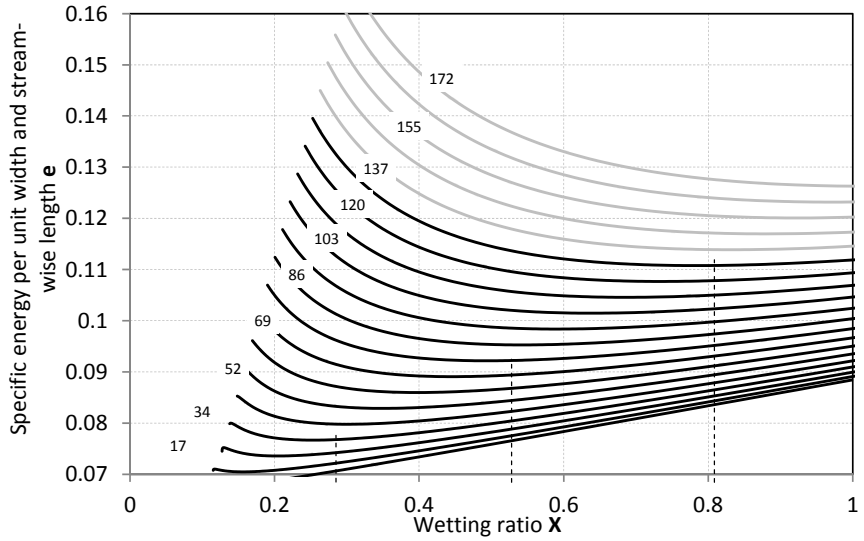

Fig. 4.5 Specific energy [J·m^{-2}] -wetting ratio diagram for LiBr/H_2O at 25°C and 60% concentration

Accordingly the values of X for decreasing Reynolds correspond to the abscissa of the local minima of the black curves in figure 4.5 (see dashed lines referring to the secondary axis). Grey curves correspond to conditions resulting energetically disadvantageous with respect to the uniform film configuration.

Repeating the calculation for a value of the surface width λ equal to 0.05m (Table 4.2), it can be observed that the minimum stable thickness δ_0 is higher than that characterising the 0.022m width surface. This means that the uniform film configuration results to be stable for a narrower range of operative conditions when the characteristic scale of the problem increases.

Table 4.2 Calculation results for the critical condition of a uniform film for different wall widths

λ [m]	δ_0 [m]	θ_0[rad]	X_0	R[m]	$e_{riv,0}$[J·m^{-2}]
0.022	0.000449	0.785398	0.746554	0.001735	0.108431
0.050	0.000470	0.785398	0.817097	0.001736	0.113897

Figures 4.6 (a) and (b) depict the critical condition (as the set of critical thickness of the uniform film δ_0 and critical stable extension of the rivulet X_0, which are energetically equivalent conditions in this case) at the two reference values of surface width. The first reference value λ equal to 0.022m corresponds to Taylor instability length for LiBr/H_2O at 25°C and 60% concentration.

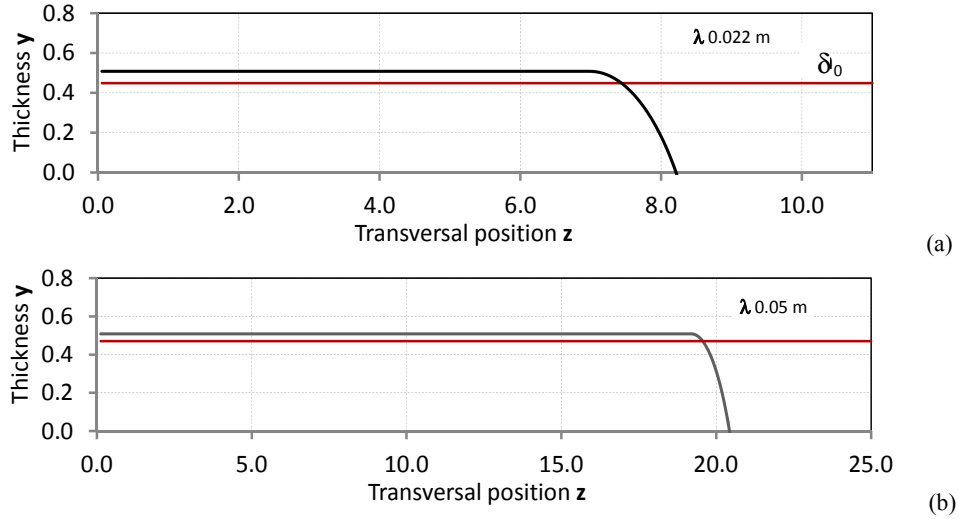

Fig. 4.6 Critical thickness δ_0 [mm] and rivulet extension X_0 at the critical condition for a plain vertical wall of width (a) 50mm (b) 22mm

However, the minimum of the specific energy correspond to a similar radius R, and, as a consequence, the stable rivulet has a higher wetting ratio X'_0 at the critical condition (Fig. 4.7 and Fig.s 4.6 (a) and (b)).

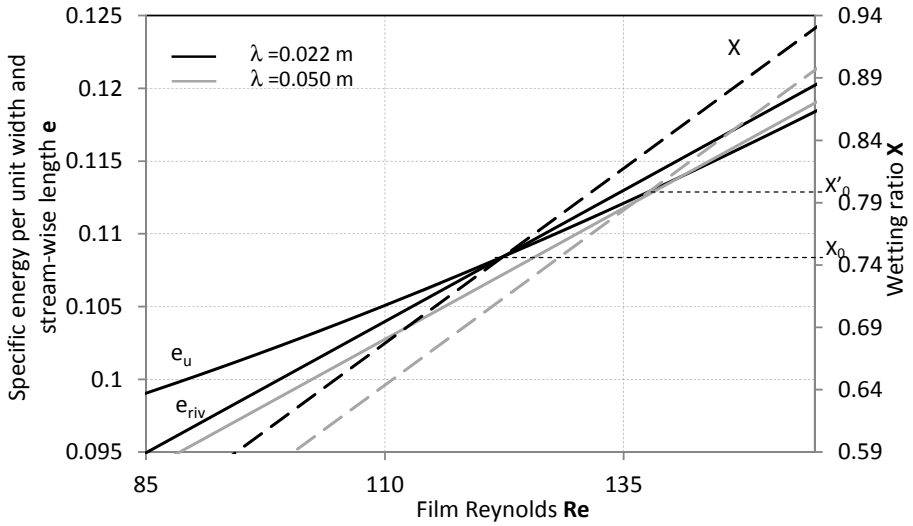

Fig. 4.7 Specific energy [J·m^{-2}] and wetting ratio as a function of film Reynolds for different wall widths

The effect of a different contact angle is portrayed in figure 4.9 and described in table 4.3.

In general, the bigger the contact angle θ_0 the higher the minimum stable thickness δ_0 of the uniform film. Accordingly, film breaking into rivulet occurs at higher Reynolds, but the wetting ratio at the critical condition X_0 slightly increases.

Table 4.3 Calculation results for the critical condition of a uniform film for different contact angles

λ [m]	δ_0 [m]	θ_0[rad]	X_0	R[m]	$e_{riv,0}$[J·m^{-2}]
0.022	0.000449	0.785398	0.746554	0.001735	0.108431
0.022	0.000507	1.047200	0.762593	0.001131	0.125617

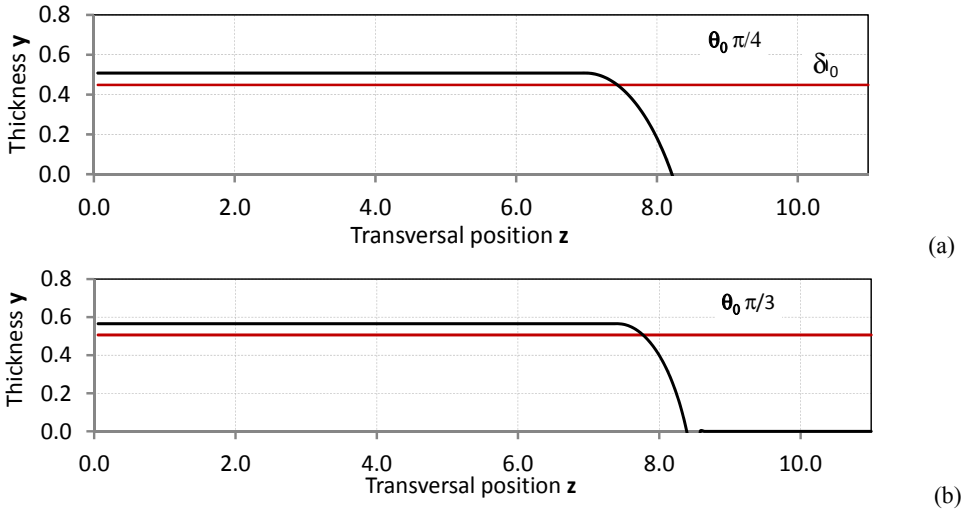

Fig. 4.8 Critical thickness δ_0 [mm] and rivulet extension at the critical condition X_0 of a liquid with contact angle (a) 45° and (b) 60° for a plain vertical wall of width 22mm

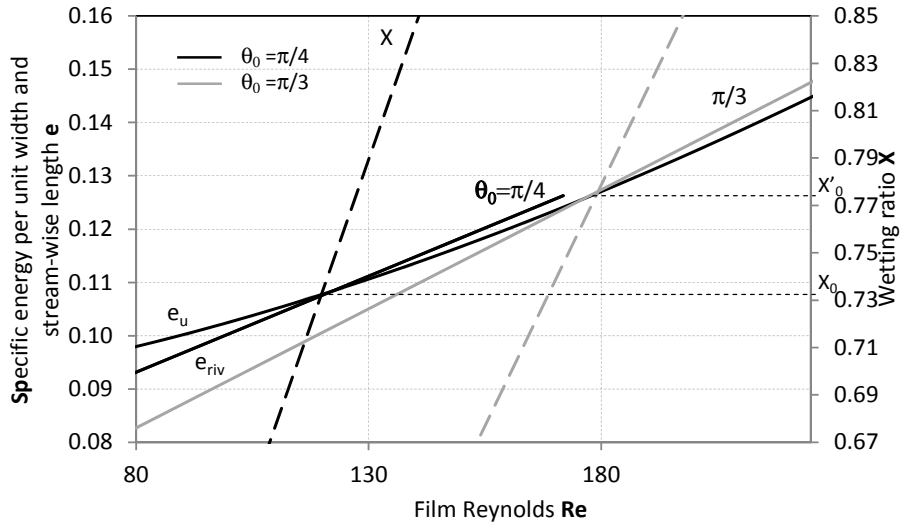

Fig. 4.9 Specific energy [J·m^{-2}] and wetting ratio as a function of film Reynolds for different contact angles [rad]

When the inclination of the plain surface is reduced (Fig. 4.11) the minimum stable thickness δ_0 of the uniform film increases and the wetting ratio at the critical condition X_0 remains almost constant (Table 4.4). Pointing out how a slower film (direct consequence of a lower surface inclination β on a fully developed Nusselt film; see eq. 3.2) has a lower stability and a poorer wettability, owing to a stronger influence of surface tension.

Table 4.4 Calculation results for the critical condition of a uniform film for different wall inclinations

β [rad]	δ_0 [m]	θ_0[rad]	X_0	R[m]	$e_{riv,0}$[Jm^{-2}]
$\pi/2$	0.000449	0.785398	0.746554	0.001735	0.108431
$\pi/4$	0.000510	0.785398	0.733507	0.001992	0.107343

The effect of the surface inclination β can be mainly related to the reduction of the velocity profile, which makes the film slower and thicker for the same mass flowrate.

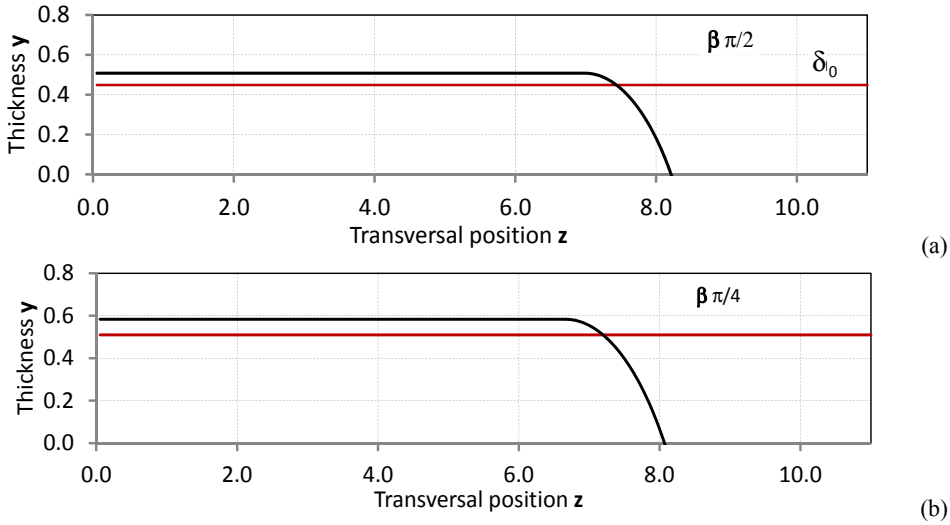

Fig. 4.10 Critical thickness δ_0 [mm] and rivulet extension at the critical condition X_0 of a liquid with contact angle 45° for a plain vertical wall of width 22mm, with inclination (a) 90° and (b) 45°

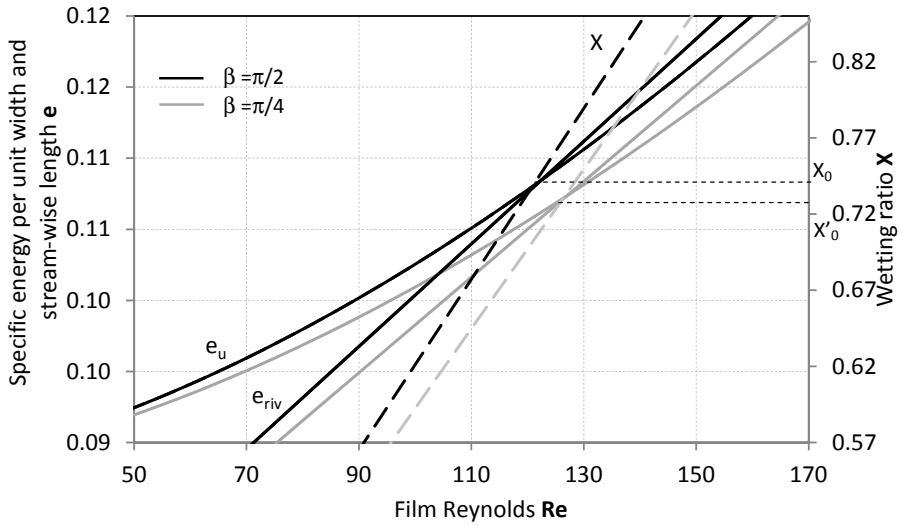

Fig. 4.11 Specific energy [J·m^{-2}] and wetting ratio as a function of film Reynolds for different wall inclinations

4.3 Wetting behaviour of falling films over a vertical plain wall

Experimentally, three different minimum wetting rates related to three different critical conditions of a uniform film have been distinguished in previous literature [92-93]:

– Γ_D is established when a liquid is wetting a surface which was initially completely dry, gradually increasing its mass flowrate,

– Γ_{Wet} is established in the same way, but on an initially wetted surface,

– Γ_0 occurs when the liquid flowrate is reduced to the point at which the rivulet configuration becomes stable.

The last condition is represented by figure 4.12, where, starting from a uniform film configuration, mass flowrate is reduced quasi-statically until the film critical thickness δ_0 is reached and the film brakes into the rivulet configuration.

Further decreasing the mass flowrate, the rivulet reduces its extension following the path identified by the set of minimal energy configurations.

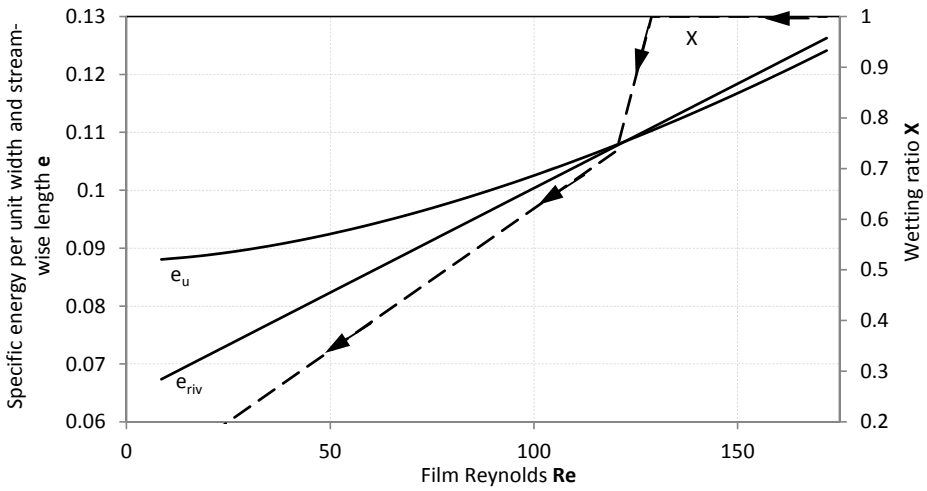

Fig. 4.12 Specific energy per unit width [$J \cdot m^{-2}$] and wetting ratio as a function of film Reynolds for decreasing mass flowrates (dashed line)

Since the Rivulet configuration is a stable configuration, characterised by a minimum energy condition, for quasi-statically increasing mass flowrates (i.e. Reynolds number, once the liquid properties are set constant) the rivulet configuration is maintained until the rivulet base cover the whole surface (red line in Fig. 4.13).

Even though the energy of the uniform configuration is lower after the critical condition Re_0, the sudden change to the uniform configuration would require passing through configuration at higher energy (Fig. 4.5).

Furthermore, this statement is supported by experimental observation and previous theoretical studies, with the sole difference of the rivulet cross-section shape. Accordingly, the values of X for increasing Reynolds correspond to the abscissa of the local minima in figure 4.5.

As a result, the previously presented model is able to make evidence of the wetting behaviour hysteresis of falling film (Fig. 4.13).

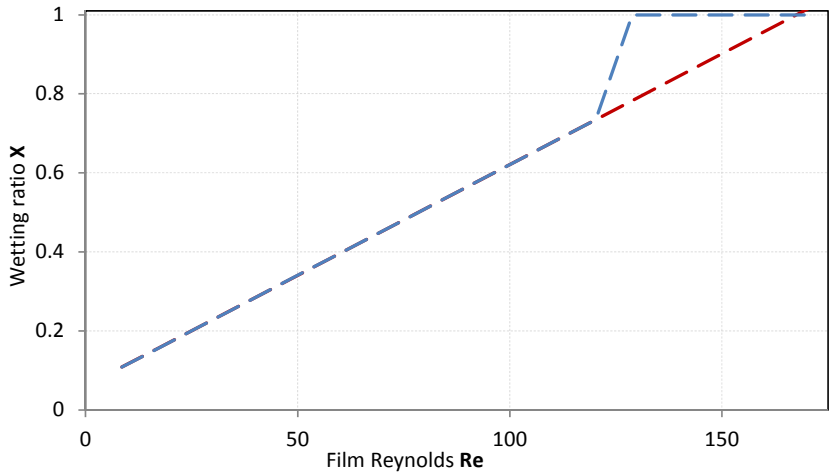

Fig. 4.13 Wetting ratio X as a function of film Reynolds for decreasing (blue line) and increasing (red line) mass flowrates

It can also be observed that the wetting behaviour X has a linear dependence on Reynolds number (as in J. Mikielewicz and J. R. Moszynski (1976) [99]).

4.4 Transient wetting model

The previously presented model establishes the critical condition at which the break-up of the film occurs and describes the stable configuration of the rivulet corresponding to that condition. However, in order to predict the wetting behaviour of thin films over plain inclined surfaces, a generalised method, able to deal with different mass flowrates, is needed. Observing the actual behaviour of flowing film (Fig. 4.14) after their break-up, the main obvious feature is related to the gradual transition from uniform film to the stable rivulet configuration. A newly developed method for estimating the film wetting behaviour under different operative and geometrical conditions combines a Lagrangian approach for the approximation of the transition from uniform film to the steady rivulet configuration and the energy minimisation method for the identification of the latter. The resulting theory generalises earlier theories by T. Hobler et al. (1968) [98] and J. Mikielewicz et al. (1976) [99].

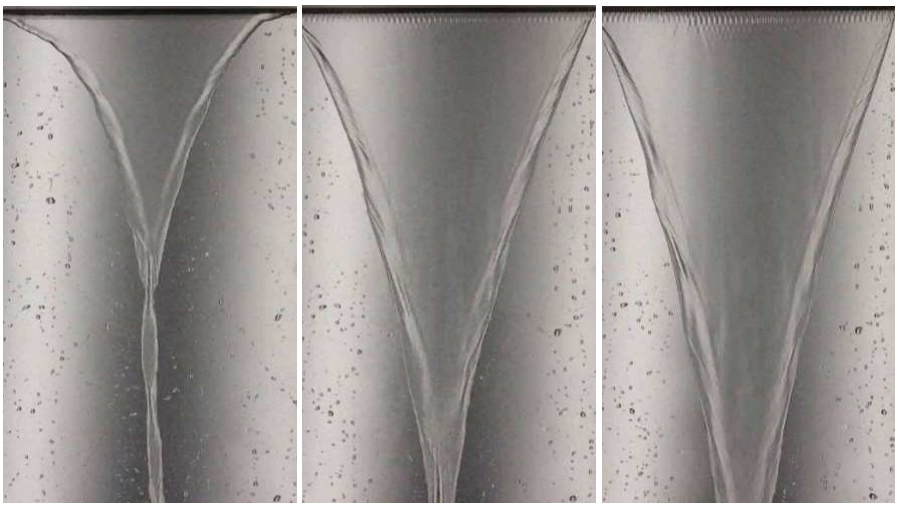

Fig. 4.14 Flow visualisation on a vertical aluminium wall

The particle at the edge of the rivulet is considered under a Lagrangian point of view. The particle is assumed to represent the whole rivulet wetting behaviour and moves along a line under the effect of a force derivable from the potential related to the energy difference between the steady rivulet configuration and the rivulet at time t (position $x=u_{av}t$). Finally, its trajectory is obtained from the numerical integration of Lagrange equation at static operability.

Accordingly, for fixed inlet temperature and concentration of the solution, constant contact angle θ_0 and defined geometric features of the plain surface (width λ and inclination β), the critical condition of the uniform film δ_0 is calculated, the thickness of the film δ_u at a given mass flowrate is compared to the critical value and, if lower, the stable condition of the rivulet (X_∞, R_∞ and Z_∞) is identified by minimising its total mechanical energy.

Although not energetically stable, due to an ideally functioning distributor at the initial stream-wise position (x=0), the rivulet is assumed to cover completely the transversal extension of the surface and its cross-section shape (R and Z) can be determined by the continuity relation (eq. 4.9) and eq. 4.6 for a fixed wetting ratio (X_1=1). The energy associated to this configuration can be calculated with reference to eq. 4.11.

The Lagrangian function of the particle at the edge of the rivulet is defined by the difference of kinetic E_k and potential energy Y (eq. 4.16).

$$\Upsilon = e_k(X_i,t) - Y(X_i,t) \tag{4.15}$$

The potential energy Y responsible for the transition of the rivulet configuration and the particle kinetic energy in the transversal direction e_k are calculated, respectively, according to eq. 4.16 and eq. 4.17. This quantity is made

corresponding to the difference between the energy of the rivulet in its stable configuration and the energy related to a rivulet of wider extension at the generic position x, gradually approaching its minimum energy (the stable configuration X_∞, R_∞ and Z_∞).

$$Y(X_i,t) = e_{riv}(X_i) - e_{riv}(X_\infty) \tag{4.16}$$

$$e_k(X_i,t) = \frac{1}{2} m_{riv} \left(\frac{\partial z}{\partial t} \right)^2 \approx \frac{1}{2} m_{riv} \left(-u_{av} \lambda \frac{\partial X}{\partial x} \right)^2 \tag{4.17}$$

Where m_{riv} can be calculated given the cross-sectional shape of the rivulet. The Lagrange equation is given by eq. 4.18.

$$\frac{d}{dt}\left(\frac{\partial \Upsilon}{\partial \dot{X}} \right) - \frac{\partial \Upsilon}{\partial X} = 0 \tag{4.18}$$

The problem is considered under a static and steady point of view. Accordingly, the Lagrangian is constant and its value is determined considering the stable rivulet condition at which the both kinetic and potential energy are null. As a consequence, the Lagrangian is constantly zero, but, even if they cancel each other, kinetic and potential energy are not necessarily and singularly null.

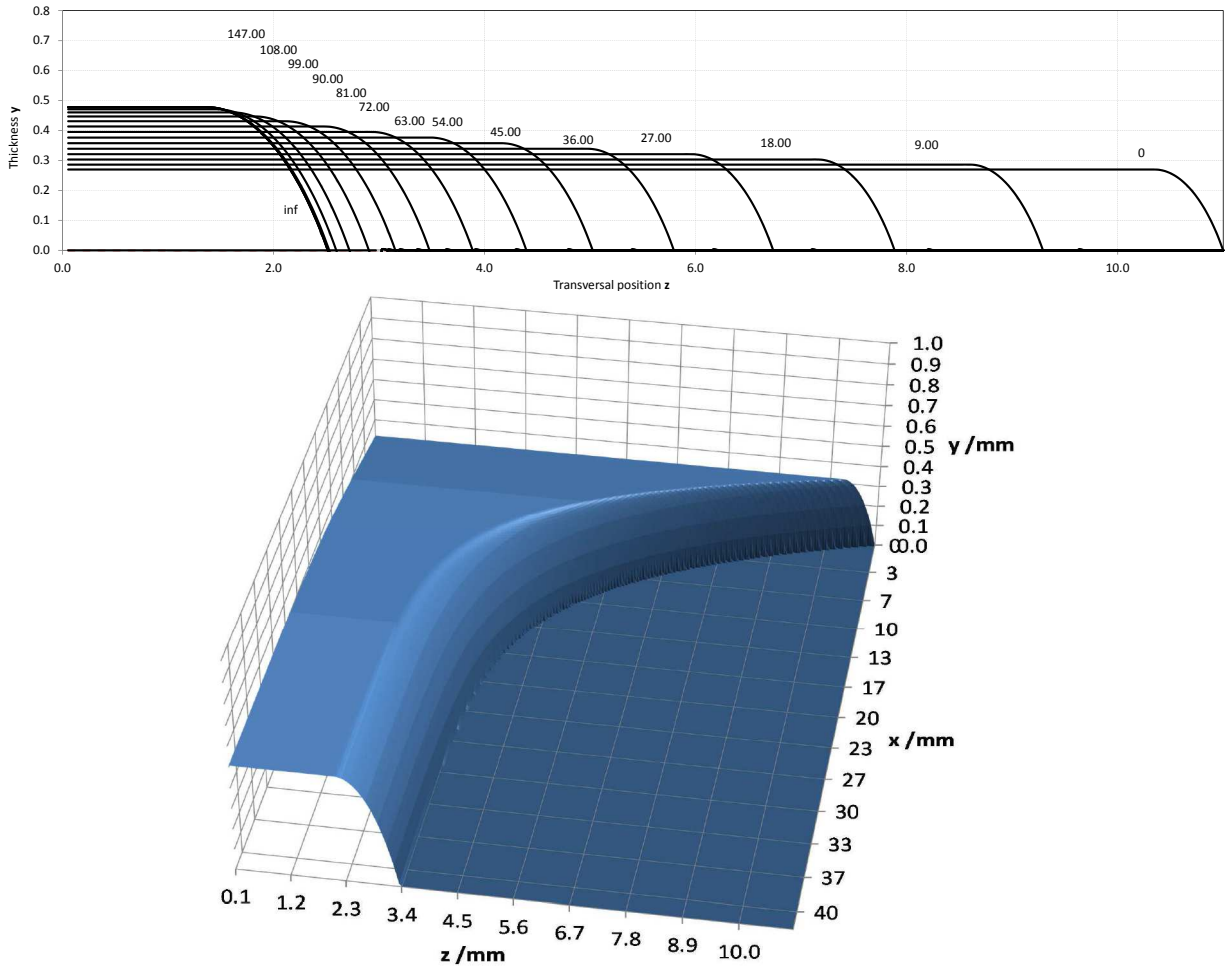

Fig. 4.15 Calculation results for the gradual transition from uniform film to the stable rivulet configuration

Eq. 4.19 gives the wetting ratio distribution over a surface with defined width λ and inclination β.

$$\frac{\partial X}{\partial x} = -\sqrt{\frac{\left[e_{riv}(X_i) - e_{riv}(X_\infty)\right]}{\lambda\rho\left[\frac{R^2}{4}(\theta_0 - \sin\theta_0) + ZR(1-\cos\theta_0)\right]u_{av}{}^2}} \tag{4.19}$$

Calculations have been carried out for different surface geometries and fluid operative conditions, analysing the effect of the main significant parameters.

Figure 4.15 shows an example of calculation results. The effect of mass flow rate, contact angle and surface inclination on the wetting behaviour of a 40℃ and 60% LiBr-H_2O can be summarised as follows.

In general, for increasing mass flowrates the rivulet increases the extension of the transition region from the inlet to the stable rivulet configuration and improves its wetting ability. The latter observation can be explained considering that the average speed of the rivulet increases when flowrate is augmented.

A lower contact angle causes a similar effect, but at a lower order of magnitude.

Finally, when inclination β is reduced also the wetting ability of the solution is slightly decreased. However, as pointed out previously, the minimum stable thickness δ_0 of the uniform film increases and the rivulet cross-section is also increased, due to the reduction of the velocity profile.

Moreover, the wetting behaviour map of the rivulet (Fig. 4.13) can be re-estimated with an integral approach over the specific surface for decreasing and increasing mass flowrates (Fig. 4.16). Although the wetting behaviour doesn't show a linear trend anymore with respect to the film Reynolds, the hysteresis phenomenon can still be captured. In particular, the effect of the inertia of the film delivered by the distributor generally enhances the wettability behaviour, but shows a more significant impact at higher Reynolds than at lower values of the same parameter.

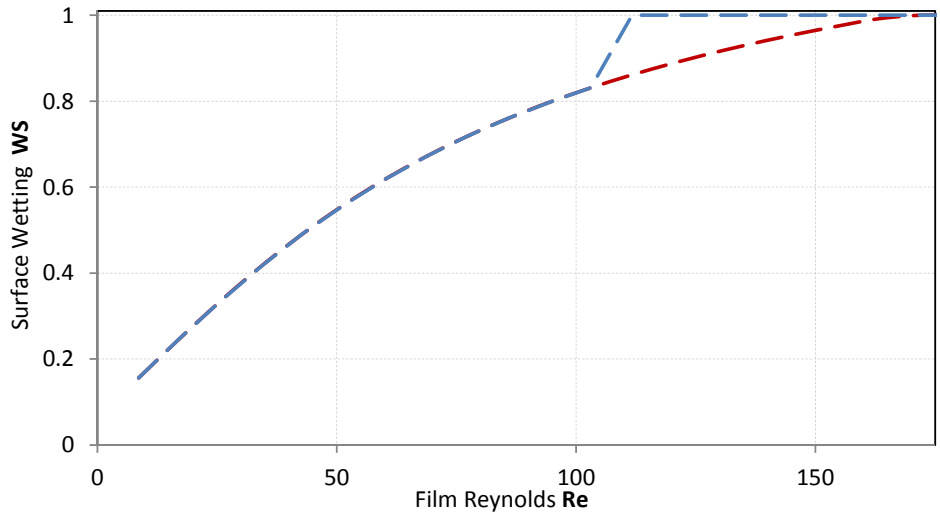

Fig. 4.16 Integral wetting ratio *WR* as a function of film Reynolds for decreasing (blue line) and increasing (red line) mass flowrates on a 200x400[mm]

4.5 Comparison with experiment and previous models

The results obtained can be compared with previous models [Mikielewicz and J. R. Moszynski (1976) [99)], T. Hobler, (1964) [98)]] (Table 4.5) or with experimental data [D. M. Maron et al., (1982) [92)]] (Fig. 4.17).

In figure 4.17 the minimum wetting rates obtained with decreasing (blue line) and increasing mass flow-rates (red line) are expressed as functions of the dimensionless group corresponding to Galileo number. The present model shows

noteworthy agreement with Γ_{Wet}, but tends to overestimate the critical wetting rate Γ_0, obtained for decreasing mass flowrates.

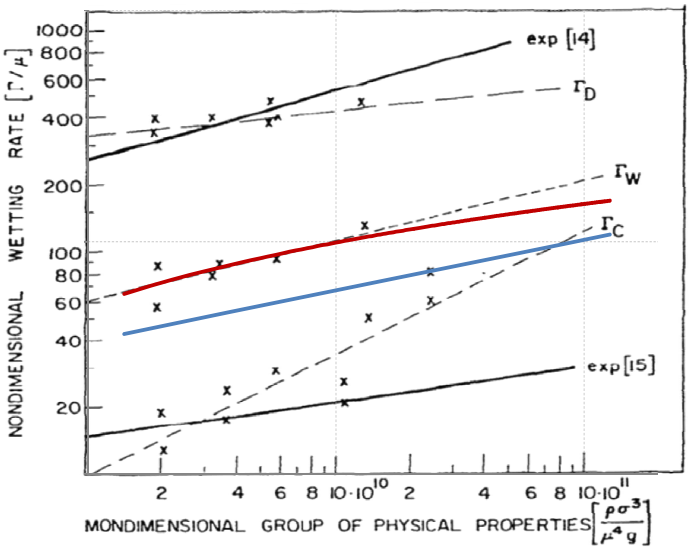

Fig. 4.17 Minimum wetting rates expressed as functions of the dimensionless group of fluid properties (from D. M. Maron et al. (1982) [92])

Defining the dimensionless parameter δ_0^+ in accordance to [Mikielewicz and J. R. Moszynski, (1976) [99]] (eq. 4.20), the critical condition resulting from this work can be compared with those obtained from previous models and experimental data (Table 4.5).

$$\delta_0^+ = \left(\frac{\rho^3 g^4}{15\mu^2\sigma}\right)^{1/5} \delta_0 \tag{4.20}$$

Table 4.5 Comparison with previous models

	Substance	θ_0 deg	Exp.	[96]	[99]	Present model
δ_0^+ -	Al	37.7	0.728	0.793	0.550	0.714
	Glass	35.8	0.787	0.777	0.540	0.699
	Cu	53.0	0.901	0.902	0.660	0.823
	Steel	36.3	0.900	0.781	0.545	0.703
	VAR	56.8	0.977	0.925	0.680	0.847

4.6 Application case: Wetting behaviour on an internally-cooled contactor

The circumstances under which dry areas appear on the exchange surface, and the extension of the wetted part of the surface, are critical to predict and control the performances of heat and mass transfer processes performed by using liquid films. Among the numerous technical applications based on this transfer method, air dehumidification can be achieved by means of an open absorption cycle in which the absorptive solution is spread in the form of a thin film flowing over the solid surface, explicitly, a desiccant contactor; a device for which the wetting behaviour is fundamental to realise the ultimate heat and mass transfer process required to the system, which constitutes, in fact, a falling film absorber.

This paragraph presents an experimental investigation, as an exemplifying application case of the theoretical construct previously presented for the prediction of film wettability. A corresponding theoretical model based on the

energy minimisation principle is presented and compared to the resulting experimental data. Both the measurement of the wetted area by image processing of the test section and the theoretical estimation highlight a hysteresis phenomenon of the film wetting behaviour for gradually increasing and decreasing mass flowrates. The modelling approach, experimental results and a first comparison are hereby presented and discussed. Quantitative and qualitative agreement is promising for a further employment of the model in actual system design and control.

Although an appropriate adjustment of air humidity is widely recognised to be critical for the preservation of human comfort and health, conventional vapour compression dehumidification systems are still inefficient, require high maintenance cost and their dehumidification capability is limited to dew point temperatures higher than 0°C. Systems employing liquid desiccant materials can be an interesting alternative approach to achieve the desired air dehumidification rate in a direct and independent way, avoiding condensation-related issues and dew-point temperature limitations to their operability. To realise a continuous steady effect, low temperature heat is required to perform the desiccant regeneration process, thus, waste or solar heat can also be conceived as their main energy sources. With the sole difference of being an open cycle, this represents an example of the vapour absorption cycle.

In these systems, the air-liquid contactor is a fundamental element for dehumidification and regeneration processes. This particular type of a falling-film absorber can be differentiated among two main categories: adiabatic (Fig. 4.18a) and internally cooled contactors (Fig. 4.18b).

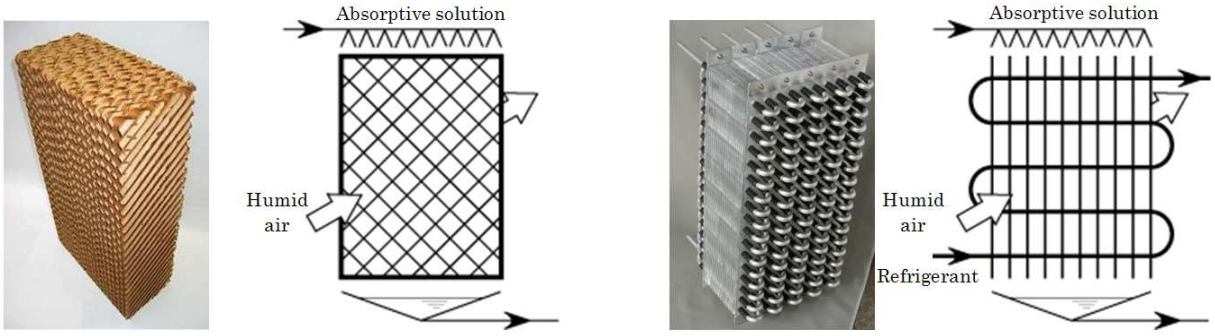

(a) (b)

Fig. 4.18 (a) Adiabatic contactor for liquid desiccant systems (b) Internally-cooled contactor for hybrid liquid desiccant systems

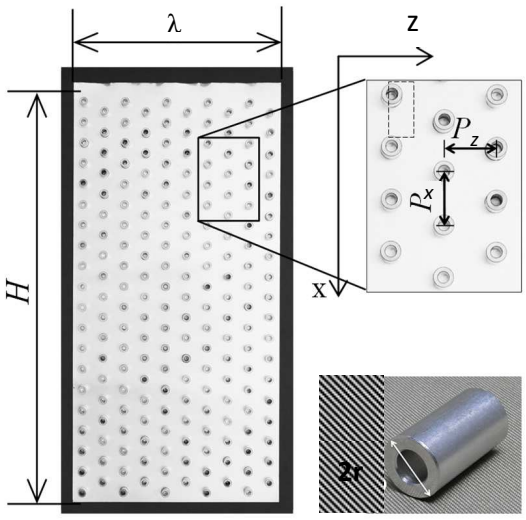

Fig. 4.19 Test section repruducing a vertical section of the fin-tube contactor

In a previous study S. Yamaguchi et al. (2011) [114] have revealed the effect of air velocity and solution mass flowrate on heat and mass transfer coefficients of adiabatic contactors. In this kind of device, due to the release of the heat of

absorption, the desiccant solution temperature rises, consequently decreasing local dehumidification (i.e. absorption) capacity.

Internally-cooled contactors integrate a contemporary heat rejection within the dehumidification process, and significant performance improvement can be expected, besides the evident reduction of the plant size. To the final aim of establishing optimal design methods of this component, this study deals with an attempt to characterise the momentum transfer occurring inside its volume in order to understand the solution wettability along the exchange surface. The fin-tube cooled contactor considered matches the one presented in figure 4.18b.

The problem considered is presented with reference to figure 4.19; a homogeneous water film of uniform thickness, with uniform surface tension, is considered to flow down over a vertical section of the contactor (single fin) and around the refrigerant tubes, only driven by gravity. Steady state is postulated and the flow is assumed to be fully developed and laminar.

Under these assumptions, the analysis can be applied to the smallest symmetrical part of the system ($P_x/2 \times P_z$, delimited by dashed borders in Fig. 4.19).

Consistently with the presence of tube base section, when the fully developed film flows around it, the mass flowrate per unit width experiences a local variation which is assumed to be represented by eq. 4.21.

$$\Gamma = \frac{2\dot{m}}{n\left(P_z - 2\sqrt{Dx - x^2}\right)} \tag{4.21}$$

Where $\dot{m}$ is the total delivered mass flowrate at the distributor and n id the number of tubes on one single row of the array. Furthermore, considering gravity g to be the only external force on the vertical isothermal pate, the air at the film interface ($y=\delta$) does not exert drag on the film and constant fluid properties, Nusselt solution of the momentum equation in the strean-wise direction x can be applied to describe the velocity field $u(y)$ (eq. 3.2). Also the film thickness can be derived from eq. 3.5 and matches eq. 3.6, when eq. 4.21 is used locally to define the mass flowrate per unit length. In the following it is assumed that the thickness δ of the uniform film configuration remains can be defined by a single value in the width direction y also when the film flows around the fin for each x position. Therefore, the mass flowrate of the uniform film configuration (eq. 4.22) can be related to the physical properties of the liquid and to a defined value of its thickness.

$$\frac{\dot{m}_u}{P_z} = \Gamma_u = \int_0^{\delta} \frac{\rho^2 g}{2\mu}\left(2\delta y - y^2\right) dy = \frac{1}{3}\frac{\rho^2 g}{\mu}\delta^3 \tag{4.22}$$

In order to model partial wetting phenomena on the contactor surface, the principle of minimising the energy contained in a given stream-wise length of the falling film is applied, first, to identify its limit of stability and, after the film breakage, to establish a method for quantifying the wet part of the contactor. To use this principle, the total mechanical energy (kinetic energy and surface energy) of a broken film configuration must be computed (eq. 4.1), minimised with respect to the parameter describing the amount of wet surface (eq. 4.23) and compared to that of the uniform film configuration. Given the small deviation highlighted in paragraph 4.4 between a simple circular segment cross-section shape and a composed geometry, for the sake of simplicity of the model, the first cross-section shape is assumed herein. Furthermore, when the flow characteristic dimension is reduced (in this case $P_z/2$ is below Taylor instability length of water at the considered range of operative conditions), precisely at higher Weber number, the relative importance of surface tension is higher and a circular geometry of the rivulet pattern seems appropriate. Namely, the film is assumed to break-up into rivulets with a cross-section shape corresponding to a circular segment and amplitude of two times the contact angle θ_0 (as in [99]).

$$X = \begin{cases} \dfrac{2R\sin\theta_0}{P_z - 2\sqrt{2rx - x^2}}, & 0 \le x \le 2r \\ \dfrac{2R\sin\theta_0}{P_z}, & 2r \le x \le P_z \end{cases} \tag{4.23}$$

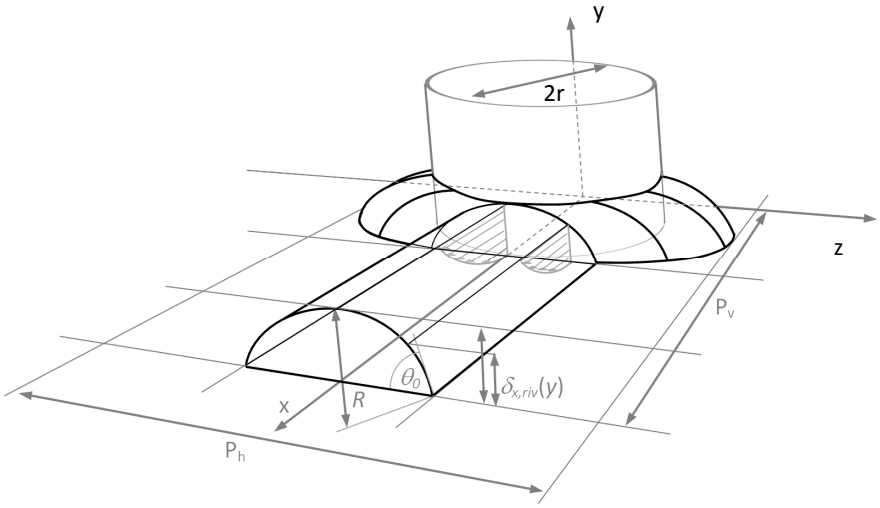

Fig. 4.20 Schematic of the rivulet configuration

Provided the circular geometry of the rivulet of radius R, the ratio WR of the rivulet base ($2R\sin\theta_0$) to the corresponding uniform unbroken film width represents the basic parameter to compute the wetted part of the surface. As a parallel result, inertial effects have a lower impact and the gradual transition to the stable configuration will be also neglected.

Consistently with the formulation previously presented[99], by decomposing the rivulet cross-section shape into strips of width dy and height $\delta_{riv}(y)$ (eq. 4.24), in such strip the velocity profile matches the profile of a uniform film of the same height.

$$\delta_{riv}(z) = R\left(\cos\theta - \cos\theta_0\right) \tag{4.24}$$

The previous relations are based on the knowledge of a suitable value of the contact angle, representing a measure of the wettability of the substrate interacting with the liquid. Ideally, this interaction is described by interfacial tensions of the three phases which come into contact. The solid surface is completely wetted only when the liquid molecules interactions are highly weaker than those between solid and liquid. Otherwise, the liquid molecular interactions tend to contract the interface area to minimize the system free energy, delineating a finite value of the contact angle. In practice, gravity or other external forces affect the shape of the interface, and the contact angle θ_0 is determined by the combination of these effects. Theoretically, once the solid-liquid system in a given environment is established, the contact angle is defined as a unique property [115] θ_Y expressed by the well-known Young-Dupree equation (eq. 4.25).

$$\sigma_{sv} = \sigma_{sl} + \sigma_{vl}\cos\theta_Y \text{ or } \cos\theta_Y = \frac{\sigma_{sg} - \sigma_{sl}}{\sigma_{gl}} = \phi \tag{4.25}$$

This quantity is associated to an ideal condition which can be satisfied only if the solid surface is chemically homogeneous and purely smooth. Even though Young contact angle θ_Y is a significant quantity for the characterization

of solid-liquid systems, the previously stated requirements imply that the Young contact angle can't be directly determined experimentally. Since the phenomenon of wetting is not necessarily a static state, a more significant method to characterise the solid-liquid interfacial system is to account for a maximal advancing contact angle θ_{0A} and a minimal receding contact angle θ_{0R} [116], namely, to estimate the difference between these two values (specifically referred as contact angle hysteresis). In fact, if a certain amount of liquid is quasi-statically condensed or added to a droplet placed on a flat solid surface, or if the plate itself is tilted, the liquid-solid interface will maintain the same contact area until a sufficient mass of liquid, or a certain tilted angle, is able to increase the contact angle up to a maximum value θ_{0A} which is then maintained while the extension of the contact area advances. If the liquid is gradually withdrawn or evaporated, the contact area remains constant until the droplet start receding with a minimum contact angle θ_{0R} at the point of contact of the three phases. The significance of this phenomenon has been extensively investigated and mainly related to surface heterogeneity, roughness and imperfections, bringing to the conclusion that advancing and receding contact angles may correspond to different equilibrium angles. Except for the case of null hysteresis a change in the interfaces shape occurs and can be regarded as an energy activation barrier that is required to be overcome so that the point of contact of the three-phases can move. This can be quantified ($E_{\sigma,gl}=\sigma_{gl}\Delta S_{gl}$, given that the solid liquid contact line is maintained constant) by the variation in the extension of the liquid-gas interface and thus in terms of interfacial free energy. The angles comprised in between advancing and receding contact angle have been described as metastable configurations. X.D. Wang et al. (2004) [117] points out that the effect of rough surfaces is equivalent to an additional tension depending on the surface roughness at the solid-liquid contact line, in other words, to a hysteresis tension f. This parameter reaches its maximum f_{max} when the contact angle equals the advancing contact angle θ_{0A}, while its minimum value f_{min} is associated to the receding contact angle θ_{0R}. When f_{max} and f_{min} are zero, there's no hysteresis and the unique contact angle θ_{0Y} corresponds is given by the Young-Dupree equation (eq. 4.25). When the contact angle varies between the two limit values the hysteresis tension is assumed to be continuously balanced by the other surface tension components at the point of contact of the three phases[117] (eq. 4.26).

$$\sigma_{sv} = \sigma_{sl} + \sigma_{vl}\cos\theta_0 + f \quad \text{or} \quad \cos\theta_0 = \phi - \frac{f}{\sigma_{vl}} \tag{4.26}$$

Consequently, eq. 4.27 is introduced [117] by assuming that maximum and minimum hysteresis tensions are equivalent with respect to their absolute values.

$$\begin{aligned} f &= f_{\max} && \left(\theta_0 \geq \theta_{0A}\right) \\ f &= \sigma_{vl}\left(\phi - \cos\theta_0\right) && \left(\theta_{0R} \leq \theta_0 \leq \theta_{0A}\right) \\ f &= f_{\min} = -f_{\max} && \left(\theta_0 \leq \theta_{0R}\right) \end{aligned} \tag{4.27}$$

To account for the effect of the hysteresis tension for a specified mass flowrate when a liquid rivulet flowing over a solid rough surface is considered (Fig. 4.21), a different geometry with respect to the static droplet, and kinetic energy of the liquid need to be incorporated in the analysis. To extend or reduce the solid-liquid interface of a flowing rivulet, namely the wetted area of the solid surface, the liquid is indeed required to either advance or recede at the line of contact of the three-phases. These circumstances can be represented by advancing and receding contact angles. Accounting for the effect of the hysteresis tension for a specified mass flowrate when a liquid rivulet flowing over a solid rough surface is considered, kinetic energy of the liquid is incorporated in the analysis of the free energy of the cross-section of a rivulet on the z-y plane.

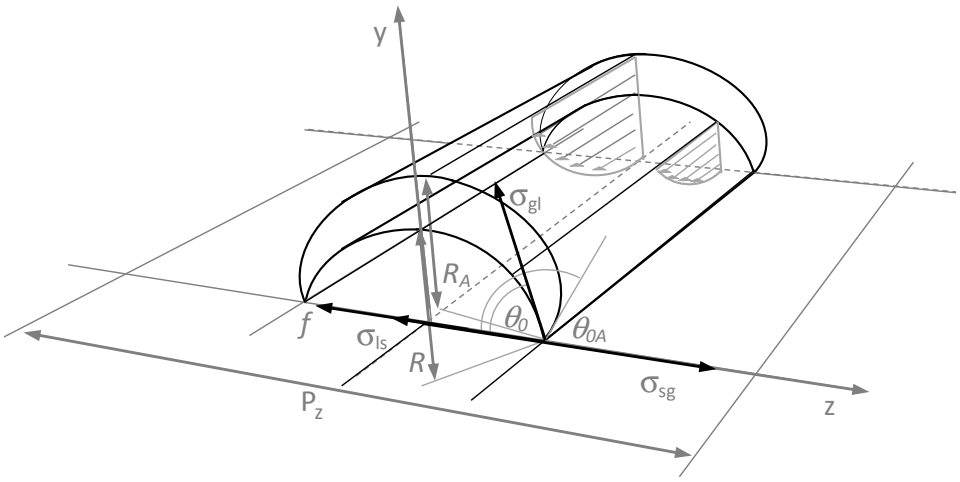

Fig. 4.21 Rivulet contact angle variation for increasing mass flowrates

The contact angle formed at the intersection of the phase interfaces is considered to be governed by the balance of the interfacial energies and the rivulet kinetic energy, namely the free energy of the system. Consequently, advancing and receding contact angles are sought after as stable states of the rivulet, in relation to its free energy, when the hysteresis tension reaches its limit values (f_{max}, f_{min}). The free-energy of the flowing rivulet (considered as the amount of work that the thermodynamic system, in this case a flowing rivulet with defined geometry, can perform) is defined by eq. 4.28 for a given mass flowrate, constant temperature, and it is assumed to be zero when the pure liquid at the reference state is quiet in a reservoir of infinite volume.

According to the problem formulation, the total energy per unit length of the rivulet and uniform film configurations are expressed by eq.s 4.28 and 4.5, respectively.

$$\begin{aligned} e_{riv} &= \frac{\rho}{P_z}\int_0^{R\sin\theta_0}\int_0^{\delta_{riv}}\left[\frac{\rho g}{2\mu}\left(2\delta y - y^2\right)\right]^2 dydz + \frac{2R\sin\theta_0}{P_z}\left(\sigma_{sl}+f\right)+\frac{2R\theta_0}{P_z}\sigma_{vl}+\frac{P_z-2R\sin\theta_0}{P_z}\sigma_{sv} \\ &= \frac{2}{15P_z}\frac{\rho^3 g^2}{\mu^2}R^6\psi(\theta_0)+\frac{2\sigma_{vl}R\sin\theta_0}{P_z}\left[\frac{\theta_0}{\sin\theta_0}-\left(\phi-\frac{f}{\sigma_{vl}}\right)\right]+\sigma_{sv} \end{aligned} \tag{4.28}$$

Where $\psi(\theta_0)$ is defined by eq. 4.12 in relation to the geometry of the rivulet cross-section. When the film breaks up into rivulets the mass flowrate for the rivulet configuration,

$$\frac{\dot{m}_{riv}}{P_z} = \Gamma_{riv} = \frac{2}{P_z}\int_0^{R\sin\theta_0}\int_0^{\delta_{riv}} u(y)dydz = \frac{2}{3P_z}\frac{\rho^2 g}{\mu}R^4 f(\theta_0) = \frac{\rho^2 g}{\mu}X\frac{R^3}{3}\frac{f(\theta_0)}{\sin\theta_0} \tag{4.29}$$

Where $f(\theta_0)$ is defined by eq. 4.8. From eq. 4.29, it is possible to relate the value of the rivulet radius R to the liquid properties and the contact angle for a given mass flowrate m_{riv} (eq. 4.30).

$$R_Y = \left(\frac{3}{2}\frac{\mu\dot{m}_{riv}}{\rho^2 g f(\theta_Y)}\right)^{1/4} \tag{4.30}$$

Given the cross-section geometry of the rivulet (eq. 4.24), eq. 4.30 yields to the relation expressed by eq. 4.31 when different configurations are analysed with respect to the contact angle θ_0 for a specified liquid flowrate.

$$\frac{dR}{d\theta_0} = -\frac{1}{4}\left[\frac{3}{2}\frac{\mu \dot{m}_{riv}}{\rho^2 g}\right]^{1/4} \left[f(\theta_0)\right]^{-5/4} f'(\theta_0) \tag{4.31}$$

Modelling the stable configuration and geometry of the rivulet is the basis to estimate its wetting ability and the extension of its interfaces. Among the potential set of states associated to different values of the contact angle for a given mass flowrate, Young's equilibrium contact angle θ_{0Y} and a value of the hysteresis tension f_{max}, and consistently with previous approaches, the geometry of the rivulet is modelled by combining eq.s 4.28-4.31 as that corresponding to a local minimum of the rivulet free energy (eq. 4.32).

$$\begin{aligned}\frac{\partial e_{riv}}{\partial \theta} &= \frac{1}{15P_z}\frac{\rho^3 g^2}{\mu^2}\left[6R^5\frac{dR}{d\theta_0}\psi(\theta_0) + R^6\psi'(\theta_0)\right] + \\ &+ \frac{dR}{d\theta_0}\frac{\sigma_{vl}}{P_z}\left[\theta_0 - \sin\theta_0\left(\phi - \frac{f}{\sigma_{vl}}\right)\right] + R\frac{\sigma_{vl}}{P_z}\left[1 - \cos\theta_0\left(\phi - \frac{f}{\sigma_{vl}}\right)\right] = 0\end{aligned} \tag{4.32}$$

Eq. 4.32 gives the equilibrium values of advancing and receding contact angle once $\phi = \cos\theta_{0Y}$ and the hysteresis tension f_{max} are fixed consistently with eq. 4.27.

Pertaining to operative conditions and features of the experimental equipment, pure water at 25°C is considered as a reference condition for a parametric analysis of the model. For a defined value of the hysteresis tension f it is always possible to identify a local minimum of the rivulet free energy for a single value of the contact angle (Fig. 4.22). In between its limit configurations associated to f_{max} and f_{min} (respectively corresponding to θ_{0A} and θ_{0R}), f is varied continuously according to eq. 4.27, and the angles comprised in the hysteresis range designate metastable configurations with a constant value of the rivulet free energy e_{riv}.

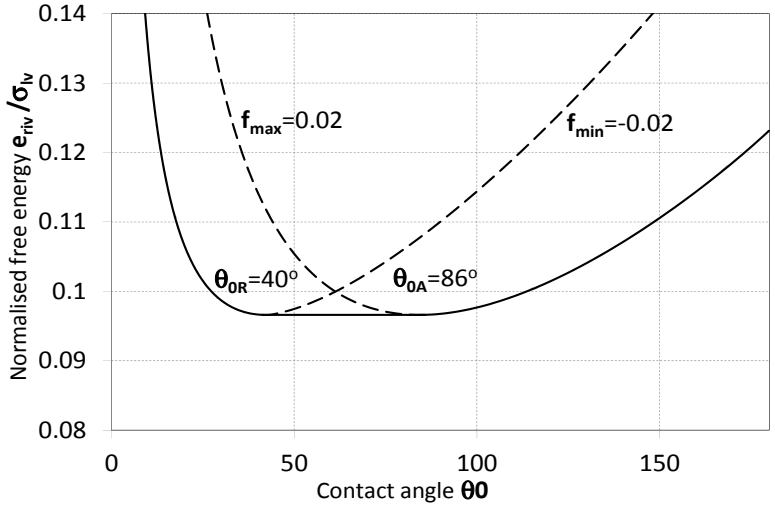

Fig. 4.22 Rivulet free-energy per unit width and per unit stream-wise length e_{riv} [J·m^{-2}] normalised with respect to the liquid surface tension σ_{lg} [J·m^{-2}] as a function of the contact angle [°] when Γ_{riv}=0.0075 [kg·m^{-1}s^{-1}], $\phi = \cos\theta_{0Y}$ = 0.423 for hysteresis tension f_{max}=0.02[J·m^{-2}]

Even though advancing and receding contact angle have been described as configurations with a high energy content if compared to Young's equilibrium contact angle, this is not conflicting with a description of their manifestation as equivalent to local minima of their free energy at given conditions. In fact, this analysis shows that the higher is the hysteresis phenomenon of the contact angle, the higher the energy of the rivulet in its limit configurations (corresponding θ_{0A} to and θ_{0R}) results to be (Fig. 4.23). Figure 4.23 presents the calculation results characterising advancing and receding contact angles of water, when the maximum value of hysteresis tension is varied.

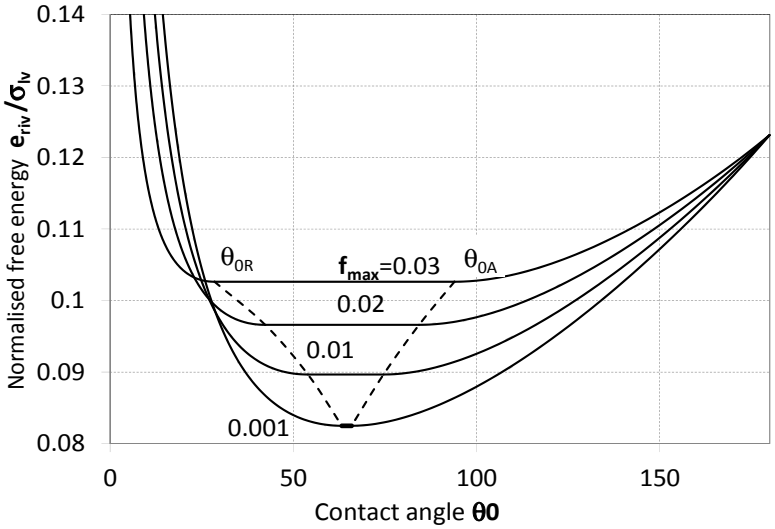

Fig. 4.23 Rivulet free-energy per unit width and per unit stream-wise length e_{riv} [J·m^{-2}] normalised with respect to the liquid surface tension σ_{lg} [J·m^{-2}] as a function of the contact angle [^{o}] when Γ_{riv}=0.0075 [kg·m^{-1}s^{-1}] ϕ= cosθ_{0Y} = 0.423 for different values of the hysteresis tension f [J·m^{-2}]

Consistently with previous analysis, the hysteresis range of the contact angle is stretched when the hysteresis tension f_{max} increases. Higher values of this parameter can be at first primarily related to higher interfaces deformations due to a higher roughness of the surface. Young's contact angle is described as the value associated to zero hysteresis tension (f=0) and gives the lowest value of the system free energy.

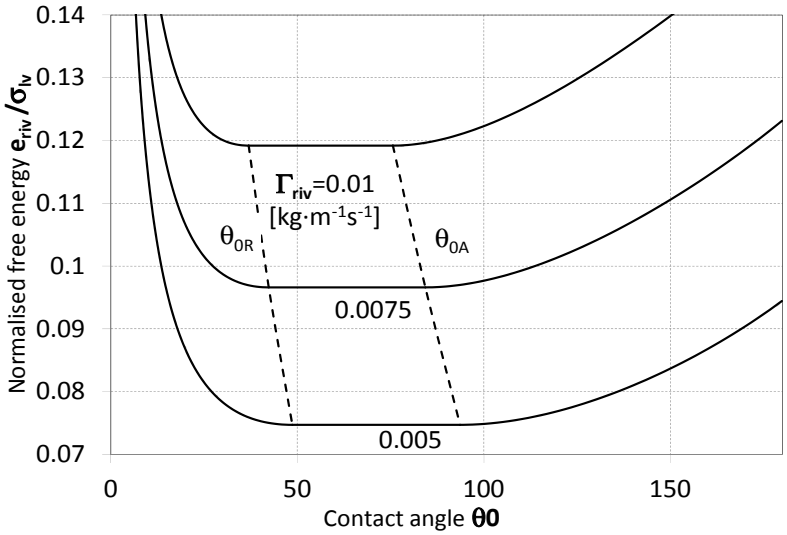

Fig. 4.24 Normalized rivulet energy as a function the contact angle [^{o}] for different values of the specific flowrate Γ_{riv} [kg·m^{-1}s^{-1}] when hysteresis tension f =0.02[J·m^{-2}], at T=25^{o}C and with ϕ= cosθ_{0Y} =0. 423

Moreover, considering Young's contact angle variations with temperature by means of the enthalpy of immersion [119], the contact angle hysteresis weakly, but not considerably, increases at higher temperatures. Thus, the effect of temperature on the contact angle hysteresis is not included in this analysis.

Comparing results obtained with the present approach and those obtained according to X.D. Wang et al. (2004) [117], kinetic energy reduces the equilibrium value of both advancing and receding contact angles (Fig. 4.24), but shows higher impact on the first. Figure 4.24 exemplifies the effect of different delivered specific mass flowrate Γ_{riv}. Higher flowrates are associated to a higher rivulet energy. Although the effect of kinetic energy doesn't have a strong impact, wettability is improved at high flowrates, whereas the hysteresis behaviour of the contact angle is slightly reduced.

On the other hand, even though this approach constitutes a formalism consistent with the following wettability analysis, in fact, this method preliminary requires the estimation of the hysteresis tension f_{max} as a function of the key variables at play. In this case of study its value is established with reference to the experimental values of the contact angle hysteresis measured on a sample of the material of the test section at hand. Extensive experimental analysis could be then reversed to correlate this parameter to the variable significant for the practical characterization of wettability properties. Therefore, figure 4.25 displays advancing and receding contact angles as directly measured on the surface of a tilted plane of the same material of the fin test section (aluminium with roughness-mean arithmetical tolerance 0.417μm). Consequently, using the measured values of θ_{0A} and θ_{0R}, eq. 4.26 and eq. 4.27 give the value of Young's contact angle ($\theta_{0Y}\approx65^{o}$) and the limit value of the hysteresis tension ($f_{max}=-f_{min}=0.0301$ J·m^{-2}). If compared with reference data from literature [118], reporting values of 34° and 73° ($\theta_Y\approx54^{o}$) respectively for receding and advancing contact angle of water on aluminium, the value of the advancing contact angle measured hereby is obviously higher. This result could be explained considering different surface characteristics and, more plausibly, could be related to different measuring procedures or hard dryness condition of the test sample for this kind of measurements. Furthermore, the contact angle hysteresis analysis suggests that a flowing configuration could be related to lower values of stable advancing and receding contact angles (Fig. 4.24).

As a result, in order to characterize the wetting ability of the liquid flowing on the contactor, the cross-section shape of the rivulet is modelled by considering that, for a narrowing extent of the solid-liquid interface when decreasing mass flowrates of liquid are delivered, the angle formed at the intersection line of the three interfaces equals the receding contact angle θ_{0R}. Conversely, to widen the solid-liquid interface when the liquid mass flowrate is increased, the contact line of the phase-interfaces cuts the solid plane with an angle equivalent to the advancing contact angle θ_{0A}.

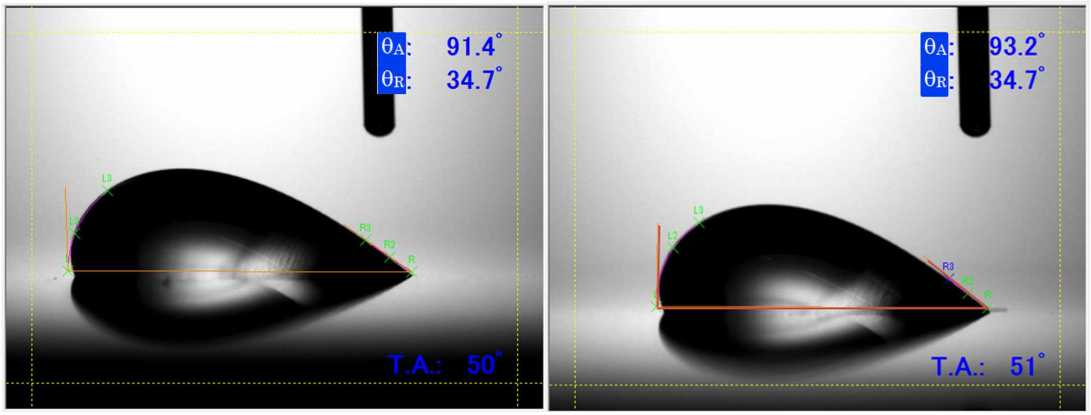

Fig. 4.25 Visualization of advancing and receding contact angles of two 50μl water droplet on a tilted plate of aluminium with mean arithmetical roughness of 0.417μm, at the maximum tilt angle before they start falling.

In order to identify the critical condition at which the film breaking occurs, the mass balance (combining eq. 3.5, 4.23 and 4.29) is required to assure continuity between the two configurations (uniform film and rivulet), yielding a relation

(eq. 4.33) between the rivulet radius R, the uniform film thickness δ and the parameter used to estimate the wet part of the surface X (eq. 4.23).

$$\left(\frac{\delta}{R}\right)^3 = X\frac{f(\theta_0)}{\sin\theta_0} \tag{4.33}$$

Substituting eq. 4.33 inside the specific energy of the rivulet (eq. 4.28), the expression is rearranged (eq. 3.34) as a function of the wetting parameter X and the uniform film thickness δ for a given liquid mass flowrate.

$$\begin{aligned} e_{riv} &= \frac{1}{15}\frac{\rho^3 g^2}{\mu^2}R^5 X\frac{\psi(\theta_0)}{\sin\theta_0}+\left[\frac{\theta_0}{\sin\theta_0}-\left(\phi-\frac{f}{\sigma_{vl}}\right)\right]X\sigma_{vl}+\sigma_{sv} = \\ &\frac{1}{15}\frac{\rho^3 g^2}{\mu^2}X^{-2/3}\left[\frac{\sin\theta_0}{f(\theta_0)}\right]^{5/3}\delta^5\frac{\psi(\theta_0)}{\sin\theta_0}+\left[\frac{\theta_0}{\sin\theta_0}-\left(\phi-\frac{f}{\sigma_{vl}}\right)\right]X\sigma_{vl}+\sigma_{sv} \end{aligned} \tag{4.34}$$

The energy minimization principle indicates that, once a proper value of the contact angle is fixed, the rivulet will be stable if its total energy shows a local minimum with respect to the local wetting ratio X for a value of this parameter lower than one. Contrarily, if the broken configuration doesn't exhibit a local minimum of its free energy in this range, or if the uniform film configuration has a lower energy value, the film will keep flowing in a continuous and uniform configuration. Hence, by differentiating eq. 4.34 with respect to X, equating to zero and solving for X (as in J. Mikielewicz and J. R. Moszynski (1976) [99]) gives a way to estimate the wetting ability of the liquid, and, introducing film- Weber and Reynolds numbers, the expression can be written as a function of these parameters, hysteresis tension f and the contact angle θ_0 (eq. 4.35).

$$X = \left[\frac{2}{5}\frac{\psi(\theta_0)}{\sin\theta_0}\left[\frac{\theta_0}{\sin\theta_0}-\left(\phi-\frac{f}{\sigma_{vl}}\right)\right]^{-1}\right]^{3/5}\frac{\sin\theta_0}{f(\theta_0)}\left(\frac{3}{4}\frac{\mathrm{Re}}{We^3}\right)^{1/5} \tag{4.35}$$

The critical condition (eq. 4.36) can be identified by a minimum value of film thickness δ_0 as a function of solution properties and contact angle, or by critical values of the dimensionless group $(Re\ \mathrm{We}^{-3})^{1/15}$ (proportional to the dimensionless critical thickness, equally to [99]). Eq. 4.36 is obtained using eq. 4.35 and equating the energies of the two configurations (eq.s 4.28 and 4.5). As a consequence, when the film thickness is lower than the minimum critical thickness ($\delta \le \delta_0$), the film is assumed to be broken and the local wetting ratio is given by eq. 4.35.

$$\frac{3}{5}\left(\frac{3}{4}\frac{\mathrm{Re}}{We^3}\right)^{1/3}+(1-\cos\theta_0)-G(\theta_0)\left(\frac{3}{4}\frac{\mathrm{Re}}{We^3}\right)^{1/5}=0 \tag{4.36}$$

Where,

$$G(\theta_0)=\frac{5}{2}\left[\frac{\sin\theta_0}{f(\theta_0)}\right]\left[\frac{2}{3}\frac{\psi(\theta_0)}{\sin\theta_0}\right]^{3/5}\left[\frac{\theta_0}{\sin\theta_0}-\left(\phi-\frac{f}{\sigma_{gl}}\right)\right]^{2/5} \tag{4.37}$$

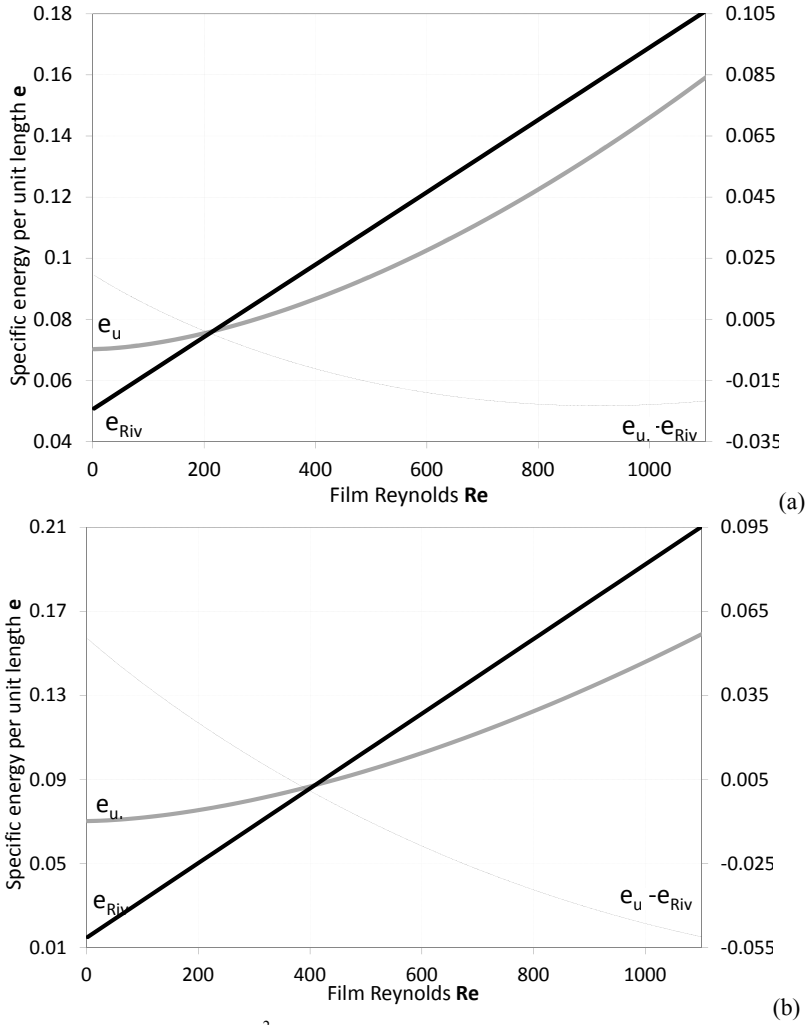

Fig. 4.26 Specific energy per unit width [J·m^{-2}] of rivulet and uniform film configurations on a vertical aluminium hybrid desiccant contactor. ϕ=0.588, T=25°C, f=0.0301 N·m^{-1} for decreasing (a) and increasing (b) liquid mass flowrates

Starting from a uniform film configuration, and as the mass flowrate quasi-statically decreases, complete wetting of the surface is maintained until the film critical thickness δ_0 is reached. Thereupon, the film will brake switching to the rivulet configuration with a contact angle θ_0 equal to the receding value θ_{0R}.

For Reynolds equal to 200, the rivulet configuration has a lower energy (Fig. 4.26a) and becomes stable for a wetting ratio of about 0.4 (Fig. 4.27a). The specific energy of the two configurations is quantified up to the value of σ_{sl}, which is assumed to be constant and, as a result, not influent in the comparison and in the differentiation operated to obtain eq. 4.35. Further decreasing the mass flowrate, the rivulet reduces its extension following the path identified by the configurations of minimum energy. Grey lines in figure 4.27 (a) represent the energy of the rivulet at Reynolds for which the uniform film configuration results to be stable for decreasing flowrates.

Since the Rivulet configuration is a stable configuration characterised by a minimum energy condition (Fig. 4.27b), for increasing mass flowrates, the rivulet configuration is maintained up until the rivulet base covers the whole surface (X=1 in Fig. 4.26b). In this case, the advancing contact angle θ_{0A} is used in the calculation. Consequently, the values of X for increasing Reynolds correspond to the abscissa of the local minima in figure 4.26 (b).

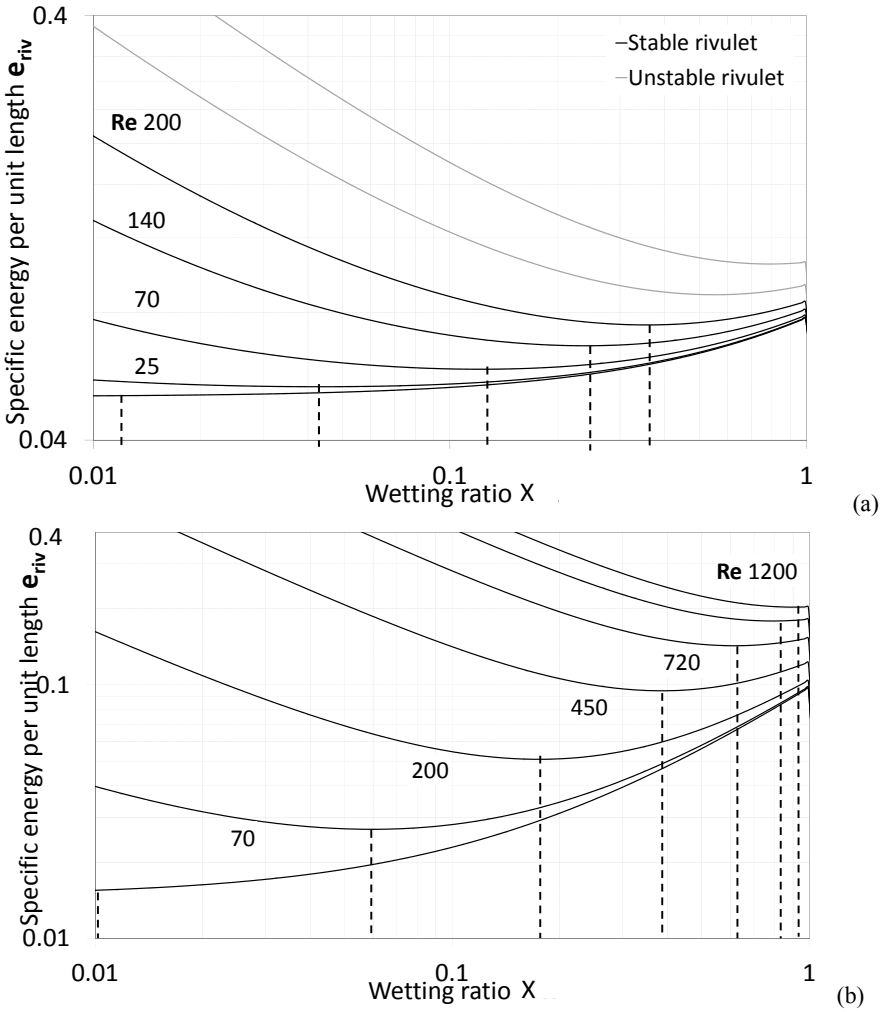

Fig. 4.27 Specific energy per unit width and per unit stream-wise length [J·m^{-2}] of a water rivulet on a vertical aluminium internally-cooled contactor. ϕ=0. 423, T=25°C, f=0.0301 N·m^{-1} for decreasing (a) ($\theta_0=\theta_{0R}$) and increasing (b) ($\theta_0=\theta_{0A}$) liquid mass flowrates

Figure 4.28 (a) shows the local film wetting behaviour for decreasing Reynolds number, locally based on the critical condition expressed by eq. 4.36 and using the receding value of contact angle θ_{0R}. When the film Reynolds decreases enough to make the local rivulet energy lower than the local uniform film configuration, the wetting ratio is given by eq. 4.35. Figure 4.28 (b) is obtained for increasing liquid mass flowrates, making evidence of the wetting ability of the rivulet configuration when the advancing contact angle θ_{0A} is used while this stable configuration is maintained until complete wetting is reached.

The surface wetting WS (eq. 4.38) is obtained from the integration of the local wetting ratio X. Figure 4.29 compares the results obtained (continuous lines) with the calculation performed ignoring the hysteresis phenomenon of the contact angle (dashed lines) ($\theta_0=\theta_{0Y}$). It can be highlighted that the hysteresis of the wetting behaviour would occur also on an ideally smooth surface, but it is intensified by the contact angle hysteresis phenomenon.

$$WS = \int_0^{P_x} X dx \tag{4.38}$$

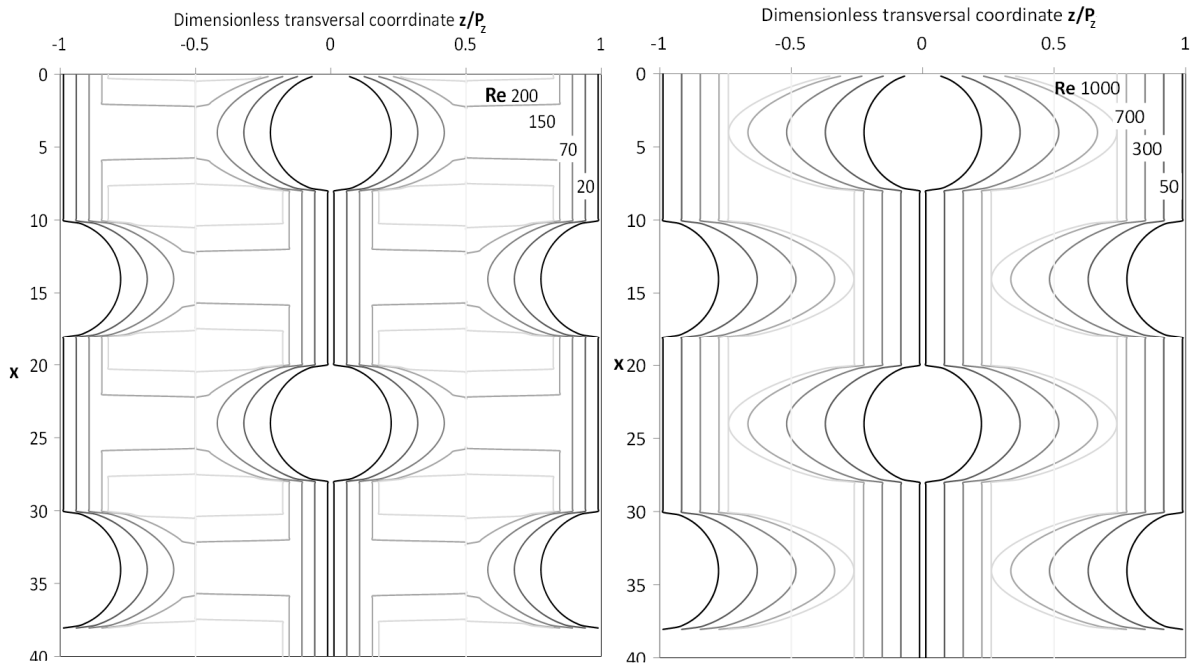

(a) (b)

Fig. 4.28 Simulated local wetting behaviour of water on a vertical aluminium test section of an internally-cooled contactor. ϕ=0. 423, T=25°C, f=0.031 [J·m^{-2}] for decreasing (a) ($\theta_0=\theta_{0R}$) and increasing (b) ($\theta_0=\theta_{0A}$) liquid mass flowrates

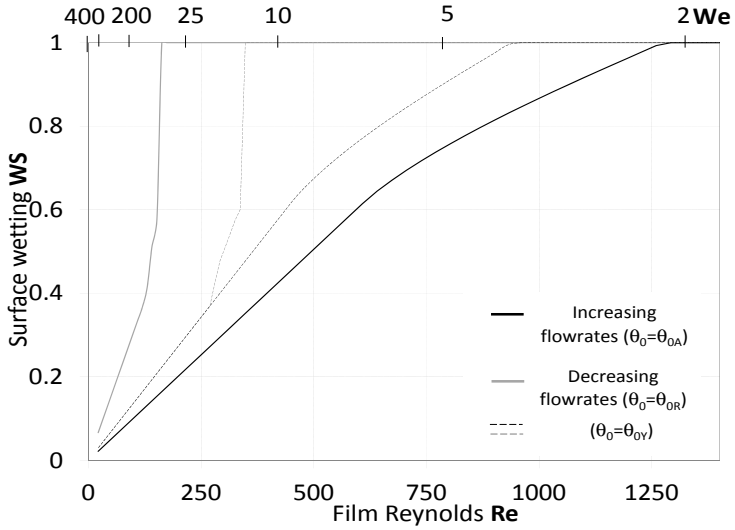

Fig. 4.29 Global wetting behaviour of water on a vertical aluminium test section of a hybrid desiccant contactor. ϕ=0. 423, T=25°C, f=0.0301 [J·m^{-2}]

4.7 Experimental equipment

Since the liquid desiccant can't be directly visualised while flowing inside the contactor, the film hydrodynamics is reproduced on a vertical test section corresponding to a single flat aluminium fin. The staggered array of tubes is arranged as shown in figure 4.19, and the geometrical features of the experimental equipment are written in Table 4.6.

The structure of the experimental apparatus is shown in figure 4.30. The test section is fixed on a polycarbonate vertical wall, above which a liquid reservoir is positioned. A slit at the bottom of the latter constitutes the distributor, assuring uniform film configuration at the inlet of the test section. At the bottom of the vertical wall a second reservoir collects the liquid and a circulation pump delivers it back to the distributor. The temperature of the liquid is measured at the inlet and at the outlet of the test section to define a single mean arithmetical value.

Table 4.6 Equipment geometrical features

Flat plate	Width	λ	mm	200
	Height	H	mm	400
Tube	Diameter	$2r$	mm	7.95
Tubes' disposition	Vertical pitch	P_x	mm	20.0
	Horizontal pitch	P_z	mm	20.0

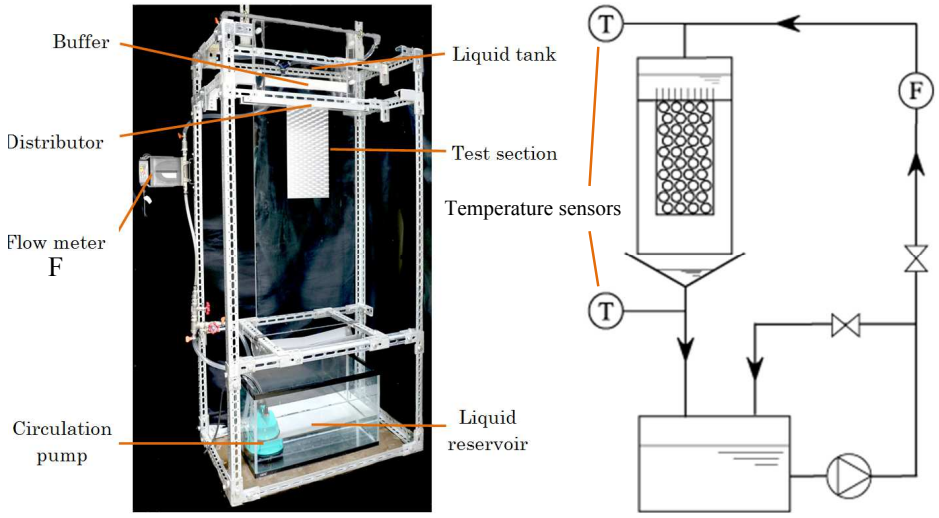

Fig. 4.30 Experimental equipment

A first series of cyclic wetting/de-wetting processes are performed by increasing and decreasing the liquid mass flowrate, to assure the absence of external impurities, and exclude conditions at which hard dryness of the surface or at the distributor could affect wetting behaviour of the liquid. Afterwards, the data collection is performed by following a quasi-static cycle between complete wetting and dryness of the test section, executed as a sequence of steady conditions obtained for increasing and decreasing mass flowrates. Each state is characterised by the amount of wetted area estimated by image processing. As a reference for a first comparison with the previously presented model and previous literature, experimental data are collected using pure water flowing over an adiabatic surface, since temperature changes within the operative range of these systems is not expected to be a major effect.

4.8 Image processing

The original image captured at steady state (Fig. 4.31a) is trimmed limiting the analysis to the test section area (Fig. 4.31b). The contours of the wet part are extracted (Fig. 4.31c). Static droplets are not considered as contribution to the wetting ability of the film. Successively, wetted parts and the corresponding dry patches are respectively changed into black and white surfaces, whereas, the tubes' sections (grey circles) are not considered into the calculation since they are not constituting flowing surface (Fig. 4.31e and 4.31d). The wetted area of the resulting image is calculated from the number of black pixels.

Results obtained are plotted with reference to the film Reynolds number and the Weber number, since, as shown in the mathematical model, inertial force, the viscous forces and surface tension are expected to significantly affect the wetting behaviour of the falling film.

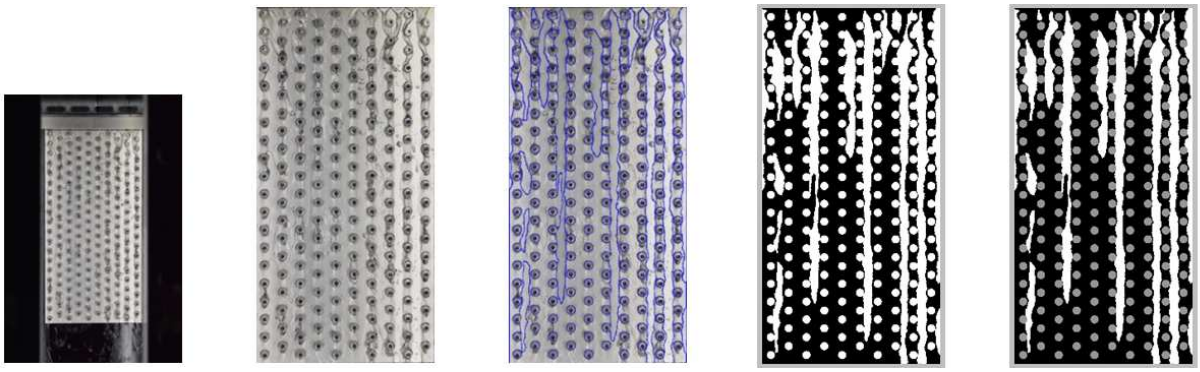

(a) (b) (c) (d) (e)

Fig. 4.31 Image processing; (a) Original image (b) Distortion correction and trimming (c) Wetted area contours extraction (d) Reduction to binary image (e) Processed image

The wetted surface *WS* (representative of the extent of the wetted area Π_{wet} against fin area, excluding the tube cross-sections, Π_{fin}) and film Weber number are respectively defined by eq. 4.39 and eq. 4.40. Γ is the mass flowrate per film unit width at the distributor. Physical properties are calculated for the arithmetical average of measured inlet/outlet temperature values.

$$WS \equiv \frac{\Pi_{\text{wet}}}{\Pi_{\text{fin}}} = \frac{1}{\Pi_{\text{fin}}} \int_{\Pi} \Pi_{\text{wet}} d\Pi \tag{4.39}$$

$$\text{We} \equiv \frac{\sigma}{\rho \bar{u}^2 L_c} \tag{4.40}$$

Where the average stream-wise velocity $\bar{u}$ and the characteristic length L_c of the fluid are, respectively, defined by eq. 4.41 and eq. 4.42.

$$\bar{u} = \frac{\rho g \delta^2}{3\mu} \tag{4.41}$$

$$L_c \equiv \left(\frac{\nu^2}{g} \right)^{1/3} \tag{4.42}$$

The relationship between the surface wetting *WS* and the film Reynolds number is shown in figure 4.32, where the secondary horizontal axis indicates Weber number. Increasing and decreasing mass flowrates correspond to the black and grey lines, respectively. Different wetting ability of the liquid on the same solid surface can be highlighted for increasing and decreasing mass flowrates. In other words, the hysteresis phenomenon of wetting is experimentally observed. Furthermore, by introducing the contact angle hysteresis, the model shows improved accuracy and noteworthy average agreement with experiments. In general, at low liquid mass flowrates, experimental data show higher wettability than the theoretical calculations. This discrepancy can be mainly related to the effect of imperfect liquid delivery at the distributor (Fig. 4.34e), locally increasing the mass flowrate delivered per unit surface width. A similar result could be ascribed to the chaotic characteristics of the local fluid flow, as can be observed in figure 4.33(e), where rivulet come to contact and join creating uniformly wetted patches.

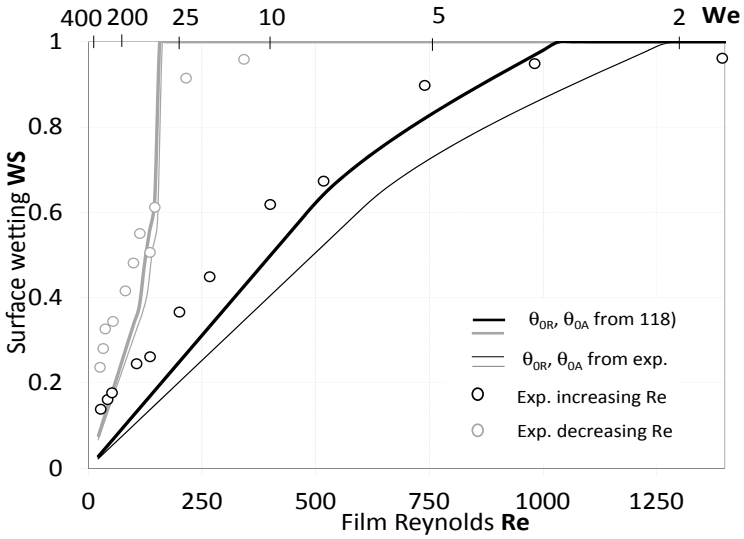

Fig. 4.32 Comparison between simulations and experiment; simulation results obtained using experimentally measured values of advancing and receding contact angle (thin lines), results for values of θ_{0R} and θ_{0A} obtained from literature [118] (thick lines) when decreasing (grey) and increasing (black) flowrates are delivered

Figure 4.33 and 4.34 represent examples of processed (binarised) images. Images 4.33 (a) to (f) obtained when the flowrate is increasing, and 4.34 (a) to (f) for reducing mass flowrates. The two sets of images in figure 4.33 and figure 4.34 depict the wetting behaviour at closely corresponding Reynolds numbers. By comparing these pictures (see, for instance, Fig.s 4.33d and 4.34c) it is possible to visualise the effect of the hysteresis phenomenon as an increased wetting ability of the same liquid flowrate when reached reducing its value if compared to the same condition established by increasing the liquid flowrate (Fig. 4.33d). In particular, figure 4.33(c) embodies the critical condition of a uniform film able to assure complete wetting. When the same critical mass flowrate is reached for increasing mass flowrates it is obvious that the rivulet configuration of the flowing liquid is maintained while the flow configuration doesn't switch back to uniform film thickness. As described by the theoretical model previously presented, the rivulet configuration gradually increases its width until it completely wets the fin surface/combines with adjacent rivulets.

In conclusion, an experimental study and a theoretical analysis based on the energy minimisation principle have been presented in order to characterise the wetting behaviour of falling liquid films on a vertical finned contactor. The analysis combines a contact angle hysteresis model with a criterion for the critical condition of a uniform film and, after the film breakage, establishes a method to estimate the wet part of the solid surface. Results obtained have been expressed as functions of contact angle, film Reynolds number and Weber number, highlighting that inertial force, viscous forces and surface tension significantly affect the wetting behaviour of the falling film.

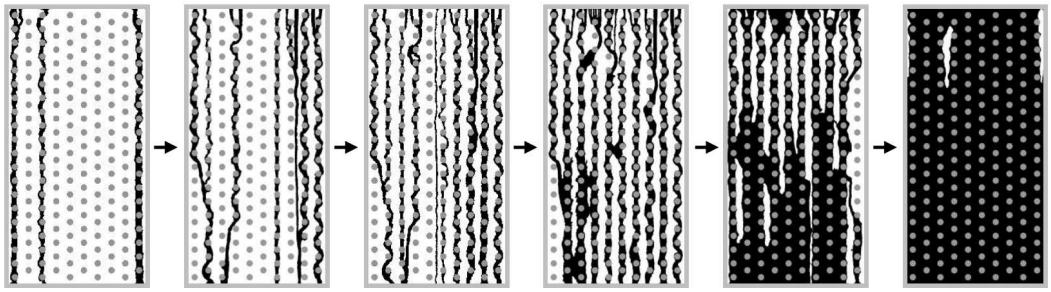

(a) (b) (c) (d) (e) (f)

Fig. 4.33 Binary images obtained for gradually increasing flowrates; (a) WS=9%, Re =20, We=656 (b) WS=18%, Re =52, We=183.0 (c) WS=24%, Re =106, We=71.0 (d) WS=37%, Re =200, We=30.4 (e) WS=62%, Re=400, We=12.1 (f) WS=95%, Re =982, We=3.65

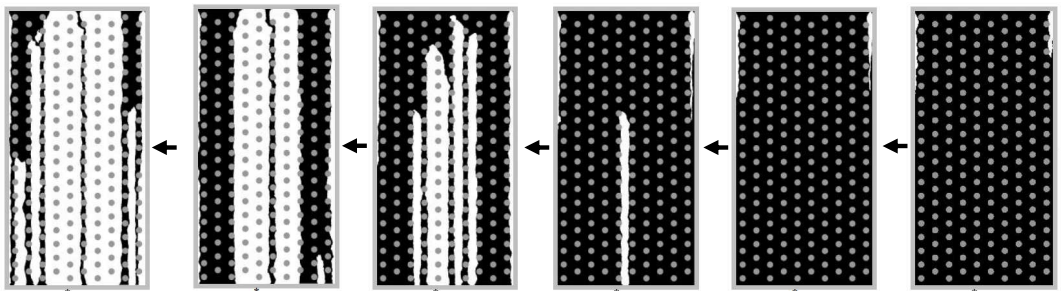

(f) (e) (d) (c) (b) (a)

Fig. 4.34 Binary images obtained for gradually decreasing flowrates; (a) WS=96%, Re =1394, We=2.29 (b) WS=96%, Re =342, We=149.0 (c) WS=91%, Re =215, We=27.7 (d) WS=61%, Re =146, We=46.2 (e) WS=48%, Re =99, We=77.8 (f) WS=24%, Re =26, We=467

According to the theoretical and experimental analysis, the following main conclusions can be stated:

When a liquid rivulet of specified geometry and flowrate is flowing over a solid rough surface, the contact angle hysteresis has been modelled by making use of the concept of an additional component taking part in the equilibrium of surface tension forces. This parameter has been introduced with the practical purpose of summarising the influence of different effects such as surface roughness and distortions of the liquid-vapour interface geometry required for widening/narrowing the extension of the rivulet base, namely the wet part of the solid surface. In parallel, its value is established referring to values of the contact angle hysteresis from literature and direct experimental measurements on a sample of the same material used to construct the desiccant contactor. Subsequently, advancing and receding contact angle are individuated as meta-stable configurations characterised by a local minimum of the liquid free energy in which kinetic energy was accounted for.

The effect of kinetic energy can be mainly summarised as giving lower advancing and receding contact angle if compared to the case of a static spherical droplet. Higher mass flowrates give a higher reduction. Hence, this approach suggests that wettability is improved at high Reynolds number and the hysteresis behaviour of the contact angle is slightly reduced.

The film stability and the hysteresis phenomenon of the wetting behaviour with respect to decreasing and increasing mass flowrates have been modelled and estimated by means of an energy minimisation approach. In general, by introducing the effect of contact angle hysteresis in the analysis, the phenomenon of wettability hysteresis is amplified.

4.9 Semi-theoretical wettability model for falling film heat exchangers

Since an established method to predict the wetting behaviour of horizontal tube falling film heat exchangers is not available at present, this work aims at the modelling and evaluation of the direct inferences of thin films break-down on this particular heat exchanger configuration (Fig. 4.35), in order to study its effects on the transfer characteristics of the absorber at low solution flowrates.

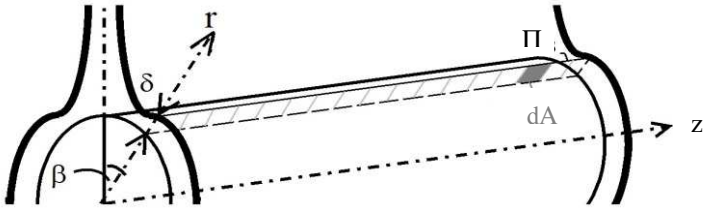

Fig. 4.35 Coordinate reference system

Taking advantage of the understanding gained in the previous paragraphs, the complexity of the flowing film hydrodynamic behaviour can be simplified by consistent assumptions. This results in a semi-empirical approach for estimating the critical condition of the uniform film and the tube partial wetting characteristics.

A homogeneous and uniform falling liquid film is considered to flow over a single horizontal tube. Steady state is postulated, the flow is fully developed and laminar, the curvature of the interface is negligible, heat and mass transfer influences are neglected. Assumptions introduced are equivalent to those stated in paragraph 4.2.

Furthermore, adopting an integral approach for the flow, Nusselt integral solution can be applied (see eq. 3.2) consistently with the numerical approach used for the solution of the coupled system of energy and species transport equations. The corresponding film thickness is given by eq. 3.6.

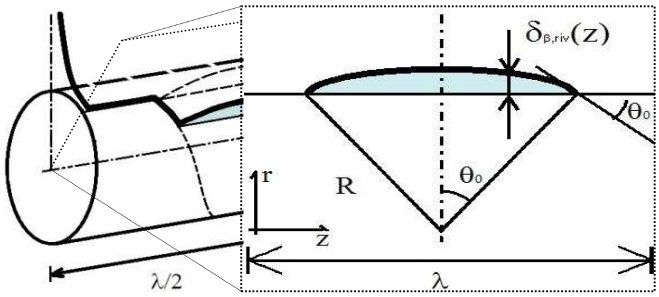

Fig. 4.36 Schematic of rivulet configuration

Considering a circular cross-section shape (eq. 4.24) of the rivulet (parallel to the tube axis) and dividing it into narrow strips of width dz and height $\delta_{\beta,riv}(z)$, the velocity profile in such a strip is assumed to be the same as the profile in a uniform film of the same height $\delta_{\beta,riv}(z)$.

Accordingly, the total energy per unit length for the rivulet and uniform film configurations, are expressed, respectively, in a similar way of eq. 4.5 and eq. 4.27, with the only differences related to the thickness distribution and a unique value of the contact angle. When the film breaks up into rivulets (Fig. 4.36), the local wetting ratio X_β (eq. 4.43) represents the basic parameter to quantify the wet part of the tube surface.

$$X_\beta = \frac{2R_\beta \sin\theta_0}{\lambda} \tag{4.43}$$

The mass balance between the two configurations (equivalent to eq. 4.35) yields a local dependence between wetting ratio X_β, rivulet radius R_β and the uniform film thickness δ_β at every angular position β. In addition, eq. 4.10 still holds true. Consistently with the energy minimization principle, the rivulet will be stable if the total energy shows a local minimum with respect to the wetting ratio X, when X<1, and if the uniform film configuration has a higher value of total energy. Hence, minimising the rivulet energy and solving for X_β gives eq. 4.44.

$$X_\beta = \left[\frac{2}{45}\frac{\rho^3 g^2 \sin^2\beta}{\mu^2\sigma}\left(\frac{\theta_0}{\sin\theta_0}-\cos\theta_0\right)^{-1}\right]^{3/5}\frac{\sin\theta_0}{f(\theta_0)}\delta_\beta{}^3 \tag{4.44}$$

From the knowledge of the value of the wetting ratio, the equality of mass flow-rates (eq. 3.35) yields the rivulet radius and, finally, the spacing between adjacent rivulets λ can be calculated from the definition of wetting ratio (eq. 4.43).

The critical condition can be identified by a value of film thickness $\delta_{0,\beta}$ as a function of solution properties and contact angle (eq. 4.45), and is obtained using eq. 4.45 and equating energies of the two configurations (eq. 4.5 and eq. 4.28). As a result, when the thickness of the uniform flowing film is lower than the minimum critical thickness ($\delta_\beta \le h_{0,\beta}$), the film is assumed to be broken and the local wetting ratio is given by eq. 4.45.

$$\delta_0^{+5} + (1 - \cos\theta_0) - G(\theta_0)\delta_0^{+3} = 0 \tag{4.45}$$

Where $G(\theta_0)$ (eq. 4.37), as well as the rivulet energy (eq. 4.28), are defined without considering the effect of the hysteresis tension (f=0). Eq. 4.46 is obtained with respect to the following definition of the dimensionless parameter δ_0^+ (eq. 4.46).

$$\delta_0^+ = \left(\frac{\rho^3 g^2 \sin^2\beta}{15\mu^2\sigma} \right)^{1/5} \delta_{0,\beta} \tag{4.46}$$

Its value is constant and can be easily calculated for a fixed characteristic contact angle.

On the other hand, the critical thickness value is a function of the angle β over the tube surface and is minimal in the vertical part of the tube. Setting the value of contact angle, 29.7° for Lithium-Bromide over copper (Soto Frances 2003), the film thickness for different value of Reynolds number has been compared to the minimum stable thickness obtained by combining J. Mikielewicz et al. (1976) [99] and Nusselt theory for film flowing over a horizontal tube (Fig. 4.37).

It can be shown that above a certain Reynolds number the film thickness is higher than the minimum stable value along the whole tube surface. Decreasing Reynolds number determine an increasing value of the incompletely wet portion of the tube (decreasing average wetting ratio). Three different zones can be accordingly identified and represented in figure 4.38:

- Complete wetting of the whole surface
- Complete wetting along part of the surface
- Partial wetting of the whole surface

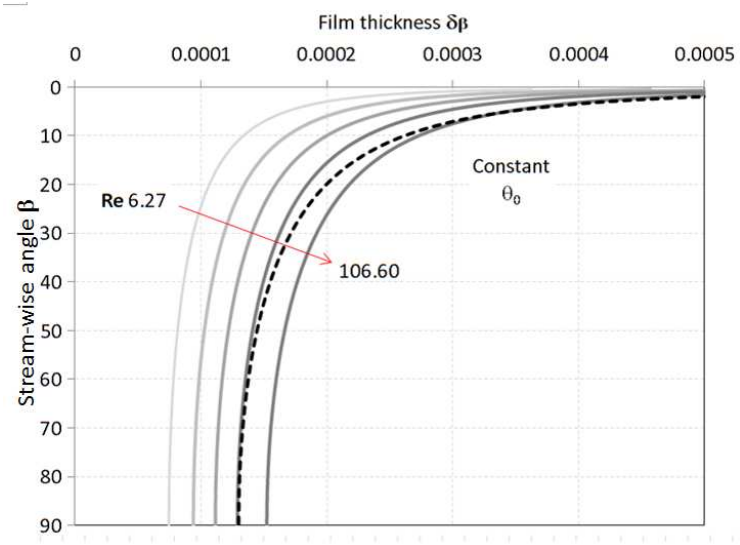

Fig. 4.37 Comparison between film thickness [m] (grey lines) and minimum stable thickness [m] (black dashed line) for different Reynolds numbers

The black line represents the minimum stable thickness and depending on -2/5 order of sinβ, its behaviour for increasing β is steeper than that of Nusselt integral solution film thickness, which has a dependence on the same factor of a lower order (-1/3).

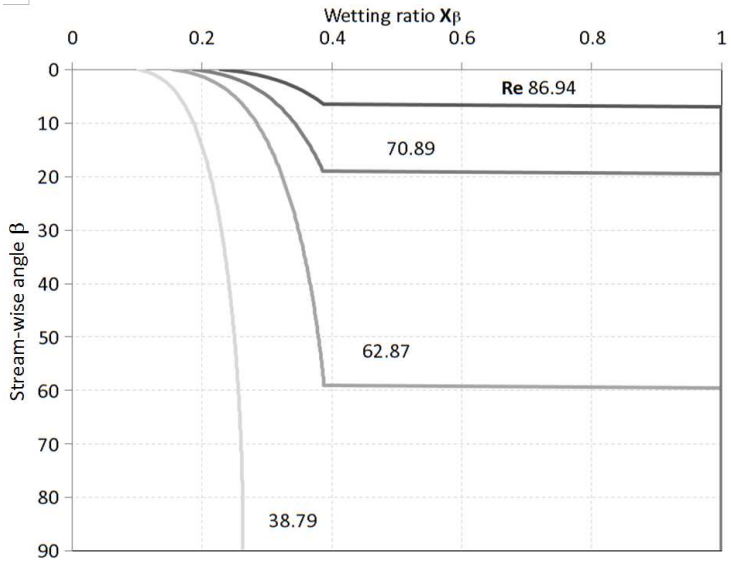

Fig. 4.38 Local values of wetting ratio for different Reynolds numbers

These three regions are limited quantitatively (eq.s 4.47, 4.48 and 4.49) by considering that when the thickness of the flowing film over the horizontal tube predicted by Nusselt theory is lower than the minimum critical thickness ($\delta_\beta \leq \delta_{0,\beta}$), the film is assumed to be broken into rivulets.

$$\delta_0^+ \left(\frac{\rho^3 g^2 \sin^2 \beta}{15 \mu^2 \sigma} \right)^{-1/5} \geq \left(\frac{3}{2} \mathrm{Re} \frac{\mu^2}{\rho^2 g \sin \beta} \right)^{1/3} \tag{4.47}$$

$$\sin \beta_0 \leq \left(\frac{\delta_0^+}{\mathrm{Re}^{1/3}} \frac{10 \rho^{1/15} \sigma^{1/5}}{\mu^{7/15} g^{2/5}} \right)^{1/5} \tag{4.48}$$

$$0 \leq \beta \leq \arcsin \left[\left(\frac{\delta_0^+}{\mathrm{Re}^{1/3}} \frac{10 \rho^{1/15} \sigma^{1/5}}{\mu^{7/15} g^{2/5}} \right)^{1/5} \right] \tag{4.49}$$

In order to obtain a single value for the whole tube surface, the results are integrated around the tube surface for a symmetry reduced range.

$$WR = \frac{\int_0^{\arcsin\left[\left(\frac{\delta_0^+}{\mathrm{Re}^{1/3}} \frac{10 \rho^{1/15} \sigma^{1/5}}{\mu^{7/15} g^{2/5}}\right)^{1/5}\right]} X_\beta d\beta + \int_{\arcsin\left[\left(\frac{\delta_0^+}{\mathrm{Re}^{1/3}} \frac{10 \rho^{1/15} \sigma^{1/5}}{\mu^{7/15} g^{2/5}}\right)^{1/5}\right]}^{\pi/2} d\beta}{\pi/2} \tag{4.50}$$

The rivulet shape assumption together with the mass balance determine an abrupt discontinuity between partial and uniform wetting, corresponding, respectively, to uniform film and rivulets configurations (Fig. 4.36).

This result finally determines an irregular behaviour of the average wetting ratio (Fig. 4.39).

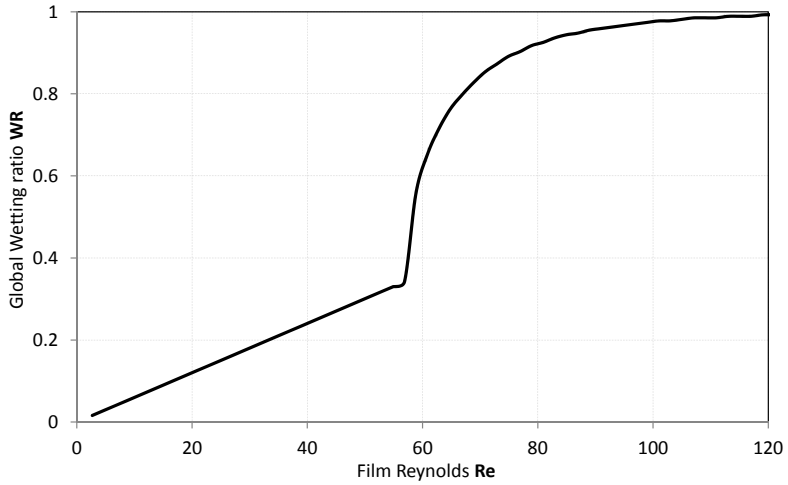

Fig. 4.39 Average Wetting Ratio over the tube surface as a function of film Reynolds number

The rivulets radius and the spacing between consecutive rivulets are results of calculation.

$$R_\beta = \delta_\beta \left(\frac{\sin\theta_0}{X_\beta f(\theta_0)} \right)^{1/3} \tag{4.51}$$

A value of rivulets radius R_β actually exists only when the film is broken in the rivulet configuration, otherwise its value represents just a mathematical solution without any physical meaning.

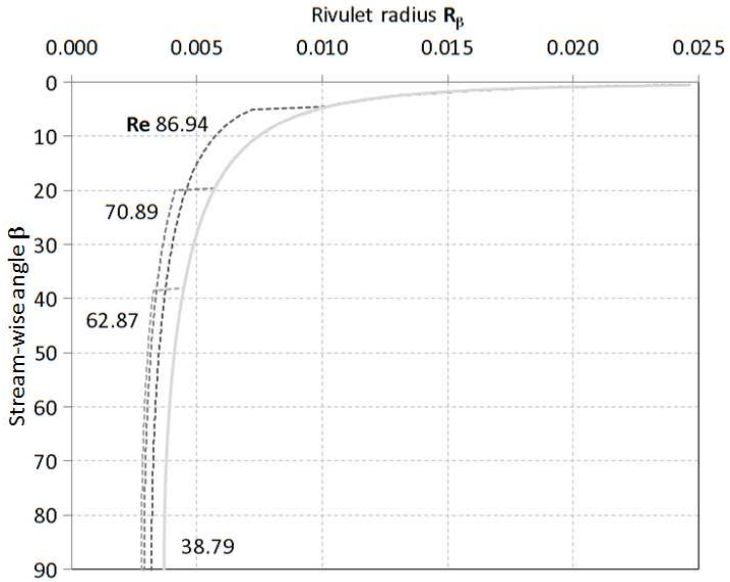

Fig. 4.40 Rivulet radius [m] distribution over the tube surface

The same concept applies to the calculation of rivulets spacing λ_β.

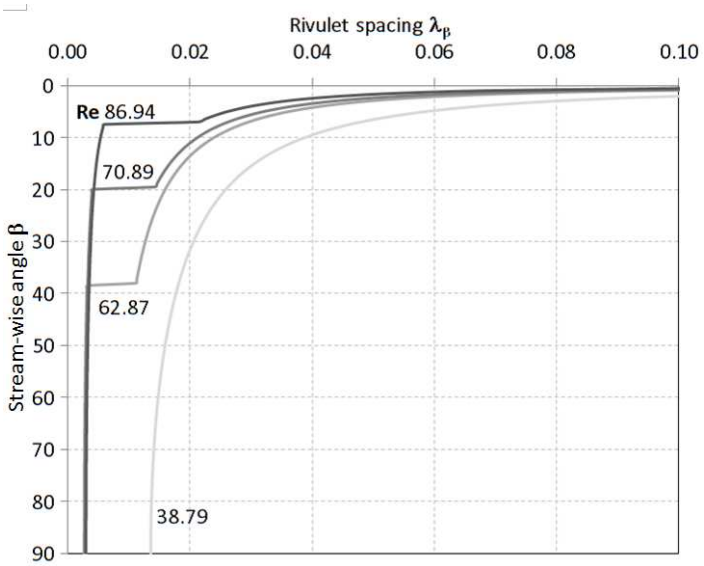

Fig. 4.41 Rivulet spacing distribution [m] over the tube surface for different values of Reynolds number

$$\lambda_\beta = \frac{2R_\beta sin\beta}{X_\beta} \tag{4.52}$$

Rivulets spacing values for different Reynolds numbers seem to be quite far from the actual flowing pattern that can be observed on a real tube bundle.

The film break-up criterion expressed by eq. 4.45 represents a threshold defined energetically and can be approached in two different ways. Contact angle can be assumed to be constant, resulting in a critical thickness distribution over the tube surface (Fig. 4.37); otherwise, a reverse can be also done, referring to a fixed value of minimum stable film thickness (Fig. 4.42), establishing a critical contact angle distribution (eq. 4.53 and Fig. 4.46).

The previously presented model exhibits a few main disadvantages. Due to the assumption of a constant value of contact angle, the corresponding critical minimum thickness distribution results in a wetting behaviour (shown in Fig. 4.38) which is qualitatively different from what can be actually observed in actual systems. Furthermore, results obtained seem to underestimate experimental values [26]. Observing that the contact angle is subjected to irregular and condition-sensible changes, difficulties occur in comparing experimental data to this theory. Consistently, M. Trela (1993) [94] observes that experimental results disagree with the assumption of considering contact angle a unique property of materials, being a characteristic dependent on the operative conditions, solid surface configurations, film flowing dynamics and flow rate. On the other hand, the value of minimal stable thickness can be referred directly to experimental data or calculated from experimental minimum wetting mass flow-rate values, for an assumed velocity distribution (see Γ_D, Γ_W and Γ_0 in paragraph 4.3).

In order to overcome some of the theoretical uncertainties and complexities, a semi-theoretical method, based mainly on experimental observations that the contact angle is a variable quantity and that the critical minimum thickness should be identified as a value defined by fluid properties and flowing conditions, is hereby presented.

The same set of principles, resulting in the equation describing the critical condition between rivulet and uniform film configuration (eq. 4.43), applies. By fixing the value of minimum critical thickness δ_0, related to fluid properties and operative conditions, a critical contact angle distribution over the tube surface is obtained. A constant value of minimum stable thickness directly implies that its dimensionless expression δ_0^+ increases with the surface angle β.

Representing the solution of the critical condition described by eq. 4.43 with a polynomial fitting curve approximating its numerical solution, contact angle distributions can be obtained for different values of dimensionless critical thickness δ_0^+ (eq. 4.53).

$$\theta_{0,\beta} = 1665\ \delta_0^{+6} - 3447\ \delta_0^{+5} + 2399\delta_0^{+4} - 459.7\delta_0^{+3} + 49.54\delta_0^{+2} + 2.974\delta_0^{+} + 0.8616 \qquad (4.53)$$

The value of minimal stable thickness can be referred directly to experimental data [99) 26)] or obtained from experimental values of minimum wetting mass flowrate [92)]. This parameter is required to summarise the complex occurrence between different hydrodynamic and thermodynamic effects; accordingly its value is critical for the model accuracy. Experimental data for the critical wetting rate Γ_0 of continuous film from D. M. Maron et al. (1982) [92)] (Fig. 4.17), has been approximated by a fitting relation, as a function of the dimensionless group summarising fluid properties (eq. 4.54). According to previous theoretical and experimental studies, both minimum wetting rates (Γ_D and Γ_W) obtained gradually increasing mass flow-rate and film critical wetting rate Γ_0 (reached with negative increments in the liquid flowrate) are recognised to increase with the dimensionless group defined by $Ga=\rho\sigma^3/\mu^4 g$ and them all can be represented by a power function of Galileo number. Eq. 4.54 is obtained from the interpolation of experimental data [92)] and is used for identifying the film breaking condition and the corresponding minimum critical thickness δ_0.

$$\Gamma_C = 8.5027\left(\frac{\sigma^3\rho}{\mu^4 g}\right)^{0.0505} \qquad (4.54)$$

Unfortunately, as can be observed in figure 4.17, sound consistency between the different studies exists only in the intermediate range of the dimensionless group.

Considering the operative conditions of a high-temperature absorber (T_i=180 C°, ω=62%) the corresponding dimensionless critical wetting rate can be obtained for the values of solution properties and calculation are performed in order to estimate the wetting ability of the solution.

When the thickness of the uniform falling film is lower than the minimum critical thickness, the film is assumed to be broken into the rivulet configuration and the local wetting ratio is that corresponding to (eq. 4.44) for the local value of contact angle and film thickness.

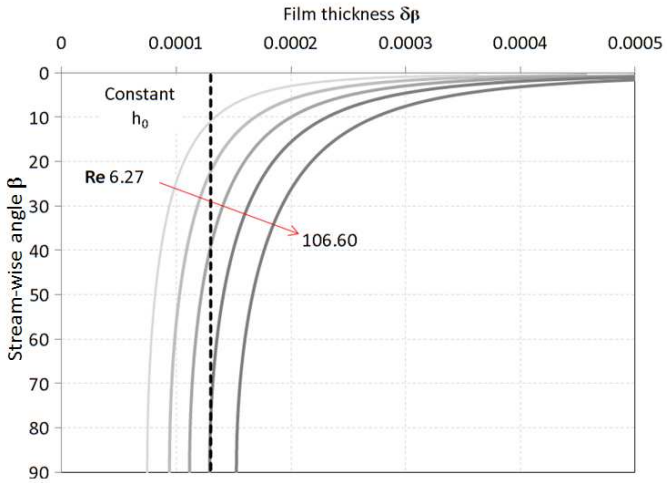

Fig. 4.42 Comparison between film thickness [m] and minimum stable thickness [m] (black dashed line) for different Reynolds

$$\beta_0 \geq \arcsin\left(\frac{3}{2}\frac{\mu^2\,\mathrm{Re}}{\delta_0^{\,3}\rho^2 g}\right) \qquad (4.55)$$

Calculations for different Reynolds numbers result in the following wetting ratio distribution over the first half of the tube surface (Fig. 4.43).

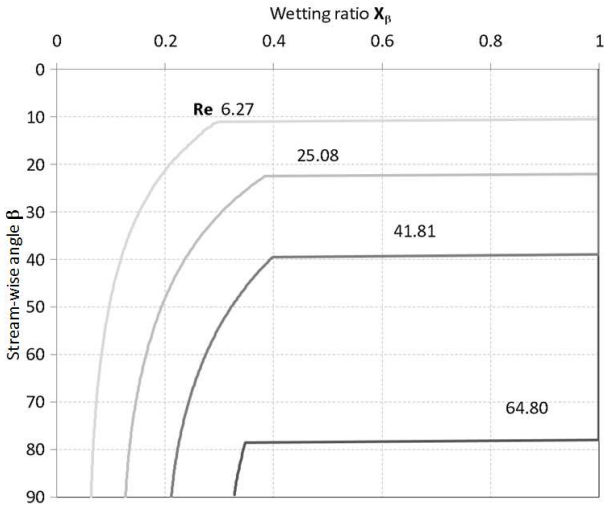

Fig. 4.43 Local values of wetting ratio for different Reynolds numbers

This different approach gives a fluid distribution closer to experimental observation. The local Wetting Ratio is unitary between the impact position and β_0, while between β_0 and the vertical portion of the tube its value is given by the modified Mikielewicz theory using the contact angle distribution obtained for film flowing over a horizontal tube.

A single value for the tube is obtained as its average value over the surface.

$$WR = \frac{\int_0^{a\arcsin\left(\frac{3\,\mu^2\,\mathrm{Re}}{2\,h_0^3\,\rho^2 g}\right)} d\beta + \int_{\arcsin\left(\frac{3\,\mu^2\,\mathrm{Re}}{2\,h_0^3\,\rho^2 g}\right)}^{\pi/2} X_\beta d\beta}{\pi/2} \tag{4.56}$$

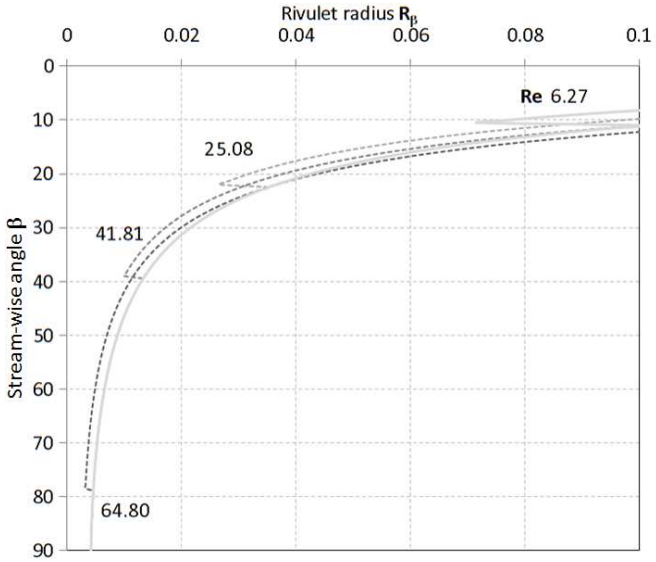

Fig. 4.44 Rivulet Radius distribution over the tube surface

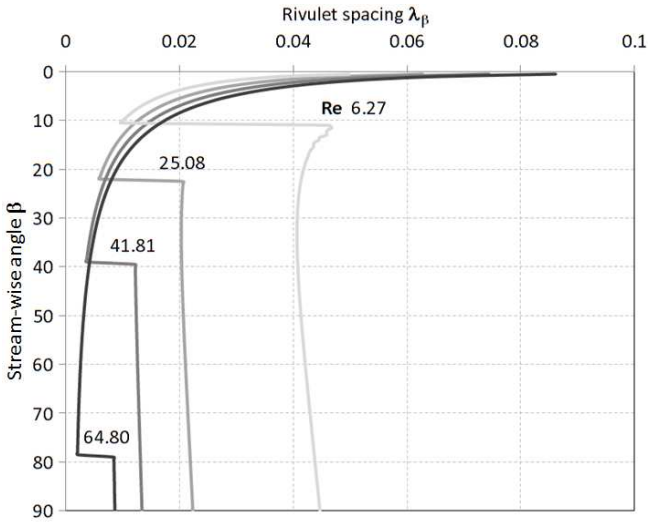

Fig. 4.45 Rivulet Spacing distribution [m] over the tube surface for different values of Reynolds number

Furthermore, rivulets radius (Fig. 4.44) and rivulets spacing distribution (Fig. 4.45) can be calculated for different Reynolds numbers. Once the film is broken, calculation results make evidence of a decreasing wetting ratio, an increasing rivulets spacing and a decreasing radius for the rivulet flowing over the tube surface, which is consistent with the direct observation of dry patches shape.

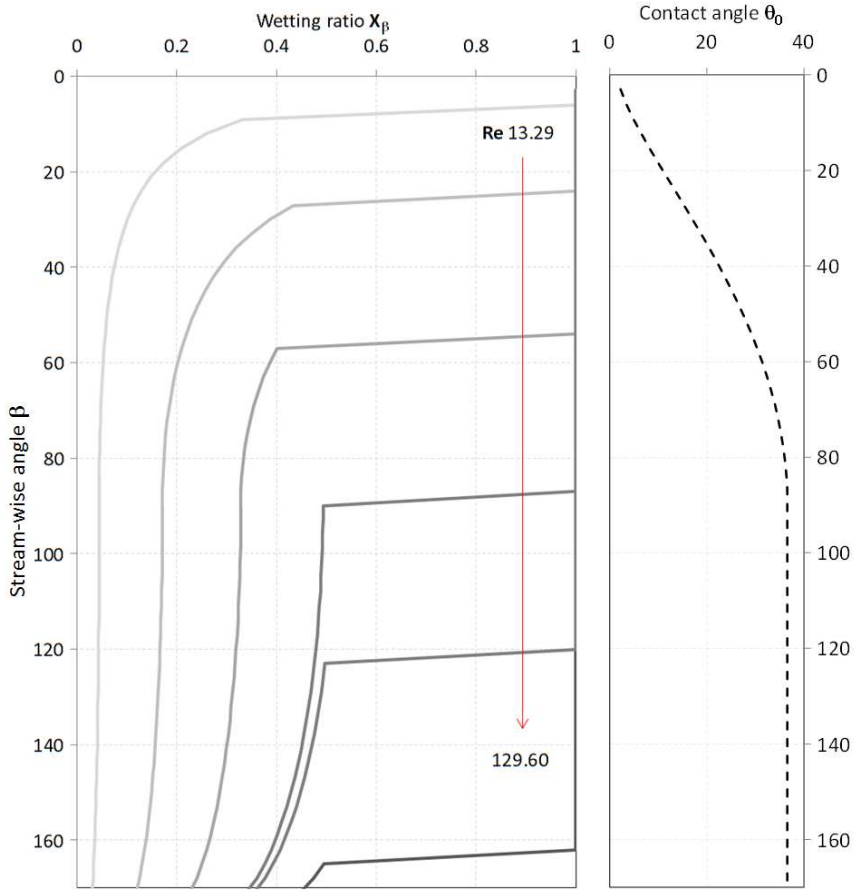

Fig. 4.46 Local values of wetting ratio and contact angle over the entire tube surface for different Reynolds numbers

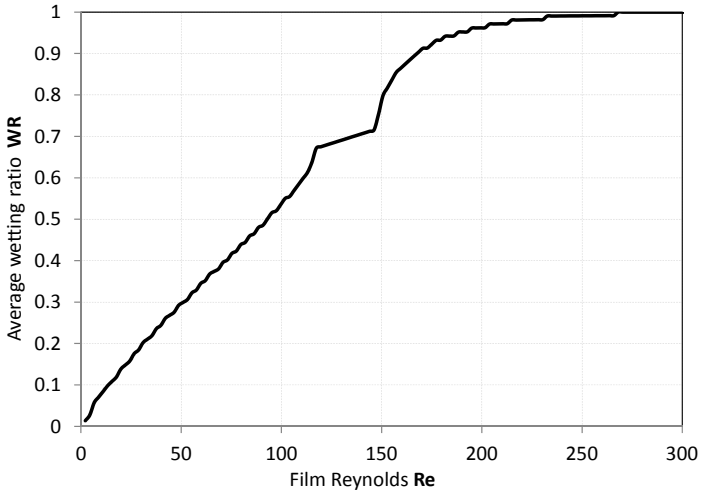

Fig. 4.47 Average Wetting Ratio over the tube surface as a function of film Reynolds number

The wetting behaviour estimation is applied to the tube surface using constant critical thickness approach for the first half of the tube, obtaining a contact angle distribution and using a constant contact angle value, corresponding to that obtained in the vertical part of the tube surface, in the second half of the tube. This approach combination avoids the sudden change from broken to uniform film configuration, which otherwise would occur using either approach.

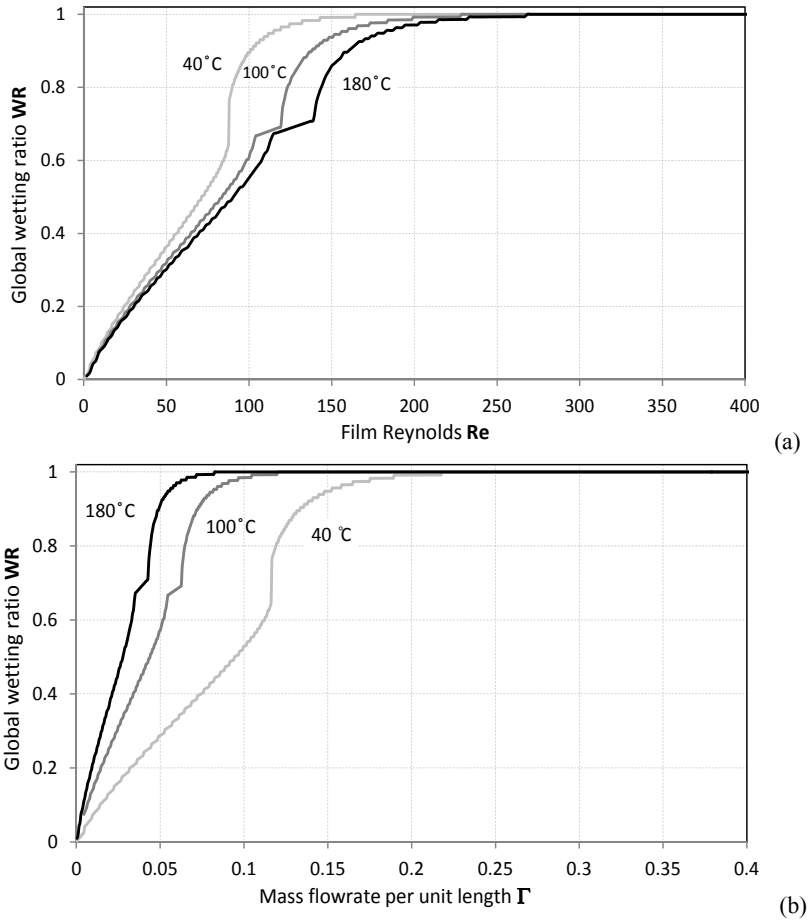

Fig. 4.48 Average wetting ratio as a function of (a) film Reynolds (b) mass flowrate per unit length for different operative temperatures

Moreover, figure 4.46 highlights a flowing pattern similar to that observed on actual systems. Practically, constant critical thickness model is applied in the first half of the tube while in the second half constant contact angle model is used. The present formulation gives a global wetting ability that can be visualised in figure 4.46.

As a consequence, the sudden change from broken to uniform film configuration is avoided. In fact, this latter behaviour can't be observed and a gradually increasing wetting ratio is also consistent with the theoretical work of A. Doniec (1988) [112] about equilibrium shape of liquid cross-section and with the experimental results presented by D. M. Maron et al., (1982) [92].

Furthermore, in order to employ the model for component analyses, the wetting model needs to be extended considering multiple tubes. Based on visual observations and according to previous models [108] and results [110], the calculation method for wetting ratio should be directly applied only for the tubes at the bottom of the bundle (after 10th tube), while the solution distribution is forced at the first tube. As a consequence, there must be a transition zone, in which wetting ratio decays following a certain law.

$$X_{\beta,j} = B(\mathrm{Re},\beta)e^{-C_\beta(j-1)} \tag{4.57}$$

Where j is the index identifying the tube number and B is a coefficient representing Reynolds number influence on the first tube, allowing consistence with the condition of absence of heat transfer in the extreme case of null solution mass flow rate.

$$B(\mathrm{Re},\beta) = \left[X_{\beta,j} + (1 - X_{\beta,j})\left(\frac{\mathrm{Re}}{\mathrm{Re}_b} \right) \right] \tag{4.59}$$

Where,

$$\mathrm{Re}_b = \frac{4\Gamma_0}{\mu} \tag{4.59}$$

Accordingly, C_β is the constant adjusted to give the value of $X_{\beta j}$ calculated by the direct application of the wetting ratio model at tube 10.

$$C_\beta = \frac{\ln\left[X_{\beta,10} + (1 - X_{\beta,10})\left(\frac{\mathrm{Re}}{\mathrm{Re}_b} \right) \right] - \ln X_{\beta,10}}{9} \tag{4.60}$$

4.10 Summary

As a summary, a criterion for the identification of the uniform film critical condition has been developed according to the energy minimisation principle. By the introduction of an additional geometrical parameter for the description of the cross-section shape of the rivulet and considering a generic inclination of the plain surface, the resulting theory generalises earlier theories.

Furthermore, the combination of the energy minimisation principle with a Lagrangian approach can be applied to estimate the local wetting behaviour of the rivulet in its transition to the stable configuration and analyse its trend with respect to the main geometrical and operative parameters. According to the results obtained and to the model presented above, the following conclusion can be stated:

- A newly developed method for the estimation of the local behaviour has been presented and explored for various geometrical features and under different operative conditions

-The partial wetting model and the critical condition show both qualitative and quantitative agreement with experiments and previous theories.

-Furthermore, the hysteresis behaviour of the wetting behaviour with respect to decreasing and increasing flowrates can be described by the present model. The occurrence of this phenomenon is believed to have a major role for the operative control of a system employing falling liquid films as transfer medium.

- Increasing the plain surface width λ and its inclination β the minimum stable thickness δ_0 decreases and wetting ratio at the critical condition X_0 increases.

- The bigger the contact angle θ_0 the higher the minimum stable thickness δ_0 of the uniform film. Accordingly, film breaking into rivulet occurs at higher Reynolds, but the wetting ratio at the critical condition X_0 slightly increases.

As a result, this approach seems to be suitable for the characterisation of thin film hydrodynamics and appears to be promising to be included in heat and mass transfer modelling of processes performed by using thin liquid films flowing on solid surfaces.

Experimental flow visualisation of water on an adiabatic vertical test section, equivalent to a single fin of a liquid desiccant contactor, has been performed as a first comparison and validation of the theoretical analysis. Visual data have been collected, and image binarisation has been used to establish a calculation method of the amount of wetted area.

The film critical condition and the partial wetting model have shown both qualitative and quantitative agreement with experiments. As a result, the current approach appears to be promising for being employed in the optimisation of internally cooled desiccant contactors, as well as in the development of the control method of the whole system, and, can be combined with heat and mass transfer models for an improved characterisation of processes performed by using thin liquid films. On the other hand, further experimental comparisons are envisaged for a refinement of the model and for extending its applicability to different application cases.

Finally, a semi-empirical approach has been used as a criterion for estimating the critical condition for a uniform film, while the energy minimisation principle has been used for describing the tube partial wetting. According to the results obtained and to the model presented in the previous paragraph, the following conclusions can be stated:

The complexity of the flowing film hydrodynamic behaviour has required significant simplifying assumptions, which have brought to neglect important phenomena like Marangoni effect, coupling with mass transfer, turbulence or wavy surface. These considerations suggest that the modelling effort could be extended including the effect of other phenomena and parameters. On the other hand, the model complexity should be compared pragmatically to the accuracy-improvement possibility related to the inclusion of such details and to the practicability of eventual employment of the model in global system simulations. In addition, this first approach can be improved by further experimental comparisons. In particular the estimation of the critical breaking condition and visual observations of partial wetting for an extended range of operative conditions can be critical for refining the model accuracy and extending its applicability.

Chapter 4,
Falling film stability and wetting behaviour

Chapter 5, Heat and mass transfer characteristics of absorptive falling film on a partially-wetted horizontal tube

Going back to the main objective of this work, a detailed numerical study characterising the absorption process of water vapour in LiBr-H_2O solution for different operative conditions, including both partial and complete wetting, is performed and this chapter describes its main results. Consistently with the numerical analysis of the absorption process developed in chapter 3, the model describing partial wetting is based on hydrodynamic description of Nusselt boundary layer integral solution, thus it can be easily adapted to be included in the transfer analysis by acting on the local film thickness. Accordingly, extended maps of heat and mass transfer coefficients of falling film heat exchangers are obtained. The resulting analysis is improved in its accuracy and extended in its applicability to the low Reynolds region.

Due to different dominant hydrodynamic effects, three main regions of the resulting heat and mass transfer coefficients can be identified (Partial wetting, uniform laminar film and film–dominated by velocity field). The influence of operating and geometric parameters is investigated to extract general and detailed observation for actual falling film absorbers design and control. Additionally, a first comparison with experimental data from literature is presented.

5.1 Numerical model

The fundamental structure of the numerical model matches the one presented in Chapter 3, paragraph 3.2 (eq. 3.1-3.18). However, in order to include the effect of partial wetting, the method presented in Chapter 4 is used at every angle step for the estimation of the local wetting behaviour X_β and contact angle θ_β. This gives the local extension and the geometry of the rivulet. Accordingly, when the film is not able to completely cover the exchange surface of the tube, energy and species transport equations are solved, applying the same boundary and initial conditions, inside the two-dimensional domain identified by the average rivulet thickness (eq. 5.1) and the angular stream-wise position; then the values of heat and mass transfer coefficients are adjusted taking into account the reduction of the transfer interfaces. Eq. 5.1 is extracted as the average thickness of the rivulet local cross-section of a circular segment shape, cutting the solid tube wall with an angle equivalent to the contact angle $\theta_{0,\beta}$.

$$\delta_{\beta,riv,av} = \frac{\delta_\beta \left(\frac{\theta_{0,\beta}}{2} - \frac{1}{2}\sin\theta_{0,\beta}\cos\theta_{0,\beta} \right)}{\left(X_\beta f(\theta_{0,\beta}) \right)^{1/3} \sin^{2/3}\theta_{0,\beta}} \tag{5.1}$$

Where $f(\theta_{0,\beta})$ is defined by eq. 4.8. To comprehensively model the transfer phenomena occurring inside the absorber, heat transfer with the cooling water inside the tube is estimated by means of the Dittus-Boelter relation, dividing the tube in an axial mesh (where Z is the number of nodes, singularly identified by the k index). Every axial tube position is characterised by inlet and outlet values of cooling water temperature and by a single value of wall temperature, establishing the wall boundary condition for energy equation solved in the film numerical domain outside the tube.

Cooling water heat transfer is coupled with the film heat and mass transfer through the heat flux across the wall at the same axial position q_k. Cooling water heat balance (eq. 5.2) gives the outlet temperature $T_{co,k}$ which constitutes the inlet value for the next axial tube position $T_{ci,k+1}$.

The convergence of the solution method towards a single value of outer tube wall temperature and a specific value of the global heat flux for that axial position on the tube q_k requires an iterative procedure (see the calculation flow diagram in Fig. 5.2).

$$h_{co,k} = h_{cin,k} + \frac{q_k}{m_c} \tag{5.2}$$

The overall heat transfer coefficient U is expressed by eq. 5.3.

$$U = \left[\frac{1}{\alpha_c} + \frac{r_c}{k_w} \ln\left(\frac{r}{r_c} \right) \right]^{-1} \tag{5.3}$$

Where the heat transfer coefficient with the cooling water inside the tube α_c is calculated by using the Dittus-Boelter relation (eq. 5.4).

$$\alpha_c = 0.023\,\mathrm{Re}_c^{0.8}\,\mathrm{Pr}_c^{0.4}\,\frac{k_c}{2r_c} \tag{5.4}$$

The schematic concept of the model is represented qualitatively by figure 5.1.

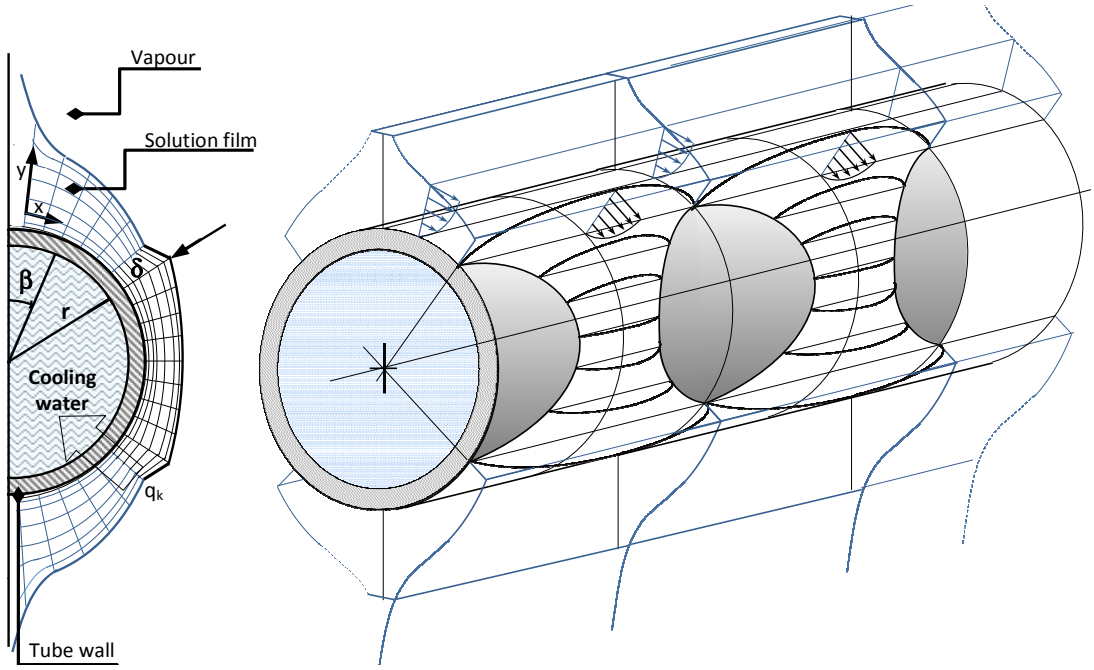

Fig. 5.1 Model of a single falling film-absorber tube

Finally, wall temperature can be calculated by integrating the heat transfer equation for cross-flow heat exchangers which makes use of a mean logarithmic temperature difference (eq. 5.5).

$$T_{w,k} = \frac{T_{cin,k}\, e^{\frac{2U\pi rL}{q_k Z}\left(T_{cin,k} - T_{co,k}\right)} - T_{co,k}}{e^{\frac{2U\pi rL}{q_k Z}\left(T_{cin,k} - T_{co,k}\right)} - 1} \tag{5.5}$$

A curvilinear coordinate transformation is adopted in the same way described in Chapter 3, to map the actual computational space from the physical flow domain to a simple rectangular domain. Dimensionless variables, $\varepsilon = \beta/\pi$ and $\eta = y/\delta$, are considered, respectively, in the circumferential and radial directions. The solution is approached using the same kind of cosine type calculation grid, and finite difference schemes matches those presented in chapter 3 (eq.s 3.14-3.18).

Solution properties are calculated for the inlet values of temperature, pressure and concentration, with the following references: density and diffusivity of water vapour [東京ガスの資料], saturation temperature and enthalpy [ASHRAE Handbook - Fundamentals (2005)], viscosity [新版・第 6 版　冷凍空調便覧 I巻, (2010)], thermal conductivity [ASHRAE Trans., 1990] and surface tension [日本物性学会編, 新編 熱物性ハンドブック, 養賢堂, (2008) 出展記述なし].

The calculation technique is represented by the block diagram displayed in figure 5.2.

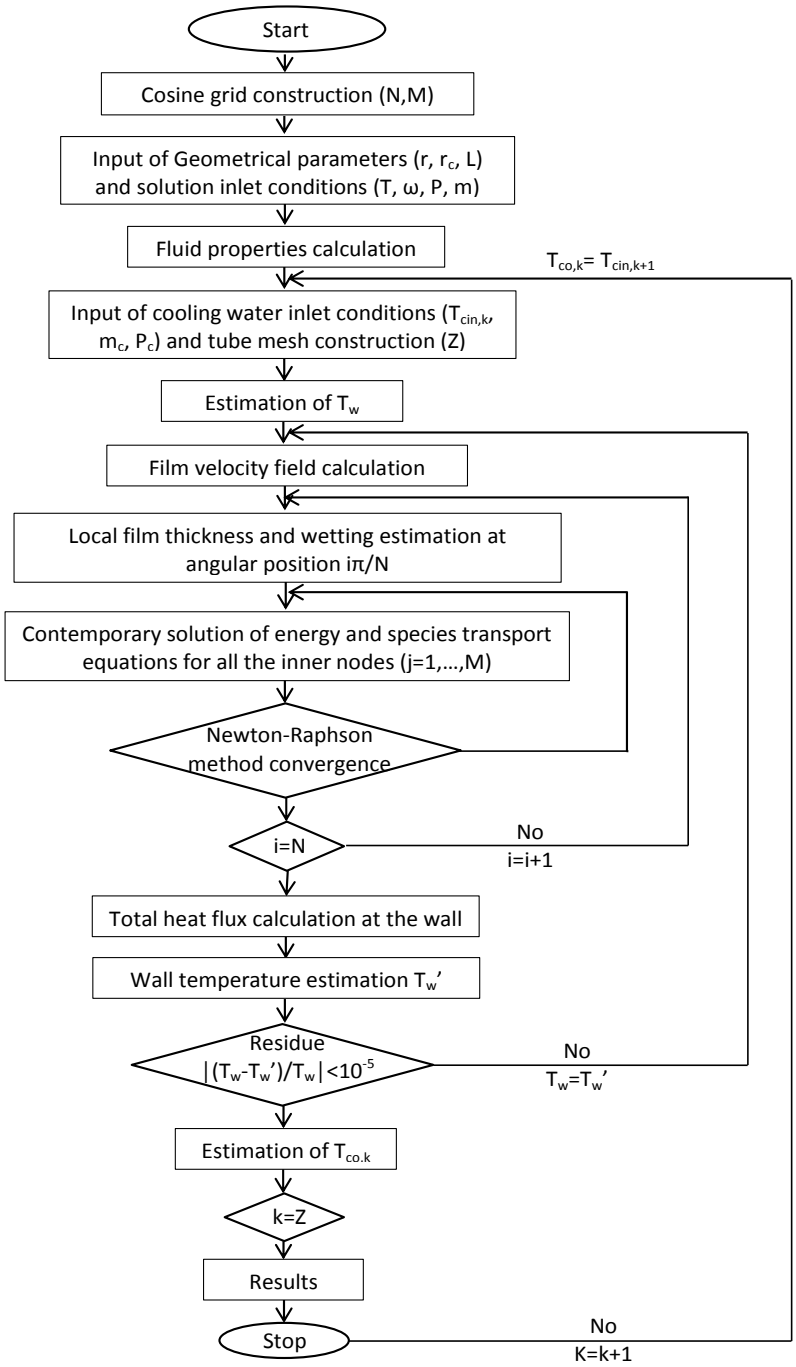

Fig. 5.2 Flow diagram of the calculation method

5.2 Local results

As a case of technical interest, the analysis is carried out for representative operative conditions of an absorber operating as a component of a LiBr-water heat transformer; 95℃ solution inlet temperature and 60% inlet concentration, 0.0125 $kg{\cdot}m^{-1}s^{-1}$ as a reference value for a low solution mass flowrate, inlet coolant temperature of 80℃, outer tube radius of 9 mm and pressure of 12.5 kPa (continuous lines in the following graphs refer to these reference conditions). A qualitative description of the uniform film configuration velocity field can be referred to figure 3.3 (a) and (b) in both its tangential and normal components for a solution flowrate of 0.045 $kg{\cdot}m^{-1}s^{-1}$. Owing to the equilibrium at the film interface, the solution of the simultaneous heat and mass transfer processes occurring inside the domain is strongly related to the solution inlet conditions as well as to the operative pressure. Since the concentration of 60% is the equilibrium concentration at about 96° C and the inlet solution is slightly sub-cooled, the absorption process starts as soon as the LiBr-H_2O solution enters the domain.

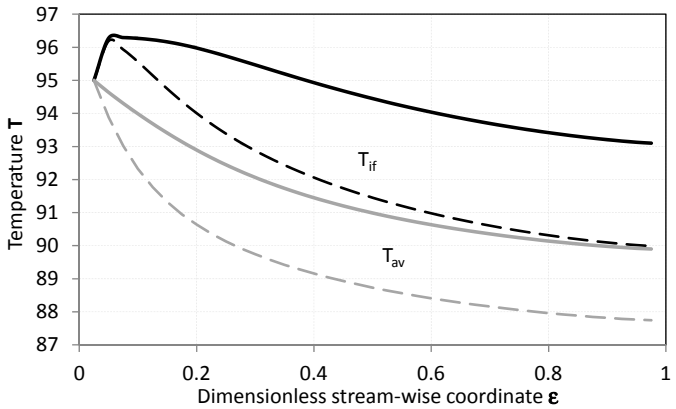

Fig. 5.3 Local interface (black lines) and average (grey lines) temperatures [°C] for the reference conditions and different mass flowrates; 0.03 $kg{\cdot}m^{-1}s^{-1}$ (continuous lines) and 0.01 $kg{\cdot}m^{-1}s^{-1}$ (dashed lines)

Temperature distribution inside the film thickness depends on the combination of interconnected effects related to the heat rejection to the coolant at the wall, vapour absorption rate at the interface and velocity field inside the film. Broadly speaking, some general observations provide the main cornerstones for a proper interpretation of the simulation results. A higher solution sub-cooling at the inlet promotes absorption at the interface, and heat rejected to the cooling water. As the layer thins, the temperature gradient is intensified together with the rate of absorption. The thickening of the film is generally responsible for the opposite effect. A higher flowrate directly intensifies the velocity field of the film, extending the entrance region and convective heat and species diffusion effects, but, at the same time, increases the film thickness.

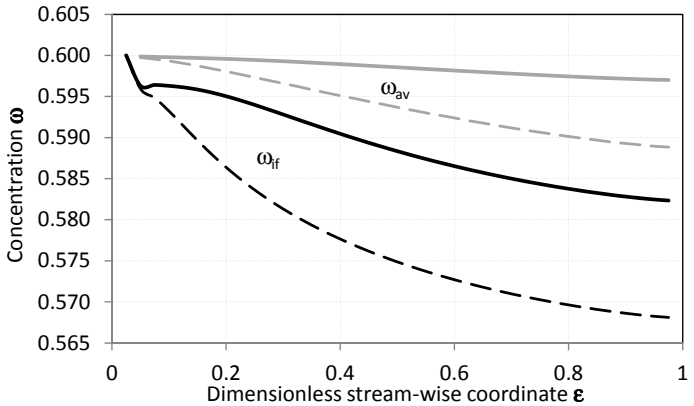

Fig. 5.4 Local interface (black lines) and average (grey lines) emperatures [°C] for the stated conditions and different mass flow rates; 0.03 $kg{\cdot}m^{-1}s^{-1}$ (continuous lines) and 0.01 $kg{\cdot}m^{-1}s^{-1}$ (dashed lines)

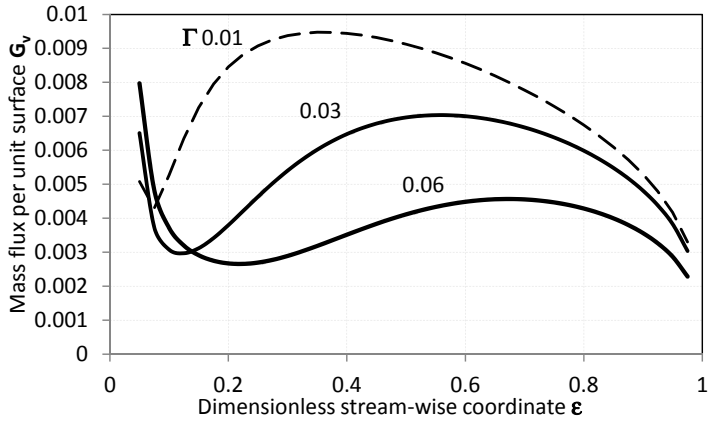

Fig. 5.5 Local mass flux per unit area [kg·s^{-1} m^{-2}] for the reference conditions and different mass flow rates [kg·m^{-1}s^{-1}]

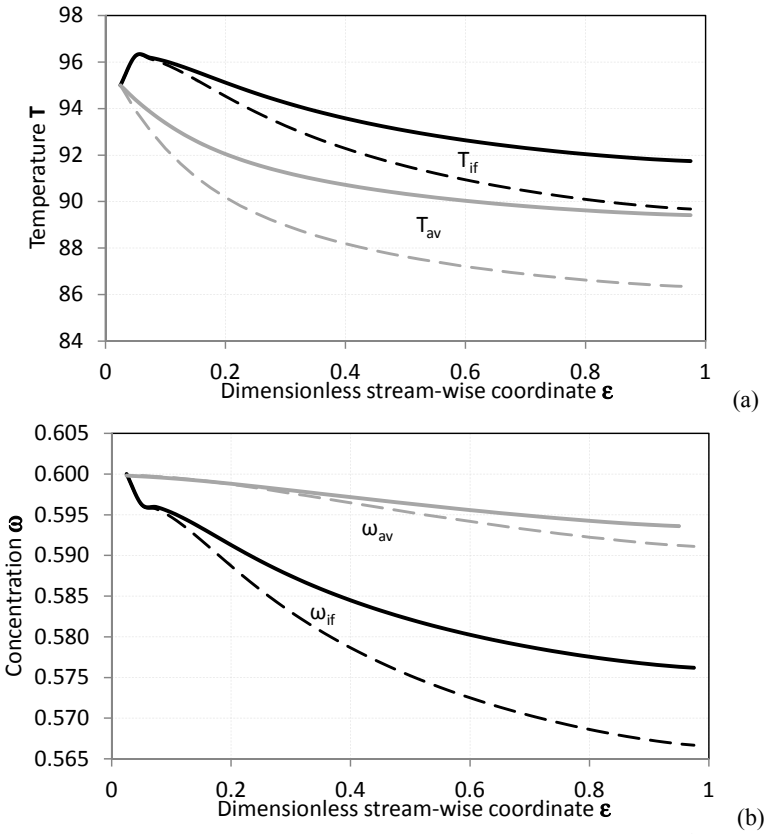

Fig. 5.6 Bulk (grey lines) and interface (black lines) concentrations (a) and (b) temperatures [^{o}C] for different tube wall temperatures; 85^{o}C for continuous lines and 83^{o}C for dashed lines; Γ=0.015 kg·m^{-1}s^{-1}, ω_{in}=60%, T_{in}=95℃, r=9.0mm, p=12.5kPa

The effects of different parameters is analysed to clarify the model ability to describe different phenomena in details. Figure 5.3 compares interface and the bulk temperature distributions for different solution mass flowrates included in the usual operative range of real horizontal tube falling film absorbers. It can be pointed out that, at lower flowrates, the slower and thinner absorptive film is increasingly affected by cooling effect of the water circulating inside the tube. Furthermore, the decrease in the solution bulk temperature is less significant than the one at the interface. This effect is related to the corresponding variation of concentration, which, in turn, is directly dependent on the vapour mass flux at the interface, hence highlighting enhanced mass transfer performance. Independently on the value of the solution

flowrate, figure 5.3 makes evidence of an approximately constant temperature difference between interface and bulk values along most of the tube surface.

Given the interdependent nature of heat transfer at the wall, velocity field and boundary condition of thermodynamic equilibrium at the solution interface for the absorber's vapour pressure, results demand to be explored from multiple points of view; a lower interface temperature constitutes a higher driving force for vapour absorption, and, consistently with first Fick's diffusion law, a higher concentration gradient brings about the same effect. Accordingly, the described influence on the temperature distribution can be related to the corresponding variation of concentration (as shown in Fig. 5.4), which, in turn, is directly dependent on the vapour mass flux per unit area at the interface (Fig. 5.5).

Figure 5.5 illustrate the effect of both a reduction and an increase in the solution mass flowrate on the mass flux per unit area at the film interface. The increasing maximum value of vapour mass flux for decreasing solution mass flow rate can be ascribed mainly to a lower interface temperature at lower flowrates. On the other hand, the increasing distance of the angular position of the local maximum from the inlet at a higher solution mass flowrate is related to the influence of the velocity field on concentration and temperature fields.

The cooling water temperature is a critical parameter for the absorber's optimisation and control, as well as for the whole system performance. Strictly targeting the absorption process, the coupled heat and mass transfer phenomena are strongly related to its value (Fig.s 5.6 and 5.7).

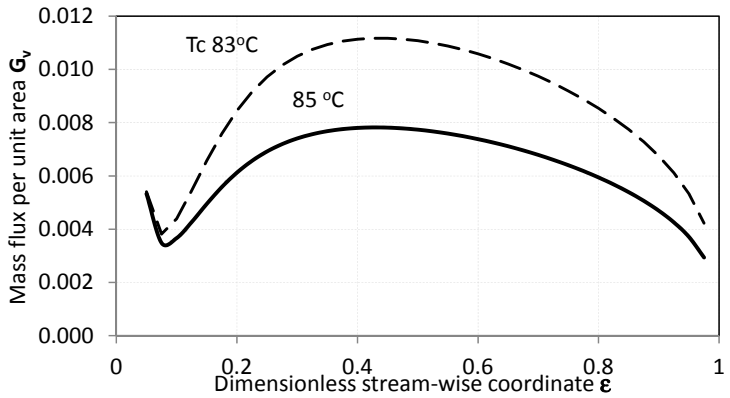

Fig. 5.7 Local mass flux per unit area [kg·s^{-1} m^{-2}] for different tube wall temperatures; 85 °C (continuous line) and 80 °C (dashed line); Γ=0.015 kg·m^{-1}s^{-1}, ω_{in}=60%, T_{in}=95 ℃, r=9.0mm, p=12.5kPa

In general, a lower cooling water temperature enhances both heat and mass transfer (Fig. 5.6 a-b). Contrarily to the effect of a lower solution mass flowrate, the reduction of the cooling water temperature mainly affects the temperature field near the wall region; indeed the decrease in the solution mean temperature is higher than that of the interface value. However, the opposite behaviour can be ascribed to the concentration field (Fig. 5.6b), which is mainly influenced at the interface, while the bulk value of concentration is slightly affected by a lower coolant temperature.

As already pointed out, a lower interface temperature constitutes a higher driving force for vapour absorption and figure 5.7 shows the directly related increase in the maximum value of vapour mass flux.

The effect of different values of the outer tube radius is also examined as a significant geometrical parameter for the process as well as for the overall size and performance of the absorber.

The direct consequences of a downsized tube are lower heat and mass transfer interfaces and a smaller flowing time of the solution, bringing about, globally, lower heat and mass transfer. This is not valid, ceteris paribus, for the cooling water circulating inside the tube, which experiences an enhancement of the heat transfer performance when the tube internal radius is reduced. As a result, a compromising optimal solution can be bordered by these two conflicting effects.

Contrarily, both local heat and mass transfer coefficients of the film outside the tube seems to be are slightly affected.

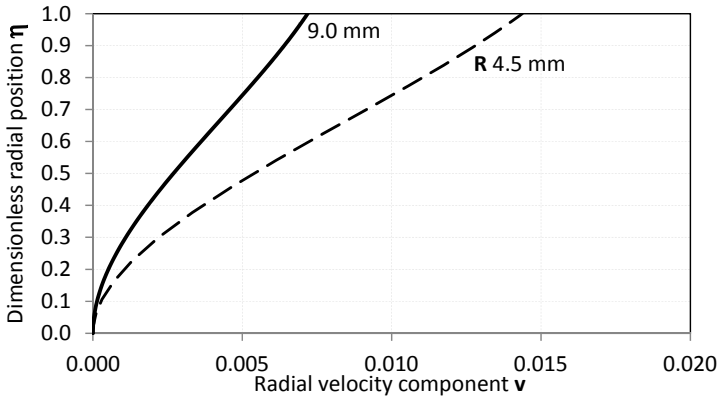

Fig. 5.8 Normal velocity distribution [m·s^{-1}] at ε=N-1/N for two different outer tube radius; 9mm (continuous line) and 4.5mm (dashed line); Γ=0.015 kg·m^{-1}s^{-1}, ω_{in}=60%, T_{in}=95 ℃, T_c=80 ℃, p=12.5kPa

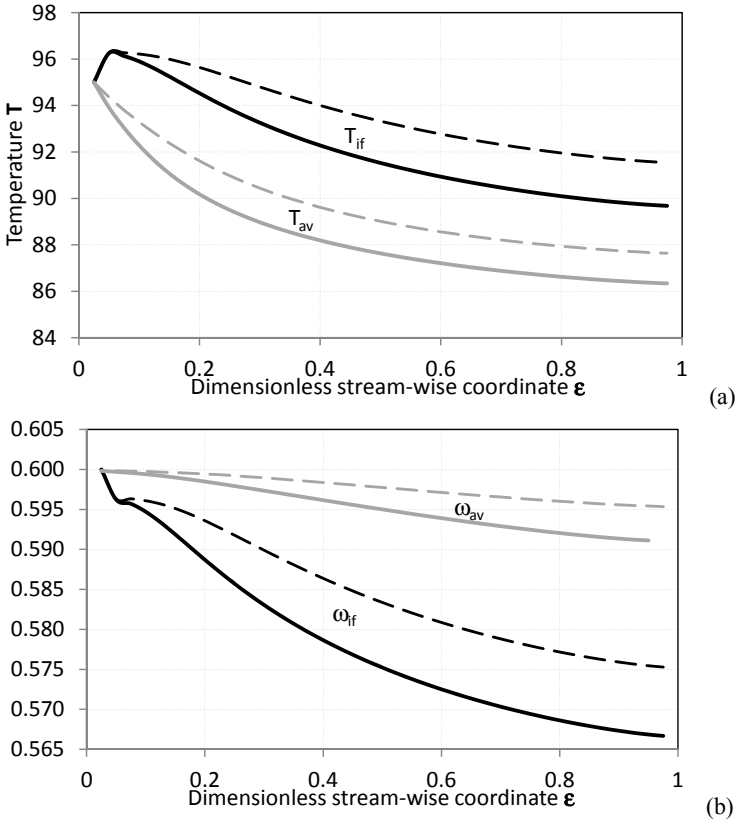

Fig. 5.9 Bulk (grey lines) and interface (black lines) concentrations (a) and temperatures (b) for two different outer tube radius; 9mm (continuous lines) and 4.5 mm (dashed lines); Γ=0.015 kg·m^{-1}s^{-1}, ω_{in}=60%, T_{in}=95 ℃, T_c=80 ℃, p=12.5kPa.

When this geometrical parameter is studied in its influence on temperature and concentration distributions, an analogy in their response to such a change is suggested. A higher radius decreases in parallel temperature and concentration in both their interface and bulk values. Furthermore, the value at the interface is the most affected for both temperature (Fig. 5.9a) and concentration (Fig. 5.9b). However, the driving difference between interface and bulk temperatures is not affected, while the difference between the corresponding values of concentration is higher for higher tube radii.

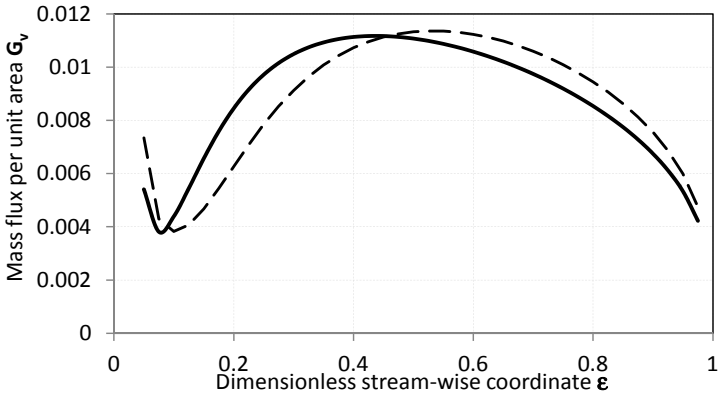

Fig. 5.10 Local mass flux per unit area [kg·s^{-1} m^{-2}] for two different outer tube radius; 9mm (continuous line) and 4.5 mm (dashed line); Γ=0.015 kg·m^{-1}s^{-1}, ω_{in}=60%, T_{in}=95 ℃, T_c=80 ℃, p=12.5kPa

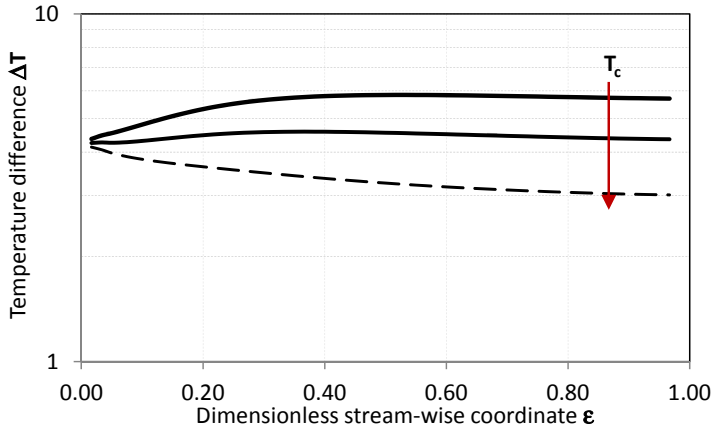

Fig. 5.11 Temperature difference [^{o}C] (between interface and bulk values) distribution for different cooling water temperature: 80 ℃, 85 ℃ and 90 ℃. Γ=0.05 kg·m^{-1}s^{-1}, ω_{in}=60%, T_{in}=95 ℃, r=9mm, p=12.5kPa

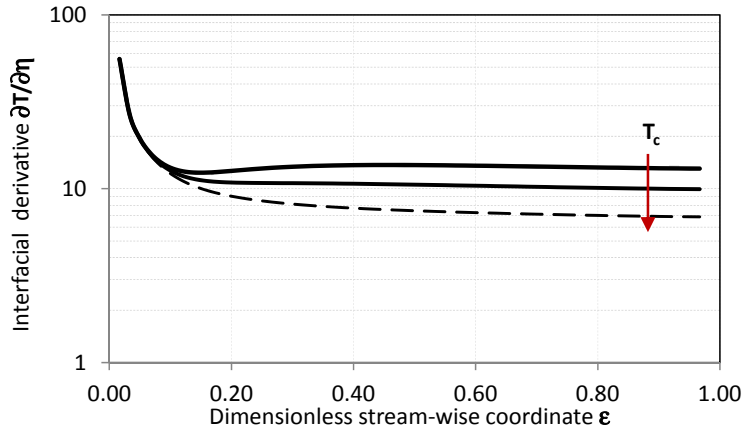

Fig. 5.12 Temperature radial derivative [^{o}C] at the interface for different cooling water temperature: 80 ℃, 85 ℃ and 90 ℃. Γ=0.05 kg·m^{-1}s^{-1}, ω_{in}=60%, T_{in}=95 ℃, r=9mm, p=12.5kPa

Simulation results highlight some characteristic features of the temperature field: temperature distribution in radial direction gradually approaches a linear trend. In fact, at sufficiently low solution flowrates, the radial distribution appears to be nearly linear for the major part of the stream-wise extension of the tube. After the entrance region (the extent of which is strongly dependent of the solution flowrate), the temperature gradient at the interface is almost constant. Temperature difference between interface and bulk values shows a variation along the tube surface below

10 % (Fig. 5.11). Figure 5.12 presents the radial temperature derivative at the interface for different cooling water temperatures.

Except for the absorber pressure, the main influence on the values of temperature difference between interface and bulk values and temperature radial derivative at the interface is related to the coolant temperature and to the mass flowrate. Furthermore, a parametric study of these two parameters suggests an approximately constant value along the tube surface except for the entrance region.

When the film uniformly wets the tube surface, the local heat transfer coefficient is calculated according to eq. 5.6, whereas, when the film is broken eq. 5.7 is used.

$$\alpha = \frac{k \left.\frac{\partial T}{\partial y}\right|_w}{T_{av} - T_w} \tag{5.6}$$

$$\alpha = X_\beta \frac{k \left.\frac{\partial T}{\partial y}\right|_w}{T_{av} - T_w} \tag{5.7}$$

Solution bulk properties are calculated according to eq. 5.8.

$$\Phi_{av} = \frac{\int_0^{\delta_\beta} \Phi u dy}{\int_0^{\delta_\beta} u dy} \tag{5.8}$$

Similarly, the mass transfer coefficient is estimated according to eq.s 5.9 and 5.10.

$$mtc = -\frac{D}{\omega_{if}} \frac{\left.\frac{\partial \omega}{\partial y}\right|_{if}}{\omega_w - \omega_{if}} \tag{5.9}$$

$$mtc = -X_\beta \frac{D}{\omega_{if}} \frac{\left.\frac{\partial \omega}{\partial y}\right|_{if}}{\omega_w - \omega_{if}} \tag{5.10}$$

The importance of the inclusion of partial wetting effect can be first highlighted at a local scale;

When the film breaking is ignored and other conditions are kept constant, a reduction in the solution mass flowrate brings about the reduction of bulk film temperature together with a thinner film, which directly causes higher heat transfer coefficients at the wall, lower interfaces temperatures and higher mass fluxes at the free surface. Furthermore, for sufficiently low flowrates, the local distribution of the heat transfer coefficient makes evidence for the occurrence of a local maximum mainly related to the dominant effect of a minimum film thickness. Contrarily, at higher solution flowrates the influence of film thickness reduction in the first half of the tube surface is overwhelmed by the effect of the flow field and no local maximum occurs. These observation points out that, without considering partial wetting at

low Reynolds number, heat transfer coefficient would increase constantly because of a decreasing heat transfer resistance related to the film thickness wearing thin. Also the mass transfer coefficient would be greatly overestimated.

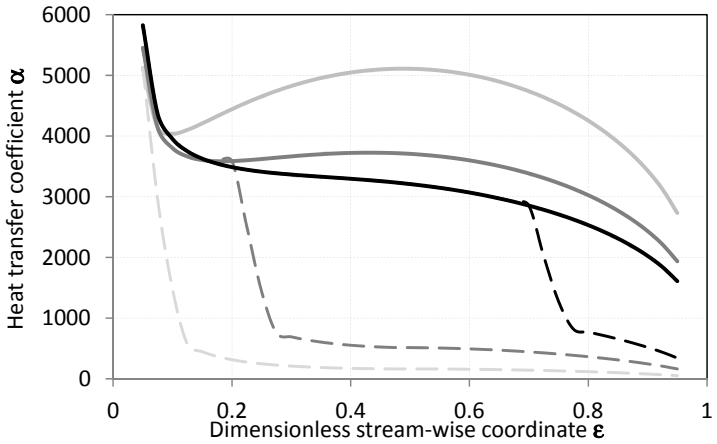

Fig. 5.13 Local heat transfer coefficient [$W \cdot K^{-1}\ m^{-2}$] for the reference inlet and pressure conditions at different mass flow rates; 0.06 $kg \cdot m^{-1}s^{-1}$ (black lines), 0.03 $kg \cdot m^{-1}s^{-1}$ (dark grey lines) and 0.01 $kg \cdot m^{-1}s^{-1}$ (light grey lines); continuous lines for uniform film and dashed lines consider the effect of partial wetting

Owing to the film break up, besides the direct reduction of the surface taking part in heat and mass transfer, the increase of the local film thickness and the velocity redistribution, reduces temperature and concentration gradients, indirectly diminishing local heat and mass transfer coefficients.

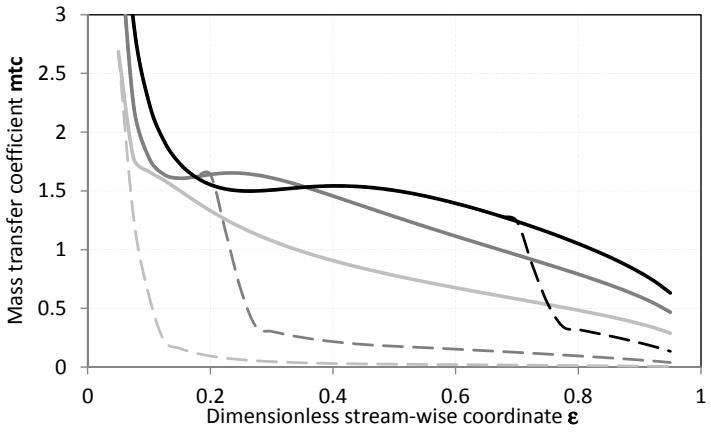

Fig. 5.14 Local mass transfer coefficient [$m \cdot h^{-1}$] for the reference inlet and pressure conditions at different mass flow rates; 0.06 $kg \cdot m^{-1}s^{-1}$ (black lines), 0.03 $kg \cdot m^{-1}s^{-1}$ (dark grey lines) and 0.01 $kg \cdot m^{-1}s^{-1}$ (light grey lines); continuous lines for uniform film and dashed lines consider the effect of partial wetting

Figures 5.13 and 5.14 present, respectively, local heat transfer and mass transfer coefficient distributions for different film flowrates and compare uniform film results (continuous lines) with the broken film ones (dashed lines).

5.3 Average heat and mass transfer coefficients

In order to map extensively heat and mass transfer coefficients of falling film absorbers, average values for the entire tube are calculated in a wide range of Reynolds. Simulations are performed for three typical operative temperatures, in order to cover operative conditions of different applications.

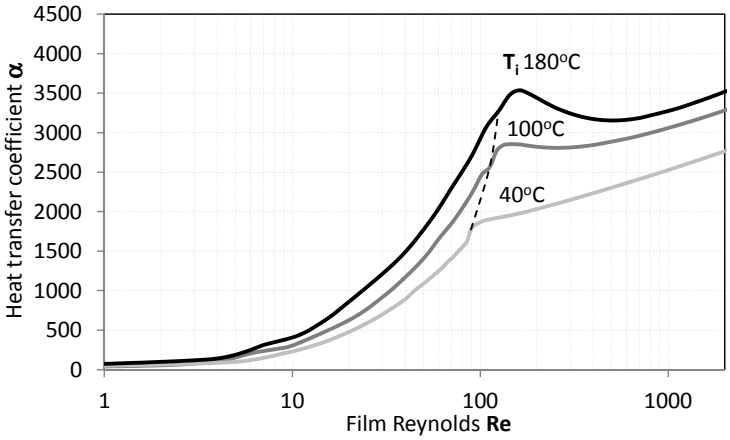

Fig. 5.15 Average tube heat transfer coefficient [$W \cdot K^{-1}\ m^{-2}$] for different solution and absorber conditions as functions of Reynolds number; 42℃ and 60% LiBr, 95℃ and 60% LiBr, 175℃ and 63% LiBr

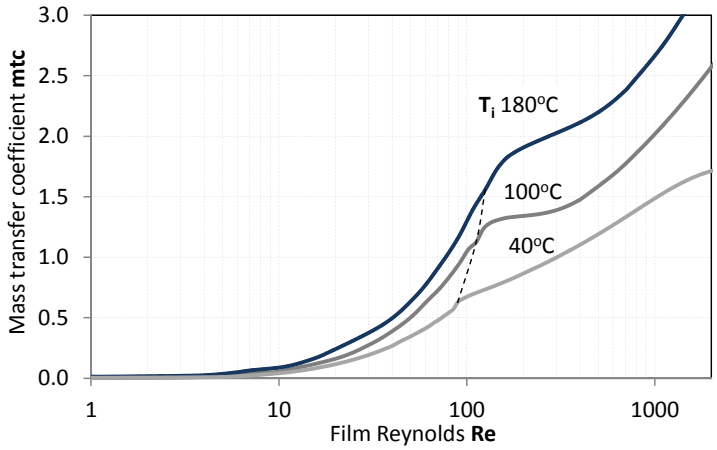

Fig. 5.16 Average tube mass transfer coefficient [$m \cdot h^{-1}$] for different solution and absorber conditions as functions of Reynolds number; 42℃ and 60% LiBr, 100℃ and 60% LiBr, 180℃ and 63% LiBr

Three main regions, mainly characterised by different hydrodynamic effects, can be accordingly identified:

- Partial wetting region (low Reynolds)
- Uniform laminar film region, in which film thickness has the main influence on heat and mass transfer (intermediate Reynolds)
- Uniform film dominated by velocity field effects (high Reynolds)

Figure 5.15 highlights that higher solution temperatures correspond to higher heat transfer coefficients. Furthermore, at high temperature operability, the influence of partial wetting ceases before α begin to increase regularly at high Reynolds for the dominant effect related to the velocity field. Accordingly, when the film is uniform at the critical condition before the break up and the occurrence of partial dry out of the exchange surface for lower delivered flowrates, the heat transfer process takes advantage of the minimum film thickness and a relative maximum of α appears. Contrarily, for low solution temperatures the partial wetting region covers a wider range of mass flow rates and the heat transfer coefficient is characterised by a relentlessly increasing trend with respect to Reynolds. The use of surfactants, in order to improve the wetting ability of the solution film, would reduce the extension of the partial wetting region, increasing that of the uniform film, thus creating the circumstance for the existence of a local maximum heat transfer coefficient also at lower temperature operability. Considering the tubes at the top of the bundle, the solution distribution could be enhanced by a proper design of the distributor.

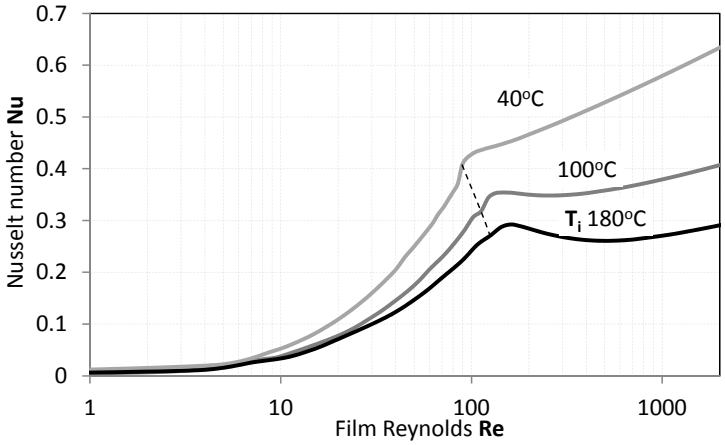

Fig. 5.17 Average tube Nusselt number for different solution and absorber conditions as functions of Reynolds number; 42℃ and 60% LiBr, 100℃ and 60% LiBr, 180℃ and 63% LiBr

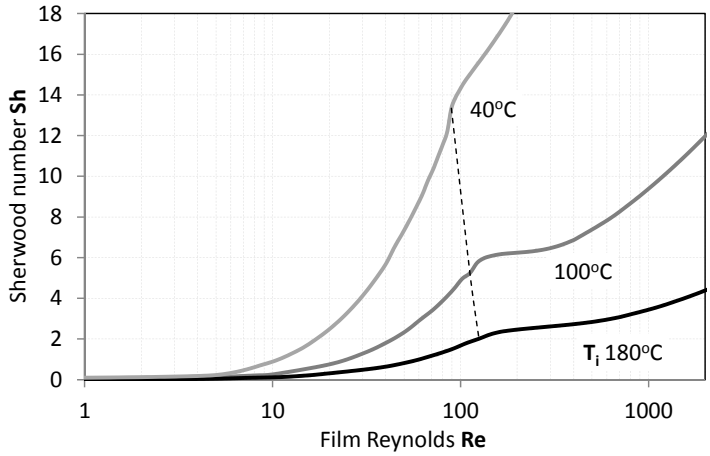

Fig. 5.18 Average tube Sherwood number for different solution and absorber conditions as functions of Reynolds number; 42℃ and 60% LiBr, 100℃ and 60% LiBr, 180℃ and 63% LiBr

A similar behaviour is followed by the mass transfer coefficient, represented in figure 5.16, but, in the transition from the region of reduced wetting to the complete covered surface, a persistently increasing trend is shown.

Figures 5.17 and 5.18 represent the absorber heat and mass transfer maps in their dimensionless form, namely, Nusselt and Sherwood numbers.

5.4 Comparison with experiments from literature

Experimental works on absorption process have been usually performed in multiple-tubes component (not usually instrumented for the local evaluation of heat and mass transfer coefficients), for a reduced range of Reynolds number and, in general, for low temperature operative conditions.

Multi-factorial experimental data from V. M. Soto Francés and J. M. Pinazo Ojer (2003) [109] are used as a reference for a first comparison with the present model. Simulations are performed by setting the operative conditions consistently with those of the experiments, and compared with these data in figures 5.19 (a) and (b).

Simulation results agree both qualitatively and quantitatively with experiments in the low Reynolds region, making evidence of the necessity to consider partial wetting for absorbers' modelling procedures. The intermediate Reynolds region can be compared with experimental data of vertical tube falling film absorbers reported by K.J. Kim et al. (1995) [120] in similar solution operative conditions. According to their study, for Reynolds between 50 and 130, measured

Nusselt and Sherwood numbers increase, respectively, between 0.3 - 0.5 and 4 - 8. While heat transfer evaluation agrees with the experiments also in this range (Fig. 5.19b), mass transfer seems to be globally over estimated.

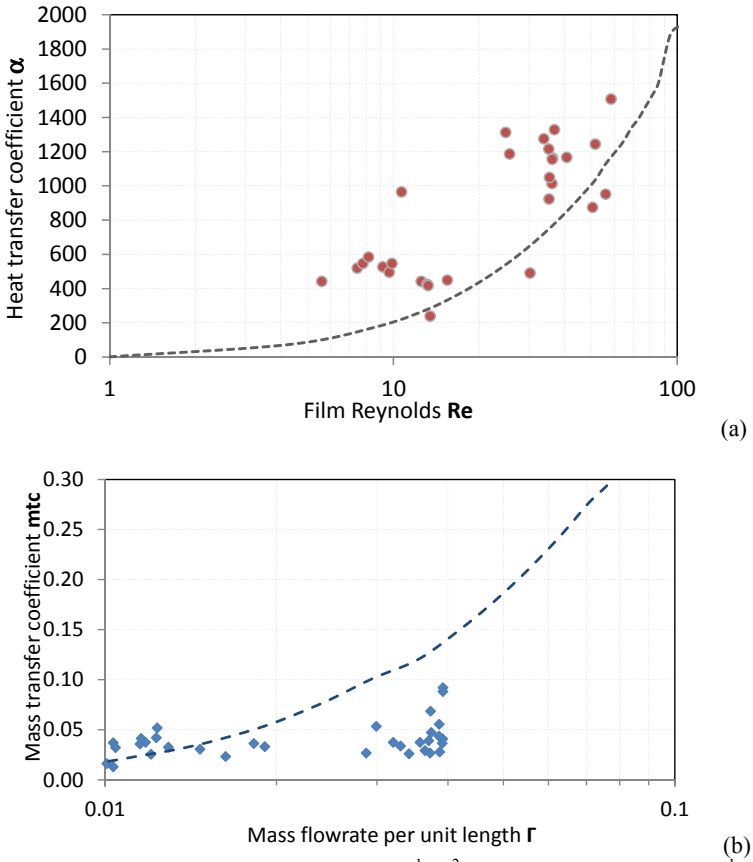

Fig. 5.19 Experimental comparison of heat transfer [$W \cdot K^{-1} m^{-2}$] (a) and mass transfer [$m \cdot h^{-1}$] (b) coefficients

5.5 Summary

As a conclusion for this chapter, results obtained can be summed up to general statements: as a whole, a detailed and widely applicable heat and mass transfer characterisation is required in order to optimise absorption systems performances and control their operability in an extended range of conditions.

From a strictly theoretical point of view, working with reduced solution mass flowrates would be highly beneficial. However, practical analysis should consider the occurrence of partial wetting as a conflicting effect. If this hydrodynamic phenomenon is included in the simulation of absorption transfer performance the accuracy of the results can be improved and their validity can be extended.

The semi-theoretical model for partial wetting of a horizontal tube developed in the previous chapter has been coupled with the physical model for absorption of a falling film and heat transfer with the cooling water circulating inside the tube. The film thickness distribution and the velocity field have been calculated from momentum and continuity equations and have been consistently modified in order to consider the redistribution in the broken rivulet configuration. The model for falling film heat and mass transfer has been based on the numerical solution of energy and species transport equations in a two dimensional domain which consider different local thickness values accounting for velocity field and partial wetting.

The influence of geometrical and operative parameters on heat and mass transfer has been explored in order to describe in detail the absorption process, improve its fundamental understanding and estimate the resolution power of the model.

By the implementation of the model in a wide range of Reynolds number and for different solution temperatures extended heat and mass transfer coefficients maps have been obtained and studied. Three different regions mainly characterised by different hydrodynamic effects can be identified:

- Partial wetting region
- Uniform laminar film region, in which film thickness has the main influence on heat and mass transfer
- Uniform film mainly subject to velocity field effects

Though incomplete, the comparison of the model with experiments from previous works gives promising agreement.

The single tube model can be employed as a module for global component and system simulations in order to optimise their performances and control their operability in an extended range of conditions.

Chapter 5,
Heat and mass transfer characteristics of absorptive falling film on a partially-wetted horizontal tube

Chapter 6, Extended range analytical expression of heat and mass transfer coefficients

As a closing modelling effort, this chapter articulates, slims down and canalises the understanding developed in the previous chapters in a detailed, widely applicable and time-saving method for predicting heat and mass transfer characteristics of horizontal tube film absorbers. Based on the foregoing numerical, theoretical and experimental studies, simplifying assumptions are introduced in order to analytically solve the coupled set of fundamental equations. As demonstrated so far, a two-dimensional model is able to capture the physics of the phenomenon. As demonstrated so far, since falling operability at low Reynolds number is attractive to increase absorption system performance and reduce their overall size, the reduction of transfer interfaces area due to partial wetting demands to be included in the model. By means of the inclusion of a film stability criterion and a linear wetting model, partial wetting phenomena are incorporated in the analysis extending the target range of the resulting heat and mass transfer coefficients expressions and increasing their accuracy. A first comparison with the numerical solution is also presented to validate the simplifying assumptions introduced.

6.1 Closed-form solution of film mass-transfer on a partially wetted absorber tube

As a first step, aiming at expressing the corresponding mass transfer coefficient in a closed form valid for an extended range of operative conditions, the interest is limited to a single side of the problem. A closed solution which takes into account the effect of incomplete wetting of the exchange surface for the gas absorption process of a laminar, gravity driven film, flowing over a horizontal tube is sought for. The species transport equation is solved for horizontal tube geometry. Small penetration for physical absorption hypothesis and constant heat flux boundary condition are introduced to reach a closed solution.

The film stability criterion for the identification of the breaking condition can be based on the energy-minimisation principle or directly related to experimental data, and the model describing partial wetting is abridged to linear distribution with reference to film Reynolds. Using a modified form of the Nusselt equation the film thickness distribution is adjusted in order to assure continuity between uniform and partial wetting. Finally, mass transfer coefficient and absorbed mass flux are expressed as functions of the leading dimensionless groups and a parametric analysis is performed to perform a first screening of the results and clarify the process. Results agree with previous numerical solution, can be used generally for different fluids, and, eventually, for actual system design and control. On the other hand, the necessity of establishing the absorption heat flux at the interface as a given boundary condition is problematic and, as a matter of fact, requires detailed information about the mirroring side of the problem, namely heat transfer and temperature distribution.

The system under consideration is exemplified schematically by figure 6.1. A single horizontal tube is considered. A thin film of LiBr-H_2O solution impinge the top of the tube (x=0) and flows down over it driven by gravity as a laminar incompressible liquid. In the meantime, vapour absorption takes place at the film interface.

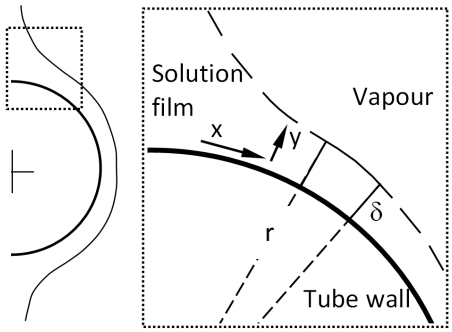

Fig. 6.1 Local coordinate system of the falling film

Mass transfer characteristics are considered under the following main assumptions: the impingement zone is supposed to be a small fraction of the total periphery. The flow is laminar and waveless at the interface [121], where shear force between the liquid film and the vapour, as well as interfacial mass transfer resistance are also overlooked. Physical solution properties remain constant as the film flows. The variation of the film flowrate due to the absorbed vapour is considered to be small enough to be neglected. According to the thin film approximation (the film thickness is small if compared to the tube diameter) introduced by G. Kocamustafaogullari (1985) [121], body fitted coordinates (x along the tube surface and y normal to it at any point) are used. The momentum equation is solved under Nusselt integral solution (eq. 3.2) hypotheses for a laminar film over a horizontal tube and the radial component of the velocity distribution (eq. 3.4) can be determined from the integration of the continuity equation. To map the flow domain of the physical space to a simple rectangular domain, the same curvilinear coordinate transformation introduced in chapter 3 is adopted [77], hence, the dimensionless variables considered in the circumferential and radial directions are, respectively, $\varepsilon=x/\pi r$ and $\eta=y/\delta$.

In order to include the effect of partial wetting at low Reynolds number, the extension of this region is estimated by experimental data for the break-up specific flowrate Γ_0 of continuous film from D.M Maron et al. (1982) [92]. A fitting relation describing the critical Reynolds number Re_0 (eq. 6.1) at which film breaking occurs, is expressed as a function of Galileo number ($Ga=\rho\sigma^3/\mu^4 g$), whereas, for lower values of Reynolds number a simplified linear wettability model (eq. 6.2) is applied. Linear wetting behaviour agrees with methods based on energy minimisation approach [99].

$$\mathrm{Re}_0 = 34.1 Ga^{0.051} \tag{6.1}$$

$$WR = \frac{\mathrm{Re}}{\mathrm{Re}_0} \tag{6.2}$$

Where WR represents the basic parameter to describe the wet part of the tube surface. Alternatively, the critical condition can be referred to the theoretical expression from the direct application of the energy minimisation principle to a plain surface (eq. 4.38). Furthermore, a closed analytical solution requires considering WR as an independent function of the angular position β (WR, as an average global parameter, also correspond to the local value since it is considered to be a constant along the tube surface). Accordingly, given the film mass flowrate per unit length Γ, the film thickness distribution is adjusted in order to assure continuity between uniform and partial wetting using a modified form of the Nusselt equation as in S. Jeong anf S. Garimella (2002) [106] (eq. 6.3).

$$\delta = \left(\frac{3\mu\Gamma}{WR\rho^2 g \sin\pi\varepsilon} \right)^{1/3} \tag{6.3}$$

For a steady flow with constant properties, the two-dimensional form of species transport equations is given by eq. 6.4.

$$\frac{\partial\omega}{\partial\varepsilon} = \frac{\pi r D}{u\delta^2}\frac{\partial^2\omega}{\partial\eta^2} + \left(\frac{\eta}{\delta}\frac{d\delta}{d\varepsilon} - \frac{\pi r v}{u\delta} \right)\frac{\partial\omega}{\partial\eta} \tag{6.4}$$

Where,

$$\frac{d\delta}{d\varepsilon} = -\left(\frac{\mu\Gamma\pi^3}{9WR\rho^2 g} \right)^{1/3} \frac{1}{\tan\pi\varepsilon \sin^{1/3}\pi\varepsilon} \tag{6.5}$$

For a small penetration distance of the vapour into the falling film thickness and a short contact time (physical absorption), the velocity field can be represented by the corresponding values of tangential and normal components at the interface (η=1). Thus, the velocity field is abridged to eq.s 6.6 and 6.7.

$$u = u_{\max}(\varepsilon) = \frac{\rho g \delta^2}{2\mu} \sin \pi\varepsilon \tag{6.6}$$

$$v = v_{\max}(\varepsilon) = -\frac{\rho g \delta^3}{6\mu r} \cos \pi\varepsilon \tag{6.7}$$

Under these last assumptions, the term in brackets in the form of the species transport equation represented by eq. 6.4 (6.8) is,

$$\left(\frac{\eta}{\delta} \frac{d\delta}{d\varepsilon} - \frac{\pi r v}{u \delta} \right) = (1-\eta) \left(\frac{\pi}{3} \frac{1}{\tan \pi\varepsilon} \right) \tag{6.8}$$

As a result, under the assumption of small penetration distance ($\eta \approx 1$) the following simplified expression is obtained.

$$\frac{\partial \omega}{\partial \varepsilon} = \frac{\pi r D}{u_{\max} \delta^2} \frac{\partial^2 \omega}{\partial \eta^2} \tag{6.9}$$

Developing non-constant terms, and defining the dimensionless diameter $d^+ = 2r/L_c$,

$$\begin{aligned} \sin^{-1/3} \pi\varepsilon \frac{\partial \omega}{\partial \varepsilon} &= \left(\frac{4}{3} \frac{WR}{\mathrm{Re}} \right)^{4/3} \frac{\pi d^+}{Sc} \frac{\partial^2 \omega}{\partial \eta^2} \\ \sin^{-1/3} \pi\varepsilon \frac{\partial \omega}{\partial \varepsilon} &= c^2 \frac{\partial^2 \omega}{\partial \eta^2} \end{aligned} \tag{6.10}$$

Finally, it can be expressed in a dimensionless form, representing the behaviour of the function $\gamma(\varepsilon,\eta) = \omega(\varepsilon,\eta)/\omega_{in}$.

$$\sin^{-1/3} \pi\varepsilon \frac{\partial \gamma}{\partial \varepsilon} = c^2 \frac{\partial^2 \gamma}{\partial \eta^2} \tag{6.11}$$

In order to obtain the concentration field, the problem formulation needs to be closed by consistent boundary conditions. The solution concentration at the distributer or, assuming that a complete mixing occurs, the bulk values of the previous tube is established as the inlet condition at ε=0 and 0<η<1 as γ=1. The boundary condition at the tube surface assures non-permeability of the wall (η=0 and 0< ε<1, $\partial\gamma/\partial\eta$=0). Absorption heat transfer is reduced to a constant value of Biot number *Bi* and the normalised form of the heat of absorption Λ (defined by eq. 6.12) at the interface.

$$\Lambda = \frac{i_{abs}}{c_p \Delta T} \tag{6.12}$$

Temperature gradient at the phases interface η=0 and 0< ε<1) is assumed to be constant and related to the temperature difference between interface and bulk temperatures ΔT ($\partial T/\partial\eta=Bi\Delta T$). This last parameter is considered constant also in other works [106] and numerical results presented previously (see Chapter 5) validate this assumption Consequently, the interface concentration is determined from Fick's law of diffusion combined with the thermal effect of absorption; the heat produced is assumed to be entirely transferred by conduction through the film towards the tube surface:

$$\left.\frac{\partial\gamma}{\partial\eta}\right|_{if}\frac{1}{\gamma_{if}}=-\frac{BiLe}{\Lambda} \tag{6.13}$$

The method of separation of variables is used to find an analytical solution. The method assumes the dependent function to be a product of a number of functions, each being dependent on a single variable.

$$X(\varepsilon,\eta)=E(\varepsilon)H(\eta) \tag{6.14}$$

$$\frac{1}{c^2\sin^{1/3}\pi\varepsilon}\frac{E'}{E}=\frac{H''}{H} \tag{6.15}$$

Considering that both ε and η can be varied independently, the equality between the two sides of eq. 6.15 can hold true for any value of ε and η only if eq. 6.15 is equal to a constant. Further, this latter must be a negative constant in order to obtain a solution which is not constantly zero in the calculation domain.

$$\frac{1}{c^2\sin^{1/3}\pi\varepsilon}\frac{E'}{E}=-\xi^2 \tag{6.16}$$

$$\frac{H''}{H}=-\xi^2 \tag{6.17}$$

Whose general solutions are,

$$E=C_1e^{-\xi^2c^2\int\sin^{1/3}\pi\varepsilon d\varepsilon} \tag{6.18}$$

$$H=C_2\cos(\xi\eta)+C_3\sin(\xi\eta) \tag{6.19}$$

These, combined together as in eq. 6.14 give the general form of the lithium bromide concentration distribution.

$$X=e^{-\xi^2c^2\int\sin^{1/3}\pi\varepsilon d\varepsilon}\left[A\cos(\xi\eta)+B\sin(\xi\eta)\right] \tag{6.20}$$

Where A and B ($A=C_1C_3$, $B=C_2C_3$) are arbitrary constants that can be determined by applying the boundary and initial conditions. The boundary condition at the wall requires that B is null B=0).

$$\left.\frac{\partial\gamma}{\partial\eta}\right|_0=0\rightarrow B=0 \tag{6.21}$$

Under the assumption of constant heat flux at the interface the boundary condition at the film interface gives the characteristic equation, or the set of eigenfunctions (eq. 6.22).

$$\left.\frac{\partial \gamma}{\partial \eta}\right|_{if} \frac{1}{\gamma_{if}} = -\frac{BiLe}{\Lambda} \rightarrow \xi_n \tan \xi_n = \frac{BiLe}{\Lambda} \tag{6.22}$$

The roots of eq. 6.22 are the characteristic values of the solution, or eigenvalues. Since the characteristic equation is implicit in this case, the characteristic values ξ_n need to be determined iteratively. Consequently, the solution is a linear combination of an infinite series of functions with similar form and decreasing influence.

$$\gamma = \sum_{n=0}^{\infty} A_n e^{-\xi_n^2 c^2 \int \sin^{1/3} \pi\varepsilon d\varepsilon} \cos(\xi_n \eta) \tag{6.23}$$

The constants A_n are determined from the boundary condition at the inlet by means of the Sturm-Liouville orthogonality condition.

$$\gamma(0,\eta) = 1 \rightarrow 1 = \sum_{n=1}^{\infty} A_n \cos(\xi_n \eta) \tag{6.24}$$

Multiplying both sides by the term $\cos(\xi_m \eta)$ and integrating in the radial direction, it can be shown that all integrals vanish except when $n=m$.

$$\int_0^1 \cos(\xi_n \eta) d\eta = A_n \int_0^1 \cos^2(\xi_n \eta) d\eta \tag{6.25}$$

$$A_n = \frac{4\sin(\xi_n)}{2\xi_n + \sin(2\xi_n)} \tag{6.26}$$

As a result, the solution can be expressed in its complete form as follows (eq. 6.27).

$$\omega(\varepsilon,\eta) = \omega_{in} \sum_{n=0}^{\infty} \frac{4\sin(\xi_n)}{\left(2\xi_n + \sin(2\xi_n)\right)} \cos(\xi_n \eta) e^{-\xi_n^2 \left(\frac{4WR}{3\,\mathrm{Re}}\right)^{4/3} \frac{\pi d^+}{Sc} \int_0^{\varepsilon} \sin^{1/3} \pi\varepsilon d\varepsilon} \tag{6.27}$$

From the concentration field inside the solution film, the local mass transfer coefficient *mtc* is calculated according to eq. 5.9, whereas the local absorbed mass flux G_v refers to eq. 6.28.

$$G_v = -WR \frac{\rho D}{\delta \omega_{if}} \left.\frac{\partial \omega}{\partial \eta}\right|_{if} \tag{6.28}$$

In order to consider the tube partial wetting, an expression averaged for the tube length is obtained under the assumption that the reduction of the surface taking part to the vapour absorption can be represented by the value of *WR*.

$$Sh=\frac{\dfrac{WR^{4/3}}{\omega_{in}}\left(\dfrac{4}{3}\dfrac{\sin\pi\varepsilon}{\mathrm{Re}}\right)^{1/3}\displaystyle\sum_{n=0}^{\infty}\frac{4\xi_n\sin^2\xi_n}{2\xi_n+\sin(2\xi_n)}e^{-\xi_n^2\left(\frac{4WR}{3\,\mathrm{Re}}\right)^{4/3}\frac{\pi d^+}{Sc}\int_0^{\varepsilon}\sin^{1/3}\pi\varepsilon d\varepsilon}}{\displaystyle\sum_{n=0}^{\infty}\sum_{i=0}^{n}\frac{8\sin(2\xi_i)\sin\xi_{n-i}(1-\cos\xi_{n-i})}{(2\xi_k+\sin(2\xi_i))(2\xi_{n-i}+\sin(2\xi_{n-i}))}e^{-\left(\xi_i^2+\xi_{n-i}^2\right)\left(\frac{4WR}{3\,\mathrm{Re}}\right)^{4/3}\frac{\pi d^+}{Sc}\int_0^{\varepsilon}\sin^{1/3}\pi\varepsilon d\varepsilon}}} \tag{6.29}$$

$$G_v=\frac{WR^{4/3}\rho D}{L_c}\left(\frac{4}{3}\frac{\sin\pi\varepsilon}{\mathrm{Re}}\right)^{1/3}\frac{\displaystyle\sum_{n=0}^{\infty}\frac{4\xi_n\sin^2\xi_n}{2\xi_n+\sin(2\xi_n)}e^{-\xi_n^2\left(\frac{4WR}{3\,\mathrm{Re}}\right)^{4/3}\frac{\pi d^+}{Sc}\int_0^{\varepsilon}\sin^{1/3}\pi\varepsilon d\varepsilon}}{\displaystyle\sum_{n=0}^{\infty}\frac{2\sin(2\xi_n)}{2\xi_n+\sin(2\xi_n)}e^{-\xi_n^2\left(\frac{4WR}{3\,\mathrm{Re}}\right)^{4/3}\frac{\pi d^+}{Sc}\int_0^{\varepsilon}\sin^{1/3}\pi\varepsilon d\varepsilon}}} \tag{6.30}$$

6.2 Parametric analysis

In order to obtain significant results for actual system analysis, a parametric study is to be carried out for typical conditions of a the absorber; in this demonstrating case, 40℃ LiBr-H_2O solution inlet temperature, 60% LiBr inlet concentration and outside pressure of 1.0 kPa. The solution properties are calculated for the inlet values of temperature, pressure and concentration, according to ASHRAE Trans. (1990) [80]. Figure 6.2 qualitatively shows the concentration field solution results. Table 6.1 presents the eigenvalues obtained from the solution at the reference condition (T_{in}=40, ω_{in}=60%, Re=43, Le=110, A=341, Sc=2567 and d^+=181) for different Biot numbers.

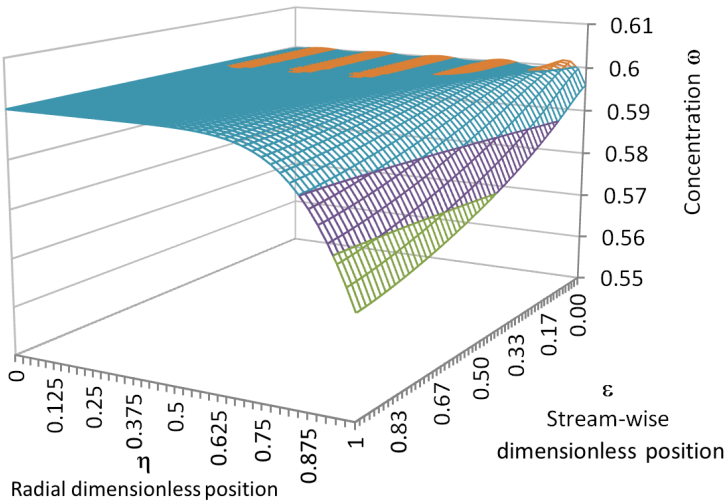

Fig. 6.2 concentration distribution in the 2-dimensional rectangular calculation domain

Figures 6.3 and 6.4 show different concentration distribution obtained for different interface condition in terms of Biot Number. The agreement of present analytical results with previous numerical works supports the simplifying assumptions preliminarily introduced. Figure 6.3 makes evidence that mass transfer boundary layer influences a reduced part of the film thickness (23%), supporting the assumption of small penetration theory. Observing figures 6.3 and 6.4, higher interface Biot number are directly related to, and are meant to represent, higher absorption rates.

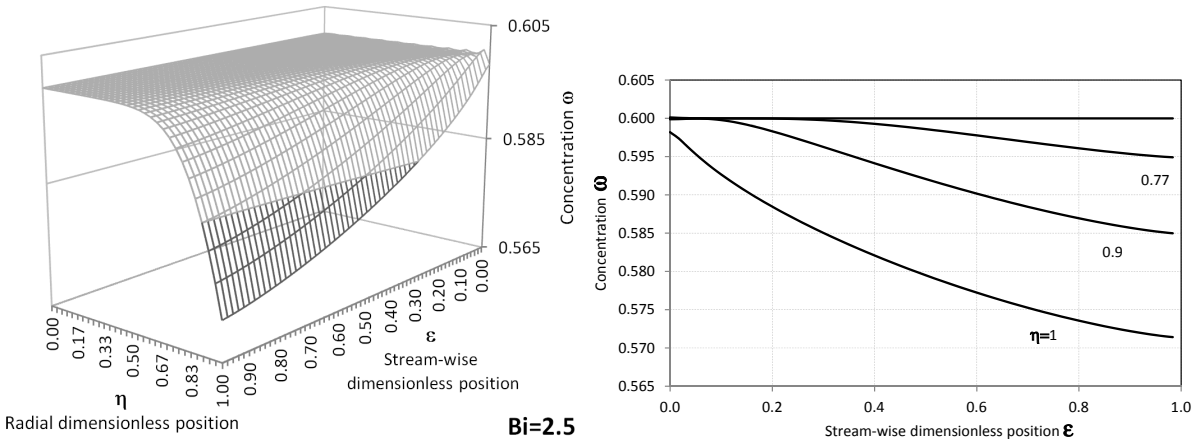

Fig. 6.3 Concentration distribution in the 2-dimensional rectangular calculation domain; Bi=2.5

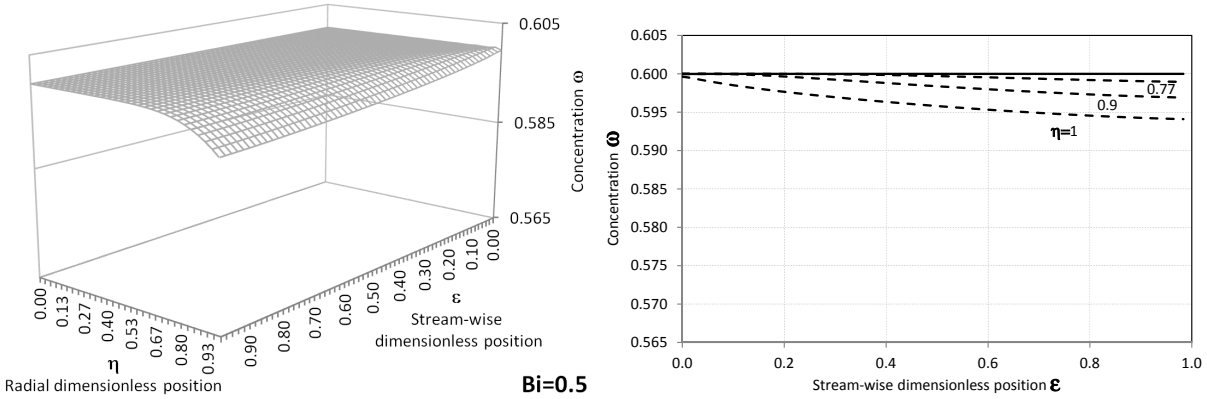

Fig. 6.4 Concentration distribution in the 2-dimensional rectangular calculation domain; Bi=0.5

Table 6.1 First 20 eigenvalues for different values of Biot number;

ξ_n	Bi 0.1	Bi 0.5	Bi 2.5	Bi 12.5
0	0.17921	0.39232	0.79546	1.26796
1	3.15189	3.19240	3.37743	3.94157
2	6.28835	6.30891	6.40915	6.81995
3	9.42822	9.44197	9.50992	9.81678
4	12.5690	12.5793	12.6305	12.8718
5	15.7100	15.7183	15.7594	15.9570
6	18.8513	18.8582	18.8925	19.0593
7	21.9926	21.9985	22.0280	22.1722
8	25.1340	25.1392	25.1650	25.2918
9	28.2755	28.2801	28.3030	28.4162
10	31.4170	31.4211	31.4417	31.5439
11	34.5585	34.5622	34.5810	34.6740
12	37.7000	37.7034	37.7206	37.8060
13	40.8415	40.8447	40.8606	40.9395
14	43.9830	43.9860	44.0007	44.0741
15	47.1246	47.1273	47.1411	47.2096
16	50.2661	50.2687	50.2816	50.3459
17	53.4077	53.4101	53.4223	53.4828
18	56.5492	56.5515	56.5630	56.6202
19	59.6908	59.6930	59.7039	59.7581

Sherwood Number can be calculated locally at the film interface (Fig. 6.5).

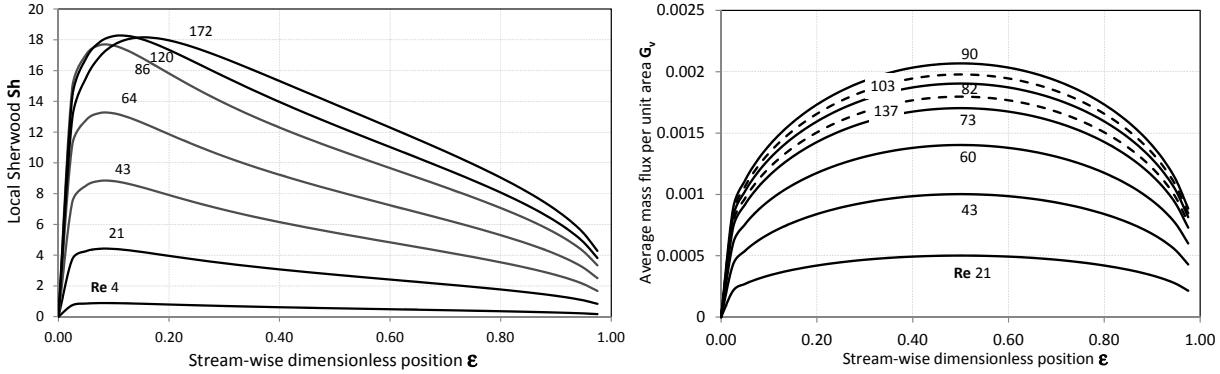

Fig. 6.5 Local distributions of Sherwood Number (a) and mass flux per unit area [kg·s^{-1} m^{-2}] (b) for different Reynolds numbers; Bi=0.1;

An increasing maximum with in increasing Reynolds can be observed in the entrance region, where absorption starts occurring. When Reynolds increases the position of the maximum slightly moves to higher normalised angular positions and after it a monotonous decreasing behaviour is shown.

Average Sherwood Number for different Reynolds Numbers can be compared to the results obtained without considering partial wetting of the tube surface. In the range covered, constantly increasing trend can be observed in both cases, as shown in figure 6.6.

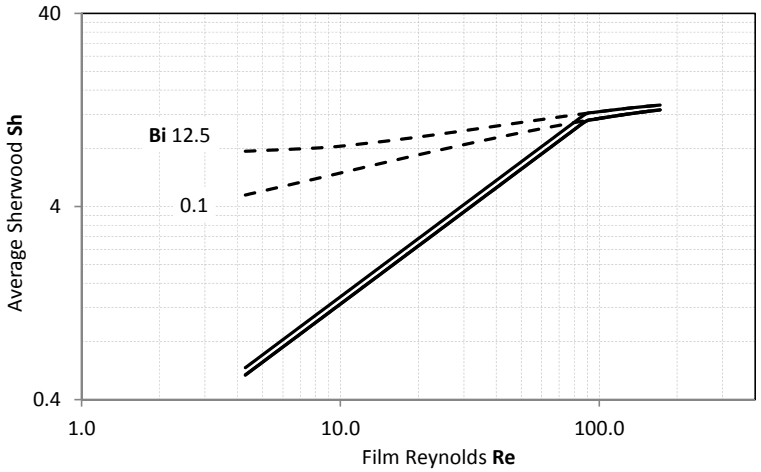

Fig. 6.6 Comparison between uniform film (dashed lines) and partially wetted film (continuous lines) Sh as a function of Re for different Bi.

Considering the proposed partial wetting model, the critical condition of the uniform film, at which breaking occurs and the film has its minimum stable thickness, identifies a maximum value of the absorbed mass flux G_v. The effect of an increasing *Bi* is to globally enhance the absorbed mass flux at the interface (Fig. 6.7). A higher heat flux (otherwise, a greater distance of the solution condition from the thermodynamic equilibrium with the absorbed species) can be related to a stronger influence of internal heat transfer (lower cooling water temperature), which, as renown, reciprocally enhance mass transfer.

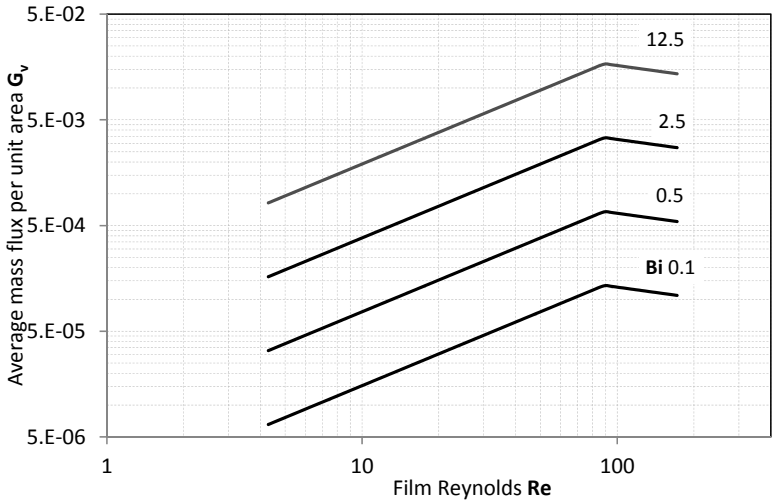

Fig. 6.7 Average mass flux [kg·s^{-1} m^{-2}] per unit area as a function of Reynolds number for different value of Biot number

A reduced tube radius has a similar influence on Sherwood number. However, it doesn't affect the interfacial mass flux.

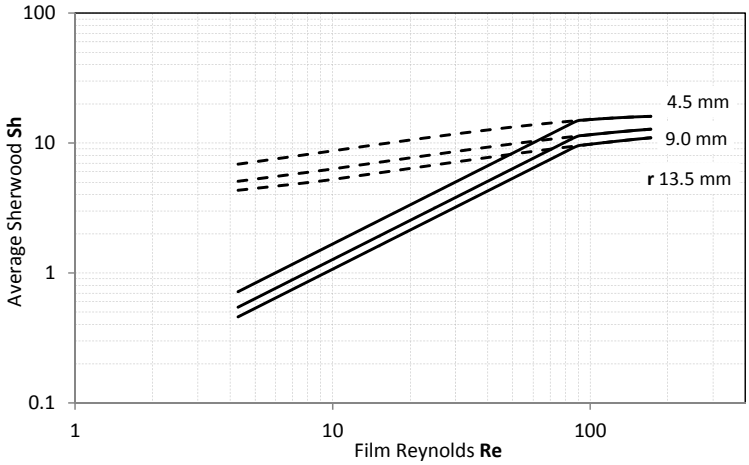

Fig. 6.8 Sherwood number as a function of Reynolds for different tube radii [mm]

With the aim of characterising the effect of Lewis number on the mass transfer solution, different operative conditions are considered.

The followings three values of *Le* refer to typical condition of the absorber for different applications: cooling system absorber, heat transformer absorber, high temperature absorber of a multistage heat transformer. Table 6.2 presents the eigenvalues obtained for these representative Lewis values. Observing figure 6.9, a local minimum characterises the uniform film solution when the calculation range is extended to very low value of solution mass flow-rate, and the occurrence of this minimum moves to higher Reynolds for decreasing Lewis numbers. This behaviour can be explained considering that, reducing the solution flowrate, the penetration distance of the diffusing species reach the tube wall. As a consequence, the mass transfer coefficient increases because of the reduction of the concentration difference between the value at the interface and that at the wall. This behaviour is conflicting with the assumption of small penetration theory. On the other hand, such low values of solution mass flowrate are, in general, outside of the practical range of operative conditions.

Table 6.2 First 20 eigenvalues for different values of Lewis number;

ξ_n	Le 110	Le 38	Le 16
0	0.79546	0.51326	0.34174
1	3.37743	3.23089	3.17980
2	6.40915	6.32886	6.30247
3	9.50992	9.45536	9.43766
4	12.6305	12.5893	12.5760
5	15.7594	15.7264	15.7157
6	18.8925	18.8649	18.8560
7	22.0280	22.0043	21.9967
8	25.1650	25.1442	25.1376
9	28.3030	28.2846	28.2786
10	31.4417	31.4251	31.4198
11	34.5810	34.5659	34.5610
12	37.7206	37.7068	37.7023
13	40.8606	40.8478	40.8437
14	44.0007	43.9889	43.9851
15	47.1411	47.1300	47.1265
16	50.2816	50.2712	50.2679
17	53.4223	53.4125	53.4094
18	56.5630	56.5538	56.5508
19	59.7039	59.6951	59.6923

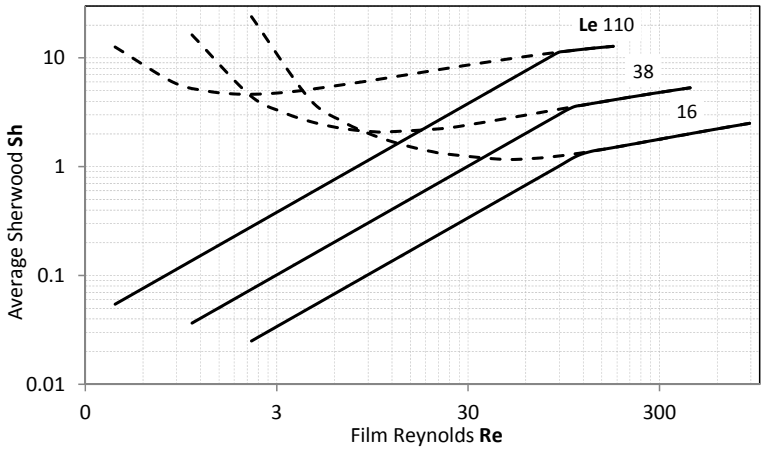

Fig. 6.9 Average Sherwood number as a function of Reynolds for different values of Lewis number

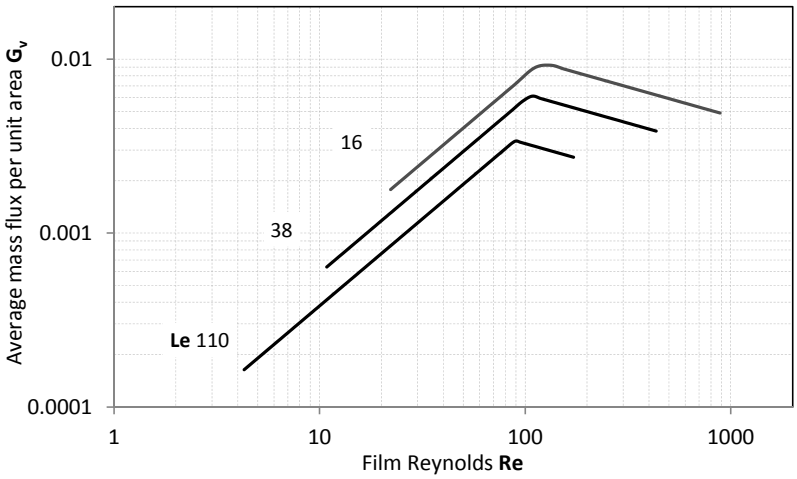

Fig. 6.10 Average mass flux [kg·s^{-1} m^{-2}] per unit area as a function of Reynolds number for different values of Lewis number

According to the definition of the normalised heat of absorption Λ, a different value can be ascribed to a different heat of absorption h_{abs}, a different solution or a different value of the temperature difference ΔT between the film bulk and the interface temperatures. Since Λ appears in the characteristic equation, its solutions (the eigenvalues in Table 6.3) depend on its value. Figure 6.11 shows that Sherwood number is almost independent on this parameter in the Reynolds range of interest. Contrarily, the higher the normalised heat of absorption the higher the absorbed mass flux at the interface.

Table 6.3 First 20 eigenvalues for different values of normalised heat of absorption Λ;

ξ_n	Λ 228	Λ 325	Λ 683
0	0.92241	0.79546	0.59701
1	3.47828	3.37743	3.26524
2	6.46920	6.40915	6.34704
3	9.55156	9.50992	9.46762
4	12.6622	12.6305	12.5986
5	15.7849	15.7594	15.7338
6	18.9138	18.8925	18.8711
7	22.0463	22.0280	22.0096
8	25.1811	25.1650	25.1489
9	28.3173	28.3030	28.2887
10	31.4546	31.4417	31.4288
11	34.5927	34.5810	34.5693
12	37.7314	37.7206	37.7099
13	40.8705	40.8606	40.8506
14	44.0100	44.0007	43.9915
15	47.1497	47.1411	47.1325
16	50.2897	50.2816	50.2736
17	53.4299	53.4223	53.4147
18	56.5702	56.5630	56.5558
19	59.7106	59.7039	59.6971

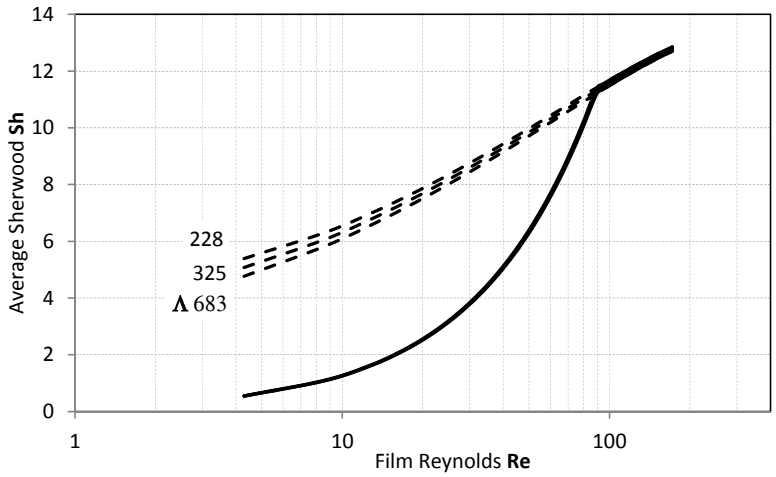

Fig. 6.11 Sherwood number as a function of Reynolds for different values of dimensionless absorption heat

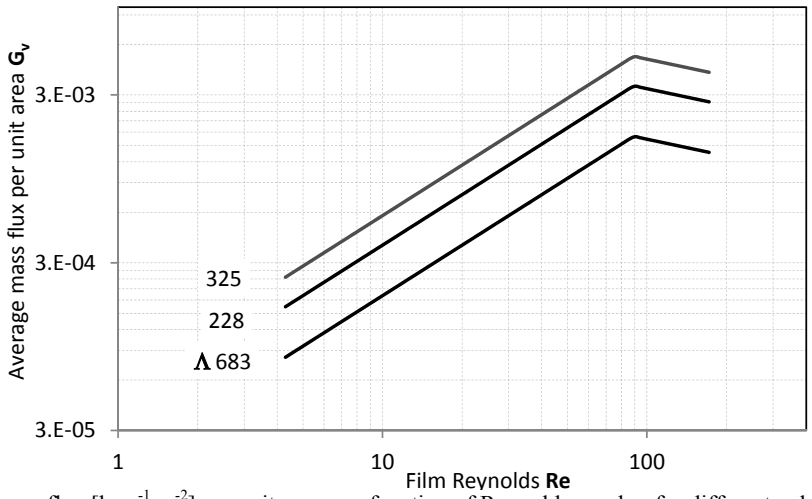

Fig. 6.12 Average mass flux [kg·s^{-1} m^{-2}] per unit area as a function of Reynolds number for different values of dimensionless absorption heat

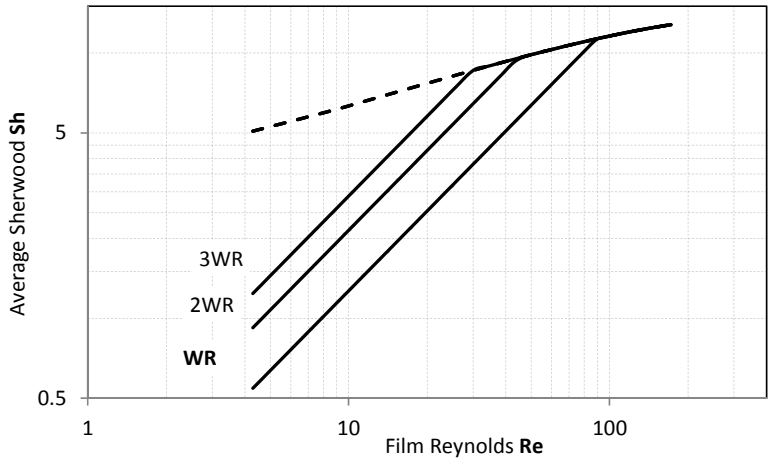

Fig. 6.13 Sherwood number as a function of Reynolds for different film breaking criteria

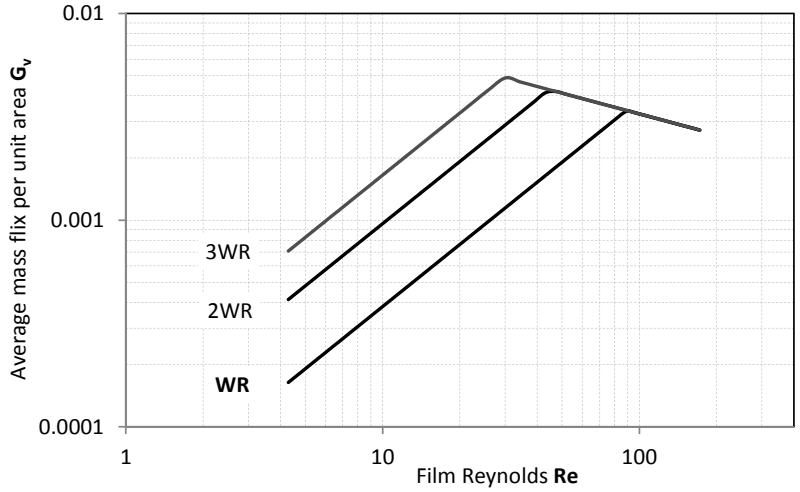

Fig. 6.14 Average mass flux [kg·s^{-1} m^{-2}] per unit area as a function of Reynolds number for different film breaking criteria

The present model refers to simple LiBr-H_2O solution behaviour, but if tensio-active substances would be considered the film breaking would occur at a lower *Re* [122]. As a result, the maximum value of absorbed mass flux would increase and occur at a lower *Re* (Fig 6.14). This condition would be advantageous also for increasing heat transfer to the cooling water circulating inside the tube.

In this paragraph a two-dimensional analytical solution for mass transfer into laminar absorptive film over a single horizontal tube has been obtained with the method of separation of variables and studied. This solution, which gives the concentration distribution inside the falling film, has been used in order to characterise falling film absorption mass transfer phenomena. Moreover, a simplified linear model for partial wetting has been used to extend the accuracy of the solution to the low Reynolds operative conditions. A dimensionless parametric analysis has been performed in order to study exhaustively the dependence on the groups of interest and obtain widely applicable performance maps for an extended range and variety of operative conditions. The comparison with numerical solution of the coupled energy and species transport equations validates the present solution.

Conversely, given the relative importance of heat transfer performance (reduced to the role of constant boundary conditions in the current solution) on the mass transfer process, this mirroring side of the problem under consideration requires to be handled appropriately. Furthermore, the assumption of small penetration distance constitutes a limiting aspect at low solution flowrates, which are considered relevant for a comprehensive analysis.

6.3 Analytical study of coupled heat and mass transfer characteristics of falling film absorption on a partially wetted horizontal tube

With the same purposes previously stated, and in order to solve the weaknesses of the analytical solution presented in the previous paragraph, an analytical model, and the related expression of heat and mass transfer coefficients, of horizontal tube falling film absorber are herein presented.

Simplifying assumptions regarding film hydrodynamics and a linear saturation model are introduced in order to analytically solve the fundamental equations. Partial wetting phenomena are included in the analysis by means of a linear model equivalent to that introduced in the previous analytical solution. In this way the target range of the resulting heat and mass transfer coefficients expressions is extended and their accuracy is increased. Fourier solution method is used and the eigenvalues obtained from the characteristic equation depend on Lewis number and the dimensionless heat of absorption, in turn established with reference to the inlet conditions of the solution, boundary conditions and the pressure of the absorber. Considering a constant temperature at the tube wall, two-dimensional temperature and concentration fields of the laminar film can be expressed analytically as functions of Prandtl, Schmidt, Reynolds numbers, the tube dimensionless diameter and the wetting ratio of the exchange surface. As a result, the expressions of local and average heat and mass transfer coefficients are obtained and analysed as a first screening of the results.

In chemical and engineering technology, several processes involve coupled heat and mass transfer phenomena that cannot be considered separately. Absorption systems (chillers, heat pumps or heat transformers) belong to this set of technology and represent highly complex examples, as well as an opportunity towards clean and efficient energy conversion systems. Besides, in order to improve efficiency of absorption systems, increasingly complex multistage configurations are under development and demand accurate and simple models for predicting, optimising and controlling their performance.

Prior experimental studies on falling film absorption, L. Hoffmann et al. (1997) [123] and I. Kyung et al. (2007) [124], report a limited amount of results, with high uncertainties and for a narrow range of operative conditions, which is not sufficient for a reliable prediction of different absorption systems performance. In terms of modelling efforts, owing to the complexity of the fundamental problem, recently, solutions have been directed towards numerical approaches. M. Mittermaier et al. (2014) [125] studied simultaneous heat and mass transfer of an absorbing or desorbing laminar liquid film flowing over a vertical isothermal plate, by using homogeneous velocity and constant film thickness as simplifying assumptions, but they consider effects such as the change in properties and differential heat of solution due to

interdiffusion. J.W. Andberg et al. (1999) [57] and P.V. Papaefthimiou (2012)[58] presented simplified models for falling film absorption of water vapour over a horizontal tube, similarly using boundary layer assumptions for transport of mass, momentum and energy equations. They solved the problem with a finite difference method and studied the effect of different parameters on the coupled heat and mass transfer processes.

On the one side, numerical analysis and CFD have a great potential and could be used to reach very accurate solutions and descriptions if the problem is formulated properly; however, the time required to reach this accurate solution, and the fact that this solution validity is restricted to the specific case and the operative condition under analysis, should be well-thought-out. Additionally, these specific solutions don't provide general guidelines and cannot be generalised. Under this point of view, in order to extend the validity of the solution and capture the physics of the problem, analytical approaches still maintain their fundamental importance.

To the authors' knowledge, analytical solutions were found only for the corresponding vertical film problem, assuming thermodynamic equilibrium of the solution at the inlet and neglecting the effect of partial wetting at reduced Reynolds operability [126-127]. T. Meyer and F. Ziegler (2014) [128] present an analytical solution obtained by using the Laplace transform and, since temperature and mass fraction profiles are obtained independently from the originally unknown constant temperature and mass fraction boundary conditions at the interface, arbitrary correlation for phase equilibrium are applicable. The main limitations of the previous models lie in the geometry of the problem, the assumptions of uniform velocity profile and film thickness. According to G. Grossmann (1983) [127], this assumption is responsible for deviations of about 20% in the heat and mass transfer coefficient and for an underprediction of about 40% in the distance required for thermal boundary layer development.

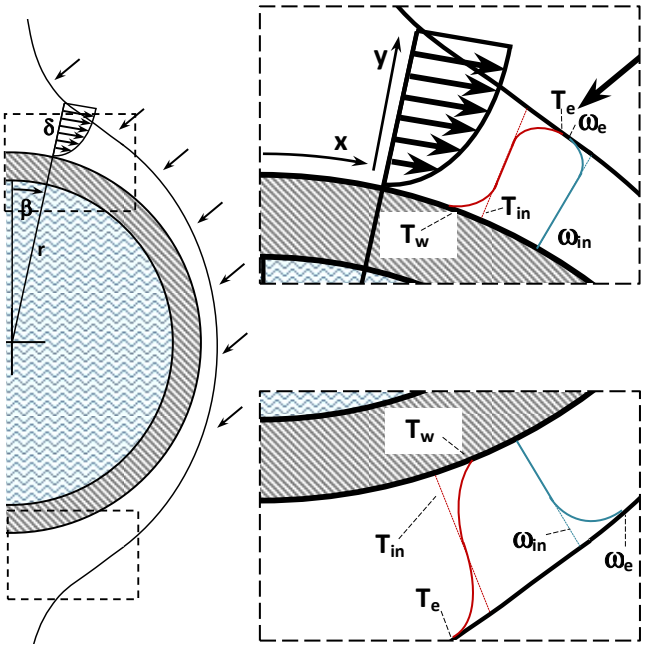

Fig. 6.15 Local coordinate system and illustration of the system considered

As a result, the main purpose of this work is to obtain a closed and accurate solution for absorption process of a laminar, gravity driven film, flowing over a horizontal tube, giving careful attention to the film hydrodynamic description and film thickness distribution with regards to the effect of incomplete wetting/reduction of the solution-vapour interface.

Heat and mass transfer processes are considered under the following main assumptions summarising the understanding gained along this modelling path:

- The zone of impingement is supposed to be a small fraction of the total periphery and the thermal boundary layer is assumed to start its growth from the upper stagnation point (x≈0).
- Assuming that both the tube circumference and length are large if compared to the film thickness, disturbance at the edges of the system are neglected.
- The flow is laminar and there is no interfacial shear force and interfacial waves [121].
- Thermodynamic equilibrium exists at the film inlet-interface with the vapour at the heat exchanger pressure.
- Pressure drops are negligible.
- Physical solution properties remain constant and, as a corollary, convection and Marangoni effects are not taken into account.
- Heat transfer to vapour phase is neglected.
- The variation of mass flow rate due to absorption of water vapour is negligible.
- According to the thin film approximation, body fitted coordinates (x along the tube surface and y normal to it at any point) are used because the film thickness is small if compared to the tube diameter. The dimensionless variables considered in the circumferential and radial directions are, respectively, $\varepsilon=x/\pi r$ and $\eta=y/\delta$.

Tangential (eq. 6.31) and normal (eq. 6.32) velocity components, based on Nusselt integral solution of continuity and momentum equations, are employed in their complete two-dimensional form and expressed as functions of the dimensionless coordinates.

$$u = \frac{\rho g \delta^2}{2\mu} \sin \pi\varepsilon \left(2\eta - \eta^2\right) \tag{6.31}$$

$$v = -\frac{\rho g \delta^2 \eta^2}{2\mu r} \left[\frac{1}{\pi} \frac{d\delta}{dx} \sin \pi\varepsilon + \delta \left(1 - \frac{\eta}{3}\right) \cos \pi\varepsilon \right] \tag{6.32}$$

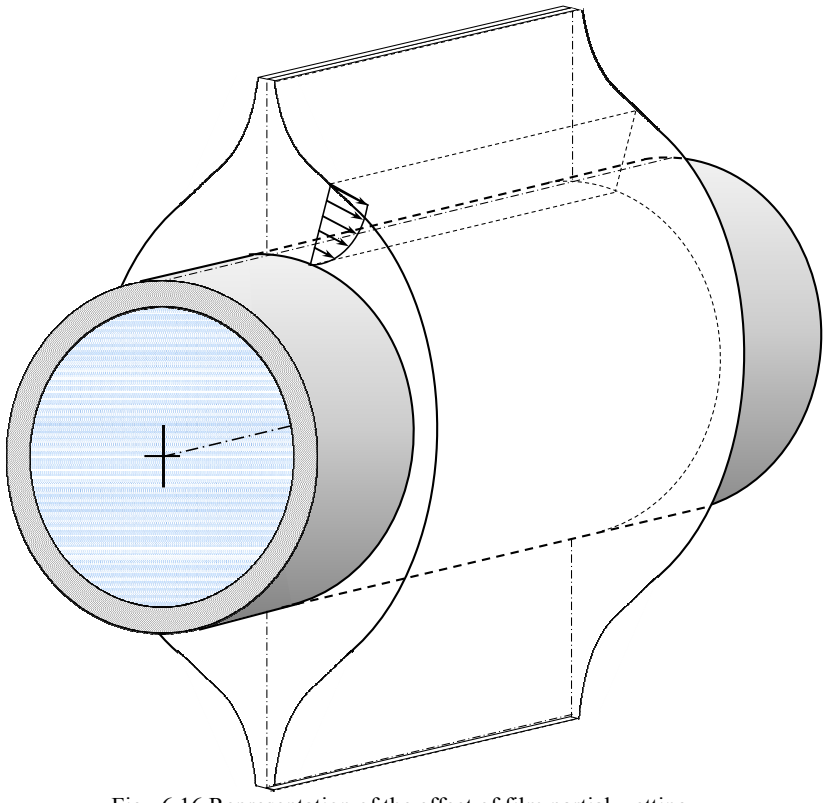

Fig. 6.16 Representation of the effect of film partial wetting

To account for the effect of partial wetting of the low Reynolds region, the extension of that region is identified by the critical condition for a uniform film, referred to as the minimum wetting rate Γ_0, corresponding to the critical Reynolds number Re_0. The latter can be measured experimentally [92] or estimated analytically [99] for a surface with generic inclination, once the thermo-fluid-dynamic properties of the liquid and the characteristic contact angle, representative of the affinity of the solid-liquid interaction, can be estimated. For lower values of Reynolds number a simplified linear wettability model has been applied. The approach matches the one presented in the previous paragraph and, precisely, by eq. 6.2, which evaluates the basic parameter to describe the wet part of the tube surface. Furthermore, as already pointed out, a closed solution requires considering X (and WR, as a consequence) as an independent function of the angular position on the tube surface. Accordingly, the film thickness distribution is, once again, adjusted (eq. 6.3) in order to assure continuity between uniform and partial wetting using a modified form of the Nusselt equation as in S. Jeong and S. Garimella (2002) [106].

The system of differential equations representing a steady flow with constant properties, without internal heat generation and viscous dissipation, and neglecting diffusion terms in the flowing direction, in a two-dimensional form includes energy and species transport equations, given, respectively, by eq. 6.33 and eq. 6.34.

$$\frac{\partial T}{\partial \varepsilon} = \frac{\pi r a}{u\delta^2}\frac{\partial^2 T}{\partial \eta^2} + \left(\frac{\eta}{\delta}\frac{d\delta}{d\varepsilon} - \frac{\pi r v}{u\delta}\right)\frac{\partial T}{\partial \eta} \tag{6.33}$$

$$\frac{\partial \omega}{\partial \varepsilon} = \frac{\pi r D}{u\delta^2}\frac{\partial^2 \omega}{\partial \eta^2} + \left(\frac{\eta}{\delta}\frac{d\delta}{d\varepsilon} - \frac{\pi r v}{u\delta}\right)\frac{\partial \omega}{\partial \eta} \tag{6.34}$$

It is demonstrated that eq. 6.35 holds true, in general, for the velocity distribution expressed by eq.s 6.31 and 6.32.

$$\left(\frac{\eta}{\delta}\frac{d\delta}{d\varepsilon} - \frac{\pi r v}{u\delta}\right) = 0 \tag{6.35}$$

As a result, the following simplified expression is obtained.

$$\frac{\partial T}{\partial \varepsilon} = \frac{\pi r a}{u\delta^2}\frac{\partial^2 T}{\partial \eta^2} \tag{6.36}$$

$$\frac{\partial \omega}{\partial \varepsilon} = \frac{\pi r D}{u\delta^2}\frac{\partial^2 \omega}{\partial \eta^2} \tag{6.37}$$

An analytical solution of the coupled set of equations is approached with the final aim to obtain Nusselt and Sherwood numbers expressions as functions of the operative parameters, geometrical features and boundary conditions. It is advantageous for the problem solution to reach a dimensionless form by the introduction of dimensionless variables.

$$\theta(\varepsilon,\eta) = \frac{T(\varepsilon,\eta) - T_w}{T_e - T_w} \tag{6.38}$$

$$\gamma(\varepsilon,\eta) = \frac{\omega(\varepsilon,\eta) - \omega_{in}}{\omega_e - \omega_{in}} \tag{6.39}$$

T_e and ω_e are defined as in G. Grossmann (1983) [127], that is, respectively, the equilibrium temperature of the solution at concentration ω_{in} and ω_e the equilibrium concentration of the solution at temperature T_{in}. Their physical significance corresponds to the temperature and the concentration that would be reached if thermodynamic equilibrium could be obtained without changes in concentration and temperature, respectively. Accordingly, T_e–T_w represents the sub-cooling at the wall, while ω_e–ω_{in} embodies the driving force for vapour diffusion at the inlet. The dimensionless tube diameter and the characteristic length L_C are defined by eq. 6.40 and eq. 6.41.

$$d^+ = \frac{2\pi r}{L_c} \tag{6.40}$$

$$L_c = \left(\frac{\mu^2}{\rho^2 g} \right)^{1/3} \tag{6.41}$$

Finally, developing non-constant terms and using dimensionless variables and parameters, energy and species transport equations can be written as eq. 6.42 and eq. 6.43, where independent variables are separated.

$$\frac{1}{d^+ \sin^{1/3} \pi\varepsilon} \left(\frac{3\,\text{Re}}{4WR} \right)^{4/3} \frac{\partial \theta}{\partial \varepsilon} = \frac{1}{\text{Pr}\left(2\eta - \eta^2\right)} \frac{\partial^2 \theta}{\partial \eta^2} \tag{6.42}$$

$$\frac{1}{d^+ \sin^{1/3} \pi\varepsilon} \left(\frac{3\,\text{Re}}{4WR} \right)^{4/3} \frac{\partial \gamma}{\partial \varepsilon} = \frac{1}{Sc\left(2\eta - \eta^2\right)} \frac{\partial^2 \gamma}{\partial \eta^2} \tag{6.43}$$

The solution is approached with the following boundary and inlet conditions, including the solution temperature and concentration at the distributer or, assuming that a complete mixing occurs, the bulk values of the previous tube ($x \approx 0$ and $0<y<\delta$; $T=T_{in}$, $\omega=\omega_{in}$), at the tube wall ($y=0$; $T=T_w$, $\partial\omega/\partial y=0$), and at the phase interface ($y=\delta$; $T=T_{sat}(\omega_{if},p)$, $\omega=\omega_{if}$).

$$\vartheta(0,\eta) = \vartheta_{in} \tag{6.44}$$

$$\gamma(0,\eta) = 0 \tag{6.45}$$

$$\left.\frac{\partial \gamma}{\partial \eta}\right|_w = 0 \tag{6.46}$$

$$\vartheta(\varepsilon,0) = 0 \tag{6.47}$$

$$\left.\frac{\partial \vartheta}{\partial \eta}\right|_{if} = \frac{\Lambda}{Le} \left.\frac{\partial \gamma}{\partial \eta}\right|_{if} \tag{6.48}$$

The last condition (eq. 6.48) constitutes a rearrangement of Fick's law of diffusion, where ω_{if} has been approximated as ω_e, and Fourier law, assuring that the heat produced by absorption is conducted through the film towards the tube surface. Where the dimensionless form of the heat of absorption is defined according to eq. 6.49,

$$\Lambda = -\frac{i_{abs}\left(\omega_e - \omega_w\right)}{\omega_e c_p \left(T_e - T_w\right)} = const. \tag{6.49}$$

In addition, it is necessary to know the condition of vapour pressure equilibrium at the interface. A linear relation between ϑ_{if} and γ_{if}, $f(\vartheta_{if}, \gamma_{if})=0$, was found in good agreement for a wide range of operative conditions of LiBr-H_2O solution and a thermodynamic justification, albeit limited to electrolytic solutions, has been given in G. Grossmann (1982) [129]. Accordingly, in terms of the dimensionless variables at constant pressure, the relation expressed by eq. 6.50 is obtained.

$$\gamma_{if} = 1 - \vartheta_{if} \tag{6.50}$$

6.4 Solution method

The method of separation of variables is employed. Dependent functions are assumed to be the series of a product of two main functions terms, each being dependent on a single variable. As in N.I. Grigor'eva and V.E. Nakoryakov (1977) [126] and G. Grossmann (1983) [127], the solution is written in the form of two infinite series of eigenfunctions.

$$\theta(\varepsilon,\eta) = \sum_{n=1}^{\infty} A_n F_n(\eta) E_n(\varepsilon) \tag{6.51}$$

$$\gamma(\varepsilon,\eta) = 1 - \sum_{n=1}^{\infty} B_n G_n(\eta) H_n(\varepsilon) \tag{6.52}$$

The application of the method results in four ordinary differential equations.

$$\frac{1}{d^+ \sin^{1/3} \pi\varepsilon}\left(\frac{3\,\mathrm{Re}}{4WR}\right)^{4/3} \frac{E_n'}{E_n} = \frac{1}{\Pr\left(2\eta - \eta^2\right)} \frac{F_n''}{F_n} = -\xi_n^{\,2} \tag{6.53}$$

$$\frac{1}{d^+ \sin^{1/3} \pi\varepsilon}\left(\frac{3\,\mathrm{Re}}{4WR}\right)^{4/3} \frac{H_n'}{H_n} = \frac{1}{Sc\left(2\eta - \eta^2\right)} \frac{G_n''}{G_n} = -\varsigma_n^{\,2} \tag{6.54}$$

The general solutions of the left members of both eq. 6.53 and eq. 6.54 are,

$$E_n(\varepsilon) = e^{-\xi_n^{\,2} d^+ \left(\frac{4WR}{3\,\mathrm{Re}}\right)^{4/3} \int_0^{\varepsilon} \sin^{1/3} \pi\varepsilon \, d\varepsilon} \tag{6.55}$$

$$H_n(\varepsilon) = e^{-\varsigma_n^{\,2} d^+ \left(\frac{4WR}{3\,\mathrm{Re}}\right)^{4/3} \int_0^{\varepsilon} \sin^{1/3} \pi\varepsilon \, d\varepsilon} \tag{6.56}$$

Where ξ_n e ς_n are the eigenvalues corresponding to the eigenfunctions F_n and G_n. Moreover, for the linear equilibrium condition at the interface (eq. 6.50), which must be satisfied for every ε, it is required for every n that $\xi_n=\varsigma_n$. Considering the right-side members of eq. 6.53 and eq. 6.54, eq. 6.57 and eq. 6.58 can be written.

$$F_n'' + \xi_n^{\,2} \Pr\left(2\eta - \eta^2\right) F_n = 0 \tag{6.57}$$

$$G_n'' + \xi_n^2 Sc\left(2\eta - \eta^2\right) G_n = 0 \tag{6.58}$$

The boundary condition at the wall, eq. 6.46 and eq. 6.47 require, correspondingly, $F_n(0)=0$ and $G_n'(0)=0$. While at the interface, eq. 6.48 and eq. 6.50 indicate, respectively,

$$A_n F_n(1) = B_n G_n(1) \tag{6.59}$$

$$A_n F_n'(1) = -\frac{\Lambda}{Le} B_n G_n'(1) \tag{6.60}$$

Since, eq. 6.59 and eq. 6.60 are two homogeneous equations for A_n and B_n, a significant solution can be reached on condition that the determinant equals zero.

$$\frac{F_n'(1)}{F_n(1)} = -\frac{\Lambda}{Le}\frac{G_n'(1)}{G_n(1)} \tag{6.61}$$

Eq. 6.61 represents the characteristic equation for determining the eigenvalues ξ_n once the solution for F_n and G_n has been determined. Power series solutions for eq. 6.57 and eq. 6.58 can be written in the following form.

$$F_n(\eta) = \sum_{i=0}^{\infty} a_{n,i}\eta^i \tag{6.62}$$

$$G_n(\eta) = \sum_{i=0}^{\infty} b_{n,i}\eta^i \tag{6.63}$$

Substituting these solution form in eq. 6.57 and eq. 6.58 and using the boundary conditions $F_n(0)=0$ and $G_n'(0)=0$, coefficients $a_{n,i}$ and $b_{n,i}$ can be found and calculated by the recursive relations represented by eq. 6.65 and eq.6.67.

$$a_{n,0} = 0, a_{n,1} = 1, a_{n,2} = 0, a_{n,3} = 0 \tag{6.64}$$

$$a_{n,i} = \frac{\xi_n^2 \Pr\left(a_{n,i-4} - 2a_{n,i-3}\right)}{i\left(i-1\right)}, i \geq 4 \tag{6.65}$$

$$b_{n,0} = 1, b_{n,1} = 0, b_{n,2} = 0, b_{n,3} = -\xi_n^2 / 3 \tag{6.66}$$

$$b_{n,i} = \frac{\xi_n^2 Sc\left(b_{n,i-4} - 2b_{n,i-3}\right)}{i\left(i-1\right)}, i \geq 4 \tag{6.67}$$

Coefficients A_n and B_n are determined by means of a Sturm-Liouville orthogonality condition at the inlet, using also boundary conditions at the interface eq. 6.48 and eq. 6.50. The procedure [127], in this case, enables to obtain a solution when the inlet temperature value is different from the constant value at the wall and from the equilibrium value (namely, allows the user to consider sub-cooling or superheating of the solution at the inlet). Multiplying eq. 6.57 and eq. 6.58 by the eigenfunctions F_m and G_m, in that order, and integrating with respect to η, yields eq. 6.68 and eq.6.69.

$$\xi_n^{\,2}\,\mathrm{Pr}\int_0^1\left(2\eta-\eta^2\right)F_mF_n d\eta=-\int_0^1 F_mF_n''\,d\eta=F_m(0)F_n'(0)-F_m(1)F_n'(1)+\int_0^1 F_m'F_n'\,d\eta \tag{6.68}$$

$$\xi_n^{\,2}Sc\int_0^1\left(2\eta-\eta^2\right)G_mG_n d\eta=-\int_0^1 G_mG_n''\,d\eta=G_m(0)G_n'(0)-G_m(1)G_n'(1)+\int_0^1 G_m'G_n'\,d\eta \tag{6.69}$$

By proceeding in the same way for eigenvalues and eigenfunctions with index *m* (eq. 6.70 and eq. 6.71),

$$\mathrm{Pr}\,\xi_m^{\,2}\int_0^1\left(2\eta-\eta^2\right)F_nF_m d\eta=F_n(0)F_m'(0)-F_n(1)F_m'(1)+\int_0^1 F_n'F_m'\,d\eta \tag{6.70}$$

$$Sc\,\xi_m^{\,2}\int_0^1\left(2\eta-\eta^2\right)G_nG_m d\eta=G_n(0)G_m'(0)-G_n(1)G_m'(1)+\int_0^1 G_n'G_m'\,d\eta \tag{6.71}$$

And subtracting the corresponding equations and using the boundary conditions expressed by $F_n(0)=0$ and $G_n'(0)=0$, eq. 6.72 and eq. 6.73 can be written.

$$\mathrm{Pr}\left(\xi_n^{\,2}-\xi_m^{\,2}\right)\int_0^1\left(2\eta-\eta^2\right)F_nF_m d\eta=F_n(1)F_m'(1)-F_m(1)F_n'(1) \tag{6.72}$$

$$Sc\left(\xi_n^{\,2}-\xi_m^{\,2}\right)\int_0^1\left(2\eta-\eta^2\right)G_nG_m d\eta=G_n(1)G_m'(1)-G_m(1)G_n'(1) \tag{6.73}$$

The coupling between the previous two conditions is established by using eq. 6.59 and eq. 6.60.

$$F_n(1)F_m'(1)-F_m(1)F_n'(1)=-\frac{\Lambda}{Le}\frac{B_nB_m}{A_nA_m}\left[G_n(1)G_m'(1)-G_m(1)G_n'(1)\right] \tag{6.74}$$

Eq. 6.74 enables eq. 6.72 and eq. 6.73 to be combined.

$$Sc\left(\xi_n^{\,2}-\xi_m^{\,2}\right)\int_0^1\left(2\eta-\eta^2\right)\left(\mathrm{Pr}\,LeA_nA_mF_nF_m+Sc\Lambda B_nB_mG_nG_m\right)d\eta=0 \tag{6.75}$$

Which directly implies,

$$\int_0^1\left(2\eta-\eta^2\right)\left(\mathrm{Pr}\,LeA_nA_mF_nF_m+Sc\Lambda B_nB_mG_nG_m\right)d\eta\begin{cases}=0, n\neq m\\ \neq 0, n=m\end{cases} \tag{6.76}$$

Using the boundary conditions as in eq. 6.44 and eq. 6.45,

$$\sum_{n=1}^{\infty}A_nF_n(\eta)=\theta_{in} \tag{6.77}$$

$$\sum_{n=1}^{\infty} B_n G_n(\eta) = 1 \tag{6.78}$$

The summation of the integrals,

$$\begin{aligned}&\sum_{n=1}^{\infty}\int_0^1 \left(2\eta-\eta^2\right)(\mathrm{Pr}\, Le A_n A_m F_n F_m + Sc\Lambda B_n B_m G_n G_m)d\eta \\ &= \int_0^1 \left(2\eta-\eta^2\right)(\mathrm{Pr}\, Le\theta_{in} A_m F_m + Sc\Lambda B_m G_m)d\eta\end{aligned} \tag{6.79}$$

According to eq. 6.76, the first relation between A_n and B_n can be obtained (eq. 6.80), while the second one is offered by either eq. 6.59 or eq. 6.60.

$$\int_0^1 \left(2\eta-\eta^2\right)(\mathrm{Pr}\, Le A_n{}^2 F_n{}^2 + Sc\Lambda B_n{}^2 G_n{}^2)d\eta = \int_0^1 \left(2\eta-\eta^2\right)(\mathrm{Pr}\, Le\theta_{in} A_n F_n + Sc\Lambda B_n G_n)d\eta \tag{6.80}$$

Finally, solving for A_n and B_n,

$$A_n = B_n \frac{G_n(1)}{F_n(1)} \tag{6.81}$$

$$B_n = \frac{\displaystyle\int_0^1 \left(2\eta-\eta^2\right)\left(\mathrm{Pr}\, Le\theta_{in}\frac{G_n(1)}{F_n(1)}F_n(\eta) + Sc\Lambda G_n(\eta)\right)d\eta}{\displaystyle\int_0^1 \left(2\eta-\eta^2\right)\left(\mathrm{Pr}\, Le\frac{G_n{}^2(1)}{F_n{}^2(1)}F_n{}^2(\eta) + Sc\Lambda G_n{}^2(\eta)\right)d\eta} \tag{6.82}$$

As a result, temperature and concentration fields can be expressed as follows.

$$T(\varepsilon,\eta) = T_w + \left(T_e - T_w\right)\sum_{n=1}^{\infty}\left[A_n\sum_{i=0}^{\infty}\left(a_{n,i}\eta^i\right)e^{-\xi_n{}^2 d^+\left(\frac{4WR}{3\mathrm{Re}}\right)^{4/3}\int_0^{\varepsilon}\sin^{1/3}\pi\varepsilon d\varepsilon}\right] \tag{6.83}$$

$$\omega(\varepsilon,\eta) = \omega_e + \left(\omega_{in} - \omega_e\right)\sum_{n=1}^{\infty}\left[B_n\sum_{i=0}^{\infty}\left(b_{n,i}\eta^i\right)e^{-\xi_n{}^2 d^+\left(\frac{4WR}{3\mathrm{Re}}\right)^{4/3}\int_0^{\varepsilon}\sin^{1/3}\pi\varepsilon d\varepsilon}\right] \tag{6.84}$$

6.5 Temperature and concentration distributions

LiBr-H_2O solution properties are calculated for the inlet values of temperature, pressure and concentration, and the following analysis is carried out for two sets of representative operative conditions of the absorber in a cooling system and in a single stage heat transformer (Table 6.4). The influent dimensionless parameters are shown in Table 6.5.

Table 6.4 Reference operative conditions

T_{in} (°C)	T_w (°C)	ω_{in}	P (kPa)	r (m)
40	32	0.60	1.0	0.009
95	85	0.60	15	0.009

Table 6.5 Reference values of the main dimensionless parameters

Le	Λ	Sc	Pr	d*	Re
110.8	5.515	2567	23.17	568.4	42.95
41.67	4.076	394.5	9.467	333.3	101.9

Tables 6.6 and 6.7 show the eigenvalues and the corresponding coefficients of the eigenfunctions used for the particular chosen solutions.

Table 6.6 Eigenvalues and eigenfunction coefficients for an absorber operating in a refrigeration machine

n	ξ_n	A_n	B_n
1	0.0418	0.129	1.34
2	0.116	0.135	-0.555
3	0.189	0.154	0.369
4	0.259	0.178	-0.278
5	0.326	0.169	0.197
6	0.392	0.116	-0.124
7	0.462	0.0538	0.0613
8	0.533	0.0213	-0.0267
9	0.607	0.00303	0.00406

Table 6.7 Eigenvalues and eigenfunction coefficients for an absorber operating in a single stage heat transformer

n	ξ_n	A_n	B_n
1	0.1004	0.242	1.33
2	0.278	0.254	-0.533
3	0.445	0.258	0.317
4	0.605	0.179	-0.175
5	0.771	0.0774	0.0769
6	0.948	0.0256	-0.0269
7	1.13	0.00789	0.00813
8	1.31	0.00842	-0.00769
9	1.49	0.0253	0.0186

Figures 6.17 and 6.18, respectively, compare temperature and concentration fields obtained with the first 9 eigenfunctions of the present analytical solution, with the corresponding numerical solutions of energy and species transport equations. Good agreement can be recognised for both fields. However, regarding the temperature distribution the approximation appears to be rough at the wall entrance region.

Considering an increased number of eigenvalues (Tables 6.8 and 6.9) it is possible to model the entrance effect at the wall with an increased accuracy, but higher eigenvalues and an increased number of terms representing the eigenfunctions F_n and G_n creates instability far from the wall (η=0) and, in particular, close to the entrance at the interface (η=1).

The temperature field close to the tube surface obtained with the first 14 eigenvalues is compared to the corresponding numerical solution in figure 6.19. As obvious, an increased number of eigenvalues enables the solution to model the film entrance region at the wall. For this reason, in the followings, the heat transfer at the tube surface will be estimated considering 14 eigenvalues, while mass transfer can be better evaluated with the first 9 eigenvalues, which do not cause instabilities at the interface.

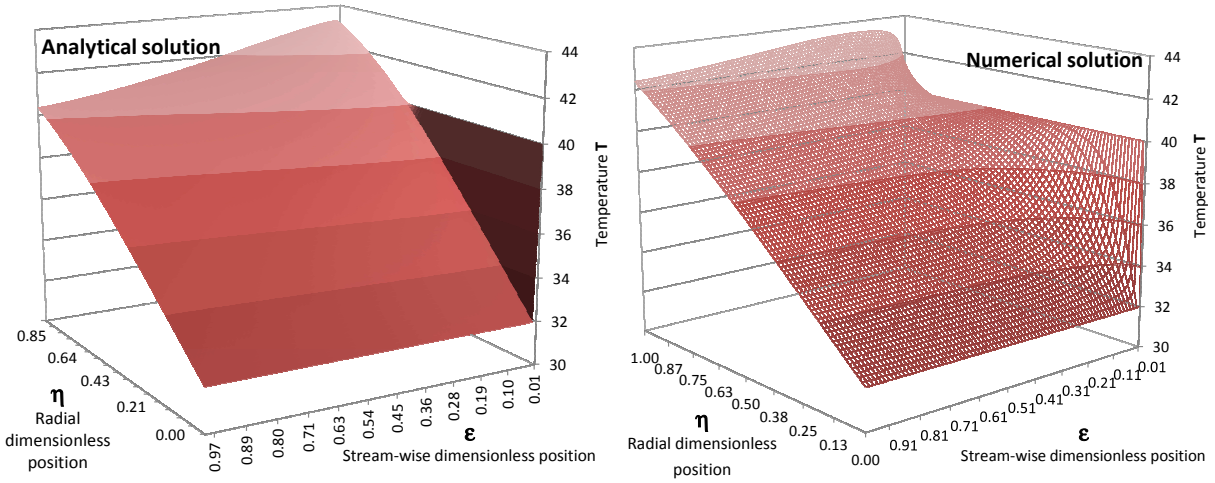

Fig. 6.17 Comparison of analytical and numerical solutions of the film temperature field [^{o}C] for the reference conditions of a refrigerating machine

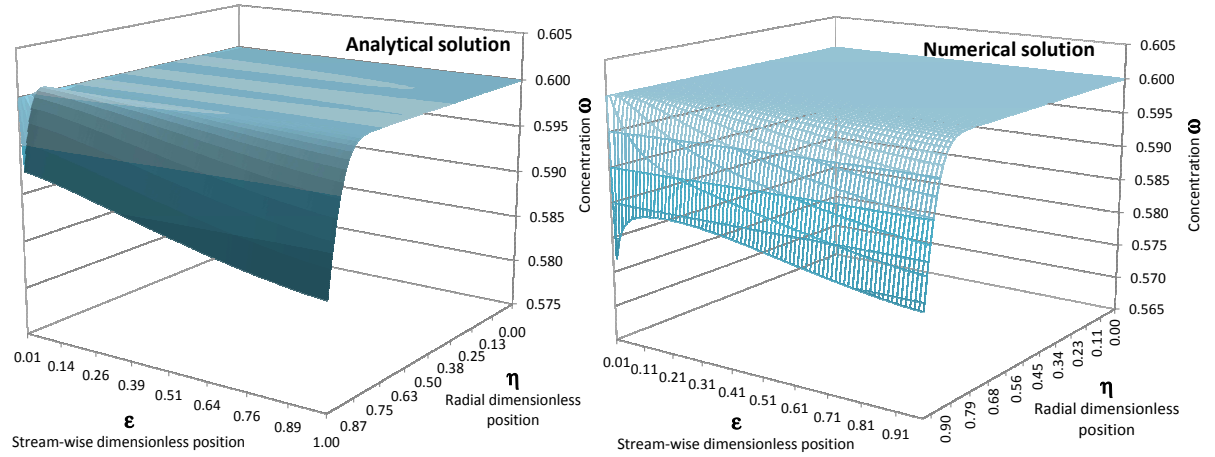

Fig. 6.18 Comparison of analytical and numerical solutions of the film concentration field for the reference conditions of a refrigerating machine

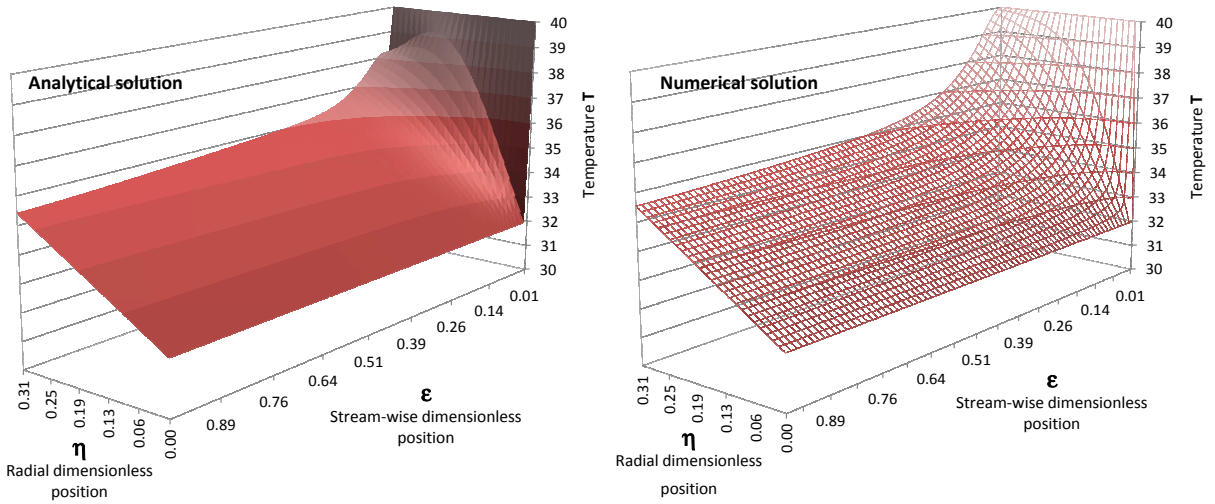

Fig. 6.19 Comparison of analytical and numerical solutions of the film temperature field in proximity to the tube wall for the reference conditions of a refrigerating machine

Table 6.8 Increased number of eigenvalues and coefficients for typical condition of an absorber in a cooling system

n	ξ_n	A_n	B_n
1	0.0418	0.129	1.34
2	0.116	0.133	-0.551
3	0.189	0.154	0.369
4	0.259	0.176	-0.275
5	0.326	0.168	0.196
6	0.392	0.113	-0.121
7	0.462	0.0536	0.0610
8	0.533	0.0194	-0.0243
9	0.607	0.00328	0.00440
10	2.26	1.28	-9.00E-45
11	3.06	-0.368	-1.00E-70
12	3.91	1.26	-3.00E-45
13	4.72	-0.504	-1.00E-107
14	5.53	1.27	-8.00E-121

Table 6.9 Increased number of eigenvalues and coefficients for typical condition of an absorber in a heat transformer

n	ξ_n	A_n	B_n
1	0.1004	0.242	1.33
2	0.278	0.254	-0.533
3	0.445	0.258	0.317
4	0.605	0.179	-0.175
5	0.771	0.0774	0.0769
6	0.948	0.0256	-0.0269
7	1.13	0.00789	0.00813
8	1.31	0.00842	-0.00769
9	1.49	0.0253	0.0186
10	3.58	1.57	-6.25E-17
11	4.82	-0.355	-2.14E-30
12	6.08	1.26	-3.73E-49
13	7.34	-0.392	-1.52E-65
14	8.61	1.21	-1.46E-78

6.6 Nusselt and Sherwood numbers

Local heat and mass transfer coefficient (α and *mtc*) are calculated according to eq. 6.85 and eq. 6.86. In order to consider the tube partial wetting, an expression averaged for the tube length is obtained under the assumption that the reduction of the surface taking part to the vapour absorption can be represented by the value of *WR*.

$$\alpha = WR \frac{k \left.\frac{\partial T}{\partial y}\right|_w}{T_{av} - T_w} \tag{6.85}$$

$$mtc = -WR \frac{D}{\omega_{if}} \frac{\left.\frac{\partial \omega}{\partial y}\right|_{if}}{\omega_W - \omega_{if}} \tag{6.86}$$

The dimensionless analytical expression of the local heat and mass transfer coefficients (i.e. Nusselt and Sherwood Numbers) are given by eq. 6.87 and eq. 6.88.

$$Nu(\varepsilon)=\left(\frac{4}{3}\frac{WR^4\sin\pi\varepsilon}{\mathrm{Re}}\right)^{1/3}\frac{\sum_{n=1}^{\infty}\left[\frac{G_n(1)}{F_n(1)}B_n a_{n,1}e^{-\xi_n^2 d^+\left(\frac{4WR}{3\mathrm{Re}}\right)^{4/3}\int_0^{\varepsilon}\sin^{1/3}\pi\varepsilon d\varepsilon}\right]}{\sum_{n=1}^{\infty}\left[\frac{G_n(1)}{F_n(1)}B_n\sum_{i=0}^{\infty}\left(\frac{a_{n,i}}{i+1}\right)e^{-\xi_n^2 d^+\left(\frac{4WR}{3\mathrm{Re}}\right)^{4/3}\int_0^{\varepsilon}\sin^{1/3}\pi\varepsilon d\varepsilon}\right]} \tag{6.87}$$

$$Sh(\varepsilon)=\frac{\left(\frac{4}{3}\frac{WR^4\sin\pi\varepsilon}{\mathrm{Re}}\right)^{1/3}\sum_{n=1}^{\infty}\left[B_n\sum_{i=1}^{\infty}(ib_{n,i})e^{-\xi_n^2 d^+\left(\frac{4WR}{3\mathrm{Re}}\right)^{4/3}\int_0^{\varepsilon}\sin^{1/3}\pi\varepsilon d\varepsilon}\right]}{\left\{\omega_e+(\omega_{in}-\omega_e)\sum_{n=1}^{\infty}\left[B_n\sum_{i=0}^{\infty}(b_{n,i})e^{-\xi_n^2 d^+\left(\frac{4WR}{3\mathrm{Re}}\right)^{4/3}\int_0^{\varepsilon}\sin^{1/3}\pi\varepsilon d\varepsilon}\right]\right\}\sum_{n=1}^{\infty}\left[B_n\sum_{i=1}^{\infty}(b_{n,i})e^{-\xi_n^2 d^+\left(\frac{4WR}{3\mathrm{Re}}\right)^{4/3}\int_0^{\varepsilon}\sin^{1/3}\pi\varepsilon d\varepsilon}\right]} \tag{6.88}$$

6.7 Parametric analysis

After the model has been developed, compared with equivalent numerical solutions, and presented in the preceding paragraph, in order to obtain significant results for actual system analysis, the effects of the main parameters is studied for typical conditions of a single absorber tube in two different system applications, comparing the effect of partial wetting (continuous lines) with the uniform film solution (dashed lines, since deviating from an accurate prediction of absorption transfer performance) and considering different numbers of eigenvalues.

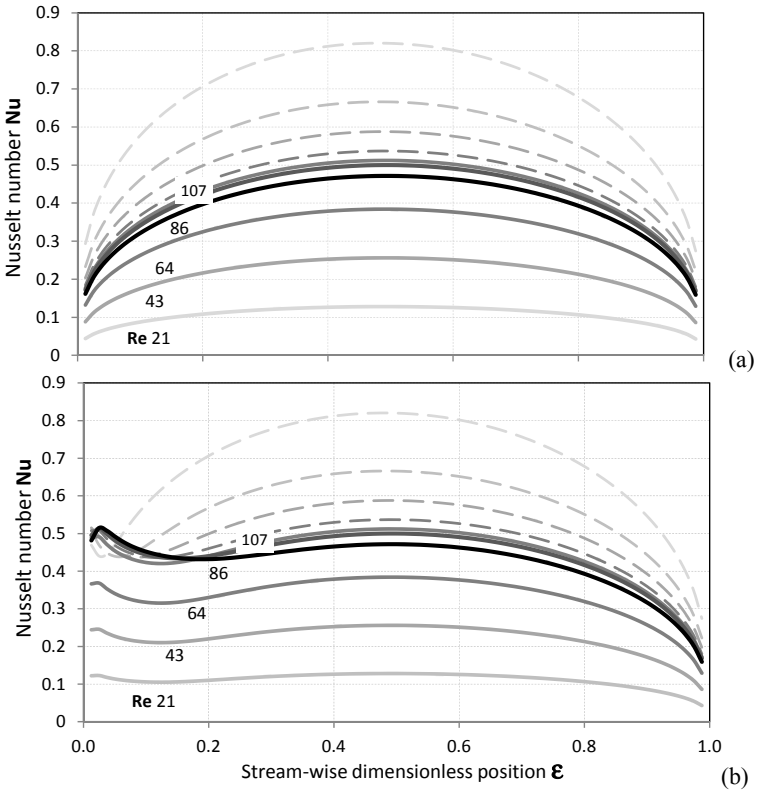

Fig. 6.20 Local Nusselt number for different solution mass flowrates (a) corresponding to the first 9 eigenfuntions (b) corresponding to the first 14 eigenfuntions, at the reference conditions of a refrigerating machine

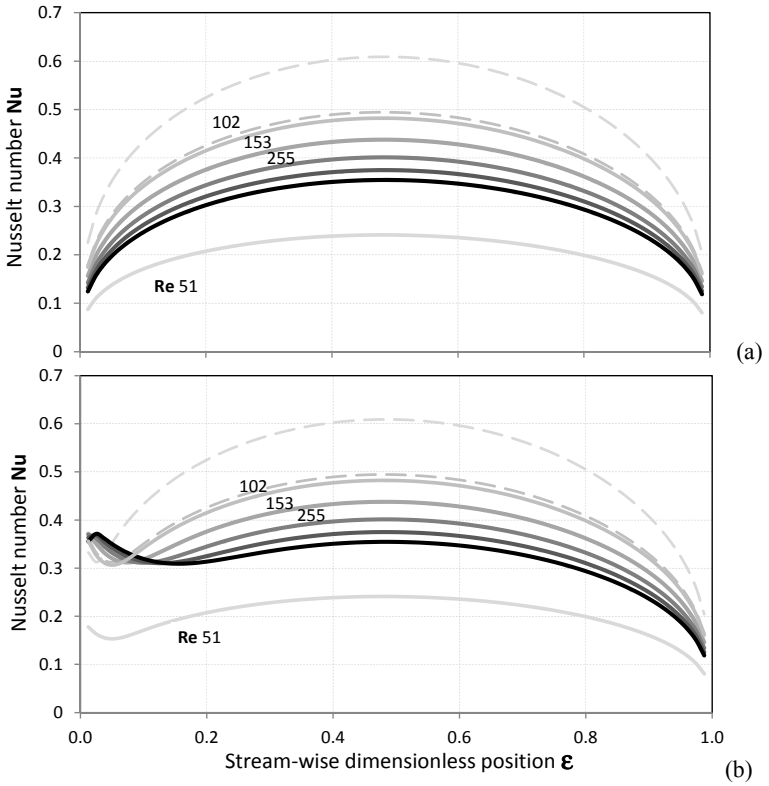

Fig. 6.21 Local Nusselt number for different solution mass flowrates (a) corresponding to the first 9 eigenfuntions (b) corresponding to the first 14 eigenfuntions, at the reference conditions of a single stage heat transformer

Curves representing the absorptive mass flux per unit area at the interface G_v, the heat flux per unit area at the tube wall q, Nusselt and Sherwood numbers are given locally as functions of the stream-wise normalised length ε.

Solid lines represent results obtained considering partial wetting and gradually darkening colours stand for increasing values of the considered parameter, while dashed lines of the corresponding colour make evidence of the different results that would be obtained for a constantly uniform film.

Figure 6.20 highlights the local trend of Nusselt number for different solution mass flowrates, making evidence of a local maximum corresponding to the position at which the film assumes its minimum thickness. In figures 6.20 and 6.21, lines of the same colour correspond to the same value of mass flowrate per unit length. Different values of the solution properties increase Reynolds at higher temperature and the graphs suggests of the reduced extension (in terms of solution mass flowrate per unit length) of the partial wetting region for the heat transformer application.

The local heat flux at the wall (Fig. 6.22 (b) and 6.23 (b)) shows a peak due to the entrance effect, related to the constant temperature boundary condition, and a relative maximum whose value decreases, when the film is uniform, and increases, when the film is broken, with increasing Reynolds. The position of the maximum on the tube wall moves forward in the stream-wise direction with increasing Reynolds, when the film is uniform. Contrarily, its position is slightly influenced when *WR* is taken into account in the partial wetting region.

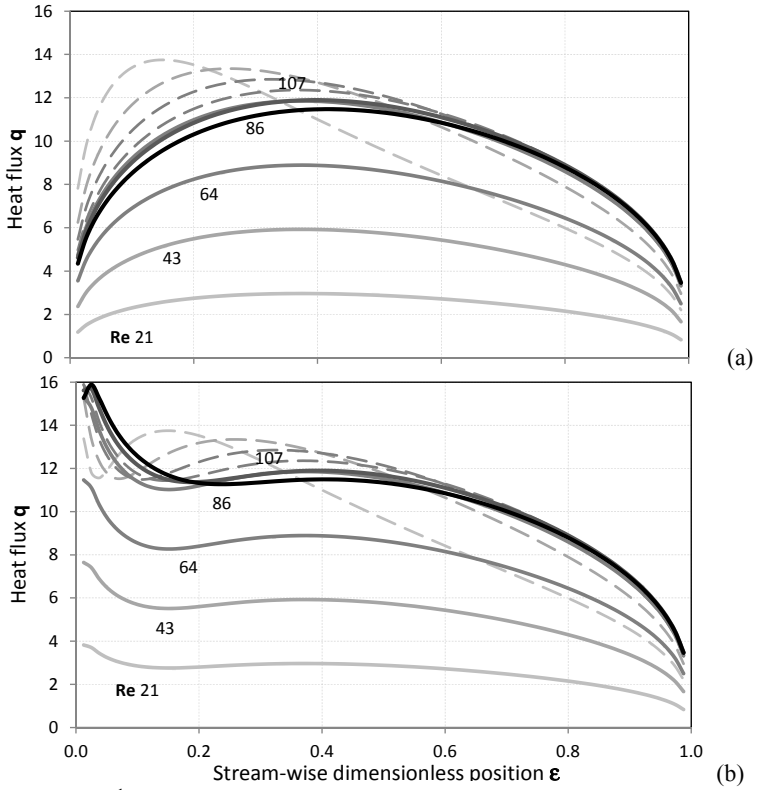

Fig. 6.22 Local heat flux [kW·m^{-1}] at the tube wall for different solution mass flowrates (a) corresponding to the first 9 eigenfuntions (b) corresponding to the first 14 eigenfuntions, at reference conditions of a refrigerating machine

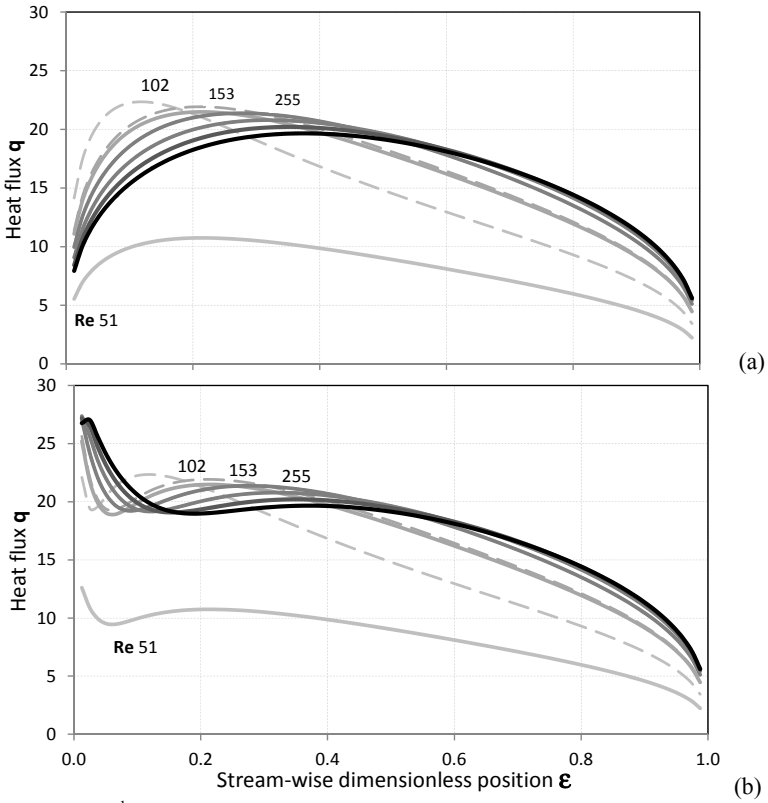

Fig. 6.23 Local heat flux [kW·m^{-1}] at the tube wall for different solution mass flowrates (a) corresponding to the first 9 eigenfuntions (b) corresponding to the first 14 eigenfuntions, at the reference conditions of a single stage heat transformer

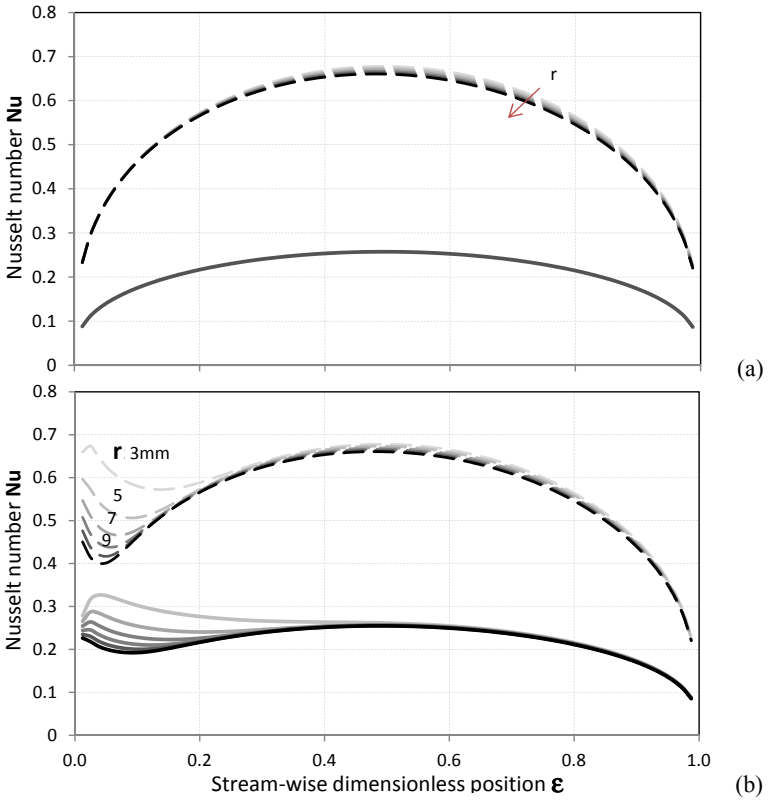

Fig. 6.24 Local Nusselt number for different tube radii (a) corresponding to the first 9 eigenfuntions (b) corresponding to the first 14 eigenfuntions, at the reference conditions of a refrigerating machine

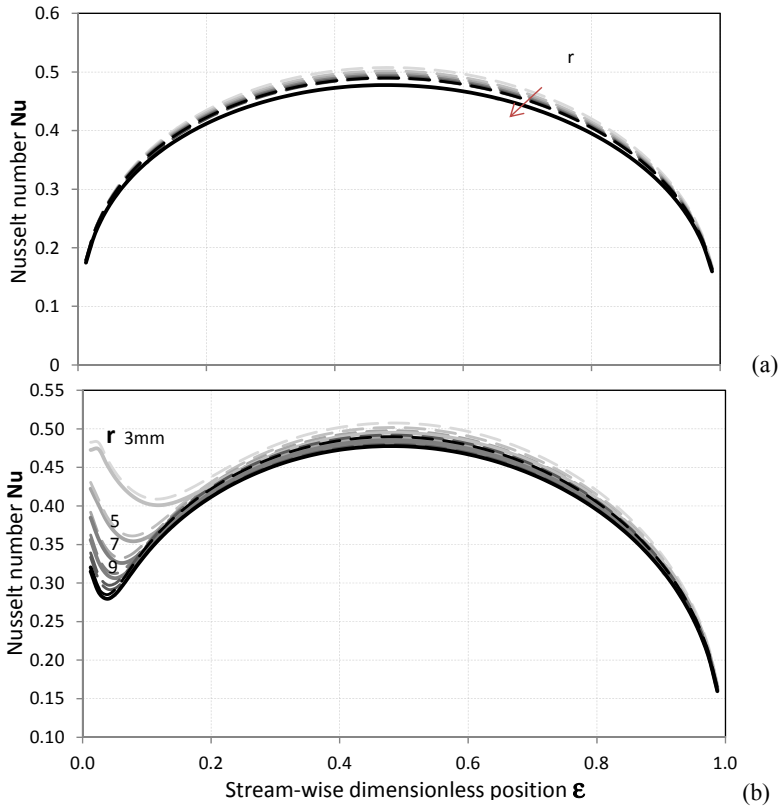

Fig. 6.25 Local Nusselt number for different tube radii (a) corresponding to the first 9 eigenfuntions (b) corresponding to the first 14 eigenfuntions,at the reference conditions of a single stage heat transformer

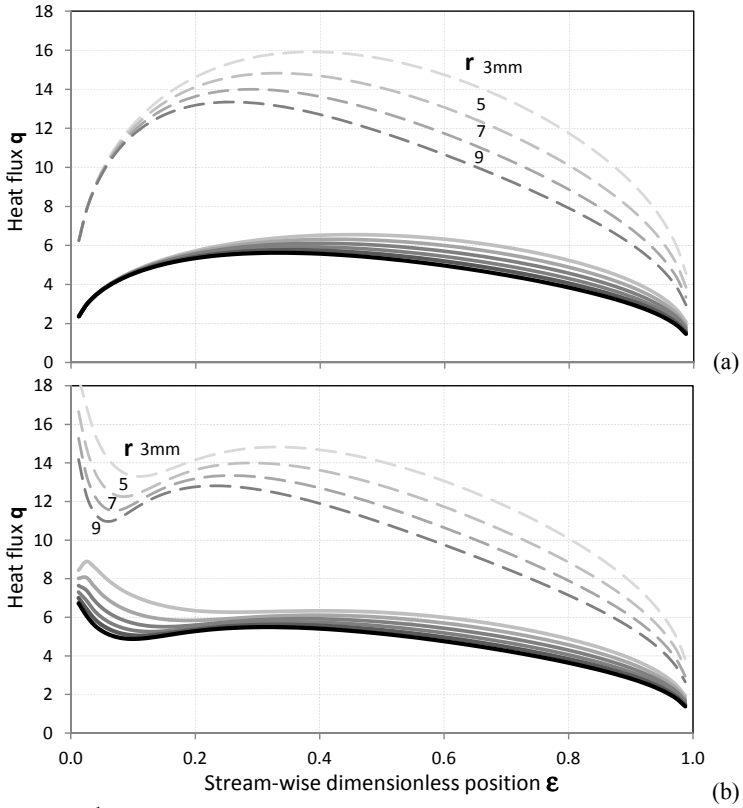

Fig. 6.26 Local heat flux [kW·m^{-1}] at the tube wall for different tube radii (a) corresponding to the first 9 eigenfuntions (b) corresponding to the first 14 eigenfuntions, at reference conditions of a refrigerating machine

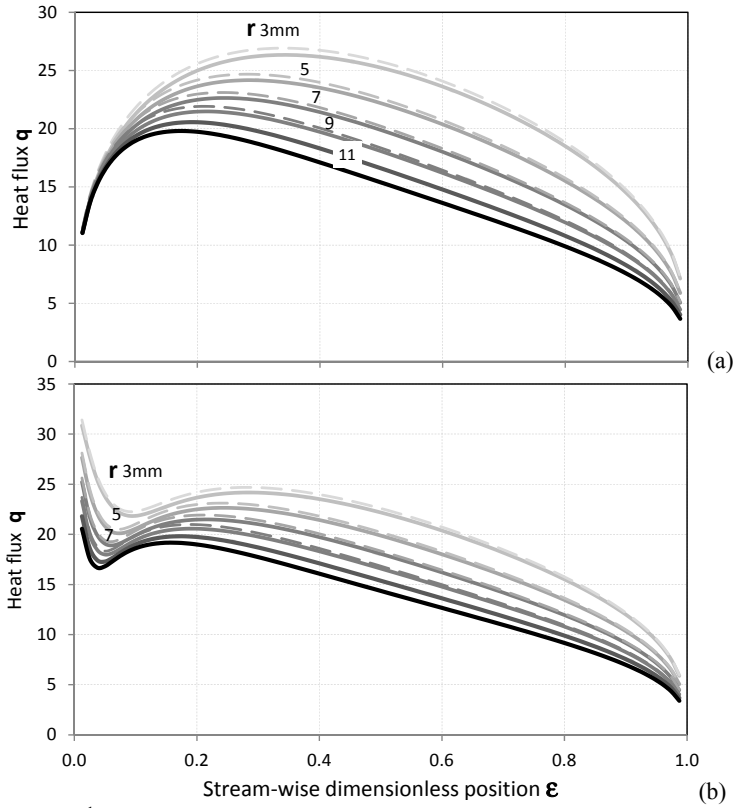

Fig. 6.27 Local heat flux [kW·m^{-1}] at the tube wall for different tube radii (a) corresponding to the first 9 eigenfuntions (b) corresponding to the first 14 eigenfuntions, at the reference conditions of a single stage heat transformer

Figures 6.24 and 6.25 show, respectively, the local Nusselt number and heat flux at the wall for different outer tube radii. Same trend, but different influence of this parameter is shown for different applications.

The tube radius mainly affects the entrance region. In the chiller application it principally influences the extension of the entrance region (the smaller the tube the higher the extension). Contrarily, for the heat transformer application, the absolute value of Nusselt Number in the entrance region is mostly affected (the smaller the tube the higher the *Nu* value). This different behaviour can be explained considering that, although the same solution mass flow rate is considered, different applications have different values of *WR* (eq. 6.2) and, according to eq. 6.87 and eq. 6.88, the higher is the *WR* the steeper is the exponential term, which indirectly means shorter impact of the eigenfunctions determining the entrance region.

As for low solution mass flowrate, the local heat transfer distribution makes evidence for the occurrence of a local maximum related to the film thickness variation. Contrarily, with higher solution mass flowrates, if the entrance region is modelled, this effect is overwhelmed by the flow field and no local maximum occurs. By using smaller tube the heat flux at the wall is enhanced and the position of the local maximum value moves towards higher dimensionless stream-wise positions ε (Fig. 6.26).

In general, figures 6.20-6.27 highlight the importance of including the entrance region at the wall for evaluating locally the heat transfer performance of both the chiller and the heat transformer.

In figures 6.28 and 6.29, mass transfer at the film interface is considered locally as represented by Sherwood number. They make evidence for a maximum value, increasing and moving forward when solution flowrate increases in the partial wetting region, but when solution flowrate is increased in the complete wetting region the value of the maximum starts decreasing.

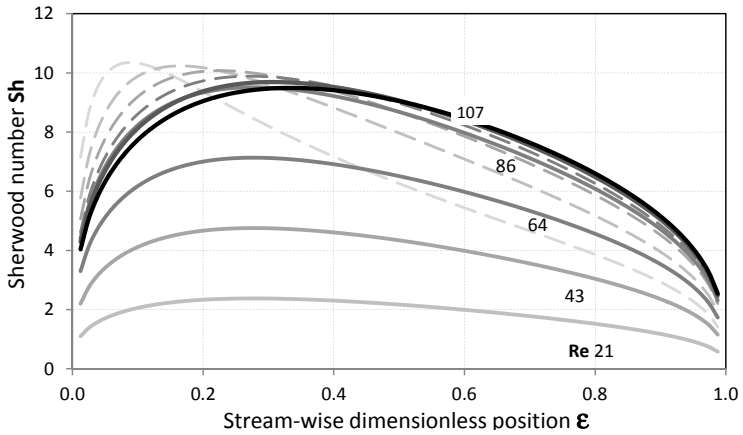

Fig. 6.28 Local Sherwood number for different solution mass flowrates at the reference conditions of a refrigerating machine

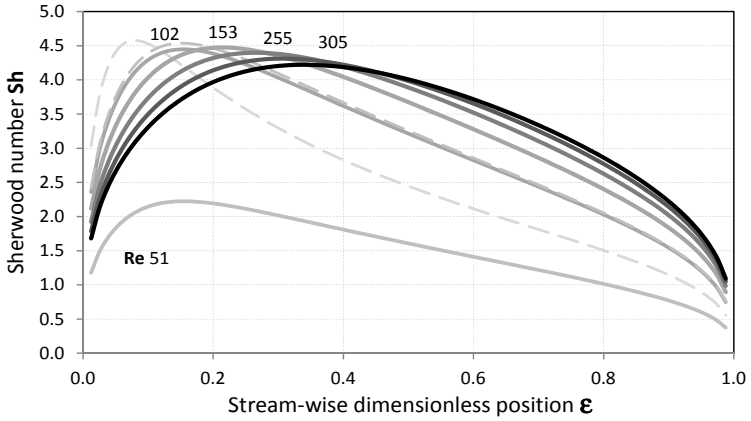

Fig. 6.29 Local Sherwood number for different solution mass flowrates at the reference conditions of a single stage heat transformer

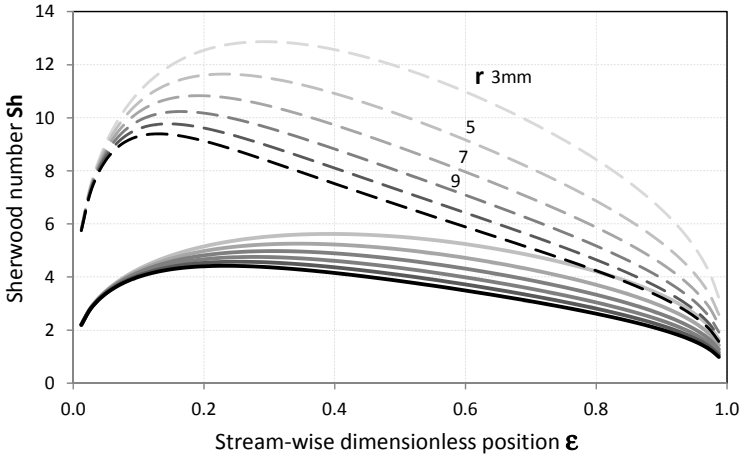

Fig. 6.30 Local Sherwood number for different tube radii at the reference conditions of a refrigerating machine

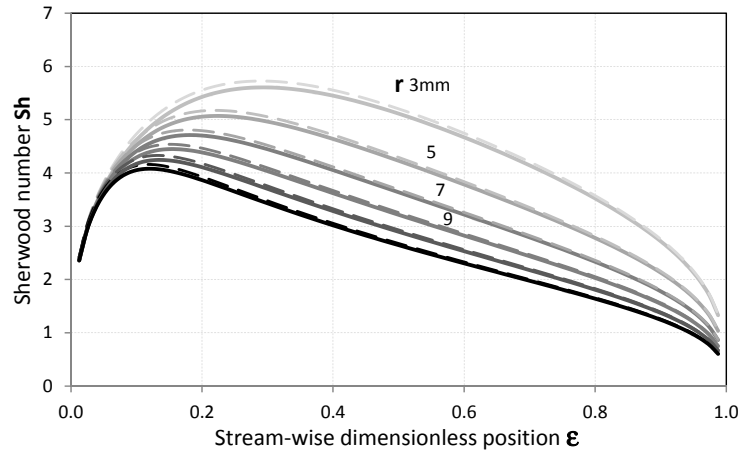

Fig. 6.31 Local Sherwood number for different tube radii at the reference conditions of a single stage heat transformer

A reduction in the outer tube radius always increases absorption and the local maximum corresponds to increasing value of the dimensionless stream-wise coordinate on the tube surface ε. This is shown in figures 6.30 and 6.31; where Sherwood number is plotted against the dimensionless stream-wise coordinate, for different tube radii.

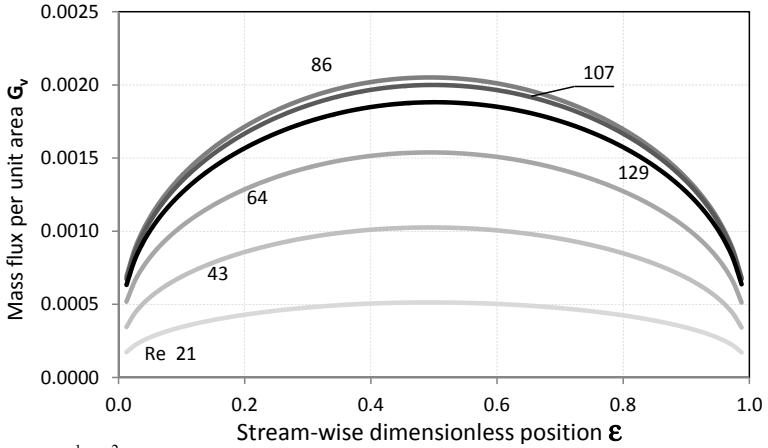

Fig. 6.32 Local mass flux [$kg \cdot s^{-1} m^{-2}$] at the tube wall for different Reynolds numbers at reference conditions of a refrigerating machine

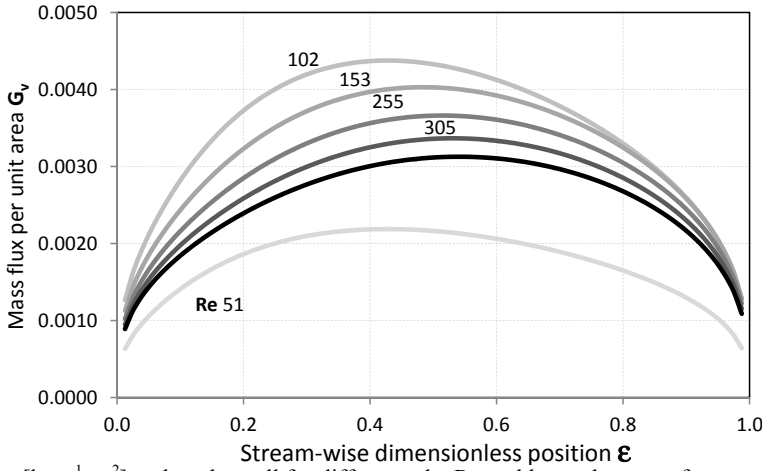

Fig. 6.33 Local mass flux [kg·s^{-1} m^{-2}] at the tube wall for different tube Reynolds numbers at reference conditions of a single stage heat transformer

Absorption mass flux per unit area at the interface is primarily influenced by the film thickness and by the effect of partial wetting (Fig. 6.32). G_v appears to be almost independent from the outer tube radius and different curves overlap on a single one.

Since the characteristic equation depends on the value of the tube wall temperature, when this parameter is changed eigenvalues and eigenfunctions coefficients assume different values. Tables 6.10 and 6.11 display eigenvalues and respective eigenfunctions coefficients for two different temperature-boundary conditions at the tube wall of the absorber (respectively 28 and 36℃) in a chiller application.

As a rule, a lower wall temperature brings about an enhancement of heat and mass transfer, both locally and globally. Further, it reduces the extension of the entrance effect.

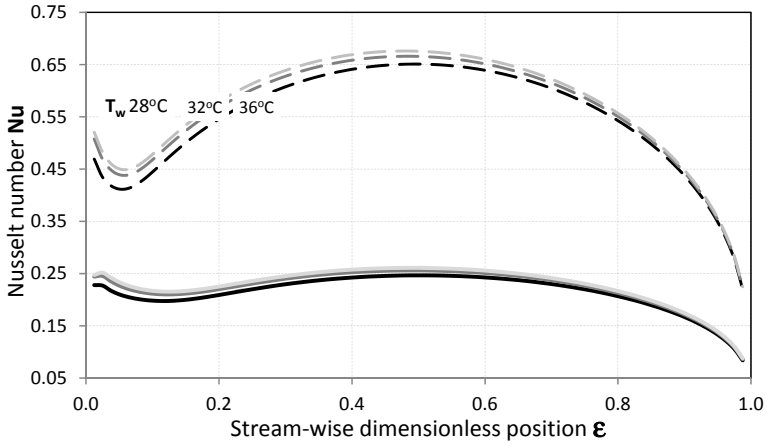

Fig. 6.34 Local Nusselt number for different tube wall temperatures at the reference conditions of a refrigerating machine

What is interesting, and constitutes a confirmation of what was suggested by temperature and concentration fields obtained from the numerical solution presented in the previous chapter, is the result showing how a different wall temperature affects mass transfer more than heat transfer itself. This behaviour can be explained considering the importance of the consequent change in the interface concentration. Adopting a global system point of view and referring to the thermodynamic optimisation described in chapter 3, the cooling water temperature seems appear to be a fundamental parameter to enhance and control the whole system performance, by governing mass transfer inside the absorber and, accordingly, the amount of refrigerant that can be steadily circulated in the thermal cycle.

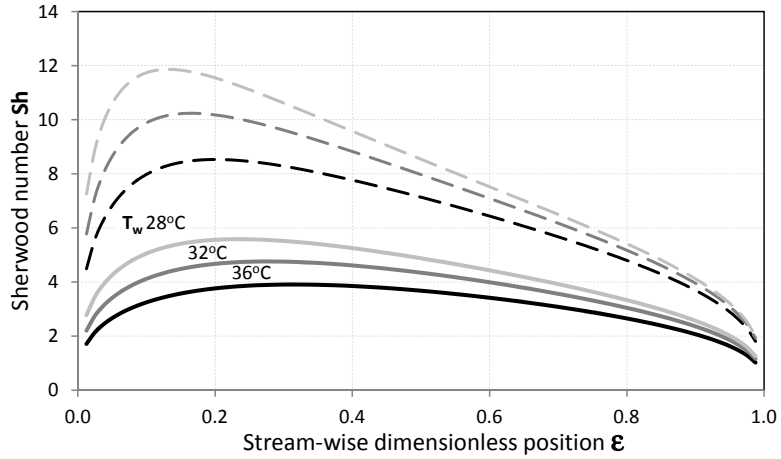

Fig. 6.35 Local Sherwood number for different tube wall temperatures at the reference conditions of a refrigerating machine

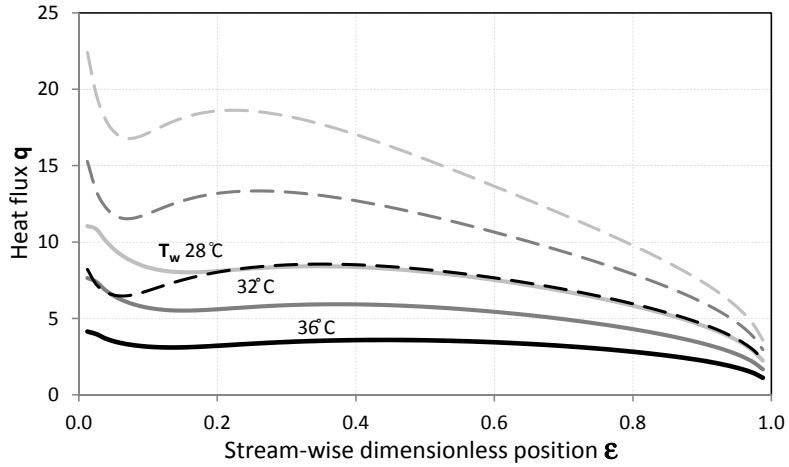

Fig. 6.36 Local heat flux [$kW \cdot m^{-1}$] at the tube wall for different tube wall temperatures at reference conditions of a refrigerating machine

Table 6.10 Eigenvalues and coefficients for typical condition of an absorber in a cooling system with 28℃ wall temperature

n	ξ_n	A_n	B_n
1	0.0424	0.10289	1.34502
2	0.11787	0.112024	-0.57098
3	0.19141	0.144256	0.407294
4	0.26177	0.198829	-0.33727
5	0.32739	0.231232	0.271454
6	0.39118	0.168275	-0.18522
7	0.45881	0.081898	0.104843
8	0.53077	0.036791	-0.05544
9	0.60513	0.017746	0.02958
10	2.23407	1.39557	-1.E-43
11	3.02517	-0.28193	-9.E-70
12	3.82638	1.24079	-4.E-89
13	4.63491	-0.31637	-4.E-106
14	5.44862	1.1987	-2.E-119

Table 6.11 Eigenvalues and coefficients for typical condition of an absorber in a cooling system with 36℃ wall temperature

n	ξ_n	A_n	B_n
1	0.04085	0.171263	1.32792
2	0.11387	0.162211	-0.51733
3	0.18554	0.155852	0.310494
4	0.25596	0.136615	-0.196495
5	0.32538	0.097162	0.112812
6	0.39473	0.047738	-0.049748
7	0.46499	0.005373	0.005431
8	0.53659	-0.020453	0.020743
9	0.60935	-0.033977	-0.034529
10	2.29883	0.991112	-3.E-46
11	3.09535	-0.418891	-1.E-71
12	3.89694	1.0555	-8.E-91
13	4.70315	-0.597441	-4.E-107
14	5.51332	1.18287	-2.E-120

Figure 6.37 shows the global performances of the absorber tube operating in a chiller plant, in an extended range of Reynolds numbers, for different tube wall temperatures, highlighting the possibility to maximise heat and mass transfer selecting the proper solution mass flowrate for fixed inlet and operative conditions. In particular, in order to optimise the system, the importance of considering partial wetting is revealed. Similarly, figure 6.38 represents a global analysis performed considering the tube radius as a parameter.

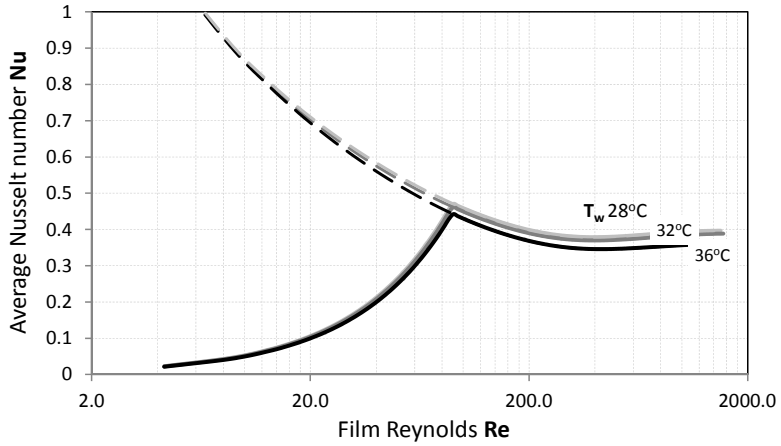

Fig. 6.37 Global Nusselt Number for different tube wall temperatures at the reference conditions of a refrigerating machine

A lower tube radius increases heat and mass transfer coefficient, but, due to a lower heat transfer surface, reduces the heat flux per unit length. Accordingly, the best selection of the tube size results from the compromise between these conflicting effects. It can be observed that the tube radius has a small effect on the global mass transfer, except in the high Reynolds region. This can be explained considering that, as previously stated, the tube size essentially influences the local heat transfer coefficient at the entrance, and, as a result, for high mass flowrates the extension of the entrance region increases and so does the effect of the radius on global heat transfer coefficient. While the highest heat transfer coefficients is always obtained at the breaking condition, mass transfer and heat flux can be maximised for different solution mass flowrates depending on the tube size.

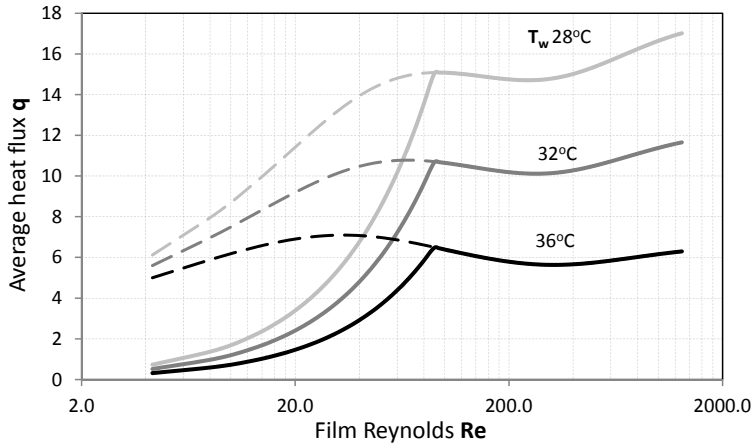

Fig. 6.38 Global heat flux at the tube wall [$kW \cdot m^{-1}$] for different tube wall temperatures at the reference conditions of a refrigerating machine

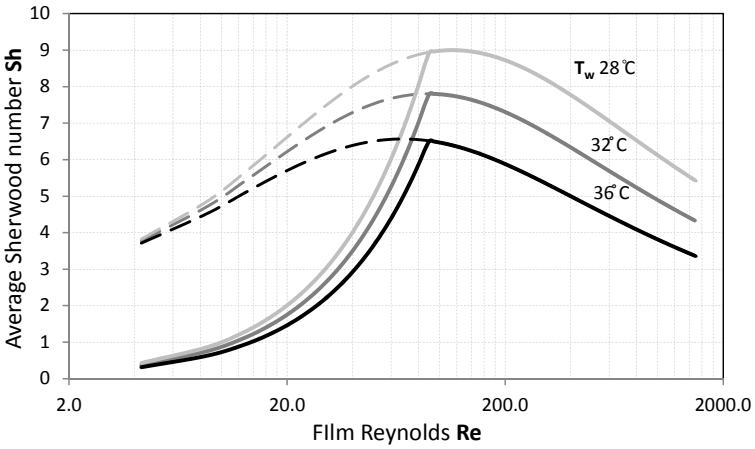

Fig. 6.39 Global Sherwood Number for different tube wall temperatures at the reference conditions of a refrigerating machine

In general, the global performances can be clarified considering the respective local behaviour.

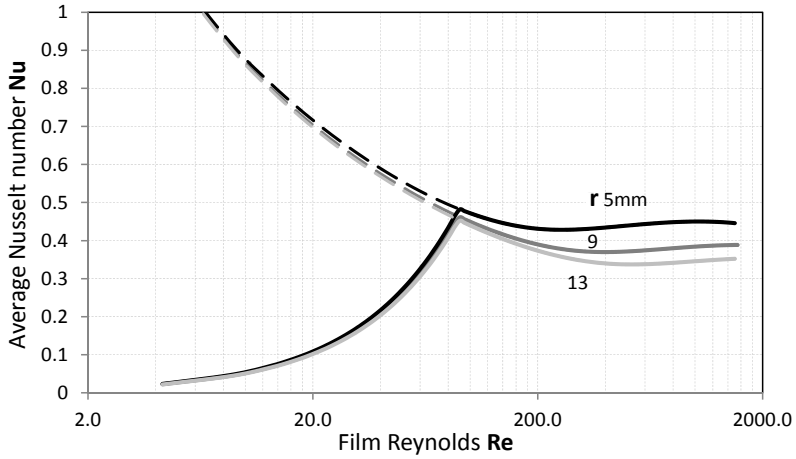

Fig. 6.40 Global Nusselt Number for different tube radii at the reference conditions of a refrigerating machine

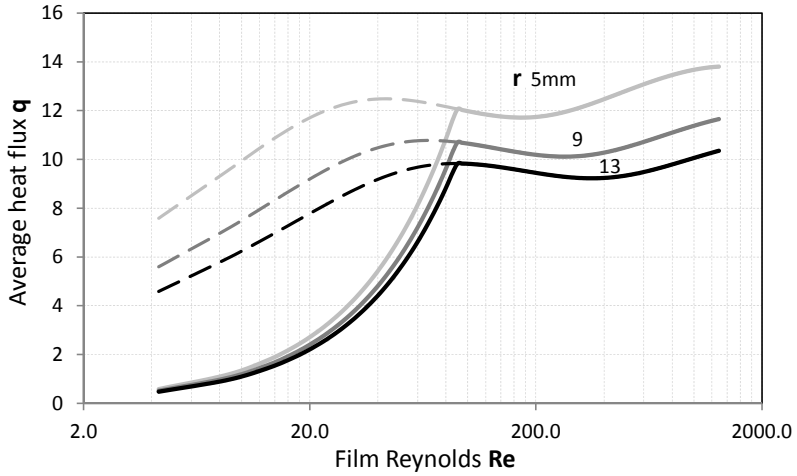

Fig. 6.41 Global heat flux [$kW \cdot m^{-1}$] for different tube radii at the reference conditions of a refrigerating machine

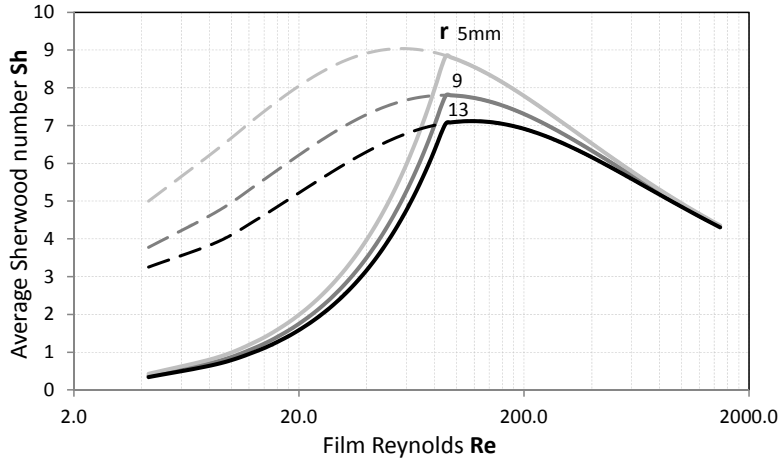

Fig. 6.42 Global Sherwood number for different tube radii at the reference conditions of a refrigerating machine

The wettability of LiBr-H_2O solution can be increased if tensio-active substances are added and the film breaking would occur at a lower Re and thinner film would become stable. Contrarily, if the affinity between the tube surface and the solution gets worse, due to impurities, surface material or surface roughness, dry patches would occur also at higher Re. These two cases are qualitatively represented, respectively, by the lines labelled as 2WR and WR/2.

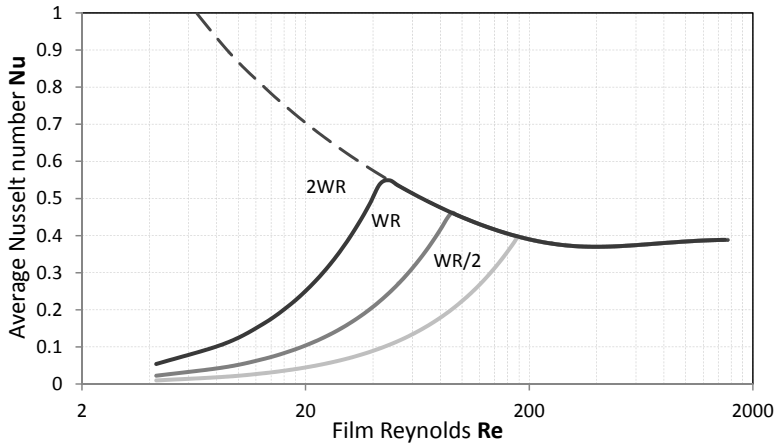

Fig. 6.43 Global Nusselt Number for different solution wettability at the reference conditions of a refrigerating machine

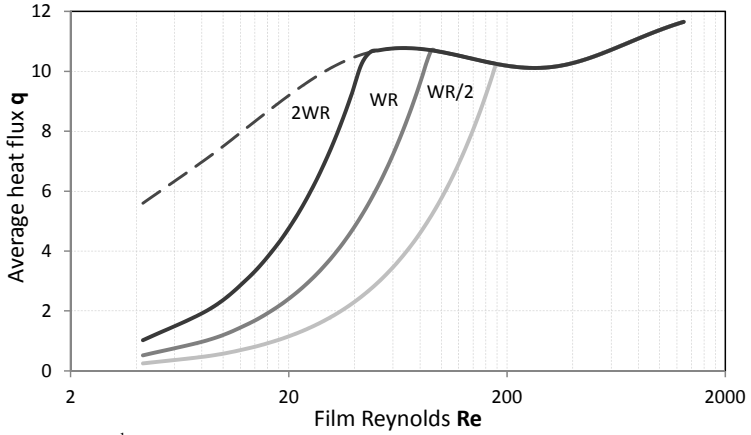

Fig. 6.44 Global heat flux [kW·m^{-1}] for different solution wettability at the reference conditions of a refrigerating machine

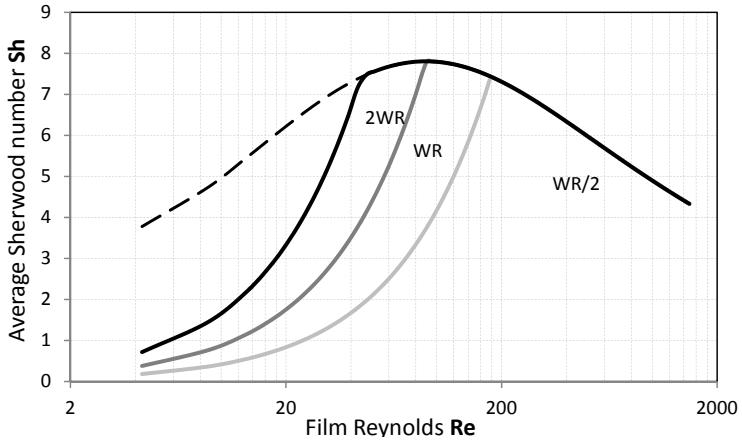

Fig. 6.45 Global Sherwood number for different solution wettability at the reference conditions of a refrigerating machine

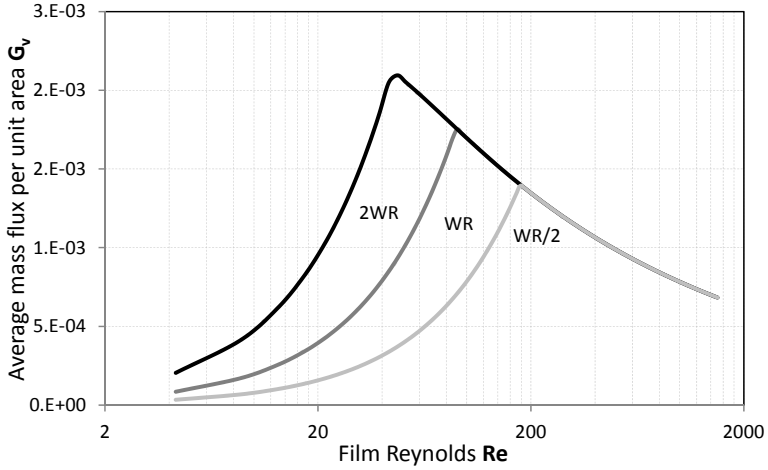

Fig. 6.46 Global mass flux per unit area [kg·s^{-1}m^{-2}] for different solution wettability at the reference conditions of a refrigerating machine

Figures 6.43-6.46 are representative of a chiller application and highlight that both heat and mass transfer can be critically improved by improving the solution wettability, increasing the advantage of low Reynolds operability.

In the following a global performances comparison between the chiller and the heat transformer application is carried out. Higher temperature applications take advantage of the lower viscosity of the fluid and the higher thermal

conductivity, respectively making possible the operation with thinner homogenous films and increasing proportionally the absolute value of heat transfer coefficient (eq. 6.85).

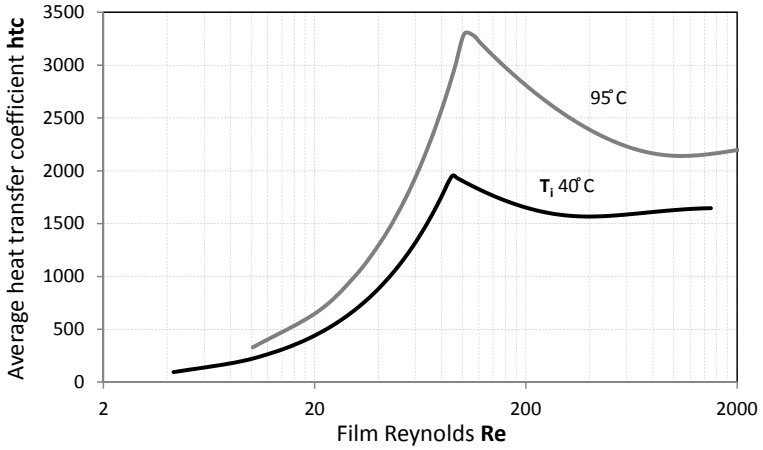

Fig. 6.47 Comparison of the global heat transfer coefficient [$W \cdot K^{-1} m^{-2}$] between chiller and heat transformer applications

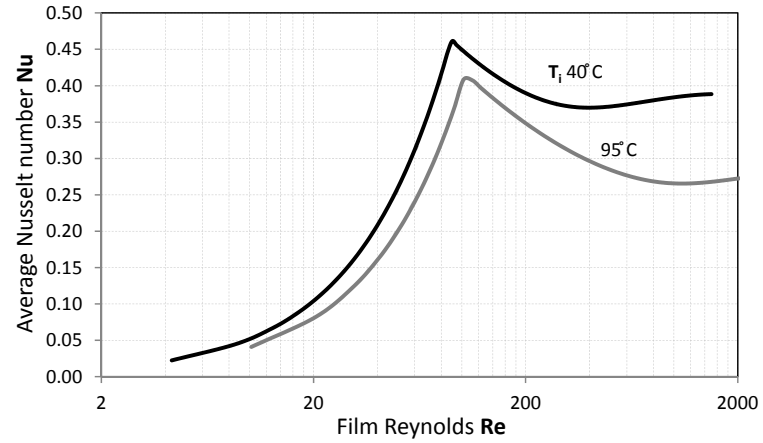

Fig. 6.48 Comparison of the global Nusselt number between chiller and heat transformer applications

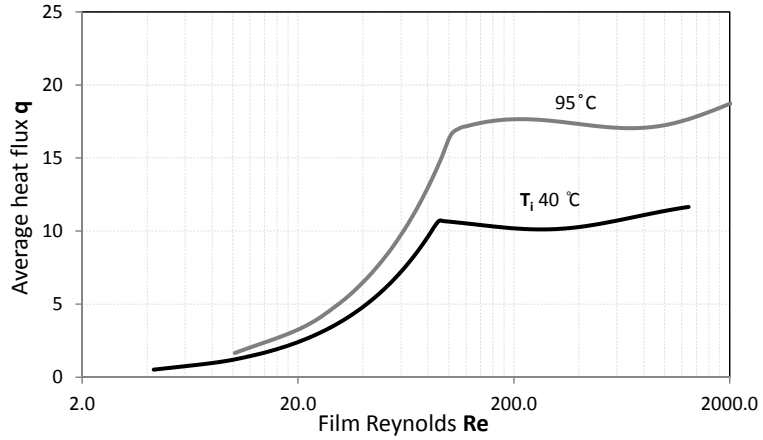

Fig. 6.49 Comparison of the global heat flux per unit length [$kW \cdot m^{-1}$] between chiller and heat transformer applications

Similarly, mass transfer coefficient (Fig. 6.50) is higher for higher temperature applications. This can be explained considering again the lower value of viscosity and the higher mass diffusivity, respectively making possible the

operation with thinner homogenous films and increasing proportionally the absolute value of mass transfer coefficient (eq. 6.86).

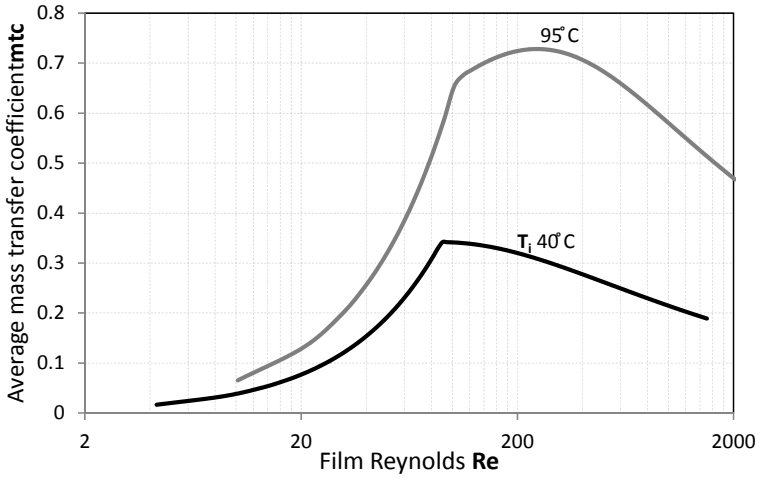

Fig. 6.50 Comparison of the global mass transfer coefficient [$m \cdot h^{-1}$] between chiller and heat transformer applications

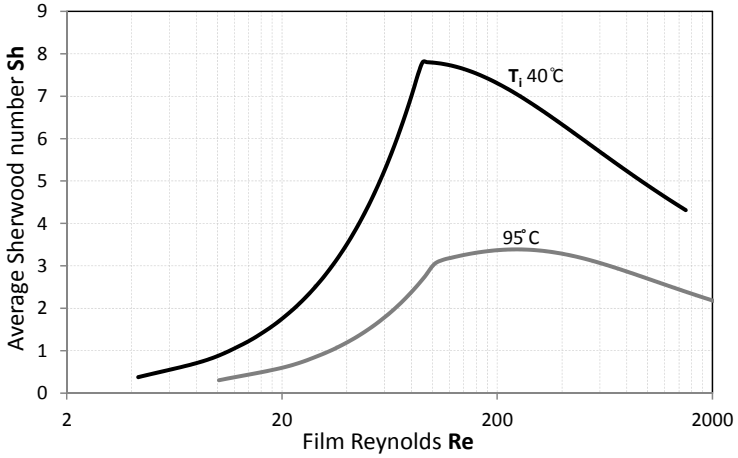

Fig. 6.51 Comparison of the global Sherwood number between chiller and heat transformer applications

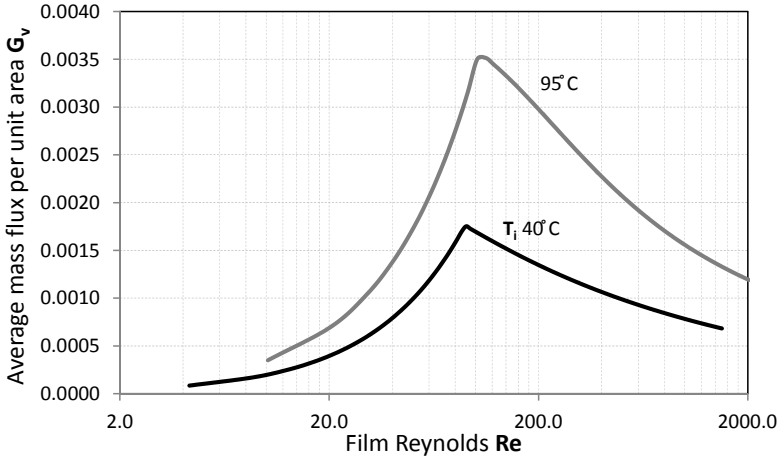

Fig. 6.52 Comparison of the global mass flux per unit area [$kg \cdot s^{-1}\ m^{-2}$] between chiller and heat transformer applications

6.8 Summary

An analytical study of the two-dimensional governing equation of falling film absorption over a horizontal cooled tube has been presented. The exact solution for coupled mass transfer into laminar absorptive film over a single horizontal tube has been obtained with the method of separation of variables as Fourier series functions and exponential terms. The Nusselt integral solution for the two dimensional velocity field and film thickness distribution, have been assumed. Furthermore, a simplified linear model for partial wetting has been used to extend the accuracy of the solution to the low Reynolds operative conditions. The solution, which gives the concentration distribution inside the falling film, has been used in order to characterise the coupled heat and mass transfer phenomena occurring. A parametric analysis has been performed in order to study exhaustively the dependence of the solution on geometrical and operative parameters of interest. Different correlated phenomena have been described and results can be used to maximise heat and mass transfer performances of the system.

The single tube model can be employed as a computationally light and accurate module in component and system simulations for actual application design and control.

Chapter 6,
Extended range analytical expression of heat and mass transfer coefficients

Chapter 7, Experimental transfer performances of horizontal tube falling absorbers

In this chapter, the experimental apparatus employed to perform a first validation of the model presented is described in its features and in its operability. This machine is equipped with suitable sensors for a reliable evaluation of the global heat transfer coefficient, and with a couple of windows for direct visual access inside the absorber. In this configuration, flow visualisation can be compared to the data gathered through the acquisition system in order to support the quantitative measurement with a qualitative description of the flow, which in turn is useful to appraise the consistency of the introduced simplifying assumptions in the modelling efforts presented in the previous chapters.

7.1 Experimental equipment

As a critical component of absorption systems in all their configurations, the absorber realises refrigerant saturation into the liquid solution in order to effectively pump the latter to a higher pressure level (heat pump or chiller) or to produce a thermal useful effect by the release of the heat of absorption characteristic of the process (heat transformer). Accordingly, besides the fact that a validation of the modelling efforts illustrated in the previous chapters is required, an experimental characterisation of the performance of this device is always of substantial importance for the scientific and technical progress, as well as a continuous development of better prediction tools, regardless the possible availability of well-validated models. Thus, a horizontal tube heat exchanger resembling commercial falling film absorbers was conceived and built as the measuring test section to characterise experimentally the performance of these devices.

To operate the system steadily reproducing the operative condition of absorbers working in existing plants or systems yet to be designed, the main chamber is sealed and evacuated, and integrated with the absorptive solution circuit (aqueous Lithium Bromide). This latter consist of inlet distributer, outlet port, solution pump and a flooded heater to generate (desorb) vapour and increase the concentration of the solution to be delivered at the inlet of the absorber.

The cooling system is the counter-part assuring heat balance and steady operability of the absorber. Furthermore, a condenser supplied by the cooling water circuit is required for the control of the solution concentration.

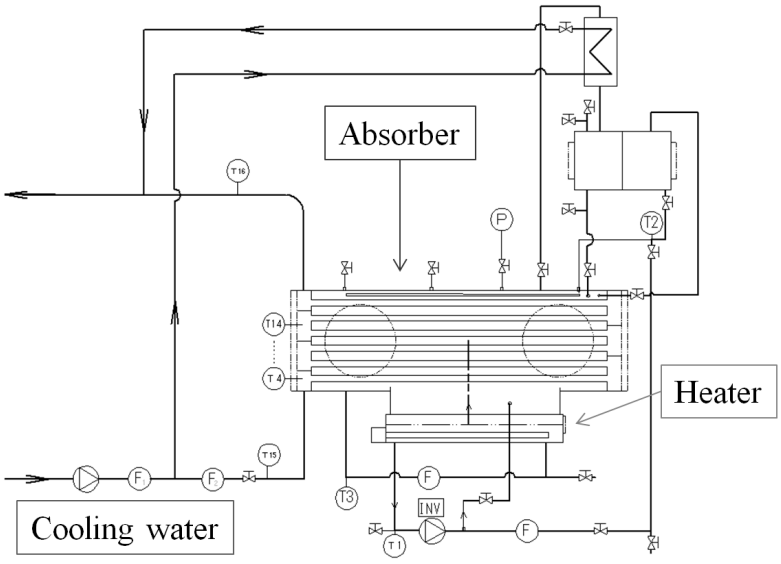

Fig. 7.1 Conceptual schematic of the experimental apparatus

Figure 7.1 represents the system conceptually, whereas the main geometrical features of the absorber are summarised in Table 7.1.

Table 7.1 Geometrical features of the absorber

Parameter	Unit	Value
Outer diameter	mm	16
Tube length	mm	856
No. of tubes	/	10
Tube columns	/	1

The absorber's tubes employed are smooth plain-surface copper tubes, as shown in figure 7.2.

Fig. 7.2 Plain surface copper tubes employed in the experimental apparatus

To reach the desired conditions the vessel is preliminary vacuumed. At this phase, the cooling water is not flowing inside the tube to avoid vapour absorption. Successively, while circulating low solution flow-rate, the inlet concentration is increased by heating the solution to desorb water vapour, which is gathered and liquefied in the condenser, where the cooling water is delivered at 5^{o}C. Once the concentration has reached the desired level, the cooling water is delivered inside the tube in order to increase its inlet temperature to 32^{o}C at the desired mass flowrate. This temperature is kept constant with an independent system. Finally, the solution mass flowrate is brought to the desired value and controlled with the solution pump inverter; meanwhile, concentration and vapour pressure are accurately adjusted by means of the heater and the condensed water reserve, respectively, to 63% and 0.87 kPa.

The steady operability of the absorber can be described as follows; vapour is generated by heating the weak solution coming from the absorber, and is supplied to the absorber vessel. The highly concentrated solution from the heated reservoir is delivered to the distributor, which releases it uniformly on the first tube. The solution is cooled down by the cooled tube and absorption occurs at the solution interface. The heat released by this exothermic process is rejected to the cooling water circulating inside the tube. Then, depending on the hydrodynamic conditions the solution flows to the next tube in the form of either droplets or liquid jets. When the solution leaves the last tube its concentration reaches the lowest value (weak solution). By transporting this lowly concentrated solution to the heated reservoir, the cycle can be repeated steadily for the sake of an accurate measurement of the details at play.

The measuring system includes flowmeters, thermos-resistors, pressure sensors and data acquisition hard-drive, positioned as shown in figure 7.1, and as listed in Table 7.2.

The actual system is displayed in figure 7.2 before being wrapped with thermal insulating material to guarantee minimal heat loss towards the outer environment.

The construction of the two poli-carbonate windows for direct visual access requires paying careful attention to the temperature level reached during the machine operability. Accordingly, operative conditions typical of the absorber in a heat transformer application cannot be tested on this machine. To explore these conditions will be necessary to substitute the poli-carbonate with glass, or operate without a direct visual access.

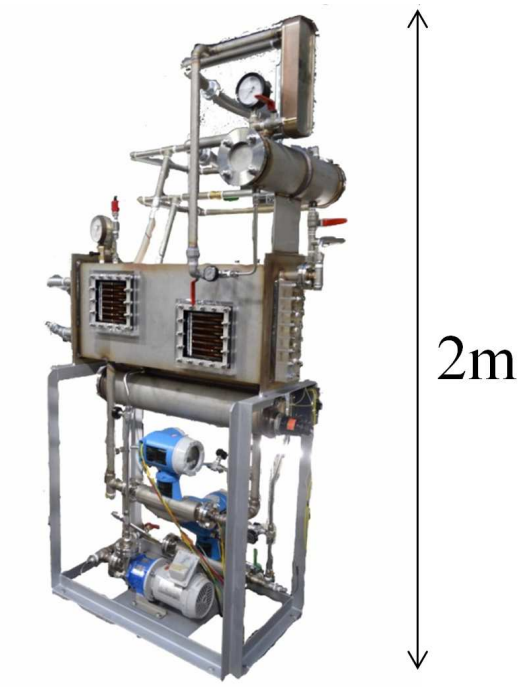

(a)

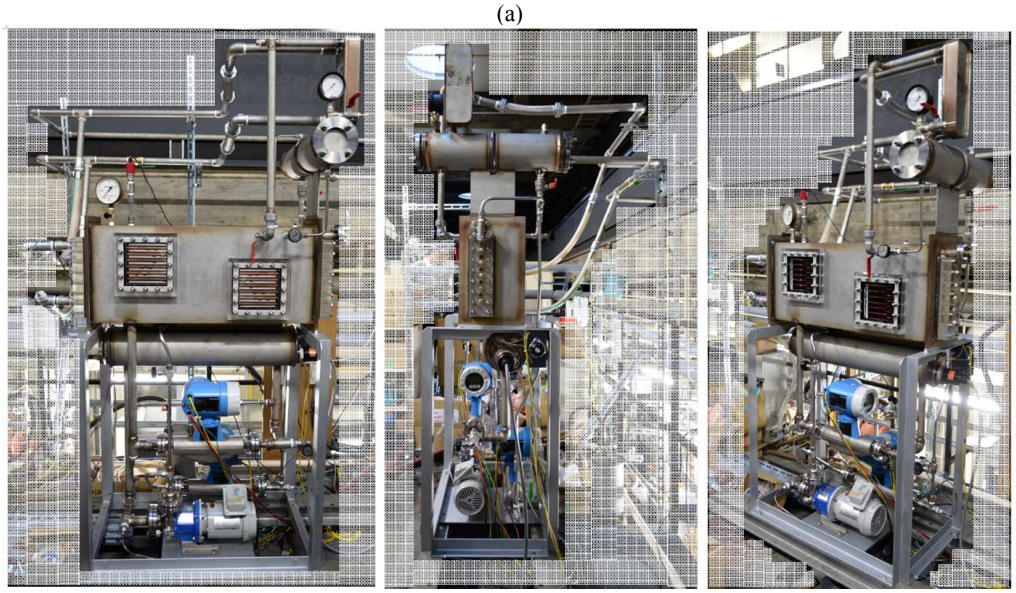

(b)

Fig. 7.3 Actual machine in its testing environment (b) and isolated from the background (a)

7.2 Data reduction

In order to extract the value of the external heat transfer coefficient from the measured quantities, the overall heat transfer coefficient is defined and calculated as in eq. 7.1 employing logarithmic temperature difference.

$$U = \frac{Q_g}{A_g}\left(\frac{\Delta T_1 - \Delta T_2}{\ln\left(\Delta T_1 / \Delta T_2\right)}\right)^{-1} \tag{7.1}$$

Where the total heat transferred Q is calculated from the measured inlet/outlet temperature and the mass flowrate of the cooling water (eq. 7.2).

Table 7.2 List of the active sensors

Type	Manufacturer	Accuracy/ Range	Active sensors Number
thermo resistance Pt100Ω	Tokyonetu kagaku	±0.15℃	14
Dpharp transmitter - Difference pressure transmitter	Yokogawa	±0.2% / 0 to 3 kPa	1
Promass 80 Coriolis flow meter	Endress + Hauser	±0.0005 g/cm3	1
Promass 80 Coriolis flow meter	Endress + Hauser	±0.15%	1

$$Q_g = \dot{m} C_p \left(T_{c,in} - T_{c,o} \right) \tag{7.2}$$

And the temperature differences refer to the temperature difference between solution and cooling water, respectively, at the inlet and at the outlet of the absorber.

$$\begin{aligned} \Delta T_1 &= T^*_{s,in} - T_{c,in} \\ \Delta T_2 &= T^*_{s,o} - T_{c,o} \end{aligned} \tag{7.3}$$

Since the heat transfer coefficient inside the tube (cooling water side) can be estimated reliably from the well-established Dittus-Boelter relation (eq. 7.4) with the support of well-established fluid properties data [1980SI 日本機械学会蒸気表], the external heat transfer coefficient can be readily obtained from the definition of the overall heat transfer coefficient (eq. 7.5).

$$Nu_c = \frac{\alpha_c d_c}{\lambda_c} = 0.023 Re_c^{0.8} Pr_c^{0.3} \tag{7.4}$$

$$\frac{1}{U} = \frac{1}{\alpha_c} + \frac{1}{r/\lambda} \ln \frac{r}{r_c} + \frac{1}{\alpha} \tag{7.5}$$

7.3 Comparison

Given the accuracy of the sensors installed in the experimental equipment and the data reduction calculation-procedure described in the previous paragraph the uncertainty related to the obtained data can be estimated as follows, and with reference to [130].

Respectively, for the evaluation of the uncertainties of solution flowrate per unit length and Γ external heat transfer coefficient α, eq.s 7.6 and 7.7 are used.

$$d\Gamma = \frac{\partial \Gamma}{\partial \dot{m}_{s,in}} d\dot{m}_{s,in} \tag{7.6}$$

Standard uncertainties components are estimated with reference to Table 7.3, and uncertainties bars are represented in figures 7.4 and 7.6.

$$d\alpha = \frac{\partial \alpha}{\partial U}\frac{\partial U}{\partial T^*_{s,in}}\frac{\partial T^*_{s,in}}{\partial \omega_{s,in}}\frac{\partial \omega_{s,in}}{\partial T_{s,in}}dT_{s,in} + \frac{\partial \alpha}{\partial U}\frac{\partial U}{\partial T^*_{s,o}}\frac{\partial T^*_{s,o}}{\partial \omega_{s,o}}\frac{\partial \omega_{s,o}}{\partial T_{s,o}}dT_{s,o} + \frac{\partial \alpha}{\partial U}\frac{\partial U}{\partial T^*_{s,in}}\frac{\partial T^*_{s,in}}{\partial \omega_{s,in}}\frac{\partial \omega_{s,in}}{\partial \rho_{s,in}}d\rho_{s,i}$$
$$+\frac{\partial \alpha}{\partial U}\frac{\partial U}{\partial T^*_{s,o}}\frac{\partial T^*_{s,o}}{\partial \omega_{s,o}}\frac{\partial \omega_{s,o}}{\partial \rho_{s,o}}d\rho_{s,o} + \left(\frac{\partial \alpha}{\partial U}\frac{\partial U}{\partial T^*_{s,in}}\frac{\partial T^*_{s,in}}{\partial p} + \frac{\partial \alpha}{\partial U}\frac{\partial U}{\partial T^*_{s,o}}\frac{\partial T^*_{s,o}}{\partial p}\right)dp$$
$$+\left(\frac{\partial \alpha}{\partial \alpha_c}\frac{\partial \alpha_c}{\partial \lambda_c}\frac{\partial \lambda_c}{\partial T_{c,in}} + \frac{\partial \alpha}{\partial \alpha_c}\frac{\partial \alpha_c}{\partial Re_c}\frac{\partial Re_c}{\partial \mu_c}\frac{\partial \mu_c}{\partial T_{c,in}} + \frac{\partial \alpha}{\partial \alpha_c}\frac{\partial \alpha_c}{\partial Pr_c}\frac{\partial Pr_c}{\partial T_{c,in}} + \frac{\partial \alpha}{\partial U}\frac{\partial U}{\partial \dot{Q}}\frac{\partial \dot{Q}}{\partial C_{p,c}}\frac{\partial C_{p,c}}{\partial T_{c,in}} + \frac{\partial \alpha_o}{\partial U}\frac{\partial U}{\partial \dot{Q}}\frac{\partial \dot{Q}}{\partial T_{c,in}}\right.$$
$$\left.+\frac{\partial \alpha}{\partial U}\frac{\partial U}{\partial T_{c,in}}\right)dT_{c,in} + \left(\frac{\partial \alpha}{\partial \alpha_c}\frac{\partial \alpha_c}{\partial \lambda_c}\frac{\partial \lambda_c}{\partial T_{c,o}} + \frac{\partial \alpha}{\partial \alpha_c}\frac{\partial \alpha_c}{\partial Re_c}\frac{\partial Re_c}{\partial \mu_c}\frac{\partial \mu_c}{\partial T_{c,o}} + \frac{\partial \alpha}{\partial \alpha_c}\frac{\partial \alpha_c}{\partial Pr_c}\frac{\partial Pr_c}{\partial T_{c,o}} + \frac{\partial \alpha}{\partial U}\frac{\partial U}{\partial \dot{Q}_g}\frac{\partial \dot{Q}_g}{\partial C_{p,c}}\frac{\partial C_{p,c}}{\partial T_{c,o}}\right. \quad (7.7)$$
$$\left.+\frac{\partial \alpha}{\partial U}\frac{\partial U}{\partial \dot{Q}_g}\frac{\partial \dot{Q}_g}{\partial T_{c,o}} + \frac{\partial \alpha}{\partial U}\frac{\partial U}{\partial T_{c,o}}\right)dT_{c,in} + \left(\frac{\partial \alpha_o}{\partial \alpha_i}\frac{\partial \alpha_i}{\partial Re}\frac{\partial Re}{\partial \dot{m}_{cw}} + \frac{\partial \alpha_o}{\partial K_o}\frac{\partial K_o}{\partial \dot{Q}_g}\frac{\partial \dot{Q}_g}{\partial \dot{m}_{cw}}\right)d\dot{m}_c$$

Table 7.3 Sensors uncertainty budget

Standard uncertainty component	Source of uncertainty	Value ±		Probability distribution	Divisor	Standard uncertainty		Sensitivity coefficient		Standard uncertainty	
$un(T_{s,in})$	repetition of solution inlet temperature	0.1936	K	-	1	0.1936	K	-0.008195	kW/(m^2·K)/K	0.002878	kW/(m^2·K)
	uncertainty of thermometer	0.2728		Rectangular	√3	0.1575					
$un(T_{s,o})$	repetition of solution outlet temperature	0.1638	K	-	1	0.1638	K	-0.01205	kW/(m^2·K)/K	0.003621	kW/(m^2·K)
	uncertainty of thermometer	0.2370		Rectangular	√3	0.1368					
$un(\rho_{s,in})$	repetition of solution inlet density	1.034	kg/m^3	-	1	1.034	kg/m^3	-0.01558	kW/(m^2·K)/(kg/m^3)	0.1060	kW/(m^2·K)
	uncertainty of densimeter	10.00		Rectangular	√3	5.774					
$un(\rho_{s,o})$	repetition of solution outlet density	1.018	kg/m^3	-	1	1.018	kg/m^3	-0.02394	kW/(m^2·K)/(kg/m^3)	0.1626	kW/(m^2·K)
	uncertainty of densimeter	10.00		Rectangular	√3	5.774					
$un(p)$	repetition of pressure	0.02317	kPa	-	1	0.02317	kPa	-7.199	kW/(m^2·K)/kPa	0.1947	kW/(m^2·K)
	uncertainty of pressure gauge	0.006705		Rectangular	√3	0.003871					
$un(T_{c,in})$	repetition ofcooling water inlet temperature	0.1412	K	-	1	0.1412	K	-0.1004	kW/(m^2·K)/K	0.02658	kW/(m^2·K)
	uncertainty of thermometer	0.2140		Rectangular	√3	0.1236					
$un(T_{c,o})$	repetition of cooling water outlet temperature	0.1582	K	-	1	0.1582	K	0.4729	kW/(m^2·K)/K	0.1378	kW/(m^2·K)
	uncertainty of thermometer	0.2305		Rectangular	√3	0.1331					
$un(\dot{m}_c)$	repetition of cooling water mass flow rate	0.01375	kg/s	-	1	0.01375	kg/s	10.80	kW/(m^2·K)/(kg/s)	0.1563	kW/(m^2·K)
	uncertainty of mass flow meter	0.001244		Rectangular	√3	0.0007185					
Combined standard uncertainty : $un_c(x_i)$										0.3460	kW/(m^2·K)
Expanded uncertainty (Coverage factor = 2.0) : Un										0.69	kW/(m^2·K)

Table 7.4 presents the operative conditions selected for this experiment. As can be observed the target application is an absorber operating in a chiller plant with highly concentrated solution.

The range of solution mass flowrates is limited by the maximum pump capacity, the size of the holes in the distributer and the cross-sectional area of the pipe connecting the heated vessel to the distributer.

Since the attention is focused on the transfer processed occurring outside the tube, on the cooling water side of the equipment, fixed inlet cooling water temperature $T_{c,in}$ and cooling water flowrate are controlled and kept steadily constant in order to assure equivalent heat transfer conditions while changing the solution flowrate outside the tube.

Table 7.4 Operative conditions selected for the experimental validation

ω_{in}	p [kPa]	$T_{v,sat}$ [^{o}C]	$T_{c,in}$ [^{o}C]	u_c [m·s^{-1}]
63%	0.87	5	32	1.5

Simulation performed both with the numerical and analytical models in this same condition are compared with the experimental data in figure 7.4. Noteworthy agreement can be observed for both analytical and numerical modelling approaches. Moreover, in case a partial wetting model was not included, simulated heat transfer coefficients would have followed an increasing trend for decreasing solution mass flowrates. This makes evidence of the necessity to consider

partial wetting phenomena in the standard operative range of absorbers operating in commercial and industrial plants. The main discrepancy between simulation and experiments can be related to that part of the process that occurs on the bottom of the tube during droplet formation and free falling, which are neglected in the present modelling effort. The first phenomenon increases the contact time of the solution with the tube, and, most of all, introduces recirculating convective motions inside the growing droplet, which mixes the solution promoting in turn higher absorption rates. These phenomena increase their importance at low mass flowrates and at low surface wetting [106].

The change of slope highlights the breaking point of the uniform film into partially wetting rivulets. The range of solution mass flowrates is limited by the maximum pump capacity, the size of the holes in the distributer and the cross-sectional area of the pipe connecting the heated vessel to the distributer. The diverging behaviour of the simulations is occurring locally, since also the analytical solution starts increasing at higher flowrates, and can be explained considering a higher effect of the entrance region of the solution film colliding with the tube at its stagnation point on the numerical solution in predicting.

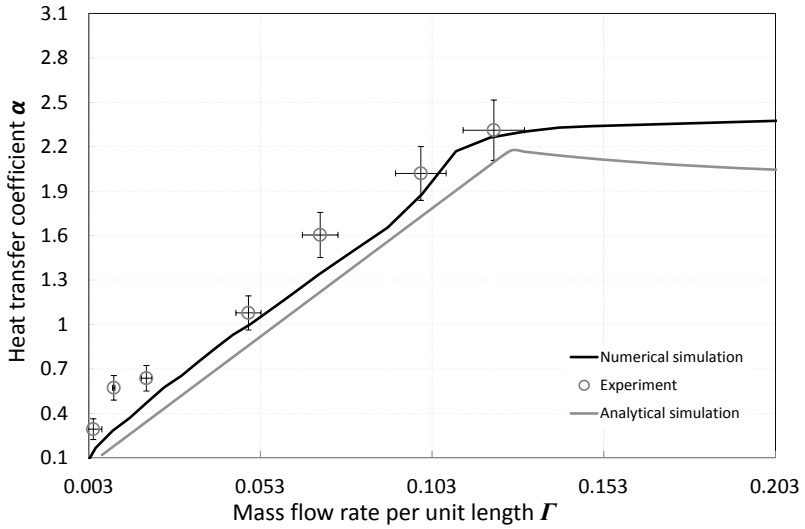

Fig. 7.4 Comparison between the heat transfer coefficient [$W \cdot K^{-1} m^{-2}$] obtained from simulations and experiments

Video were recorded through the side visual access with a (Photron FASTCAM SA5) (high-speed camera). This helps identifying the film breaking point Re_b and gives the way for a first estimation of the wetting ratio at lower Reynolds (see Fig.s 7.5 a-f). The images are not completely clear because of droplets formed on the window.

As shown in the technical drawings in the appendix, the two windows face the bottom five (on the right side) and the top five tubes (on the upper left side).

A first glance of the captured photos, gives a qualitative description of the wetting behaviour; the wetting ability of the 63% concentration aqueous Lithium-Bromide solution increases regularly as the flowrate is augmented. Also, observing locally the wetted area of the tube it is possible to state that in general the first half of the cylindrical surface is better wetted by the solution than in the second half of the tube.

Additionally, as the droplet frequency increases the rivulet extension increases, but the distance between them remains almost constant (close to Taylor instability length), thus, the wetting ability is globally improved.

According to figure 7.5f, a solution flowrate of 12.4 kg/ms^2 is able to wet completely the exchange surface of the absorber.

It can be also stated that this result matches the prediction of the stability criterion of a uniform film presented previously (Fig. 7.4 and Fig. 7.6).

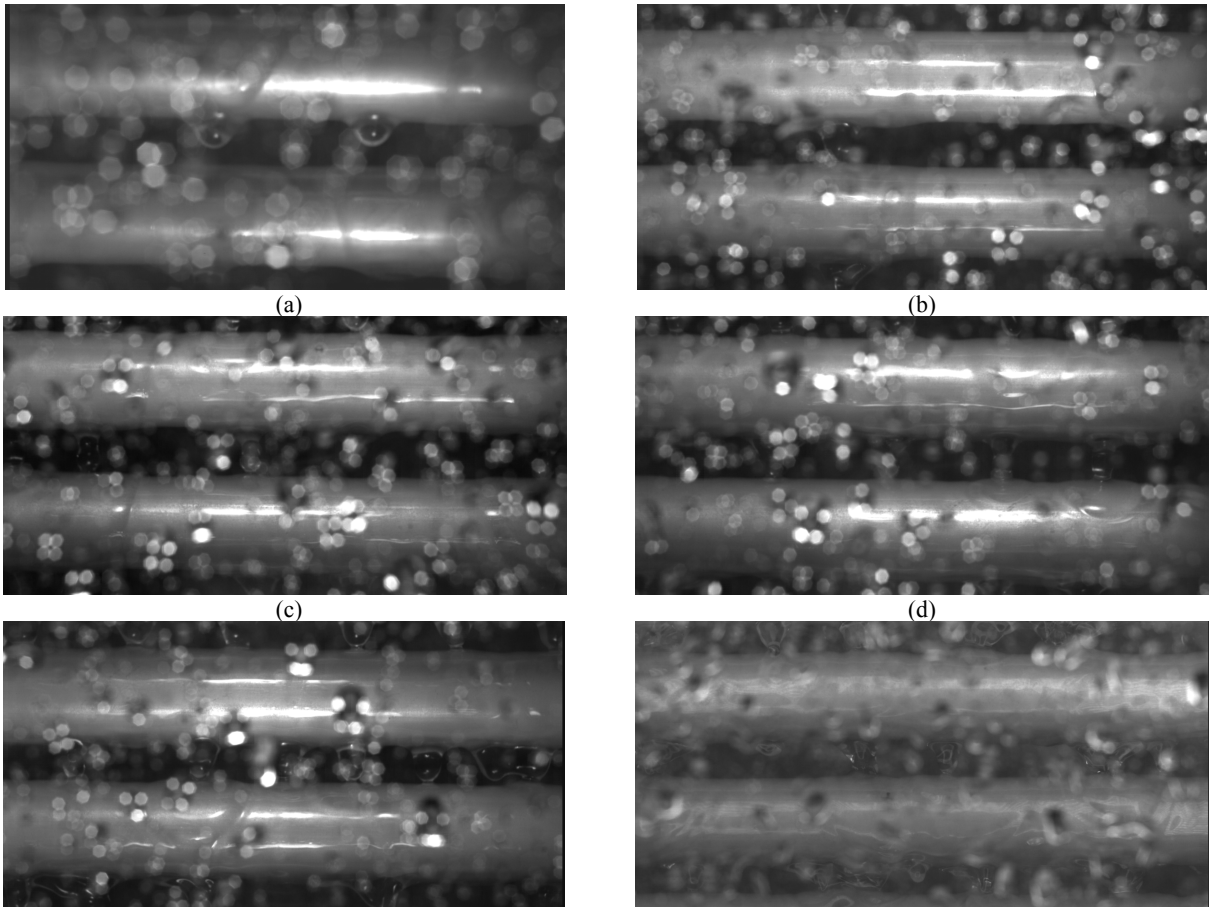

Fig. 7.5 Direct flow visualisation of the data plotted in Fig 7.4 for different solution specific mass flowrates (a) 1.03 [kg·min^{-1}] (b) 3.09 [kg·min^{-1}] (c) 4.10 [kg·min^{-1}] (d) 7.21 [kg·min^{-1}] (e) 10.2 [kg·min^{-1}] (f) 12.4 [kg·min^{-1}]

This range of mass flowrates would be wide enough to capture the change of slope due to the threshold between uniform film and rivulet configurations, in case surfactants additives are mixed with the aqueous lithium bromide solution.

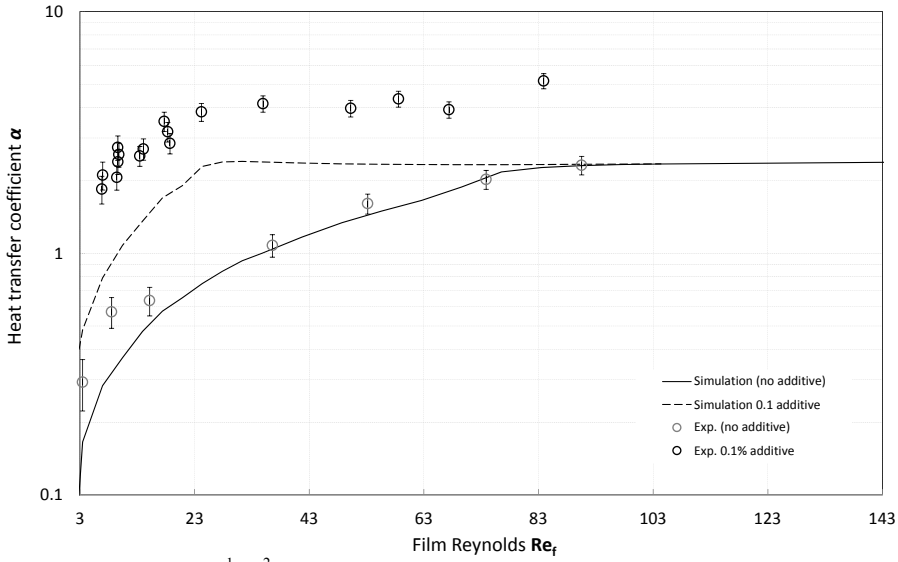

Fig. 7.6 Heat transfer coefficient [W·K^{-1} m^{-2}] from simulations and experimental data including operability with surfactants additive

However, in order to predict heat and mass transfer coefficients, the enhancement related to Marangoni effect (observable in Fig. 7.7) needs to be accounted for. Nonetheless, figure 7.6 highlights the change of slope of the curve and how the breaking point can be predicted by the model presented in this thesis. The value of surface tension has been adjusted with reference to literature [131] when 0.1% of ethanol is added as a surfactant.

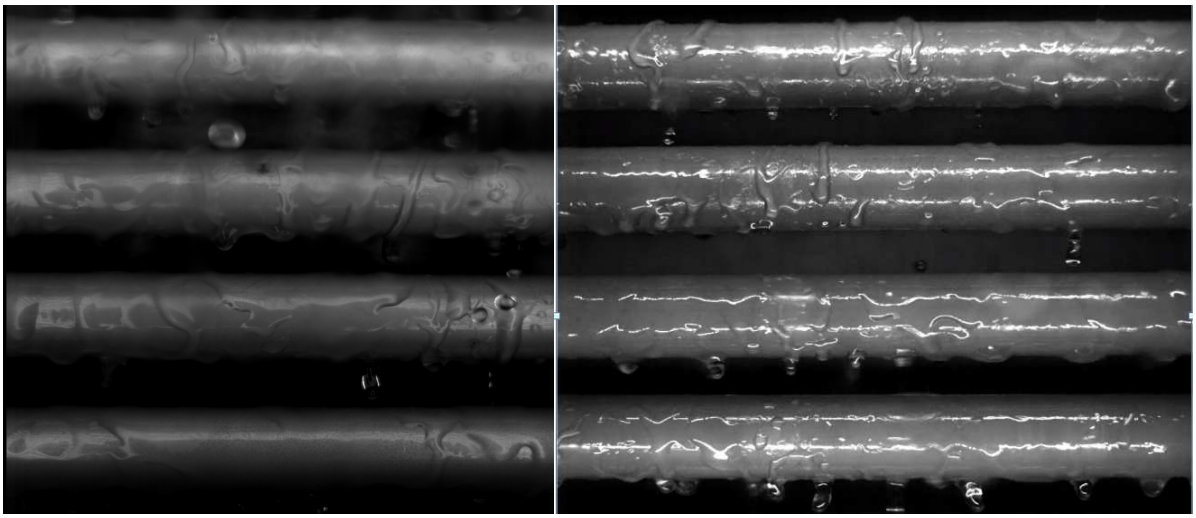

(a) (b)

Fig. 7.7 Flow visualisation with surfactants additives (a) Γ=0.026 [kg・$m^{-1}s^{-1}$] (b) [Γ=0.01 kg・$m^{-1}s^{-1}$]

Additionally simulations agree with previously measured experimental data, obtained on a different machine but characterised by a similar concept and instrumented correspondingly to evaluate the absorber's heat transfer coefficient. Operative conditions obtained for different concentrations, pressure and temperature are displayed in Table 7.5, and plotted as functions of the film Reynolds number.

Table 7.5 Operative conditions of previously performed experiments on a different apparatus

Pr	ω_{in}	T_{in} [°C]	T_c [°C]	P [kPa]
4.89	63%	179	162	149
5.02	56%	150	134	104
7.57	59%	160	140	118
8.89	61%	120	98	25
12.5	60%	80	50	10
15.3	60%	60	32	2

According to the previous assumptions and calculation method, the following diagrams have been obtained for a 10 tube absorber. Different working conditions, regarding solution temperature (between 180-60℃) and concentration, have been considered and set consistently with those of the experimental data. Higher temperatures are associated to higher transfer coefficients and better wetting ability. Numerical simulations which model partial wetting behaviour are able to follow experimental results accurately in a wide range of conditions (Fig. 7.8).

If data are mapped in a dimensionless form, where the independent parameter is the ratio of Reynolds to the value of the critical Reynolds at which breaking occurs, results collapse on a single curve (Fig. 7.9) and can be approximated by a dimensionless empirical correlation (eq. 7.8) for the broken film region, obtained using Reynolds and Galileo numbers.

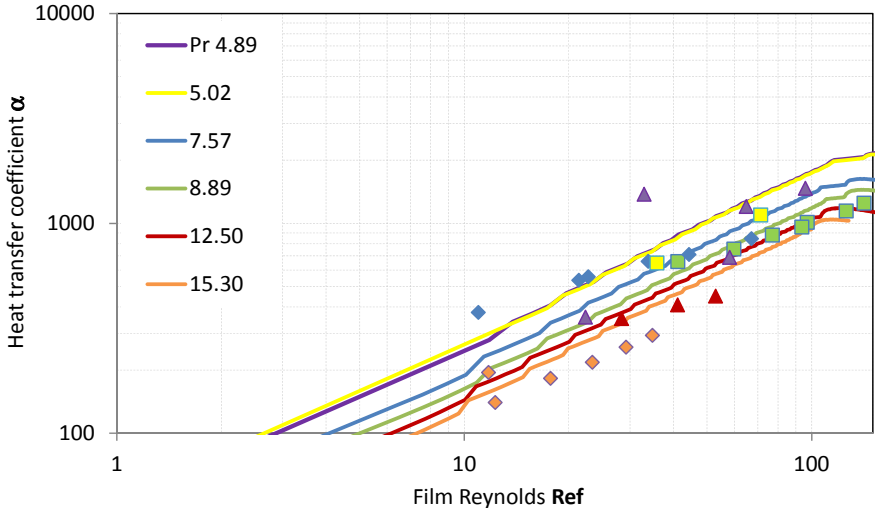

Fig. 7.8 Comparison between simulated heat transfer coefficient [$W \cdot K^{-1}\ m^{-2}$] and experiments as a function of Reynolds number for different temperature operability

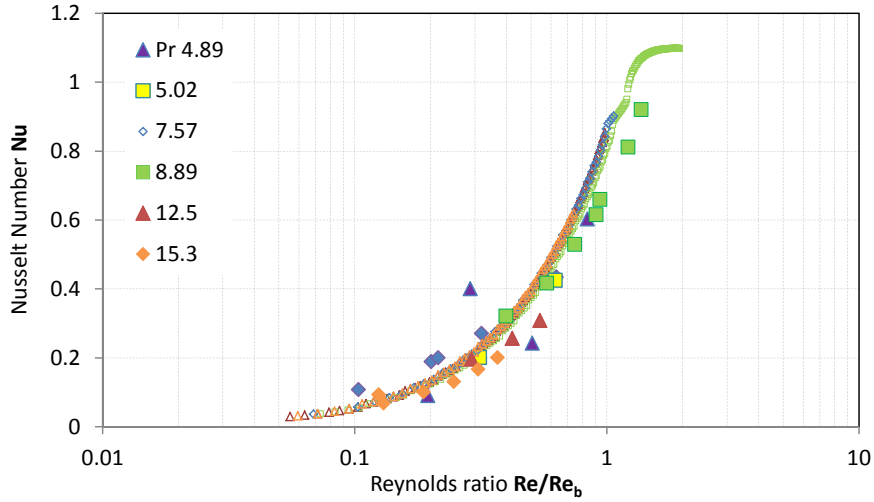

(a)

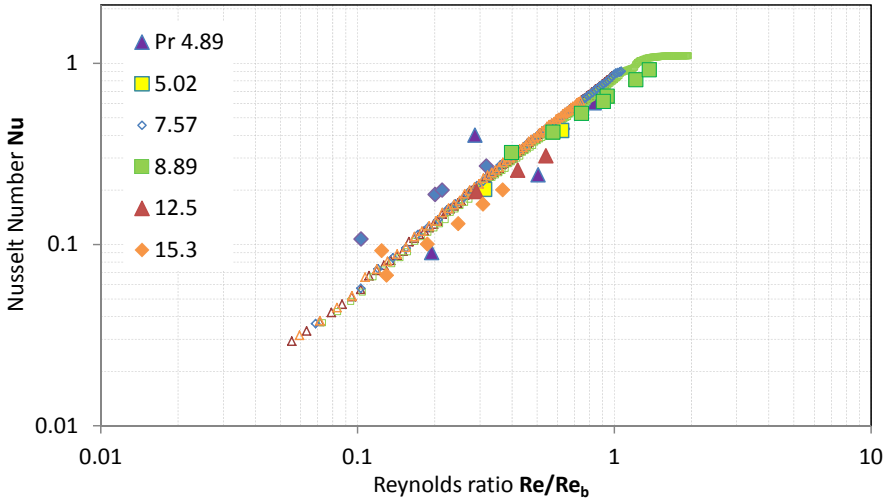

(b)

Fig. 7.9 Comparison and data reduction of simulated and measured Nusselt number as a function of film Reynolds for different operative temperatures of the solution (a) linear (b) logarithmic *y* axis

$$Nu_{\delta m}=0.018152\frac{\mathrm{Re}^{1.0449}}{Ga^{0.052767}} \tag{7.8}$$

In figures 7.8 and 7.9 Prandtl number is used to identify different operative conditions. Despite the simplifying assumptions introduced in the simulation, which have brought to neglect important phenomena like Marangoni effect, coupling with mass transfer, turbulence or wavy surface, both qualitative and quantitative agreements with experiment are shown. Accordingly, further modelling efforts to include the effect of other phenomena and parameters should be compared pragmatically to the possibility of accuracy-improvement related to the inclusion of such details and to the practicability of the eventual employment in global system simulations. In addition, this first approach can be improved by further experimental comparisons. In particular the estimation of the critical breaking condition and visual observations of partial wetting for an extended range of operative conditions can be critical for refining the model accuracy and extending its applicability. Referring to figure 7.4, the most advantageous condition for a falling film heat exchanger corresponds to the critical condition of a uniform film. The semi-empirical relation expressed by eq. 7.6 can be used for actual system design and control, in the low Reynolds region.

-The wetting model, combined with the simplified Nusselt approach for the film heat transfer characterization, shows both qualitative and quantitative agreement with experiments.

-The most advantageous condition for a falling film heat exchanger is the critical condition of a uniform film, hence, to maximise transfer performance of this component, the solution mass flowrate should be controlled in order to assure the proximity to this particular condition.

-The low Reynolds region for falling film heat exchangers, associated with the occurrence of partial tube wetting, can be characterised by a single relation of a reduced number of properly defined dimensionless parameters, with an acceptable accuracy.

-A semi-empirical relation of Nusselt number (eq. 7.6), resulting from the employment of the proposed model, has been obtained and can be used for component design and control in the low Reynolds region.

7.4 Summary

In order to validate the modelling approach developed and presented up to this point of the study, the transfer performance of a real falling film absorber is measured directly on the experimental apparatus designed specifically to reproduce the operability of this component during its operability in actual plants. By instrumenting the machine with suitable sensors for a reliable evaluation of the global heat transfer coefficient, and with a couple of windows for direct visual access inside the absorber, flow visualisation can be compared to the data gathered through the acquisition system in order to support the quantitative measurement with a qualitative description of the flow. Furthermore this is useful to evaluate the consistency of the simplifying assumptions introduced in the modelling efforts presented in the previous chapters.

Experiments validate the model in the partial wetting region and, given the observed qualitative and quantitative agreements, the single tube model can be employed as an accurate module in component and system simulations for actual application design and control.

Chapter 7,
Experimental transfer performances of horizontal tube falling absorbers

Chapter 8, Conclusions and future plan

As pointed out in the preface of this thesis, the main objective of this work arises from the awareness that, even though the recent technical progress in the field of absorption heat pumps is undeniable, this has not been running parallel to the theoretical background needed for an accurate prediction, optimisation and control of their performance, which instead, in some circumstances, falls short when directly put into play. As a result, when accurate models are lacking, systems designed and operated empirically might be not optimised for their purpose and working far from their best condition. Furthermore, this remark is more and more significant when increasingly complex configurations are considered. As a result, the research effort carried out and presented aims at contributing to reduce this discrepancy.

The author believes that by narrowing this gap and bringing theory and practice to a close cooperation is fundamental for the realisation of efficient technical solutions for energy conversion systems.

This chapter is intended to summarise the results obtained in order to draw significant conclusions and future prospects.

8.1 Conclusions and future plan

In conclusion, the modelling approach adopted enabled the author to address a specific issue, namely the effect of partial wetting of the exchange surface on the transfer performance of falling film absorbers, while keeping in mind the overall system performance. This work gives a way to a widely applicable and physically based approach which is believed to be helpful for actual system design and optimisation. Additionally, the modelling approach developed is believed to provide useful information also for the control of these devices.

Accordingly, by employing a heat and mass transfer model that includes the effect of wetting phenomena, and by using the optimisation criteria hereby developed, the specific device as well as the whole system performance can be maximised and carefully controlled in a wide range of conditions. Equivalently, for the same performance of the system the plant can be reduced in its size, thus reducing its weight and its cost.

Referring to each chapter, the following main conclusive considerations can be stated:

By combining the fundamental thermodynamic principles and by analytically modelling the fundamental transformations constituting absorption cycles, chapter 2 presents a general thermodynamic optimisation criterion for three thermal absorption systems and define dimensionless parameters suitable for an overall system design and control. Also, by including the second principle of thermodynamics process limitations and characteristics are highlighted in a way that shows how to improve existing systems performance, thus enabling the engineer to perform plant diagnostics. In particular, dimensionless temperature difference parameters give a method for controlling the system in its operability by acting on driving fluid and cooling water inlet temperatures.

This method has been exemplified for a chiller and a heat transformer application cases, referring to experimental data of systems described in previous literature and showing that these are not operating at the maximum of their performance. However, by adjusting the inlet temperatures of the fundamental heat exchangers it is possible to enhance significantly these systems performance for given design features.

From the parametric analysis performed, general design guidelines have been extracted and the potentiality of these systems has been mapped for a wide range of features and operative conditions, highlighting the critical importance of optimised components and, more precisely, of the absorber.

The local analysis and the numerical model presented in chapter 3 provide detailed information about the transfer performances of the absorption process, which have been integrated to a global scale to optimise the component with reference to the ultimate duty of the system. Hence, optimisation criteria have been defined separately for heat transformers and absorption chillers, and, as a rule, suggest the importance to operate with low solution flowrates with a thin uniform film, avoiding dry patches formation on the exchange surface.

By combining entropy generation minimisation and targeting the global system performance, the optimisation criterion characterises the quality of the energy conversion process, identifies its limitations and brings the absorber in a condition useful to maximise the efficiency of the whole plant. Furthermore, especially when the scale of the analysis is close enough to the scale of microscopic phenomena, entropy represents a critical variable for the understanding of the process itself and the model could still be refined including local effects (entropy jump at the interface, local mixing and turbulence) that could have a significant influence. Consequently, entropy could be a critical parameter with regards to the description of absorption phenomena, and the potential of this local model shows promising results to be expanded and applied to different cases with different purposes.

In order to include partial wetting effect in the absorber model, a criterion for film stability has been presented and its wetting behaviour has been predicted by considering the energetic content of two flow configurations; uniform film and rivulet configurations. This method has been applied to different surface geometries and compared with previous model, experimental data from literature and flow visualisation images directly captured on an experimental test section. Hysteresis phenomena of the film wettability and the solution contact angle have been described and can be used to control accurately and efficiently the system operability.

At the same time, the modelling approach employed can be further improved by including the effects of viscosity and the coupling influence of heat and mass transfer for predicting wetting behaviour and surface tension related phenomena.

To include these hydrodynamic effects in the transfer process the average film thickness and the extension of the film interfaces can be adjusted to consider the partial wetting of a geometrically defined rivulet configuration. As a result the numerical model presented in chapter 5 describes in details the inferences of partial wetting phenomena on heat and mass transfer characteristics of a horizontal tube falling film absorber. Broadly speaking, for the same equilibrium condition (same working pair), three main different regions can be mainly related to different hydrodynamics effect:

- Partial wetting region
- Uniform laminar film region, in which film thickness has the main influence on heat and mass transfer
- Uniform film mainly subject to velocity field effects

To extend the validity of the modelling effort presented and capture the physics of the problem, analytical solutions still maintain their fundamental importance. Hence, as a closing modelling effort, chapter 6 articulates, slims down and summarises the understanding developed in the previous chapters in a detailed, widely applicable and time-saving method to predict heat and mass transfer characteristics of horizontal-tube falling film absorbers. In particular, as demonstrated so far, a two-dimensional model is able to capture the physics of the phenomenon. The solution considers the horizontal tube cylindrical geometry. Also, by means of the inclusion of a film stability criterion and a linear wetting model, partial wetting phenomena are incorporated in the analysis, thus extending the target range of the resulting heat and mass transfer coefficients expressions and, in parallel, increasing their accuracy. The choice of a linear trend with respect to Reynolds number is supported by the theoretical solution given by the application of energy based approaches. A first comparison with the numerical solution is presented and used as a reference to test the validity of the simplifying assumptions introduced.

Finally, experiments and data collections have been performed as a closing point and validate the theoretical absorption model in a wide range of operative conditions.

As a final remark, by repeating the calculation for the optimisation criterion presented in chapter 3 and by using the absorption model that consider also partial wetting phenomena (presented in chapter 5), it is possible to re-establish and refine the conclusions that can be extracted from this approach. In particular, figures 8.1 and 8.2 compare the results obtained neglecting partial wetting and those obtained when this phenomenon is included. Figure 8.1 shows the results obtained for a chiller application case, with reference to the specific parameter *DA* appositely defined in chapter 3, confirming the advantage of operating at low solution flowrates to optimise the operability of the absorber with respect to the final target of the energy conversion system it belongs to.

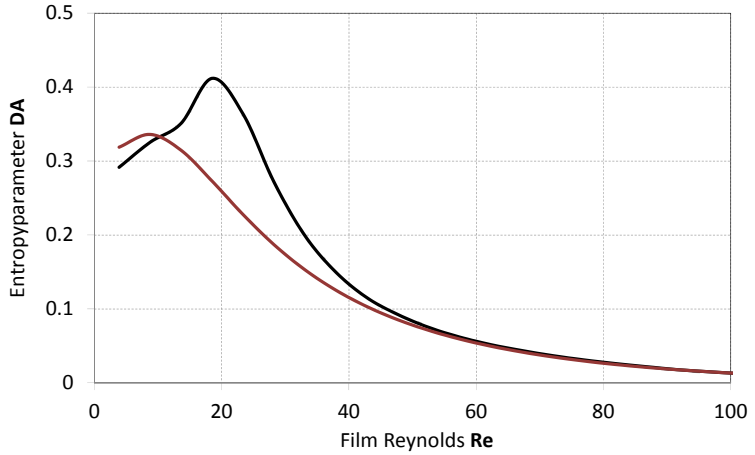

Fig. 8.1 Dimensionless parameters *DA* as a function of film Reynolds number at chiller representative conditions, considering partial wetting (black line) and neglecting partial wetting (red line); ω_{in}=60%, T_{in}=46.6℃, T_w=32.0℃, p=1.0 kPa (T_e=46.6℃)

Correspondingly, figure 8.2 re-establishes the results valid for a heat transformer application case. These results make evidence for higher maxima, showing that although both useful effect and irreversibility are lowered by the effect of partial wetting, the latter is reduced to a higher rate. In contrast, chiller and heat transformers optimal Reynolds move towards higher values for the first and towards lower values for the latter.

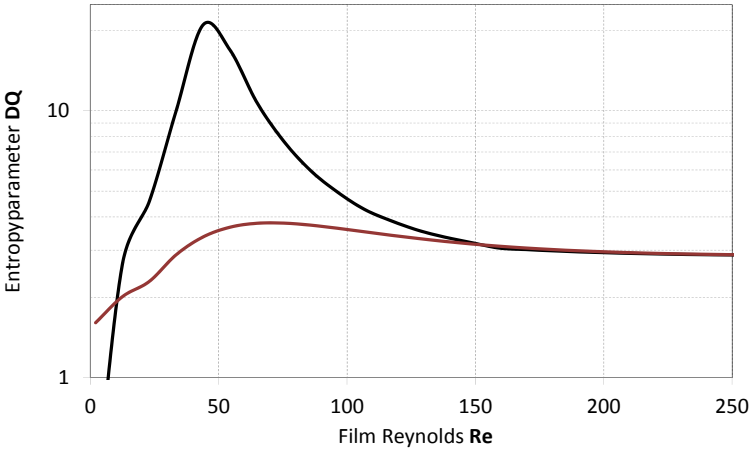

Fig. 8.2 Dimensionless parameters *DQ* as a function of film Reynolds number at heat transformer representative conditions, considering partial wetting (black line) and neglecting partial wetting (red line) T_w=85.0℃, ω_{in}=60%, T_{in}=97.1℃, p=12.5kPa

Given the promising results of the adopted method, further refinements (such as the inclusions of viscous dissipation or the influence of heat and mass transfer) are planned to be carried out in parallel with direct flow visualisation and experiments. Since the prediction of flow configurations is of critical importance in a number of other technical cases, further research efforts aims at the estimation of the dry-out conditions in micro/mini channels, or transfer processes realised by small liquid droplets where fluid characterised by high surface tension are employed.

8.2 Results summary

Vapour absorption constitutes one of the first refrigeration methods a renewed opportunity towards clean and efficient energy conversion. On one side, the recent technical development of absorption systems pushes towards increasingly complex plant configurations, but, on the other hand, seems to stand a step forward with respect to the theoretical background needed for an accurate prediction, optimisation and control of their performance. This work arises from the awareness of this discrepancy.

Since the global system performance constitutes, in fact, the starting point as well as the final target to be addressed, this thesis is structured with a convergent approach, originating from the development of a general model representing the fundamental thermodynamic structure of these systems in their interactions with the outer environment. A large spectrum thermodynamic analysis provides general guidelines for the optimisation of each component of the system with respect to the ultimate duty of the whole plant. The combination of first and second principle of thermodynamics extend the potentiality of the method, by providing a qualitative description which identifies performance limitations, suggests how to improve system COP and can be used to perform existing plant diagnostic. This approach defines a general thermodynamic criterion for the characterisation of three-thermal irreversible systems, exemplified for absorption chiller and heat transformer application cases. The influence of the main parameters is highlighted in a way that shows how to change them in order to improve the overall efficiency, pointing out the importance properly designed components and in particular of the absorber.

Taking advantage of the understanding gained from this general analysis, a detailed numerical model of falling film absorbers is presented and used as the basis for the development of an optimisation criterion of the component which targets the ultimate duty of the system. Since local details are believed to play a major role on the global performance of the process and might have leading impact on the plant operability, local results are summed up to a higher scale, and used globally to optimise transfer performance of the absorber, its design and operational regime. Among the possible scenarios, entropy generation minimisation can be used to characterise the quality of energy-conversion processes, and develop consistent criteria for the design, optimisation and control of the whole system. Besides, entropy constitutes a critical variable especially at the small characteristic scale of the processes involved in transport phenomena in general, and absorption in particular. From this standpoint, a local numerical analysis of the absorption entropy generation is used as the basis to define suitable dimensionless objective parameters to maximise heat and mass transfer of the absorber in a way that would bring the system closer to its highest efficiency. As a rule, results suggest the importance to work at reduced mass flowrates with a thin uniform film to increase the system performance and/or reduce its size.

At these operative conditions, specifically at low Reynolds numbers, the standard modelling assumption of a film with uniform thickness and complete wetting of the transfer surface can't be considered even approximately rigorous, and leads to an unacceptable inaccuracy of simulations results (the obtained trend itself disagrees with measurements). Furthermore, partial wetting is recognised to occur even at typical system operative conditions. Accordingly, the inadequacy of previously available models of falling film absorbers can be ascribed to a major weakness associated to this particular phenomenon. In general, these devices require conditions which avoid thin liquid films to break into a series of rivulets, leaving the solid heat transfer surface partly uncovered and/or lowering the extension of the liquid-vapour interface, where mass transfer occurs. Both a criterion of film stability to identify the minimum wetting rate able to ensure a complete wetting and, after the film breakage, a method to estimate the wet part of the surface are demanded for an accurate description of these processes. Unfortunately, there is not a general agreement on the precise mechanism of film break-down and data on a variety of parameters such as surface inclination, mode of liquid distribution, temperature level and thermo-physical properties, which may have an important effect on maintaining fully wetted surfaces, are incomplete and affected by large deviations. Considering the main features and the characteristic scale of falling film absorption, the influences of inertia (in the specific case of interest, directly caused by gravity) and surface tension result to be dominant on the film hydrodynamic behaviour. In particular, their conflicting effects (gravity forcing towards flowing configurations and iso-potential flat interfaces, whereas surface tension tends to create stationary spherical phase boundaries) establish configuration-stability limitations. Therefore, the stability of a uniform film is reduced to the identification of an energetically stable configuration characterised by a minimum of its mechanical energy (including kinetic and surface tension energy) and the definition of a concurrent broken rivulet configuration can be used to describe the liquid partial wetting behaviour. This forth chapter re-establishes an energy based criterion for the film stability for a generic inclination of the solid surface, consistently with a composed cross-section shape of the rivulet, which introduces an additional geometrical degree of freedom to the problem. Moreover, this work aims also at the local characterisation of the transition from uniform film to the steady rivulet configuration by applying a Lagrangian approach to describe the local trajectory of

the fluid particle at the edge of the rivulet. This approach is extended to include hysteresis behaviour of the fluid wettability and the contact angle when increasing or decreasing mass flowrates are delivered. An application case on a vertical fin-tube contactor is studied and compared with experiments for a first validation. Afterwards, a semi-empirical model suitable for a horizontal tube bundle is developed to match the characteristics and surface geometry of real falling film absorbers.

In this way, the effect of these phenomena can be included in the absorption model to extend its validity and increase its accuracy. The effects of different parameters is analysed numerically to clarify the model ability to describe different phenomena in detail.

Numerical analysis and CFD have a great potential and could be very accurate if the problem is formulated properly. However, the time required to reach an accurate solution and the fact that its validity is restricted to the specific case, the operative and boundary conditions specifically selected should be well-thought-out. These specific solutions cannot be directly generalised and don't provide general guidelines. Under this point of view, to readily extend the validity of the model and capture the physics of the problem, analytical solutions still maintain their fundamental importance. Hence, as a closing modelling effort, the understanding developed in the previous chapters is canalised in a detailed, widely applicable and time-saving method to predict heat and mass transfer characteristics of horizontal-tube falling film absorbers. The analytical solution developed considers the tube cylindrical geometry, also, by means of the inclusion of a film stability criterion and a linear wetting model, partial wetting phenomena are incorporated in the analysis, thus extending the target range of the resulting heat and mass transfer coefficients expressions. A first comparison with the numerical solution is used as a reference to test the validity of the simplifying assumptions introduced.

Finally, an experimental campaign is performed as a closing step to compare the theoretical model with the transfer performance of real falling film absorbers and to directly visualise partial wetting phenomena. Lastly, the eighth chapter is intended to summarise the results obtained in order to draw significant conclusions and future prospects.

This thesis contributes to improve the theoretical background for the performance prediction of vapour absorption systems and falling film absorbers with the results listed below:

- Develop a general thermodynamic model for absorption systems and
- An optimisation criterion for falling film absorbers able to improve the overall system performance.
- Model and investigate falling film partial wetting phenomena.
- Includes these phenomena in a numerical and an analytical model of falling film absorber transfer performance.
- Extend the model validity is extended to low flowrates operability.
- Results have been experimentally validated.

Chapter 8,
Conclusions and future plan

APPENDIX A, C++ script 1

```
#include<math.h>
#include <iostream>
#include <fstream>
using namespace std;
#include "CNewtonRaphsonMethod.h"
#include"CFluidParameter.h"
#include"PropertyLithiumBromide_ver05.h"
#include"PropertyWater_ver05.h"

PropertyLithiumBromide libr;
PropertyWater wat;

int main()
{

///////Variables' declaration//////////////////////////////////////////////////////////////////////////

	int Z,G,l,i,j,N,M,O,n,p,t,o,z;

	Z=10;                                                    /////Tube mesh
	N=100;                                                   /////Angle mesh
	M=50;                                                    /////Thickness mesh
	O=3;                                                     /////Parameter Analysis
	G=50;                                                    /////Mass flow rate

	double
u[100][100],v[100][100],Ti[100][100],Xi[100][100],Cw[100][100],Et[100][100],Ef[100][100],Ec[100][100]
,Ed[100][100];
	double
g,st,L,rho,myu,beta,hmin,hminp,Re,Rew,PI,f,gl,k,Reb,qf,mf,dp,Tw,d,hv,ro,ri,cp,Tsat,m,P,Pw,hwi,hwo,U,G
w,Twl,aave,bave,Xave,Tave,uave,a,htcw,htc,mtc,Tin,Xin,B,S,C,Mw,hwO,swO,Cwi;
	double
Gv[100],A[100],b[100],X[100],CA[100],h[100],dr[100],r[100],R[100],dtx[100],dty[100],dxx[100],dxy[100]
,dux[100],duy[100],dvx[100],dvy[100],Twi[100];

	double *h;

	h = new double[200];

	ofstream fout("GridTube.csv");

	if(!fout){
	cout << "ファイルをオープンできませんでした"<< endl;
    return 1;
                }
	else
		cout<< "ファイルをオープンしました" << endl;

///////flowrate loop//////////////////////////////////////////////////////////////////////////////////

for(l=1;l<=G;l++){

	m=0.05;                                          ///[kg/s]
```

```
	fout<<m<<",";

////////Experiment conditions//////////////////////////////////////////////////////////////////////

	P=12.5;                                         //[kPa]
	t=10;                                           //tube number
	L=0.878;                                        //tube length[m]
	PI=(6*asin(0.5));                               //π
	beta=PI/N;                                      //Angle
	Pw=101.325;                                     //cooling water pressure [kPa]

////////grid generation in the radial direction//////////////////////////////////////////////////////

	for(j=1;j<=M;j++){
		r[j]=1.0/2.0*(1.0-cos((j-1)/(double(M)-1)*PI));      //dimensionless position
                                                }

	for(j=1;j<=M-1;j++){
		dr[j]=r[j+1]-r[j];                      //dimensionless position difference
                                                }

	for(j=1;j<=M-2;j++){
		R[j]=dr[j+1]/dr[j];             //ratio of sequential dimensionless position difference
                                                }

///////inlet and initial conditions/////////////////////////////////////////////////////////////////

	Tin=95.0;                                       //Solution inlet temperature [^C]
	Xin=0.60;                                       //Solution inlet concentration
	Tave=Tin;
	Xave=Xin;
	Gw=0.5;                                         ///Cooling water flow rate[kg/s]

////////properties calculation///////////////////////////////////////////////////////////////////////

	st=libr.sc_st_XT(Xave,Tave);                    //////[N/m]
	rho=libr.sc_rho_XT(Xave,Tave);                  ////[kg/m3]
	myu=libr.sc_visc_XT(Xave,Tave);                 ///[Pas]
	gl=9.81;                                        //[m/s2]
	k=libr.sc_thc_XT(Xave,Tave);                    ////[W/mK]
	d=libr.sc_d_XT(Xave,Tave);                      //////[m2/s]
	cp=libr.sc_cp_XT(Xave,Tave)*1000.0;             ////[J/kgK]
	a=k/rho/cp;
	Tsat=wat.p_t( P );
	Mw=0.018015;                                    /////Molar weight [kg/mol]
	hw0=-241830;                                    /////standard water molar enthalpy [J/mol]
	sw0=188.84;                                     //////standard water molar entropy [J/molK]
	Cwi=(rho)/Mw*(1.0-Xin);

////////Partial wetting model Parameters 1////////////////////////////////////////////////////////////

	Re=4.0*m/L/myu;
		fout<<Re<<endl;
	dp=(rho*pow(st,3.0))/(pow(myu,4.0)*gl);     //dimensionless group for minimum stable thickness

////////variables initialization/////////////////////////////////////////////////////////////////////
```

```
	for(i=1;i<=N-1;i++){

		Gv[i]=0.001;		//interface mass flux per unit surface initialization [kg/m2s]

		for(j=1;j<=M;j++){

		Xi[i][j]=Xin;				//initialising concentration
			Ti[i][j]=Tin;			//initialising temperature

							}
					}

////////Parametric Analysis loop//////////////////////////////////////////////////////////////////////

	for (o=1;o<=0;o++){

	Twi[1]=85.0;					//inlet cooling water temperature [^C]
	Tw=Twi[1];					//Tube Wall temperature[^C]
	fout<<Tw<<",";
	ro=9.0/1000.0*o;				//outer tube diameter [m]
	ri=8.0/1000.0;					//inlet tube diameter [m]
	fout<<ro<<",";

////////Tube mesh loop////////////////////////////////////////////////////////////////////////////////

	for(z=1;z<=Z;z++){

////////Twall loop initialization/////////////////////////////////////////////////////////////////////

	Twl=0;

/////////Partial wetting model Parameters 2/////////////////////////////////////////////////////////////

	Reb=4.0*8.5027*pow(dp,0.0505);				//Break-up Reynolds from Maron1982
	hmin=pow(3.0*Reb/4.0*pow(myu/rho,2.0)/9.81,1.0/3.0); //minimum thickness [m] from Maron1982

////////Tw while loop/////////////////////////////////////////////////////////////////////////////////

	while(abs(Tw-Twl)>=0.001){

		Tw=Twl;

//////////////////////Average tube values////////////////////

		aave=0;
		bave=0;
		qf=0;
		mf=0;

/////////Angle loop//////////////////////////////////////////////////////////////////////////////////

	for(i=1;i<=N-1;i++){

	h[i]=pow(3.0*m/L*myu/(rho*rho*gl*sin(beta*i)),1.0/3.0);	//uniform film thickness
```

```
////////Wetting model////////////////////////////////////////////////////////////////////////////
        ////////////first half of tube surface///////////

        if(i<N/2){

                hminp=pow(((rho*rho*rho)*gl*gl*sin(beta*i)*sin(beta*i))/(15.0*myu*myu*st),0.2)*hmin;
                                // dimensionless critical thickness
                CA[i]= 1665.4*pow(hminp,6.0) - 3446.8*pow(hminp,5.0) + 2399.3*pow(hminp,4.0) -
                459.73*pow(hminp,3.0) + 49.538*pow(hminp,2.0) + 2.9741*hminp + 0.8616;
                                //Local contact Angle
                CA[i]=CA[i]/180*PI;
                                //contact angle from critical condition and minimum stable thickness

                if(h[i]>=hmin){
                                //complete wetting////////////

                        X[i]=1.0;
                        b[i]=h[i];

                                                }
                else{
                ////////////Partial wetting/////////////

                f=-1.0/4.0*pow(cos(CA[i]),3.0)*sin(CA[i]) -13.0/8.0*cos(CA[i])*sin(CA[i])
                -3.0/2.0*CA[i]*pow(sin(CA[i]),2.0) +15.0/8.0*CA[i];//f(θo)
                g=(CA[i]*(5.0/16.0+15.0/4.0*pow(cos(CA[i]),2.0) +5.0/2.0*pow(cos(CA[i]),4.0))
                -sin(CA[i])*(113.0/48.0*cos(CA[i])+97.0/24.0*pow(cos(CA[i]),3.0)
                +1.0/6.0*pow(cos(CA[i]),5.0)));                          //Ψ(θo))


        X[i]=pow((h[i]),3.0)*sin(CA[i])/f*pow(2.0/45.0*(pow(rho,3.0)*pow((9.81*sin(beta*i)),2.0)/
        (st*pow(myu,2.0)))*g/sin(CA[i])*pow((CA[i]/sin(CA[i])-cos(CA[i])),-1),3.0/5.0);

                        //wetting ratio calculation for 10th tube

                                if(X[i-1]==1){
        ///Linear transition zone between uniform and rivulets configurations///////

                                B=-15.0/PI;
                                C=15.0/double(N)*(i-1)+1;
                                S=B*PI*double(i)/double(N)+C;
                                        }
                                else{
                                S=B*PI*double(i)/double(N)+C;
                                if(S<0){
                                S=0;
                                        }
                                else{}
                                        }

                X[i]=S*(1-X[i])+X[i];
                A[i]=(log(X[i]+(1-X[i])*pow(Re/Reb,1.0))-log(X[i]))/9.0;
                        //exponential coefficient describing wetting ratio increase for previous tubes
                X[i]=(X[i]+(1-X[i])*pow(Re/Reb,1.0))*exp(-A[i]*(t-1));       //WR for tube t
                b[i]=h[i]/pow(X[i],1.0/3.0);                             //average rivulet thickness
```

```
                }
                        }////////////first half of tube surface////////////////////////////
//////////////////////////second half of tube surface////////////////////////////////////////////////

        else{

                CA[i]= CA[i-1];

                if(X[N/2-1]==1){        ///Constant contact angle criteria break-up///////

                hminp=0.1593*log(CA[i])+0.6699;
                hmin=pow(((rho*rho*rho)*gl*gl*sin(beta*i)*sin(beta*i))/(15.0*myu*myu*st),-0.2)*hminp;

                if(h[i]>=hmin){         ///////complete wetting////////////////////////
                X[i]=1.0;
                b[i]=h[i];
                        }
                else{                   ////////////////partial wetting////////////////////////

                f=-1.0/4.0*pow(cos(CA[i]),3.0)*sin(CA[i]) -13.0/8.0*cos(CA[i])*sin(CA[i])
                -3.0/2.0*CA[i]*pow(sin(CA[i]),2.0) +15.0/8.0*CA[i];          //f(θo)
                g=(CA[i]*(5.0/16.0+15.0/4.0*pow(cos(CA[i]),2.0) +5.0/2.0*pow(cos(CA[i]),4.0))
                 -sin(CA[i])*(113.0/48.0*cos(CA[i]) +97.0/24.0*pow(cos(CA[i]),3.0)
                +1.0/6.0*pow(cos(CA[i]),5.0)));              //Ψ(θo))


        X[i]=pow((h[i]),3.0)*sin(CA[i])/f*pow(2.0/45.0*(pow(rho,3.0)*pow((9.81*sin(beta*i)),2.0)/
        (st*pow(myu,2.0)))*g/sin(CA[i])*pow((CA[i]/sin(CA[i])-cos(CA[i])),-1),3.0/5.0);

                        if(X[i-1]==1){
        ///Linear transition zone between uniform and rivulets configurations///////
                        B=-15.0/PI;
                        C=15.0/double(N)*(i-1)+1;
                        S=B*PI*double(i)/double(N)+C;
                                                }
                        else{
                        S=B*PI*double(i)/double(N)+C;
                        if(S<0){
                        S=0;
                                }
                        else{}
                                }

                X[i]=S*(1-X[i])+X[i];
                A[i]=(log(X[i]+(1-X[i])*pow(Re/Reb,1.0))-log(X[i]))/9.0;
                        //exponential coefficient describing wetting ratio increase for previous tubes
                X[i]=(X[i]+(1-X[i])*pow(Re/Reb,1.0))*exp(-A[i]*(t-1));       //wR for tube t
                b[i]=h[i]/pow(X[i],1.0/3.0);                 //average rivulet thickness

                        }
                }

///////dynamic wetting ratio calculation (without minimum stable thickness comparison)///////////////

                else{
```

```
            f=-1.0/4.0*pow(cos(CA[i]),3.0)*sin(CA[i]) -13.0/8.0*cos(CA[i])*sin(CA[i])
             -3.0/2.0*CA[i]*pow(sin(CA[i]),2.0) +15.0/8.0*CA[i];//f(θo)
            g=(CA[i]*(5.0/16.0+15.0/4.0*pow(cos(CA[i]),2.0) +5.0/2.0*pow(cos(CA[i]),4.0))
            -sin(CA[i])*(113.0/48.0*cos(CA[i]) +97.0/24.0*pow(cos(CA[i]),3.0)
            +1.0/6.0*pow(cos(CA[i]),5.0)));//Ψ(θo))


        X[i]=pow((h[i]),3.0)*sin(CA[i])/f*pow(2.0/45.0*(pow(rho,3.0)*pow((9.81*sin(beta*i)),2.0)/
        (st*pow(myu,2.0)))*g/sin(CA[i])*pow((CA[i]/sin(CA[i])-cos(CA[i])),-1),3.0/5.0);

                                if(X[i-1]==1){
                                B=-15.0/PI;
                                C=15.0/double(N)*(i-1)+1;
                                S=B*PI*double(i)/double(N)+C;
                                                        }
                                else{
                                S=B*PI*double(i)/double(N)+C;
                                if(S<0){
                                S=0;
                                        }
                                else{}
                                        }

                        X[i]=S*(1-X[i])+X[i];
                        A[i]=(log(X[i]+(1-X[i])*pow(Re/Reb,1.0))-log(X[i]))/9.0;
                                //exponential coefficient describing wetting ratio increase for previous tubes
                        X[i]=(X[i]+(1-X[i])*pow(Re/Reb,1.0))*exp(-A[i]*(t-1));//wR for tube t
                        b[i]=h[i]/pow(X[i],1.0/3.0);                    //average rivulet thickness

                                }
                        }

////////////////////////////////////////////////////////////////////////////////////////////////
////////numerical solution of energy and species transport equations//////////////////////////////

/////////////////Boundary conditions/////////////////

                u[i][1]=0;
                v[i][1]=0;
                Ti[i][1]=Tw;                    //wall temperature boundary condition

/////////////////////Velocity field/////////////////////////////////////////////////////////////

                for(j=2;j<=M;j++){

                u[i][j]=(rho*gl*h[i]*h[i]*sin(PI*i/double(N))/myu)*(r[j]-1.0/2.0*r[j]*r[j]);
                v[i][j]=-(rho*gl*h[i]*h[i]*r[j]*r[j])/(2.0*myu*ro)*(1.0/PI*(-pow(myu*m/L*PI*PI*PI/
                (9.0*rho*rho*gl),1.0/3.0)*1.0/(pow(sin(PI*double(i)/double(N)),1.0/3.0)*tan(PI*double(i)/
                double(N))))*sin(PI*double(i)/double(N))+h[i]*(1.0-r[j]/3.0)*cos(PI*double(i)/double(N)));

                }

        if (i>=2){

        ////////NewtonRaphson Method/////////////////////////////////////////////////////////////
```

```
        CNewtonRaphsonMethod mnm;               // CNewtonRaphsonMethodクラスの宣言
        mnm.setup(2000,1+1e-12,1e-6);           //セットアップ　※引数はニュートン法の変数以上にする

        p=0;

        for(j=2;j<=M;j++){
        mnm.setValue( p , Ti[i][j],3.0 );
        p++;
        mnm.setValue( p , Xi[i][j],0.1 );
        p++;
        }
        mnm.setValue( p ,Gv[i],0.05  );
        p++;

        mnm.setAcc(0.7);                                //加速度勾配の入力　※なくても可

        mnm.initial();                                  //計算を開始する前に必ず初期化してください
        for(mnm.main_loop_init();mnm.main_loop_check();mnm.main_loop_reinit()){     // おまじない
                for(mnm.sub_loop_init();mnm.sub_loop_check();mnm.sub_loop_reinit()){// おまじない
                        p=0;
                        //値の設定
        for(j=2;j<=M;j++){
                        Ti[i][j] = mnm.getValue(p);
                        p++;
                        Xi[i][j] = mnm.getValue(p);
                        p++;
                                        }
        Gv[i] = mnm.getValue(p);
        p++;

        Xi[i][1]=((1.0+R[1]*R[1]+2.0*R[1])*Xi[i][2]-Xi[i][3])/(R[1]*(2.0+R[1]));
                        /// concentration boundary condition

///////Absorption heat//////////////////////////////////////////////////////////////////////////////

        hv = wat.sat_hv( Tsat )*1000.0-ibr.sc_h_XT(Xi[i][M],Ti[i][M])*1000.0;/////[J/kg]

        p=0;

for(j=2;j<=M-1;j++){

        mnm.setError( p , (Ti[i][j]-Ti[i-1][j])/(1.0/double(N))*1000.0 ,1000.0*((PI*ro*a)/(u[i][j]
                *h[i]*h[i])*((2.0*R[j-1]*Ti[i][j+1]+2.0*R[j-1]*R[j-1]*Ti[i][j-1]-2.0*R[j-1]*(1.0+
                R[j-1])*Ti[i][j])/(dr[j]*dr[j]*(1.0+R[j-1])))+(r[j]/h[i]*(-pow(myu*m/L*PI*PI*PI/
                (9.0*rho*rho*gl),1.0/3.0)*1.0/(pow(sin(PI*double(i)/double(N)),1.0/3.0)*tan(PI*
                double(i)/double(N))))-PI*ro*v[i][j]/(h[i]*u[i][j]))*((Ti[i][j+1]-R[j-1]*R[j-1]*
                Ti[i][j-1]-(1.0-R[j-1]*R[j-1])*Ti[i][j])/((1.0+R[j-1])*dr[j])) );
        p++;

///////Energy transport equation////////////////////////////////////////////////////////////////////

        mnm.setError( p ,1000.0*(Xi[i][j]-Xi[i-1][j])/(1.0/double(N)) ,1000.0*((PI*ro*d)/(u[i][j]
                *h[i]*h[i])*((2.0*R[j-1]*Xi[i][j+1]+2.0*R[j-1]*R[j-1]*Xi[i][j-1]-2.0*R[j-1]*(1.0+
                R[j-1])*Xi[i][j])/(dr[j]*dr[j]*(1.0+R[j-1])))+(r[j]/h[i]*(-pow(myu*m/L*PI*PI*PI/
                (9.0*rho*rho*gl),1.0/3.0)*1.0/(pow(sin(PI*double(i)/double(N)),1.0/3.0)*tan(PI*
                double(i)/double(N))))PI*ro*v[i][j]/(h[i]*u[i][j]))*((Xi[i][j+1]-R[j-1]*
```

```
                R[j-1]*Xi[i][j-1]-(1.0-R[j-1]*R[j-1])*Xi[i][j])/((1.0+R[j-1])*dr[j])));
        p++;

//////Species transport equation//////////////////////////////////////////////////////////////////
        ////////////Interface/////////////////////////////////////////////////////

        if(j==M-1){

        ////////////Phases Equilibrium/////////////////////////////////////////////
        mnm.setError( p , Ti[i][M] , libr.sc_T_XTsat(Xi[i][M],wat.p_t( P )) );
        p++;

        ////////////Fick's diffusion law/////////////////////////////////////////////
        mnm.setError( p , Gv[i] , -rho*d/(Xi[i][M])*((1+2.0*R[j-1])*Xi[i][j+1]+R[j-1]*R[j-1]*
                Xi[i][j-1]-(1.0+R[j-1]*R[j-1]+2.0*R[j-1])*Xi[i][j])/((1.0+R[j-1])*dr[j])/h[i]) ;//h b
        p++;

        ///////////Absorption heat Thermal Diffusion//////////////////////////////////
        mnm.setError( p , Gv[i]*hv , k*((1+2.0*R[j-1])*Ti[i][j+1]+R[j-1]*R[j-1]*Ti[i][j-1]-(1.0+
                R[j-1]*R[j-1]+2.0*R[j-1])*Ti[i][j])/((1.0+R[j-1])*dr[j])/h[i] );            ////h or b
        p++;

                                }
                        }

                // mnm.prt();                           //エラー表示
                mnm.prt_sum();                  //エラーの合計を表示

        }
        }

//////Temperature and concentration bulk values//////////////////////////////////////////////////////

                uave=0;

                for(n=2;n<=M;n++){

                        uave+=u[i][n]*dr[n-1];

                                                        }

                Tave=0;
                Xave=0;

                for(n=2;n<=M;n++){

                Tave+=u[i][n]*Ti[i][n]*dr[n-1]/uave;  //average temperature for previous angle step
                Xave+=u[i][n]*Xi[i][n]*dr[n-1]/uave;  //average concentration for previous angle step

                }

                fout<<Xave<<",";
                fout<<Tave<<endl;

////////heat and mass transfer coefficients//////////////////////////////////////////////////////////
```

```
                htc= k*(-Ti[i][3]-R[1]*(2.0+R[1])*Ti[i][1]+(1.0+R[1]*R[1]+2.0*R[1])*
                Ti[i][2])/((1.0+R[1])*dr[2])/h[i]/abs(Tave-Tw) ;      ////////////////h or b
                fout<<htc<<",";

        if(X[i]==1){
                htc= k*(-Ti[i][3]-R[1]*(2.0+R[1])*Ti[i][1]+(1.0+R[1]*R[1]+2.0*R[1])*Ti[i][2])/
                ((1.0+R[1])*dr[2])/h[i]/abs(Tave-Tw) ;                ////////////////h or b
                                        }
        else{
                htc= X[i]*k*(-Ti[i][3]-R[1]*(2.0+R[1])*Ti[i][1]+(1.0+R[1]*R[1]+2.0*R[1])*Ti[i][2])/
                ((1.0+R[1])*dr[2])/b[i]/abs(Tave-Tw) ;                ////////////////h or b
                        }
                fout<<htc<<",";

                mtc= -d/(Xi[i][M])*((1+2.0*R[M-2])*Xi[i][M]+R[M-2]*R[M-2]*Xi[i][M-2]-(1.0+R[M-2]*
                R[M-2]+2.0*R[M-2])*Xi[i][M-1])/((1.0+R[M-2])*dr[M-1])/h[i]/abs(Xi[i][1]-Xi[i][M]) ;
                                                                      ////////////////h or b

                fout<<mtc*3600<<",";

        if(X[i]==1){
                mtc= -d/(Xi[i][M])*((1+2.0*R[M-2])*Xi[i][M]+R[M-2]*R[M-2]*Xi[i][M-2]-(1.0+R[M-2]*
                R[M-2]+2.0*R[M-2])*Xi[i][M-1])/((1.0+R[M-2])*dr[M-1])/h[i]/abs(Xi[i][1]-Xi[i][M]) ;
                                                                      ////////////////h or b
                                        }

        else{
                mtc= -X[i]*d/(Xi[i][M])*((1+2.0*R[M-2])*Xi[i][M]+R[M-2]*R[M-2]*Xi[i][M-2]-(1.0+
                R[M-2]*R[M-2]+2.0*R[M-2])*Xi[i][M-1])/((1.0+R[M-2])*dr[M-1])/b[i]/abs(Xi[i][1]-
                Xi[i][M]) ;                                           ////////////////h or b
                        }

                fout<<mtc*3600<<",";

////////Tube average calculation//////////////////////////////////////////////////////////////////////

                mf +=2.0*Gv[i]*PI*ro/(double(N)-2.0);

                        if (i>=3){

                        aave +=htc/(double(N)-3.0);
                        bave +=mtc/(double(N)-3.0);
                        qf +=2.0*PI*ro*L/Z/(double(N)-3.0)*htc*(Tave-Tw);

                        }
        }

else {

                }

        }//////////////////////Angle loop/////////////////////////////////////////////////////////////

        fout<<qf<<",";
        fout<<aave<<",";
        fout<<bave*3600<<",";
```

```
        fout<<mf<<endl;

////////cooling water//////////////////////////////////////////////////////////////////////////////

        hwi=wat.sc_hl(Pw,Twi[z])*1000.0;
        hwo=hwi+qf/Gw;
        Twi[z+1]=wat.T_Ph(Pw,hwo/1000.0);
        Rew=2.0*Gw/(wat.sc_myul(Pw,Twi[z])*PI*ri);
        htcw=0.023*pow(wat.sc_Prl(Pw,Twi[z+1]),0.4)*pow(Rew,0.8)*wat.sc_laml(Pw,Twi[z])/(ri*2.0);
        U=1/(ri*2.0)/(1/htcw/(ri*2.0)+1.0/2.0/400.0*log(ro/ri));
        Twl=(Twi[z]*(exp(U/qf*2.0*PI*ri*L/Z*(Twi[z]-Twi[z+1])))-
                Twi[z+1])/((exp(U/qf*2.0*PI*ri*L/Z*(Twi[z]-Twi[z+1])))-1);

        }//////////////////////////Tw while loop/////////////////////////////////////////////////////

//////////////////////////Results print out/////////////////////////////////////////////////////////

        for(i=1;i<=N-1;i++){

                fout<<Gv[i]<<endl;
                fout<<X[i]<<",";

        if(X[i]==1){
                        fout<<h[i]<<endl;
        }
        else {
                        fout<<b[i]<<endl;
        }
        }

for(j=1;j<=M;j++){
        for(i=1;i<=N-1;i++){

                fout<<Xi[i][j]<<",";

        }
        fout<<0<<endl;
}

for(j=1;j<=M;j++){
        for(i=1;i<=N-1;i++){

                fout<<Ti[i][j]<<",";

        }
        fout<<0<<endl;
}

for(j=1;j<=M;j++){
        for(i=1;i<=N-1;i++){

                fout<<u[i][j]<<",";

        }
        fout<<0<<endl;
}
```

```
for(j=1;j<=M;j++){
        for(i=1;i<=N-1;i++){

                fout<<v[i][j]<<",";

        }
        fout<<0<<endl;
}

///////////Results Printing out/////////////////////////////////////////////////////////////////////

}////////////////////////Tube mesh loop/////////////////////////////////////////////////////////////

for(z=1;z<=Z+1;z++){

        fout<<Twi[z]<<",";

                                        }

}///////////////////////////Parametric Analysis loop/////////////////////////////////////////////////

}///////////////////////////flowrate loop/////////////////////////////////////////////////////////////

}
```

APPENDIX B, C++ script 2

```
#include<math.h>
#include <iostream>
#include <fstream>
using namespace std;
#include "CNewtonRaphsonMethod.h"
#include"CFluidParameter.h"
#include"PropertyLithiumBromide_ver05.h"
#include"PropertyWater_ver05.h"

PropertyLithiumBromide libr;
PropertyWater wat;

int main()
{
	int G,l,i,j,N,M,O,n,p,t,o;
	N=100;			/////Angle mesh
	M=50;			/////Thickness mesh
	O=13;			/////Parameter Analysis
	G=11;			/////Mass flow rate

	double
u[100][100],v[100][100],Ti[100][100],Xi[100][100],Cw[100][100],Et[100][100],Ef[100][100],Ec[100][100]
,Ed[100][100];
	double
TEG,g,st,L,dtM,DT,rho,myu,beta,hmin,hminp,Re,PI,f,gl,k,Reb,qf,mf,dp,Tw,d,hv,ro,cp,Tif,Tsat,m,P,_Tw,Gw
,Twi,ri,aave,bave,Xave,Tave,uave,a,htc,mtc,Tin,Xin,B,S,C,Mw,hwO,swO,Cwi;
	double
Gv[100],A[100],b[100],X[100],CA[100],h[100],dr[100],r[100],R[100],dtx[100],dty[100],dxx[100],dxy[100]
,dux[100],duy[100],dvx[100],dvy[100];

	ofstream fout("S.csv");

	if(!fout){
	cout << "ファイルをオープンできませんでした"<< endl;
    return 1;
	}
	else
		cout<< "ファイルをオープンしました" << endl;

////////flowrate loop//////////////////////////////////////////////////////////////////////////////

for(l=1;l<=G;l++){

	m=0.005*(l);		///[kg/s]
	fout<<m<<",";

	//fout<<N<<",";
	//fout<<M<<",";

////////Experiment conditions//////////////////////////////////////////////////////////////////////

	P=1.0;			//[kPa]
	fout<<P<<",";
```

```
        t=10;                   //tube number
        L=0.878;                //tube length[m]
        PI=(6*asin(0.5));       //π
        beta=PI/N;              //Angle

///////grid generation in the radial direction//////////////////////////////////////////////////////

        for(j=1;j<=M;j++){
        r[j]=1.0/2.0*(1.0-cos((j-1)/(double(M)-1)*PI));
                                            }

        for(j=1;j<=M-1;j++){
        dr[j]=r[j+1]-r[j];
                                            }

        for(j=1;j<=M-2;j++){
        R[j]=dr[j+1]/dr[j];
                                            }

///////first conditions//////////////////////////////////////////////////////////////////////////////

        for (o=1;o<=0;o++){
        Xin=0.60;               //Solution inlet concentration
        Tif=libr.sc_T_XTsat(Xin,wat.p_t( P ));        //fout<<Tif<<",";
        Tin=Tif-2.0;            //Solution inlet temperature [^C]
        Tave=Tin;
        Xave=Xin;
        fout<<Tin<<",";

////////properties calculation////////////////////////////////////////////////////////////////////////

        st=libr.sc_st_XT(Xave,Tave);          //////[N/m]
        rho=libr.sc_rho_XT(Xave,Tave);        ////[kg/m3]
        myu=libr.sc_visc_XT(Xave,Tave);       ///[Pas]
        gl=9.81;                              //[m/s2]
        k=libr.sc_thc_XT(Xave,Tave);          ////[W/mK]
        d=libr.sc_d_XT(Xave,Tave);            //////[m2/s]
        cp=libr.sc_cp_XT(Xave,Tave)*1000.0;   ////[J/kgK]
        a=k/rho/cp;
        Tsat=wat.p_t( P );
        Mw=0.018015;                          /////Molar weight [kg/mol]
        hw0=-241830;                          /////standard water molar enthalpy [J/mol]
        sw0=188.84;                           //////standard water molar entropy [J/molK]
        Cwi=(rho)/Mw*(1.0-Xin);

////////variables initialization/////////////////////////////////////////////////////////////////////

        for(i=1;i<=N-1;i++){
                Gv[i]=0.001;          //interface mass flux per unit surface initialization [kg/m2s]

                for(j=1;j<=M;j++){
                Xi[i][j]=Xin;         //initialising concentration
                Ti[i][j]=Tin;         //initialising temperature
                                            }
                                            }
///////Parametric Analysis loop//////////////////////////////////////////////////////////////////////
```

```
        Tw=32.0;                        //Tube Wall temperature[^C]
        fout<<Tw<<",";
        ro=9.0/1000;                    //outer tube diameter [m]
        fout<<ro<<",";
        dtM=0;
        DT=0;

////////Partial wetting model Parameters////////////////////////////////////////////////////////////

        Re=4.0*m/L/myu;
        fout<<Re<<",";
        dp=(rho*pow(st,3.0))/(pow(myu,4.0)*gl);     //dimensionless parameter group minimum thickness
        Reb=4.0*8.5027*pow(dp,0.0505);               //Break-up Reynolds from Maron1982
        hmin=pow(3.0*Reb/4.0*pow(myu/rho,2.0)/9.81,1.0/3.0);  //minimum thickness [m] from Maron1982

////////////Average tube values/////////////////////////////////////////////////////////////////////

                aave=0;
                bave=0;
                qf=0;
                mf=0;
                TEG=0;

////////Angle loop//////////////////////////////////////////////////////////////////////////////////

        for(i=1;i<=N-1;i++){
        h[i]=pow(3.0*m/L*myu/(rho*rho*gl*sin(beta*i)),1.0/3.0);//uniform film thickness

//////Wetting model//////////////////////////////////////////////////////////////////////////////////
        ////////////first half of tube surface////////////
        if(i<N/2){

        hminp=pow(((rho*rho*rho)*gl*gl*sin(beta*i)*sin(beta*i))/(15.0*myu*myu*st),0.2)*hmin;
                                        // dimensionless critical thickness
        CA[i]= 1665.4*pow(hminp,6.0) - 3446.8*pow(hminp,5.0) + 2399.3*pow(hminp,4.0) -
        459.73*pow(hminp,3.0) + 49.538*pow(hminp,2.0) + 2.9741*hminp + 0.8616;//Local contact Angle
        CA[i]=CA[i]/180*PI;//contact angle from critical condition and minimum stable thickness

                if(h[i]>=hmin){         //complete wetting/////////////

                        X[i]=1.0;
                        b[i]=h[i];
                                        }

                else{////////////Partial wetting/////////////

                f=-1.0/4.0*pow(cos(CA[i]),3.0)*sin(CA[i]) -13.0/8.0*cos(CA[i])*sin(CA[i])
                 -3.0/2.0*CA[i]*pow(sin(CA[i]),2.0) +15.0/8.0*CA[i];//f(θo)

                g=(CA[i]*(5.0/16.0+15.0/4.0*pow(cos(CA[i]),2.0) +5.0/2.0*pow(cos(CA[i]),4.0))
                -sin(CA[i])*(113.0/48.0*cos(CA[i]) +97.0/24.0*pow(cos(CA[i]),3.0)
                +1.0/6.0*pow(cos(CA[i]),5.0)));//Ψ(θo))

        X[i]=pow((h[i]),3.0)*sin(CA[i])/f*pow(2.0/45.0*(pow(rho,3.0)*pow((9.81*sin(beta*i)),2.0)/
```

```
        (st*pow(myu,2.0)))*g/sin(CA[i])*pow((CA[i]/sin(CA[i])-cos(CA[i])),-1),3.0/5.0);//wR 10th tube

        if(X[i-1]==1){///Linear transition zone between uniform and rivulets configurations///////
                              B=-15.0/PI;
                              C=15.0/double(N)*(i-1)+1;
                              S=B*PI*double(i)/double(N)+C;
                                      }
        else{
                              S=B*PI*double(i)/double(N)+C;
                              if(S<0){
                              S=0;
                                      }
                              else{}
                                      }

                X[i]=S*(1-X[i])+X[i];
                A[i]=(log(X[i]+(1-X[i])*pow(Re/Reb,1.0))-log(X[i]))/9.0;
                        //exponential coefficient describing wetting ratio increase for previous tubes
                X[i]=(X[i]+(1-X[i])*pow(Re/Reb,1.0))*exp(-A[i]*(t-1));       //weR for tube t
                b[i]=h[i]/pow(X[i],1.0/3.0);                            //average rivulet thickness

                        }
                                }//////////first half of tube surface//////////

/////////second half of tube surface////////////////////////////////////////////////////////////////
        else{

                CA[i]= CA[i-1];

                if(X[N/2-1]==1){///Constant contact angle criteria break-up///////
                hminp=0.1593*log(CA[i])+0.6699;
                hmin=pow(((rho*rho*rho)*gl*gl*sin(beta*i)*sin(beta*i))/(15.0*myu*myu*st),-0.2)*hminp;

                if(h[i]>=hmin){///////complete wetting////////////////////////
                X[i]=1.0;
                b[i]=h[i];
                                                }
                else{/////////////////partial wetting////////////////////////

                f=-1.0/4.0*pow(cos(CA[i]),3.0)*sin(CA[i]) -13.0/8.0*cos(CA[i])*sin(CA[i])
                 -3.0/2.0*CA[i]*pow(sin(CA[i]),2.0) +15.0/8.0*CA[i];//f(θo)

                g=(CA[i]*(5.0/16.0+15.0/4.0*pow(cos(CA[i]),2.0) +5.0/2.0*pow(cos(CA[i]),4.0))
                 -sin(CA[i])*(113.0/48.0*cos(CA[i]) +97.0/24.0*pow(cos(CA[i]),3.0)
                +1.0/6.0*pow(cos(CA[i]),5.0)));//Ψ(θo))

        X[i]=pow((h[i]),3.0)*sin(CA[i])/f*pow(2.0/45.0*(pow(rho,3.0)*pow((9.81*sin(beta*i)),2.0)/
        (st*pow(myu,2.0)))*g/sin(CA[i])*pow((CA[i]/sin(CA[i])-cos(CA[i])),-1),3.0/5.0);

        if(X[i-1]==1){///Linear transition zone between uniform and rivulets configurations///////
                              B=-15.0/PI;
                              C=15.0/double(N)*(i-1)+1;
                              S=B*PI*double(i)/double(N)+C;
                                                      }
        else{
                              S=B*PI*double(i)/double(N)+C;
```

```
                        if(S<0){
                        S=0;
                                }
                        else{}
                                }

                X[i]=S*(1-X[i])+X[i];
                A[i]=(log(X[i]+(1-X[i])*pow(Re/Reb,1.0))-log(X[i]))/9.0;
                        //exponential coefficient describing wetting ratio increase for previous tubes
                X[i]=(X[i]+(1-X[i])*pow(Re/Reb,1.0))*exp(-A[i]*(t-1));       //wR for tube t
                        b[i]=h[i]/pow(X[i],1.0/3.0);                  //average rivulet thickness

                                }
                        }

///////dynamic wetting ratio calculation (without minimum stable thickness comparison)///////////////

                f=-1.0/4.0*pow(cos(CA[i]),3.0)*sin(CA[i]) -13.0/8.0*cos(CA[i])*sin(CA[i])
                 -3.0/2.0*CA[i]*pow(sin(CA[i]),2.0) +15.0/8.0*CA[i];//f(θo)

                g=(CA[i]*(5.0/16.0+15.0/4.0*pow(cos(CA[i]),2.0) +5.0/2.0*pow(cos(CA[i]),4.0))
                 -sin(CA[i])*(113.0/48.0*cos(CA[i]) +97.0/24.0*pow(cos(CA[i]),3.0)
                +1.0/6.0*pow(cos(CA[i]),5.0)));//Ψ(θo))

        X[i]=pow((h[i]),3.0)*sin(CA[i])/f*pow(2.0/45.0*(pow(rho,3.0)*pow((9.81*sin(beta*i)),2.0)/
        (st*pow(myu,2.0)))*g/sin(CA[i])*pow((CA[i]/sin(CA[i])-cos(CA[i])),-1),3.0/5.0);

        if(X[i-1]==1){
                        B=-15.0/PI;
                        C=15.0/double(N)*(i-1)+1;
                        S=B*PI*double(i)/double(N)+C;
                                                }
        else{
                        S=B*PI*double(i)/double(N)+C;
                        if(S<0){
                        S=0;
                                }
                        else{}
                                }

                X[i]=S*(1-X[i])+X[i];
                A[i]=(log(X[i]+(1-X[i])*pow(Re/Reb,1.0))-log(X[i]))/9.0;
                        //exponential coefficient describing wetting ratio increase for previous tubes
                X[i]=(X[i]+(1-X[i])*pow(Re/Reb,1.0))*exp(-A[i]*(t-1));       //wR for tube t
                b[i]=h[i]/pow(X[i],1.0/3.0);                  //average rivulet thickness

                        }
                }
////////////////////////////////////////////////////////////////////////////////////////////////////

////////numerical solution of energy and species transport equations//////////////////////////////

//////////////////Boundary conditions/////////////////

        u[i][1]=0;
        v[i][1]=0;
```

```
        Ti[i][1]=Tw;            //wall temperature boundary condition

//////////////////////Velocity field//////////////////////

        for(j=2;j<=M;j++){
        u[i][j]=(rho*gl*h[i]*h[i]*sin(PI*i/double(N))/myu)*(r[j]-1.0/2.0*r[j]*r[j]);

        v[i][j]=-(rho*gl*h[i]*h[i]*r[j]*r[j])/(2.0*myu*ro)*(1.0/PI*(-pow(myu*m/L*PI*PI*PI/(9.0*rho
        *rho*gl),1.0/3.0)*1.0/(pow(sin(PI*double(i)/double(N)),1.0/3.0)*tan(PI*double(i)/double(N)))
        *sin(PI*double(i)/double(N))+h[i]*(1.0-r[j]/3.0)*cos(PI*double(i)/double(N)));

        }

if (i>=2){
////////NewtonRaphson Method////////////////////////////////////////////////////////////////////

        CNewtonRaphsonMethod mnm;               // CNewtonRaphsonMethodクラスの宣言
        mnm.setup(2000,1+1e-12,1e-6);           //セットアップ　※引数はニュートン法の変数以上にする

        p=0;

        for(j=2;j<=M;j++){
        mnm.setValue( p , Ti[i][j],3.0 );
        p++;
        mnm.setValue( p , Xi[i][j],0.1 );
        p++;
        }
        mnm.setValue( p ,Gv[i],0.05  );
        p++;

        mnm.setAcc(0.5);                                //加速度勾配の入力　※なくても可

        mnm.initial();                                  //計算を開始する前に必ず初期化してください
        for(mnm.main_loop_init();mnm.main_loop_check();mnm.main_loop_reinit()){     // おまじない
                for(mnm.sub_loop_init();mnm.sub_loop_check();mnm.sub_loop_reinit()){// おまじない
                        p=0;
                        //値の設定
        for(j=2;j<=M;j++){
                        Ti[i][j] = mnm.getValue(p);
                        p++;
                        Xi[i][j] = mnm.getValue(p);
                        p++;
                                        }
        Gv[i] = mnm.getValue(p);
        p++;

        Xi[i][1]=((1.0+R[1]*R[1]+2.0*R[1])*Xi[i][2]-Xi[i][3])/(R[1]*(2.0+R[1]));
                /// concentration boundary condition

//////////////////////Absorption heat/////////////////////////////////////

        hv = wat.sat_hv( Tsat )*1000.0-libr.sc_h_XT(Xi[i][M],Ti[i][M])*1000.0;      /////[J/kg

        p=0;

for(j=2;j<=M-1;j++){
```

```
        mnm.setError( p , (Ti[i][j]-Ti[i-1][j])/(1.0/double(N))*1000.0 , 1000.0*((PI*ro*a)/(u[i][j]
                *h[i]*h[i])*((2.0*R[j-1]*Ti[i][j+1]+2.0*R[j-1]*R[j-1]*Ti[i][j-1]-2.0*R[j-1]*(1.0+
                R[j-1])*Ti[i][j])/(dr[j]*dr[j]*(1.0+R[j-1])))+(r[j]/h[i]*(-pow(myu*m/L*PI*PI*PI/
                (9.0*rho*rho*gl),1.0/3.0)*1.0/(pow(sin(PI*double(i)/double(N)),1.0/3.0)*tan(PI*
                double(i)/double(N))))-PI*ro*v[i][j]/(h[i]*u[i][j]))*((Ti[i][j+1]-R[j-1]*
                R[j-1]*Ti[i][j-1]-(1.0-R[j-1]*R[j-1])*Ti[i][j])/((1.0+R[j-1])*dr[j])) );
        p++;

////////Energy transport equation//////////////////////////////////////////////////////////////////

        mnm.setError( p ,1000.0*(Xi[i][j]-Xi[i-1][j])/(1.0/double(N)) ,1000.0*((PI*ro*d)/(u[i][j]
                *h[i]*h[i])*((2.0*R[j-1]*Xi[i][j+1]+2.0*R[j-1]*R[j-1]*Xi[i][j-1]-2.0*R[j-1]*(1.0+
                R[j-1])*Xi[i][j])/(dr[j]*dr[j]*(1.0+R[j-1])))+(r[j]/h[i]*(pow(myu*m/L*PI*PI*PI/
                (9.0*rho*rho*gl),1.0/3.0)*1.0/(pow(sin(PI*double(i)/double(N)),1.0/3.0)*tan(PI*
                double(i)/double(N))))-PI*ro*v[i][j]/(h[i]*u[i][j]))*((Xi[i][j+1]-R[j-1]*
                R[j-1]*Xi[i][j-1]-(1.0-R[j-1]*R[j-1])*Xi[i][j])/((1.0+R[j-1])*dr[j])));
        p++;

///////Species transport equation/////////////////////////////////////////////////////////////////
////////////Interface////////////////////////////////////////////////////
        if(j==M-1){

        ///////////Phases Equilibrium/////////////////////////////////////////////////
        mnm.setError( p , Ti[i][M] , libr.sc_T_XTsat(Xi[i][M],wat.p_t( P )) );
        p++;

        ///////////Fick's diffusion law//////////////////////////////////////////////
        mnm.setError( p , Gv[i] , -rho*d/(Xi[i][M])*((1+2.0*R[j-1])*Xi[i][j+1]+R[j-1]*R[j-1]*
                Xi[i][j-1]-(1.0+R[j-1]*R[j-1]+2.0*R[j-1])*Xi[i][j])/((1.0+R[j-1])*dr[j])/h[i]) ;//h b
        p++;

        ///////////Absorption heat Thermal Diffusion//////////////////////////////////
        mnm.setError( p , Gv[i]*hv , k*((1+2.0*R[j-1])*Ti[i][j+1]+R[j-1]*R[j-1]*Ti[i][j-1]-(1.0+
                R[j-1]*R[j-1]+2.0*R[j-1])*Ti[i][j])/((1.0+R[j-1])*dr[j])/h[i] );            ///h or b
        p++;

                        }
                }

        // mnm.prt();                          //エラー表示
        mnm.prt_sum();                  //エラーの合計を表示

        }
        }

///////////////Temperature and concentration bulk values/////////////

        uave=0;
        for(n=2;n<=M;n++){
        uave+=u[i][n]*dr[n-1];
                                                }
        Tave=0;
        Xave=0;
        for(n=2;n<=M;n++){
        Tave+=u[i][n]*Ti[i][n]*dr[n-1]/uave;//average temperature for previous angle step
```

```
                Xave+=u[i][n]*Xi[i][n]*dr[n-1]/uave;//average concentration for previous angle step
                }
                //fout<<Xave<<",";
                //fout<<Tave<<endl;

//////heat and mass transfer coefficients////////////////////////////////////////////////////////

                htc= k*(-Ti[i][3]-R[1]*(2.0+R[1])*Ti[i][1]+(1.0+R[1]*R[1]+2.0*R[1])*
                Ti[i][2])/((1.0+R[1])*dr[2])/h[i]/abs(Tave-Tw) ;     ////////////////h or b
                //fout<<htc<<",";
        if(X[i]==1){
                htc= k*(-Ti[i][3]-R[1]*(2.0+R[1])*Ti[i][1]+(1.0+R[1]*R[1]+2.0*R[1])*Ti[i][2])/
                ((1.0+R[1])*dr[2])/h[i]/abs(Tave-Tw) ;               ////////////////h or b
                                        }
        else{
                htc= k*(-Ti[i][3]-R[1]*(2.0+R[1])*Ti[i][1]+(1.0+R[1]*R[1]+2.0*R[1])*Ti[i][2])/
                ((1.0+R[1])*dr[2])/h[i]/abs(Tave-Tw) ;               ////////////////h or b
                        }

                //fout<<htc<<",";

                mtc= -d/(Xi[i][M])*((1+2.0*R[M-2])*Xi[i][M]+R[M-2]*R[M-2]*Xi[i][M-2]-(1.0+R[M-2]*
                R[M-2]+2.0*R[M-2])*Xi[i][M-1])/((1.0+R[M-2])*dr[M-1])/h[i]/abs(Xi[i][1]-Xi[i][M]) ;
                                                                     ////////////////h or b
                //fout<<mtc*3600<<",";

        if(X[i]==1){
                mtc= -d/(Xi[i][M])*((1+2.0*R[M-2])*Xi[i][M]+R[M-2]*R[M-2]*Xi[i][M-2]-(1.0+R[M-2]*
                R[M-2]+2.0*R[M-2])*Xi[i][M-1])/((1.0+R[M-2])*dr[M-1])/h[i]/abs(Xi[i][1]-Xi[i][M]) ;
                                                                     ////////////////h or b
                                        }
        else{
                mtc= -d/(Xi[i][M])*((1+2.0*R[M-2])*Xi[i][M]+R[M-2]*R[M-2]*Xi[i][M-2]-(1.0+R[M-2]*
                R[M-2]+2.0*R[M-2])*Xi[i][M-1])/((1.0+R[M-2])*dr[M-1])/h[i]/abs(Xi[i][1]-Xi[i][M]) ;
                                                                     ////////////////h or b
                        }
                                                                     //fout<<mtc*3600<<",";

//////////////////////Tube average calculation////////////////////////////////////////////////////////

                mf +=2.0*Gv[i]*PI*ro/(double(N)-2.0);//per tube length starting from i 2

                if (i>=3){

                aave +=htc/(double(N)-3.0);
                bave +=mtc/(double(N)-3.0);
                qf +=2.0*PI*ro/(double(N)-3.0)*htc*(Tave-Tw); //per tube length starting from i 2

                        }

                //fout<<Ti[i][M]-Tave<<",";

                //DT +=(Ti[i][M]-Tave)/(double(N)-2.0);

///////////////Molar concentration////////////////////////////////////////////////////////////////////
```

```
            for(j=1;j<=M;j++){

            Cw[i][j]=(rho)/Mw*(1.0-Xi[i][j])-Cwi;

                                                    }
//////Velocity Temperature and concentration Gradients calculation////////////////////////////////
//////////////////////wall derivatives//////////////////////

        dtx[1]=0;

        dty[1]=(-Ti[i][3]-R[1]*(2.0+R[1])*Ti[i][1]+(1.0+R[1]*R[1]+2.0*R[1])*Ti[i][2])/
        ((1.0+R[1])*dr[2])/h[i];

        dux[1]=0;

        dvx[1]=0;

        duy[1]=(-u[i][3]-R[1]*(2.0+R[1])*u[i][1]+(1.0+R[1]*R[1]+2.0*R[1])*u[i][2])/
        ((1.0+R[1])*dr[2])/h[i];

        dvy[1]=(-v[i][3]-R[1]*(2.0+R[1])*v[i][1]+(1.0+R[1]*R[1]+2.0*R[1])*v[i][2])/
        ((1.0+R[1])*dr[2])/h[i];

        dxy[1]=0;

        dxx[1]=1.0/(PI*ro)*(Cw[i][1]-Cw[i-1][1])/(1.0/double(N));

//////////////////////Inner nodes//////////////////////////////////////

        for(j=2;j<=M-1;j++){
        dtx[j]=1.0/(PI*ro)*(Ti[i][j]-Ti[i-1][j])/(1.0/double(N));

        dty[j]=1.0/h[i]*(Ti[i][j+1]-R[j-1]*R[j-1]*Ti[i][j-1]-(1.0-R[j-1]*R[j-1])*Ti[i][j])/
        ((1.0+R[j-1])*dr[j]);

        dxx[j]=1.0/(PI*ro)*(Cw[i][j]-Cw[i-1][j])/(1.0/double(N));
        dxy[j]=1.0/h[i]*(Cw[i][j+1]-R[j-1]*R[j-1]*Cw[i][j-1]-(1.0-R[j-1]*R[j-1])*Cw[i][j])/
        ((1.0+R[j-1])*dr[j]);

        dux[j]=1.0/(PI*ro)*(u[i][j]-u[i-1][j])/(1.0/double(N));
        duy[j]=1.0/h[i]*(u[i][j+1]-R[j-1]*R[j-1]*u[i][j-1]-(1.0-R[j-1]*R[j-1])*u[i][j])/
        ((1.0+R[j-1])*dr[j]);

        dvx[j]=1.0/(PI*ro)*(v[i][j]-v[i-1][j])/(1.0/double(N));
        dvy[j]=1.0/h[i]*(v[i][j+1]-R[j-1]*R[j-1]*v[i][j-1]-(1.0-R[j-1]*R[j-1])*v[i][j])/
        ((1.0+R[j-1])*dr[j]);

        }

//////////////////////Interface//////////////////////////////////////////

        dtx[M]=1.0/(PI*ro)*(Ti[i][M]-Ti[i-1][M])/(1.0/double(N));

        dty[M]=1.0/h[i]*((1+2.0*R[M-2])*Ti[i][M]+R[M-2]*R[M-2]*Ti[i][M-2]-(1.0+R[M-2]*R[M-2]+2.0*
        R[M-2])*Ti[i][M-1])/((1.0+R[M-2])*dr[M-1]);
```

```
        dxx[M]=1.0/(PI*ro)*(Cw[i][M]-Cw[i-1][M])/(1.0/double(N));

        dxy[M]=1.0/h[i]*((1+2.0*R[M-2])*Cw[i][M]+R[M-2]*R[M-2]*Cw[i][M-2]-(1.0+R[M-2]*R[M-2]+2.0*
        R[M-2])*Cw[i][M-1])/((1.0+R[M-2])*dr[M-1]);

        dux[M]=1.0/(PI*ro)*(u[i][M]-u[i-1][M])/(1.0/double(N));

        duy[M]=1.0/h[i]*((1+2.0*R[M-2])*u[i][M]+R[M-2]*R[M-2]*u[i][M-2]-(1.0+R[M-2]*R[M-2]+2.0*
        R[M-2])*u[i][M-1])/((1.0+R[M-2])*dr[M-1]);

        dvx[M]=1.0/(PI*ro)*(v[i][M]-v[i-1][M])/(1.0/double(N));

        dvy[M]=1.0/h[i]*((1+2.0*R[M-2])*v[i][M]+R[M-2]*R[M-2]*v[i][M-2]-(1.0+R[M-2]*R[M-2]+2.0*
        R[M-2])*v[i][M-1])/((1.0+R[M-2])*dr[M-1]);

////////////////////////////////////////////////////////////////////////////////////////////////////

        //fout<<dty[M]*h[i]<<endl;
        //dtM +=dty[M]*h[i]/(double(N)-2.0);
        //fout<<dty[M]*h[i]<<",";
        //fout<<dty[1]*h[i]<<endl;

////////Entropy generation groups//////////////////////////////////////////////////////////////////

        for(j=1;j<=M;j++){

        Et[i][j]=(libr.sc_thc_XT(Xi[i][j],Ti[i][j]))/
        (Ti[i][j]*Ti[i][j])*(dtx[j]*dtx[j]+dty[j]*dty[j]);

        Ef[i][j]=(libr.sc_visc_XT(Xi[i][j],Ti[i][j]))/Ti[i][j]*
        (2.0*(dux[j]*dux[j]+dvy[j]*dvy[j])+(duy[j]+dvx[j])*(duy[j]+dvx[j]));

        Ec[i][j]=(wat.sat_cpv(Ti[i][j])*1000*Mw*(Ti[i][j]-298.15)+hw0+Ti[i][j]*
        (wat.sat_cpv(Ti[i][j])*1000*Mw*log(Ti[i][j]/298.15)+sw0))*(v[i][j]*dty[j]+u[i][j]*dtx[j])*
        (Cw[i][j])/(Ti[i][j]*Ti[i][j]);

        Ed[i][j]=-(wat.sat_cpv(Ti[i][j])*1000*Mw*(Ti[i][j]-298.15)+hw0+Ti[i][j]*
        (wat.sat_cpv(Ti[i][j])*1000*Mw*log(Ti[i][j]/298.15)+sw0))*(dxy[j]*dty[j]+dxx[j]*dtx[j])*
        (libr.sc_d_XT(Xi[i][j],Ti[i][j]))/(Ti[i][j]*Ti[i][j]);

                                                }

////////////////////////////////////////////////////////////////////////////////////////////////////

        }

else {

//////////////Inlet position parameters//////////////////////////////////

        for(j=1;j<=M;j++){

                Cw[i][j]=(rho)/Mw*(1.0-Xi[i][j])-Cwi;
                Et[i][j]=0;
                Ef[i][j]=0;
                Ec[i][j]=0;
```

```
                Ed[i][j]=0;

                                        }

                }

//////Local Results Printing out////////////////////////////////////////////////////////////


//TEG=0;

//              for(j=2;j<=M;j++){
//                      TEG +=(Et[i][j])*dr[j-1];
//                                              }

//      fout<<TEG<<",";

//      TEG=0;

//              for(j=2;j<=M;j++){
//                      TEG +=(Ef[i][j])*dr[j-1];
//                                              }

//      fout<<TEG<<",";

//      TEG=0;

//              for(j=2;j<=M;j++){
//                      TEG +=(Ec[i][j])*dr[j-1];
//                                              }

//      fout<<TEG<<",";

//      TEG=0;

//              for(j=2;j<=M;j++){
//                      TEG +=(Ed[i][j])*dr[j-1];
//                                              }

//      fout<<TEG<<",";

//TEG=0;

//              for(j=2;j<=M;j++){
//                      TEG +=(Et[i][j]+Ef[i][j]+Ec[i][j]+Ed[i][j])*dr[j-1];
//                                              }

//      fout<<TEG<<endl;

        }//////////////////////Angle loop////////////////////////////////////////////////////////

        fout<<qf<<",";
        fout<<aave<<",";
        fout<<bave*3600<<",";
        fout<<mf<<",";
        fout<<mf*hv<<",";
```

```
        //fout<<dtM<<",";
        //fout<<DT<<endl;

//////////Results printing out////////////////////////////////////////////////////////////////////////////

//fout<<0<<endl;

//      for(j=1;j<=M;j++){
//      for(i=1;i<=N-1;i++){
//              fout<<Et[i][j]/1000<<",";
                                                //}
//      fout<<0<<endl;
                                                //}

                //for(j=1;j<=M;j++){
        //for(i=1;i<=N-1;i++){
                //fout<<Ef[i][j]/1000<<",";
                        //                      }
        //fout<<0<<endl;
        //                                      }

        //              for(j=1;j<=M;j++){
        //for(i=1;i<=N-1;i++){
        //      fout<<Ec[i][j]/1000<<",";
        //                                      }
        //fout<<0<<endl;
        //                                      }

        //                      for(j=1;j<=M;j++){
        //for(i=1;i<=N-1;i++){
        //      fout<<Ed[i][j]/1000<<",";
        //                                      }
        //fout<<0<<endl;
        //                                      }

        //                              for(j=1;j<=M;j++){
        //for(i=1;i<=N-1;i++){
        //      fout<<(Et[i][j]+Ef[i][j]+Ec[i][j]+Ed[i][j])/1000<<",";
        //                                      }
        //fout<<0<<endl;
        //                                      }
        for(i=2;i<=N-2;i++){
                for(j=2;j<=M;j++){
                        TEG +=2.0*PI*ro*(Et[i][j])/double(N)*h[i]*dr[j-1];
                                                }

                                                }
        fout<<TEG<<",";

        TEG=0;

        for(i=2;i<=N-2;i++){
                for(j=2;j<=M;j++){
                        TEG +=2.0*PI*ro*(Ef[i][j])/double(N)*h[i]*dr[j-1];
                                                }
```

```
                                        }
fout<<TEG<<",";

        TEG=0;

        for(i=2;i<=N-2;i++){
                for(j=2;j<=M;j++){
                        TEG +=2.0*PI*ro*(Ec[i][j])/double(N)*h[i]*dr[j-1];
                                        }

                                        }
        fout<<TEG<<",";

        TEG=0;

        for(i=2;i<=N-2;i++){
                for(j=2;j<=M;j++){
                        TEG +=2.0*PI*ro*(Ed[i][j])/double(N)*h[i]*dr[j-1];
                                        }

                                        }
        fout<<TEG<<",";

        TEG=0;

        for(i=2;i<=N-2;i++){
                for(j=2;j<=M;j++){
                        TEG +=(Et[i][j]+Ef[i][j]+Ec[i][j]+Ed[i][j])/double(N)*dr[j-1];
                                        }

                                        }
        fout<<TEG<<",";

        TEG=0;

        for(i=2;i<=N-2;i++){
                for(j=2;j<=M;j++){
                        TEG +=2.0*PI*ro*(Et[i][j]+Ef[i][j]+Ec[i][j]+Ed[i][j])/double(N)*h[i]*dr[j-1];
                                        }

                                        }
        fout<<TEG<<endl;

        //for(i=1;i<=N-1;i++){
                //fout<<Gv[i]<<endl;
                //fout<<X[i]<<",";
        //if(X[i]==1){
                //      fout<<h[i]<<endl;
        //}
        //else {
                //      fout<<b[i]<<endl;
        //}
        //}

//for(j=1;j<=M;j++){
        //for(i=1;i<=N-1;i++){
```

```
                //fout<<Xi[i][j]<<",";
        //}
        //fout<<0<<endl;
//}

//for(j=1;j<=M;j++){
        //for(i=1;i<=N-1;i++){
                //fout<<Ti[i][j]<<",";
        //}
        //fout<<0<<endl;
//}

//for(j=1;j<=M;j++){
        //for(i=1;i<=N-1;i++){
                //fout<<u[i][j]<<",";
        //}
        //fout<<0<<endl;
//}

//for(j=1;j<=M;j++){
        //for(i=1;i<=N-1;i++){
                //fout<<v[i][j]<<",";
        //}
        //fout<<0<<endl;
//}
//////////Average Results Printing out/////////////////////////////////////////////////////////////

}/////////////////Parametric Analysis loop/////////////////////////////////////////////////////////


}/////////////////flowrate loop/////////////////////////////////////////////////////////////////////

fout<<0<<endl;

}
```

APPENDIX C, Technical drawings of the experimental apparatus

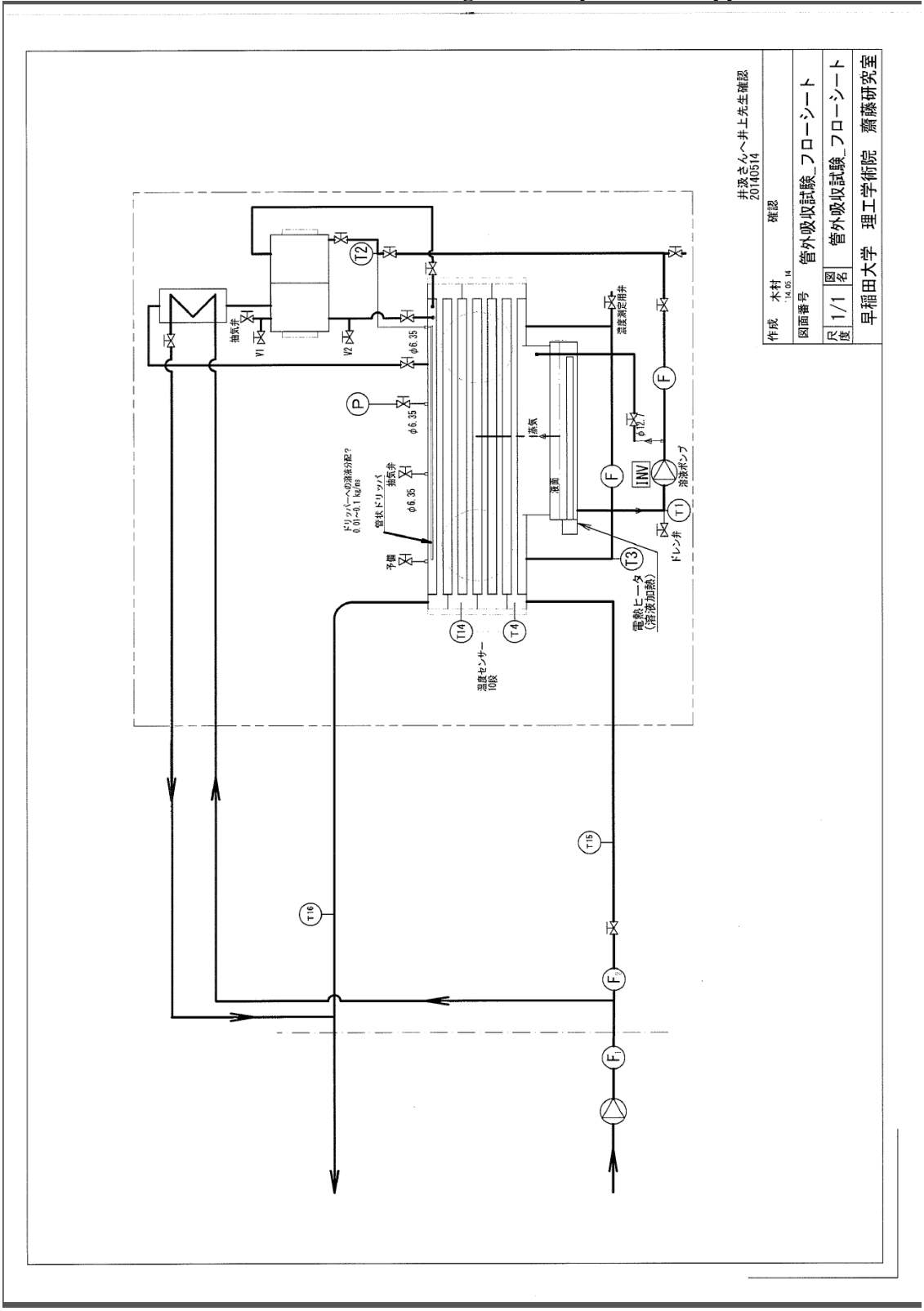

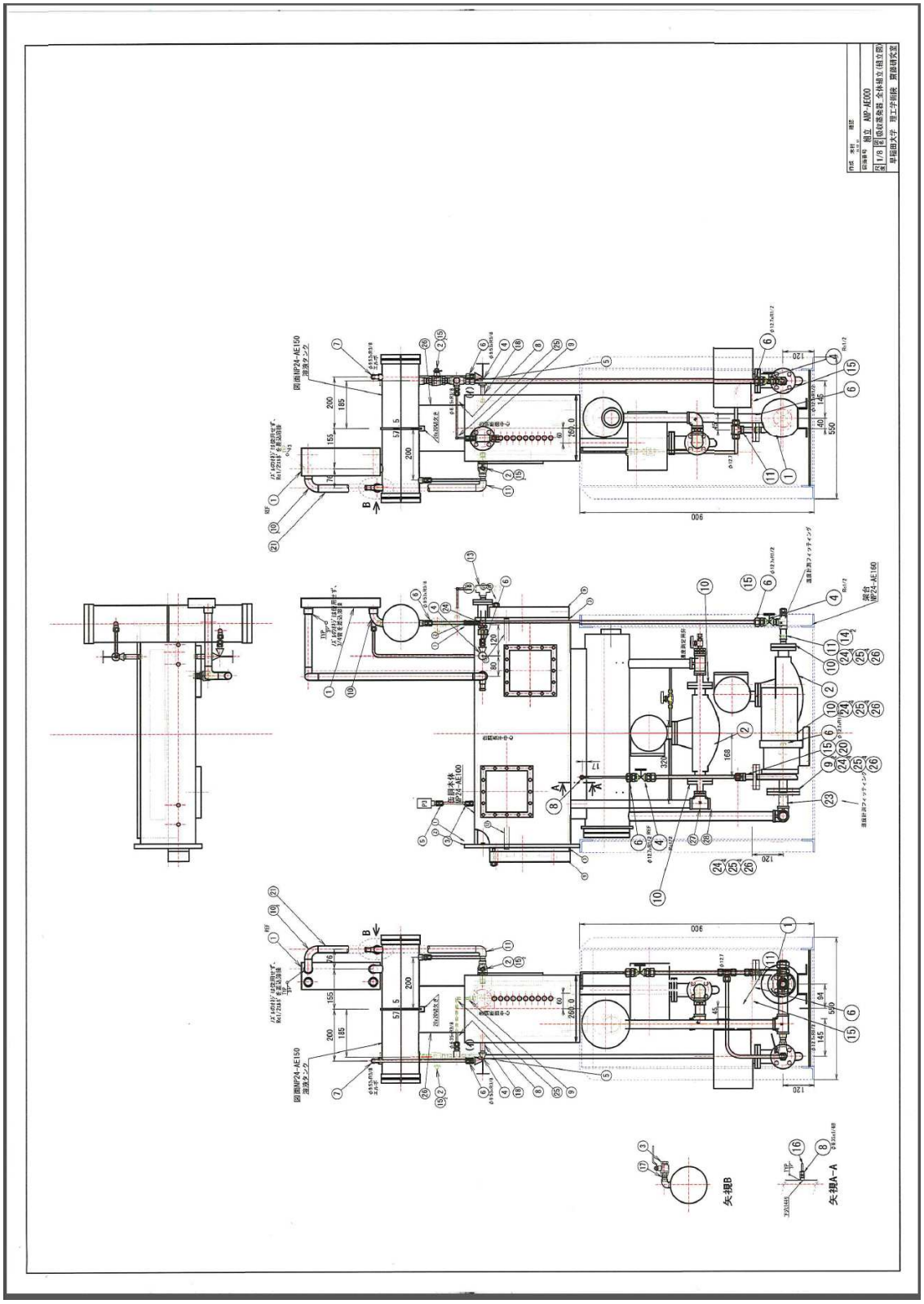
矢視B
矢視A-A

缶胴組立 ANP24-AE100(2/6)

番号	品名	個数	図面番号	材料	備考
1A	缶胴プレート(左)	1	ANP24-AE100(3/6)	SUS430	素材 12t
1B	缶胴プレート(右)	1	〃	SUS430	素材 12t
2	チューブプレート(左,右共通)	2	ANP24-AE100(4/6)	SUS430	素材 16t
4A	側板(16tx370wx854)(シェル)	1	ANP24-AE100(5/6)	SUS430	素材 16t (観察窓)
4B	側板(12tx370wx854)(シェル)	1	〃	SUS430	素材 16t
5	天板(12tx180wx854)(シェル)	1	〃	SUS430	素材 12t
6	底板(12tx180wx854)(シェル)	1	〃	SUS430	素材 12t
7	散布器(ドリッパ)	1	ANP24-AE100(?)		別途指示
8	缶胴組立(ヒーター) (再生器)	1	ANP24-AE100(6/6)		
10	散布器(ドリッパ)支え φ18使用	1	φ17.5(外)-10L	SUS304	丸棒加工 貫通穴φ13.5
11	管(ドリッパ・チューブ導管)	1	25A-129L(差込4mm)	SUS304	Sch20
12	フランジ 20A 5K	2		SUS304	
13	ソケット 20A Rp1/2	1	20A-33L	SUS304	
14	オスコネクター tube 1/2 (φ12.7)	1	DCT 8-R8 ss	SUS304	イハラサイエンス
15	パッキン フランジ 5K-20A	1			

番号	品名	個数	図面番号
18	角型サイトグラス	2	ANP24-AE100
19	パッキン・角型サイトグラス	2	
21A	水室(左)	1	ANP24-AE100(4/6)
21B	水室(右)	1	〃
22A	パッキン・水室(左)	1	
22B	パッキン・水室(左)	1	
25	スタットボルト M10-50L (角窓)	32	
26	座金 M10 (角サイトグラス)	32	
27	ナット M10 (角サイトグラス)	32	
25	ボルト M10-40L (フランジ 5K)	4	
26	座金 M10 (フランジ 5K)	4	
27	ナット M10 (フランジ 5K)	4	

支給

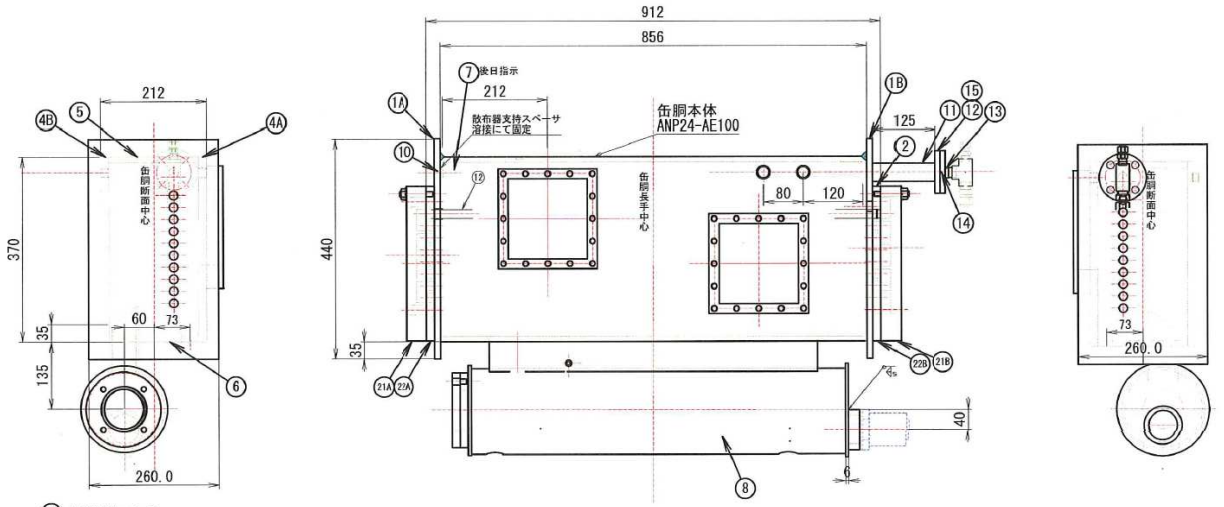

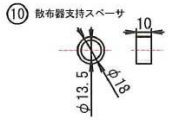

⑱ 角フランジ
⑲ 角パッキン
㉕ ~ ㉗ ボルト・ナット・ワッシャー

注記
1. TYP. 他の同様な箇所にも適用する寸法・溶接記号
2. REF. 参考寸法
3. 使用圧力
缶胴側 max 0.1 MPa(G)
水室側 max 0.1 MPa(G)

作成	井上 12.06.08	確認	中川 12.06.12	修正	ikumi 14.06.12
図面番号	缶胴組立 ANP24-AE100 (2/6)				
尺度	1/5	図名	吸収蒸発器_缶胴組立(組立図)		
早稲田大学 理工学術院 斎藤研究室					

1A 缶胴プレート（左）

材料：SUS430　　素材 12t

製作数：1個

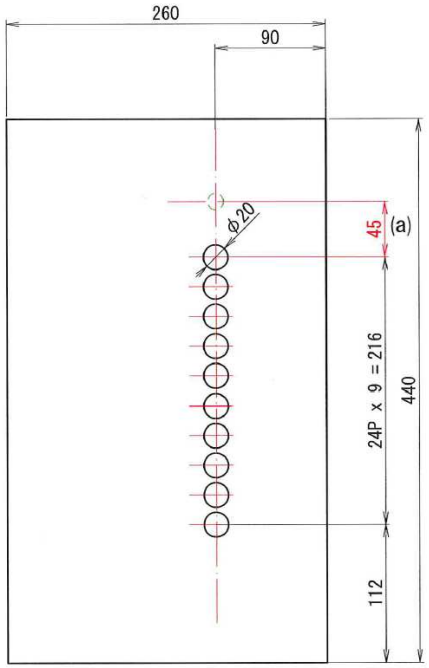

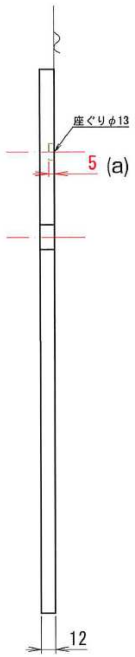

1B 缶胴プレート（右）　部品(1A)とは、勝手反対。

材料：SUS430　　素材 12t

製作数：1個

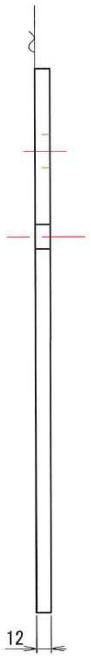

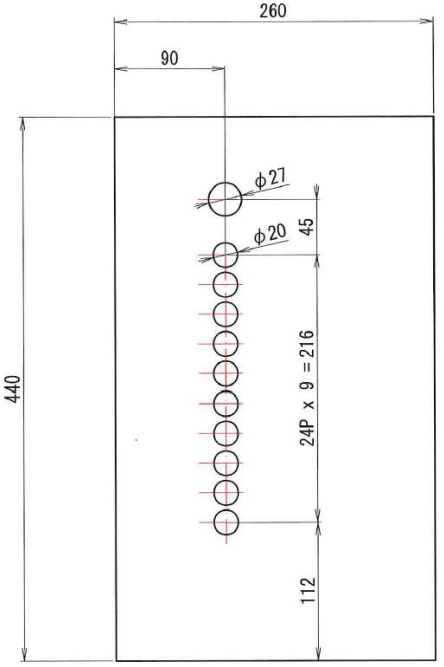

改正　(a),
座ぐり深さ，座ぐり穴位置寸法

注記
1. TYP.　他の同様な箇所にも適用する
寸法・溶接記号
2. 使用圧力　0.1MPa

作成　木村 '14.08.24	確認		
図面番号	缶胴組立　ANP24-AE100(3/6)		
尺度	1/3	図名	吸収蒸発器_缶胴組立(プレート)
早稲田大学　理工学術院　齋藤研究室			

1A チューブプレート

材料：SUS430　　素材 16t

製作数：2個

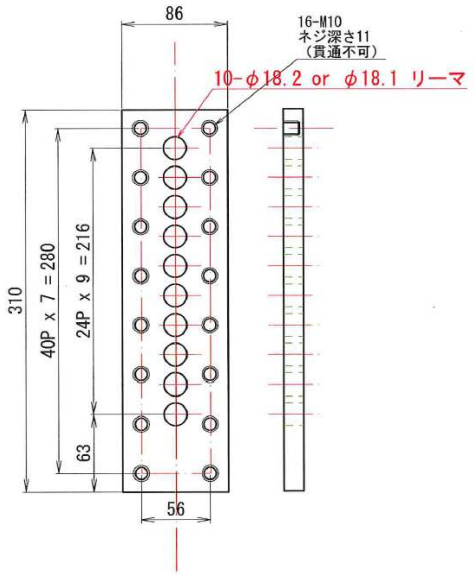

1B 水室（右）

材料：アクリル

製作数：1個

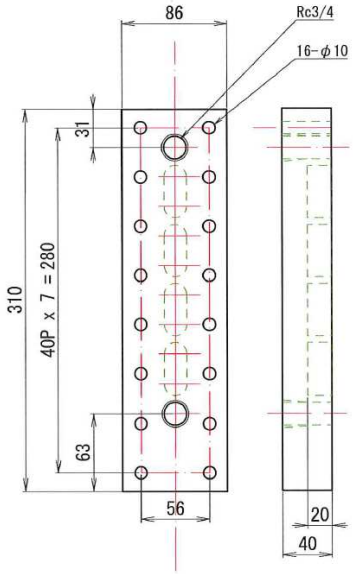

1C 水室（右）

材料：アクリル

製作数：1個

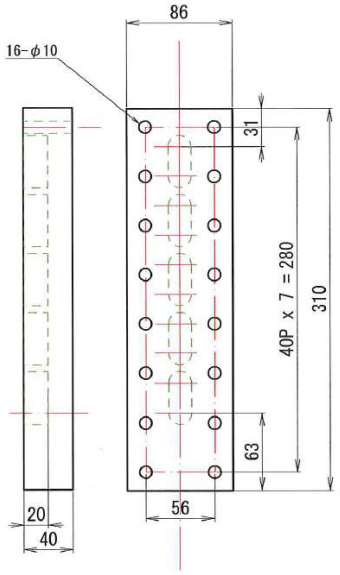

余裕寸法はエキスパンドを考慮して検討ください）

作成 木村 '14.07.15		確認	
図面番号	缶胴組立　ANP24-AE100(4/6)		
尺度	1/3	図名	缶胴組立(チューブプレート)
早稲田大学　理工学術院　齋藤研究室			

缶胴組立 ANP24-AE100(5/6)

番号	品名	個数	材料	備考
4	側板 880x490-16t	2	SUS430	
5	天板 880x180-16t	1	SUS430	
6	底板 880x180-16t	1	SUS430	

側板④詳細 (4A)(4B)

材料：SUS430
製作数 各1

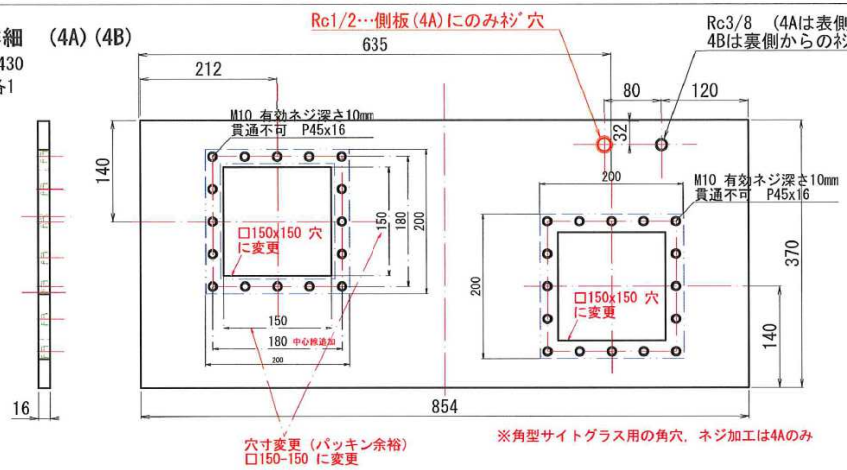

天板⑤詳細

材料：SUS430
製作数 1

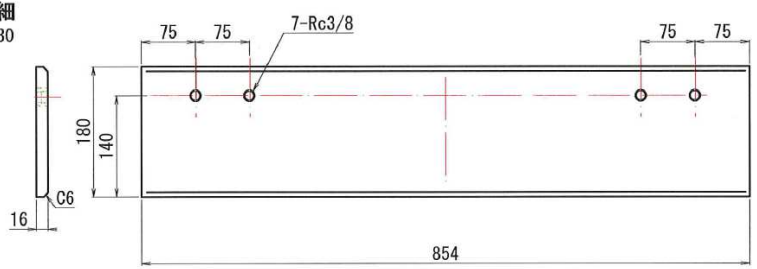

底板⑥詳細

材料：SUS430
製作数 1

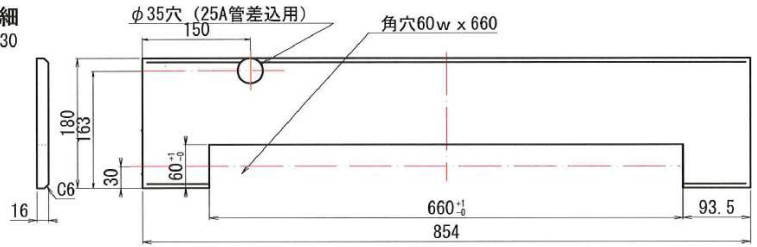

作成	木村	確認	
図面番号	缶胴組立 ANP24-AE100 (5/6)		
尺度	1/5	図名	吸収蒸発器_缶胴組立(シェル)
早稲田大学 理工学術院 齋藤研究室			

⑪ ヒーター容器

缶胴組立 NP24-AE100(6/6)

番号	品名	個数	材料	備考
1	台形板 48Wx100x135-6t	2	SUS430	
2	平板 135x660-6t	1	SUS430	
3	平板 100x660-6t	1	SUS430	
4	平板 30x660-3t	2	SUS430	
5	配管 150A-750 sch20	1	SUS430	
6	円板①	1	SUS430	図面番号 ANP24-AE100(7/7)
7	円板②	1	SUS430	図面番号 ANP24-AE100(7/7)
8	ネジ台座(ヒーターソケット) G2	1	SUS304	坂口電熱
9	ヒーター1OkW	1	SUS	坂口電熱
10	ソケット用ガスケット G2			
11	サイトグラス φ80	1式		図面番号 ANP24-AE120
12	植込みボルト M12x40	4	SUS304	
13	ばね座金 M12	4	SUS304	
14	ナット M12	4	SWRH	

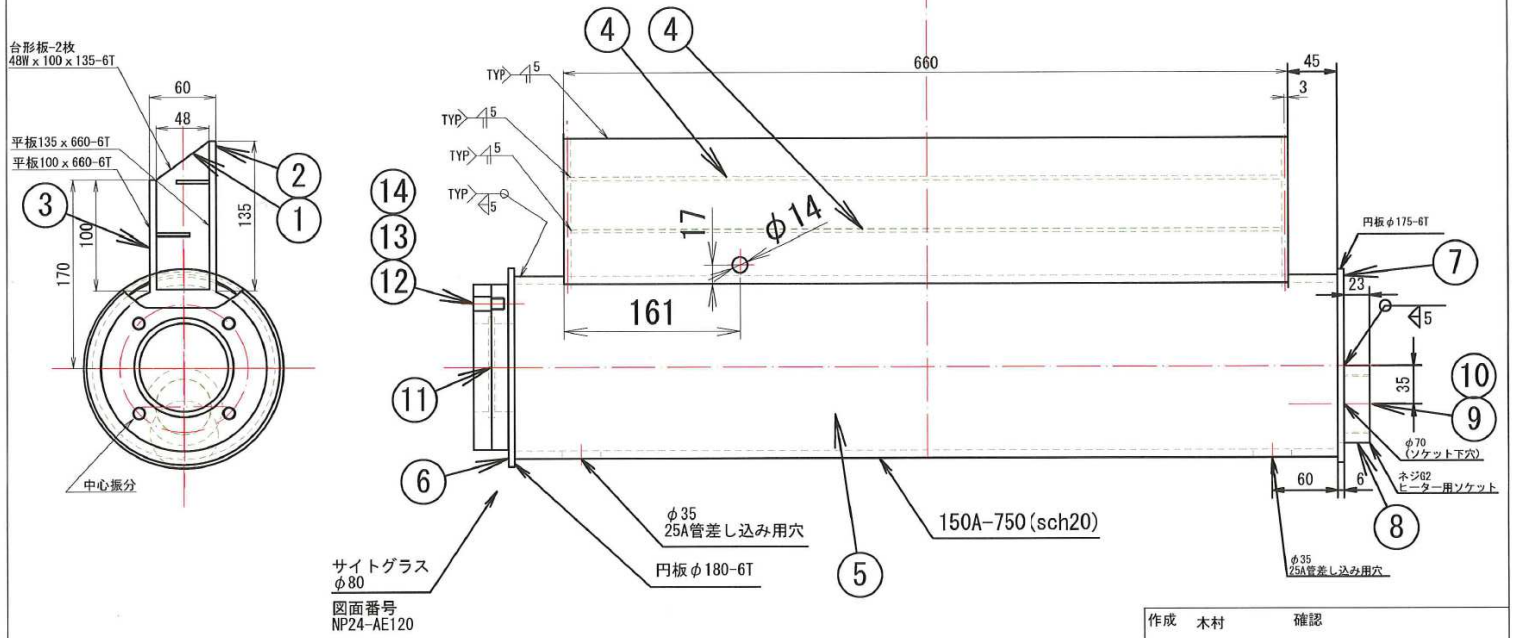

作成	木村	確認	
図面番号	缶胴組立 ANP24-AE100 (6/7)		
尺度	1/3	図名	吸収蒸発器_缶胴組立(ヒーター)
早稲田大学 理工学術院 齋藤研究室			

円板①

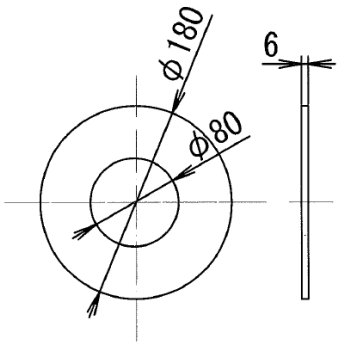

円板②

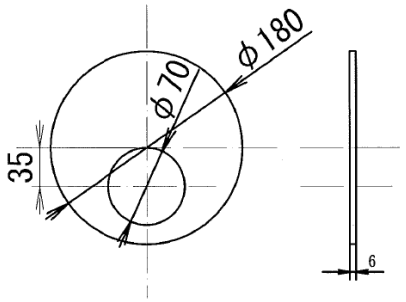

作成	木村	確認	
図面番号	缶胴組立 ANP24-AE100 (7/7)		
尺度	1/3	図名	缶胴組立(ヒーター)円板①②
早稲田大学 理工学術院 齋藤研究室			

① ｻｲﾄｸﾞﾗｽ（φ80）台座

材料：SUS430　　製作数：3個

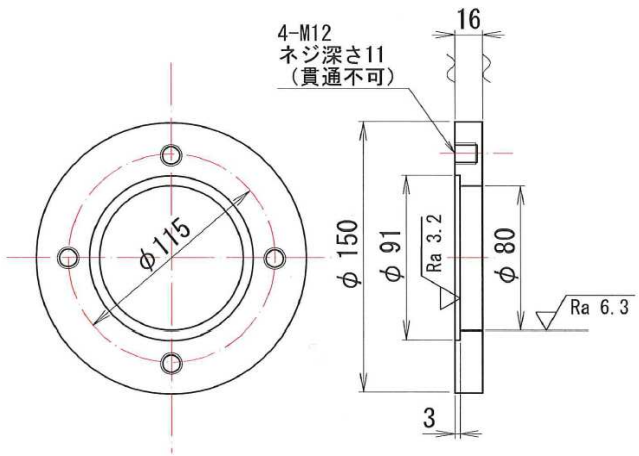

② ｻｲﾄｸﾞﾗｽ（φ80）ｶﾊﾞｰ

材料：SUS430　　製作数：3個

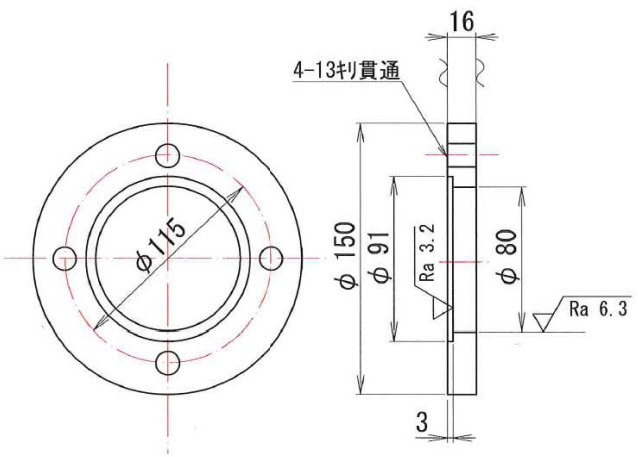

φ80サイトグラス　MP24-AE120　　使用数:全4組（下記個数は延べ個数）

	番号	品名	個数	図面番号	材料	備考
	1	サイトグラス(φ80)台座	4	NP24-AE120	SUS430	
	2	サイトグラス(φ80)カバー	4	NP24-AE120	SUS430	
支給	3	サイトグラス　φ90x12t	4		硬質ｶﾞﾗｽ	
支給	4	ガスケット　φ90x80x1.5t	8		ｼﾞｮｲﾝﾄｼｰﾄ	V#6501
	5	植込ボルト　M16x60	16		SUS304	
	6	ナット　　M16	16		SUS304	
	7	ばね座金　　M16	16		SWRH	

使用圧力：max1.0 MPa
使用温度：max180℃

作成	井上 '12.08.07	確認	中川 '12.08.07
図面番号	φ80ｻｲﾄｸﾞﾗｽ　NP24-AE120		
尺度	1/3	図名	吸収蒸発器（φ80サイトグラス）

早稲田大学　理工学術院　齋藤研究室

溶液タンク ANP24-AE150

番号	品名	個数	図面番号	材料	備考
1	鋼管 125A x 247 sch20s	2	ANP24-AE150	SUS304	タンク胴体
2	サイトグラスφ80	2	ANP24-AE120	SUS430	別紙展開
3	円板 φ156x6t	2	ANP24-AE150	SUS430	仕切板
4	Rc3/8 エルボ	1		SUS304	
5	ハーフPTソケット15A	1		SUS304	Rc1/2
6	ハーフPTソケット10A	2		SUS304	Rc3/8

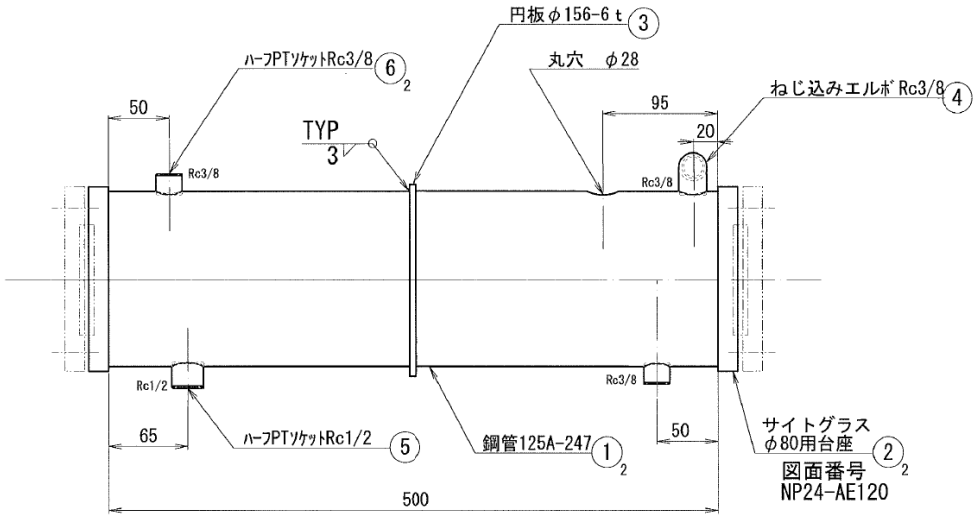

注記
1. TYP. 他の同様な箇所にも適用する寸法・溶接記号
2. 使用圧力 0.1MPa(G)

作成 木村 '14.07.15	確認		
図面番号	溶液タンク ANP24-AE150		
尺度	1/3	図名	溶液タンク組立
早稲田大学 理工学術院 齋藤研究室			

①角型サイトグラス　2枚

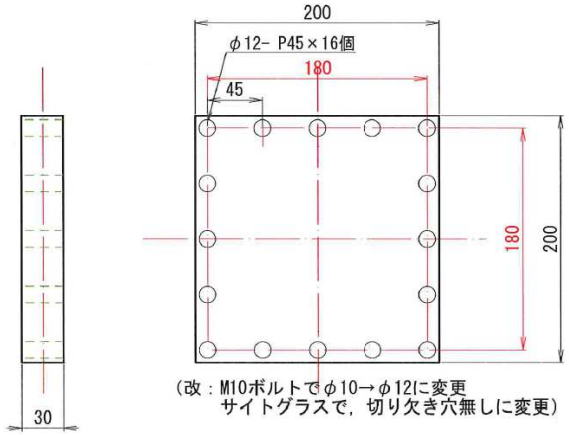

（改：M10ボルトでφ10→φ12に変更
サイトグラスで，切り欠き穴無しに変更）

②ガスケット

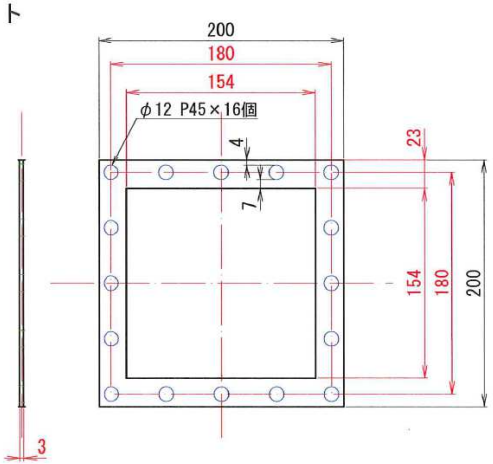

③サイトグラス押
（ポリカ割れ防止用）

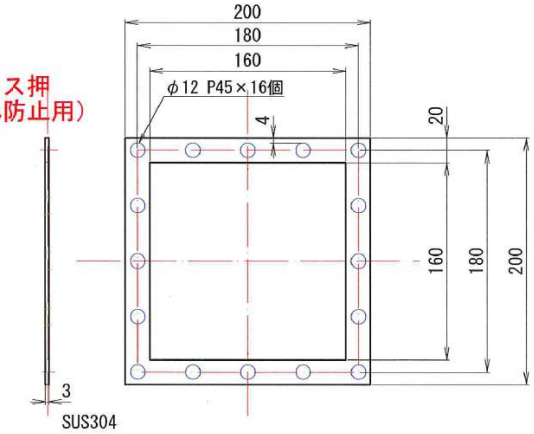

SUS304

改正：
角穴変更，ボルト穴中心線寸法，□180mmを追加
M10ボルト穴変更，

パッキン厚さ，5t→3t

・サイトグラス押さえ部品追加

作成	木村	確認	
図面番号			
尺度	1/3	図名	角型サイトグラス　ガスケット
早稲田大学　理工学術院　齋藤研究室			

架台組立　ANP24-AE160

番号	品名	個数	材料	備考
1	山形鋼 50x50x6t-900	4	SUS304	柱
2	山形鋼 50x50x6t-450	4	SUS304	梁および脚
3	山形鋼 50x50x6t-820	2	SUS304	脚
4	平鋼 50x6t-820	1	SUS304	突っ張り
5	平板 6t- 450x200	1	SUS304	循環ポンプ台座

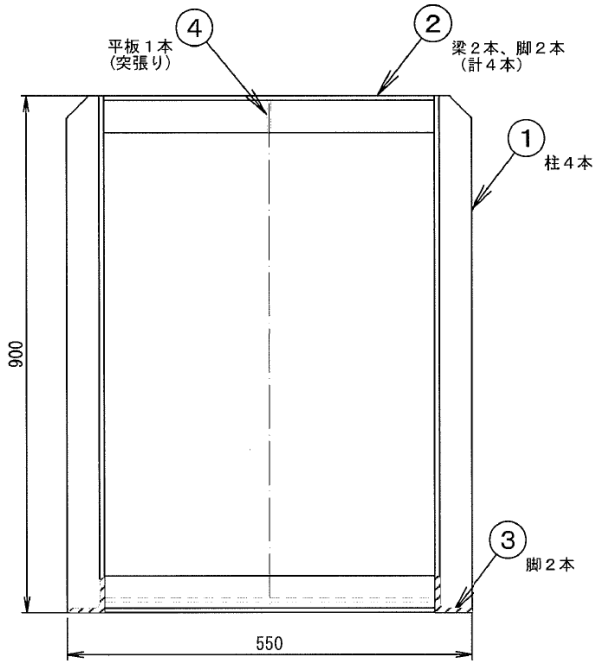

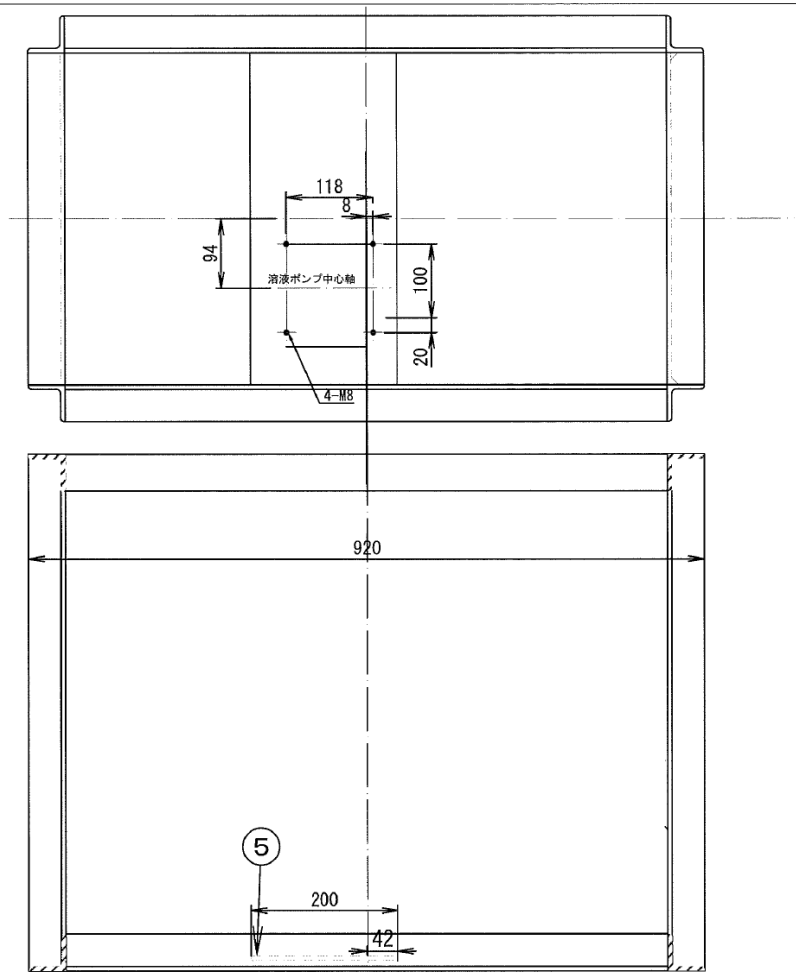

作成　木村　'14.06.24	確認	尺度	1/5	図名　管内蒸発_架台
図面番号	架台　ANP24-AE160	早稲田大学　理工学術院　齋藤研究室		

冷却水配管 NP24-AE250

番号	品名	個数	図面番号	材料	備考
支給 1	ボール弁 3/4 (フルボア)	1		SUS	キッツメクローバル クラス800
支給 2	ボール弁 1/2 (フルボア)	1		SUS	キッツメクローバル クラス800
支給 3	BaLok 1/2"xR1/2	4		SUS316	イハラサイエンス DCT 8-R8
4					
5	ねじ込異径チー Rc3/4xRc1/2	2		SUS304	
6	ねじ込エルボ Rc 1/2	1		SUS304	
7	Rc1/2ハーフアリソケット	1		SUS304	
8	R1/2ハトルニップル	1		SUS304	
9	R3/4ハトルニップル	1		SUS304	
10	R3/4片ニップル	2		SUS304	
11					
12	1/2"ステンレスチューブ(φ12.7)	1m	NP24-AE250	SUS304	現合 φ12.7x1.0t

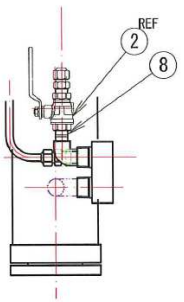

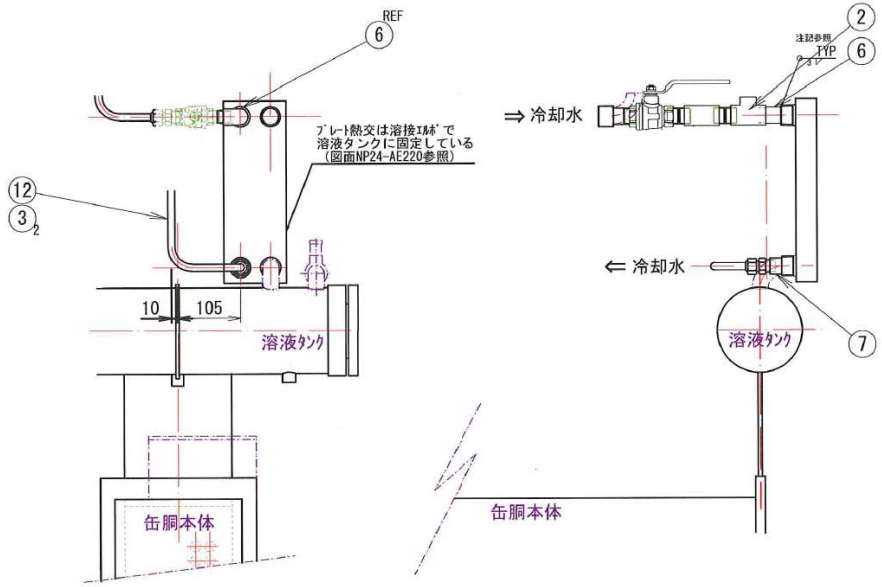

注記　熱交換器のノズルは、おねじR1は使用せず、
ノズル内径側に、管継手（6、7、10）を差込み
溶接し、他の配管と接続する。

注記　T8, T9は温度センサー取付位置を示す

作成	井上 '12.09.04	確認	中川 '12.09.04
図面番号	NP24-AE250 冷却水配管		
尺度	1/6	図名	気液分離_給水タンク配管組立
早稲田大学　理工学術院　齋藤研究室			

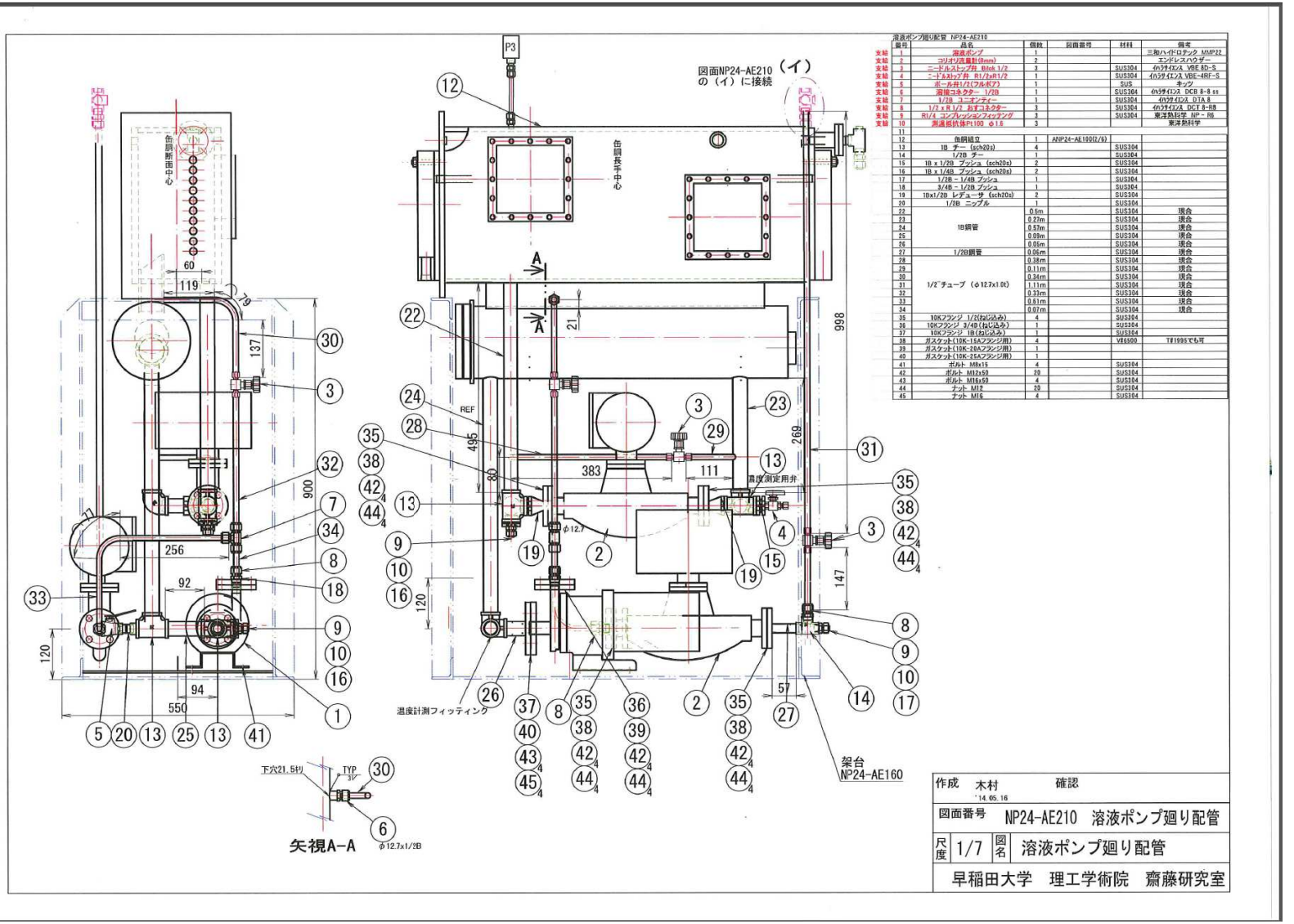

溶液ポンプ廻り配管 NP24-AE210

番号	品名	個数	図面番号	材料	備考
支給	1 溶液ポンプ	1			三和ハイドロテック MMP32
支給	2 コリオリ流量計(8mm)	2			エンドレスハウザー
支給	3 ニードルストップ弁 B½A 1/2	3		SUS304	イハラサイエンス VBE RD-S
支給	4 ニードルストップ弁 R1/2xR1/2	1		SUS304	イハラサイエンス VBE-4RF-S
支給	5 ボールギ1/2(フルボア)	1		SUS	キッツ
支給	6 溶接コネクター 1/2B	1		SUS304	イハラサイエンス DCB 8-8 ss
支給	7 1/2B ユーオンティー	1		SUS304	イハラサイエンス DTA 8
支給	8 1/2 x R1/2 おすコネクター	3		SUS304	イハラサイエンス DCT 8-RB
支給	9 R1/4 コンプレッションフィッティング	3		SUS304	東洋熱工学 NF-R6
支給	10 測温抵抗体Pt100 φ1.6	3			東洋熱工学
	11				
	12 缶胴組立	1	ANP24-AE100(2/6)		
	13 1B チー (sch20s)	4		SUS304	
	14 1/2B チー	1		SUS304	
	15 1B x 1/2B ブッシュ (sch20s)	2		SUS304	
	16 1B x 1/4B ブッシュ (sch20s)	2		SUS304	
	17 1/2B - 1/4B ブッシュ	1		SUS304	
	18 3/4B - 1/2B ブッシュ	1		SUS304	
	19 1Bx1/2B レデューサ (sch20s)	2		SUS304	
	20 1/2B ニップル	1		SUS304	
	22 1B鋼管	0.5m		SUS304	現合
	23 1B鋼管	0.27m		SUS304	現合
	24 1B鋼管	0.57m		SUS304	現合
	25 1B鋼管	0.09m		SUS304	現合
	26 1B鋼管	0.05m		SUS304	現合
	27 1/2B鋼管	0.06m		SUS304	現合
	28 1/2"チューブ（φ12.7x1.0t）	0.38m		SUS304	現合
	29 1/2"チューブ（φ12.7x1.0t）	0.11m		SUS304	現合
	30 1/2"チューブ（φ12.7x1.0t）	0.34m		SUS304	現合
	31 1/2"チューブ（φ12.7x1.0t）	1.11m		SUS304	現合
	32 1/2"チューブ（φ12.7x1.0t）	0.33m		SUS304	現合
	33 1/2"チューブ（φ12.7x1.0t）	0.61m		SUS304	現合
	34 1/2"チューブ（φ12.7x1.0t）	0.07m		SUS304	現合
	35 10Kフランジ 1/2(ねじ込み)	4		SUS304	
	36 10Kフランジ 3/4B(ねじ込み)	1		SUS304	
	37 10Kフランジ 1B(ねじ込み)	1		SUS304	
	38 ガスケット(10K-15Aフランジ用)	4		VR6500	TF1995でも可
	39 ガスケット(10K-20Aフランジ用)	1			
	40 ガスケット(10K-25Aフランジ用)	1			
	41 ボルト M8x15	4		SUS304	
	42 ボルト M12x50	28		SUS304	
	43 ボルト M16x50	4		SUS304	
	44 ナット M12	28		SUS304	
	45 ナット M16	4		SUS304	

作成	木村 '14.05.16	確認	
図面番号	NP24-AE210 溶液ポンプ廻り配管		
尺度	1/7	図名	溶液ポンプ廻り配管
早稲田大学 理工学術院 齋藤研究室			

References

1) F. Carré, Grand appareil de Ferdinand Carré pour fabriquer de la glace Illustration tirée du livre "L'eau" de Gaston Tissandier, 4e édition, (1878), Librairie Hachette Chargé par Gérard Janot.
2) J. Gladstone , John Gorrie, The Visionary. ASHRAE Journal, December (1998), 29−35.
3) E. Granryd, B. Palm, Refrigerating engineering, Stockholm Royal Institute of Technology, (2005), chap. 4-3.
4) Einstein et al., U.S. patent No. 1,781,541, Nov. 11 (1930), Refrigeration, filed Dec. (1927).
5) J.M. Gordon, K.C. Ng, Cool Thermodynamics, Cambridge International Science Publishing, (2000), UK.
6) J. D. Killion, S. Garimella, A Review of Experimental Investigations of Absorption of Water Vapor in Liquid Films Falling Over Horizontal Tubes, HVAC&R Research, 9(2), (2003),111–136.
7) S. Göktun, Er I.Deha, Performance analysis of an irreversible cascaded heat-transformer. Applied Energy, 72(2), (2002), 529–539.
8) J. Deng, R. Z. Wang, G. Y. Han, A review of thermally activated cooling technologies for combined cooling, heating and power systems. Progress in Energy and Combustion Science, 37(2), (2011), 172–203.
9) X. Wang, L. Shi, J. Yin, M. S. Zhu, A two-stage heat transformer with H2O/LiBr for the first stage and 2,2,2-trifluoroethanol (TFE)/N-methy1-2-pyrrolidone (NMP) for the second stage. Applied Energy, 71(3), (2002), 235–249.
10) F. Ziegler, Recent developments and future prospects of sorption heat pump systems. International Journal of Thermal Sciences, 38(3), (1999), 191–208.
11) N. Chekir, A. Bellagi, Performance improvement of a butane/octane absorption chiller, Energy, 36, (10), (2011), 6278-6284.
12) F. Ziegler, R. Kahn, F. Summerer, G. Alefeld, Multi-effect absorption chillers, International Journal of Refrigeration, 16, (5), (1993), 301-311.
13) T. Berlitz, P. Satzger, F. Summerer, F. Ziegler, G. Alefeld, A contribution to the evaluation of the economic perspectives of absorption chillers: Contribution à l'évaluation des perspectives économiques des refroidisseurs à adsorption, International Journal of Refrigeration, 22, (1), (1999), 67-76.
14) N. Chaiyat, T. Kiatsiriroat, Analysis of combined cooling heating and power generation from organic Rankine cycle and absorption system, Energy, 91, (2015), 363-370.
15) F. Ziegler, G. Alefeld, Coefficient of performance of multistage absorption cycles, International Journal of Refrigeration, 10, (5), (1987), 285-295.
16) M. E. Álvarez, X. Esteve, M. Bourouis, Performance analysis of a triple-effect absorption cooling cycle using aqueous (lithium, potassium, sodium) nitrate solution as a working pair, Applied Thermal Engineering, 79, (2015), 27-36.
17) W. Wu, B. Wang, W. Shi, X. Li, Absorption heating technologies: A review and perspective, Applied Energy, 130, (2014), 51-71.
18) X.Q. Zhai, M. Qu, Yue. Li, R.Z. Wang, A review for research and new design options of solar absorption cooling systems, Renewable and Sustainable Energy Reviews, 15, (9), (2011), 4416-4423.
19) Y. Kaita, Simulation results of triple-effect absorption cycles, International Journal of Refrigeration, 25, (7), (2002), 999-1007.
20) B. H. Gebreslassie, M. Medrano, D. Boe, Exergy analysis of multi-effect water–LiBr absorption systems: From half to triple effect, Renewable Energy, 35,(8), (2010), 1773-1782.
21) J. Wang, D. Zheng, Performance of one and a half-effect absorption cooling cycle of H2O/LiBr system, Energy Conversion and Management, 50, (12), (2009), 3087-3095.
22) N.A. Darwish, S.H. Al-Hashimi, A.S. Al-Mansoori, Performance analysis and evaluation of a commercial absorption–refrigeration water–ammonia (ARWA) system, International Journal of Refrigeration, 31, (7), (2008), 1214-1223.

23) R.M. Tozer, R.W. James, Fundamental thermodynamics of ideal absorption cycles, International Journal of Refrigeration, 20, (2), (1997), 120-135.
24) R. Brunet, J. A. Reyes-Labarta, G. Guillén-Gosálbez, L. Jiménez, D. Boer, Combined simulation–optimization methodology for the design of environmental conscious absorption systems, Computers & Chemical Engineering, 46, (2012), 205-216.
25) V. E. Nakoryakov, N. I. Grigoryeva, M. V. Bartashevich, Heat and mass transfer in the entrance region of the falling film: Absorption, desorption, condensation and evaporation. International Journal of Heat and Mass Transfer, 54(21-22), (2011), 4485–4490.
26) Y. Lazcano-Véliz, J. Siqueiros, D. Juárez-Romero, L. I. Morales, J. Torres-Merino, Analysis of effective wetting area of a horizontal generator for an absorption heat transformer. Applied Thermal Engineering, 62(2), (2014), 845–849.
27) M. Mittermaier, F. Ziegler, Theoretical evaluation of absorption and desorption processes under typical conditions for chillers and heat transformers, International Journal of Refrigeration, In Press, Accepted Manuscript, Available online 22 July (2015).
28) H.T. Chua, H.K. Toh, K.C. Ng, Thermodynamic modeling of an ammonia–water absorption chiller, International Journal of Refrigeration, 25, (7), (2002), 896-906.
29) J.M. Gordon, K. C. Ng, A general thermodynamic model for absorption chillers: Theory and experiment, Heat Recovery Systems and CHP, 15, (1), (1995), 73-83.
30) M. Feidt, Thermodynamique et optimisation Energetique des Systèmes et Procedés, Tec et Doc. Editeurs, Paris, France, (1987), 383-388.
31) Bejan, The Generation of Physical Structure in Power and Refrigeration Systems, Keynote, Duke University, Durham, NC 27708-0300, USA, (2001).
32) M. Feidt, Thermodynamics applied to reverse cycle machines, a review, International Journal of Refrigeration, 33, (2010), 1327-1342.
33) M. Feidt, Evolution of thermodynamic modelling for three and four heat reservoirs reverse cycle machines: A review and new trends, International Journal of Refrigeration 36, (2013), 8-23.
34) Z. Yan, J. Chen, An optimal endoreversible three heat sources refrigerator, Journal of Applied Physics 65 (1), (1989), 1-4.
35) J. Chen, Z. Yan, Unified description of endoreversible cycles, Physiscal Review A 39 (8), (1989), 4140-4147.
36) H.T. Chua, J.M. Gordon, K.C. Ng, Q. Han, Entropy production analysis and experimental confirmation of absorption systems, International Journal of Refrigeration 20, (1993), 179-190.
37) K.C. Ng, K. Tu, H.T. Chua, J.M. Gordon, T. Kashiwagi, Thermodynamics analysis of absorption chillers: internal dissipation and Process Average Temperature, Applied Thermal Engineering 18 (8), (1998), 671-682.
38) G. Grazzini, A. Rocchetti, Thermodynamic optimization of irreversible refrigerators, Energy Conversion and Management 84, (2014), 583-588.
39) G. Grazzini, F. Gori, Entropy parameters for heat exchangers design. Int. J. Heat Mass Transfer 31, (1988), 2547-2554.
40) S.F. Lee, S.A. Sherif, Thermodynamic analysis of a lithium bromide/water absorption system for cooling and heating applications, International Journal of Energy Research 25, (2001), 1019-1031.
41) R. Tozer, A. Syed, G. Maidment, Extended temperature-entropy (T-s) diagrams for aqueous lithium bromide absorption refrigeration cycles, International Journal of Refrigeration 28, (2005), 689-697.
42) R. Palacho-Bereche, R. Gonzales, S.A. Nebra, Exergy calculation of lithium bromide-water solution and its application in the exergetic evaluation of absorption refrigeration systems LiBr-H2O, International Journal of Energy Research online library, (2010).
43) D.S. Kim, C.A. Infante-Ferreira, A Gibbs energy equation for LiBr aqueous solutions, International Journal of Refrigeration 29, (2006), 36-46.

44) W. Kays, A. I. London, Compact Heat Exchangers, MacGraw-Hill, New York, (1964).
45) P. Donnellan, K. Cronin, E. Byrne, Recycling waste heat energy using vapour absorption heat transformers: A review, Renewable and Sustainable Energy Reviews, 42, (2015), 1290-1304.
46) M. Scott, Å. Jernqvist, G. Aly, Experimental and theoretical study of an open multi-compartment absorption heat transformer for different steam temperatures. Part III: application to process industry, Applied Thermal Engineering, 19 (4), (1999), 431-448.
47) X. Ma, J. Chen, S. Li, Q. Sha, Aiming Liang, Wei Li, Jiayan Zhang, Guojun Zheng, Zhihao Feng Application of absorption heat transformer to recover waste heat from a synthetic rubber plant, Applied Thermal Engineering, 23 (7), (2003), 797-806.
48) Huicochea, J. Siqueiros, R.J. Romero, Portable water purification system integrated to a heat transformer, Desalination, 165, (2004), 385-391.
49) W. Rivera, A. Huicochea, H. Martínez, J. Siqueiros, D. Juárez, E. Cadenas, Exergy analysis of an experimental heat transformer for water purification, Energy, 36 (1), (2011), 320-327.
50) Bejan, The thermodynamic design of heat and mass transfer processes and devices, International Journal of Heat and Fluid Flow, 8, 4, (1987), 258-276.
51) P. A. N. Wouagfack, R. Tchinda, Finite-time thermodynamics optimization of absorption refrigeration systems: A review, Renewable and Sustainable Energy Reviews, 21, (2013), 524-536.
52) M. Kilic, O. Kaynakli, Second law-based thermodynamic analysis of water-lithium bromide absorption refrigeration system, Energy, 32 (8), (2007), 1505-1512.
53) S.C. Kaushik, A. Arora, Energy and exergy analysis of single effect and series flow double effect water–lithium bromide absorption refrigeration systems, International Journal of Refrigeration, 32 (6), (2009), 1247-1258.
54) P. Donnellan, E. Byrne, K. Cronin, Internal energy and exergy recovery in high temperature application absorption heat transformers, Applied Thermal Engineering, 56 (1–2), (2013), 1-10.
55) Kaynakli, The first and second law analysis of a lithium bromide/water coil absorber, Energy, 33 (5), (2008), 804-816.
56) Yiğit, A numerical study of heat and mass transfer in falling film absorber, International Communications in Heat and Mass Transfer, 26 (2), (1999), 269-278.
57) J. W. Andberg, G. C. Vliet, A simplified model for absorption of vapors into liquid films flowing over cooled horizontal tubes, ASHRAE Trans, 93, (1987), 2454–66.
58) V.D. Papaefthimiou, I.P. Koronaki, D.C. Karampinos, E.D. Rogdakis, A novel approach for modelling LiBr–H2O falling film absorption on cooled horizontal bundle of tubes, International Journal of Refrigeration, 35 (4), (2012), 1115-1122.
59) K. Banasiak, J. Kozioł, Mathematical modelling of a LiBr–H2O absorption chiller including two-dimensional distributions of temperature and concentration fields for heat and mass exchangers, International Journal of Thermal Sciences, 48 (9), (2009), 1755-1764.
60) F. Babadi, B. Farhanieh, Characteristics of heat and mass transfer in vapor absorption of falling film flow on a horizontal tube, International Communications in Heat and Mass Transfer, 32 (9), (2005), 1253-1265.
61) Bejan, The Concept of Irreversibility in Heat Exchanger Design: Counterflow Heat Exchangers for Gas-to-Gas Applications, J. Heat Transfer, 99, (1977), 374-380.
62) D.P. Sekulić, C.V. Herman, One approach to irreversibility minimization in compact crossflow heat exchanger design, International Communications in Heat and Mass Transfer, 13, 1, (1986), 23-32.
63) H. Pahlavanzadeh, P. Nooriasl, Entropy Generation in Liquid Desiccant Dehumidification System, Energy Procedia, 14, (2012), 1855-1860.
64) D. La, Y. Li, Y. Dai, T. Ge, R. Wang, Effect of irreversible processes on the thermodynamic performance of open-cycle desiccant cooling cycles, Energy Conversion and Management, 67, (2013), 44-56.

65) Myat, K. Thu, N. Kim Choon, The experimental investigation on the performance of a low temperature waste heat-driven multi-bed desiccant dehumidifier (MBDD) and minimization of entropy generation, Applied Thermal Engineering, 39, (2012), 70-77.
66) N. Giannetti, A. Rocchetti, K. Saito, S. Yamaguchi, Entropy parameters for desiccant wheel design, 75, (2015), 826-838.
67) Myat et al., Entropy generation minimization: A practical approach for performance evaluation of temperature cascaded co-generation plants, Energy, Vol. 46, No. 1, pp. 493-521, 2012.
68) J.Y. San, W.M. Worek, Z. Lavan, Entropy generation in combined heat and mass transfer, International Journal of Heat and Mass Transfer, 30, 7, (1987), 1359-1369.
69) C.G. Carrington, Z.F. Sun, Second law analysis of combined heat and mass transfer in internal and external flows, International Journal of Heat and Fluid Flow, 13, 1, (1992), 65-70.
70) G. Prakash Narayan, J. H. Lienhard V, S. M. Zubair, Entropy generation minimization of combined heat and mass transfer devices, International Journal of Thermal Sciences, 49, 10, (2010), 2057-2066.
71) M. Kanoğlu, M. Özdinç Çarpınlıoğlu, M. Yıldırım, Energy and exergy analyses of an experimental open-cycle desiccant cooling system, Applied Thermal Engineering, 24, (2004), 919-932.
72) K. H. Mistry, J. H. Lienhard V, S. M. Zubair, Effect of entropy generation on the performance of humidification-dehumidification desalination cycles, International Journal of Thermal Sciences, 49, (2010), 1837-1847.
73) Chermiti, N. Hidouri, A.B. Brahim, Entropy generation in gas absorption into a falling liquid film, Mechanics Research Communications, 38, 8, (2011), 586-593.
74) N. Hidouri, I. Chermiti, A.B. Brahim, Second Law Analysis of a Gas-Liquid Absorption Film, Journal of Thermodynamics,(2013), ID 909162,10pp.
75) H. Hou, Q. Bi, H. Ma, G. Wu, Distribution characteristics of falling film thickness around a horizontal tube, Desalination, 285, (2012), 393-398.
76) D. Juric, G. Tryggvason, Computations of boiling flows, International Journal of Multiphase Flow, 24 (3), (1998), 387-410.
77) S. K. Choudhury, D. Hisajima, T. Ohuchi, A. Nishiguchi, T.Fukushima, S. Sakaguchi, Absorption of vapors into liquid films flowing over cooled horizontal tubes, ASHRAE Trans, 99, (1993),81–9.
78) L. Harikrishnan, Shaligram Tiwari, M.P. Maiya, Numerical study of heat and mass transfer characteristics on a falling film horizontal tubular absorber for R-134a-DMAC, International Journal of Thermal Sciences, 50 (2), (2011), 149-159.
79) W.G. Vincenti and C.H. Kruger, Jr., Introduction to Physical Gas Dynamics, Wiley, New Yor, (1965).
80) PROPERTIES OF LITHIUM BROMIDE-WATER SOLUTIONS AT HIGH TEMPERATURES AND CONDENSATIONS - PART I. Thermal Conductivity", ASHRAE Trans, 96, (1990).
81) D. S. Ayou, J. C. Bruno, R. Saravanan, A. Coronas, An overview of combined absorption power and cooling cycles, Renewable and Sustainable Energy Reviews, 21, (2013), 728-748.
82) H.Z. Hassan, A.A. Mohamad, A review on solar cold production through absorption technology, Renewable and Sustainable Energy Reviews, 16 (7), (2012), 5331-5348.
83) K. Parham, M. Khamooshi, D. B. Kenfack Tematio, M. Yari, U. Atikol, Absorption heat transformers – A comprehensive review, Renewable and Sustainable Energy Reviews, 34, (2014), 430-452.
84) X.Q. Zhai, R.Z. Wang, A review for absorbtion and adsorbtion solar cooling systems in China, Renewable and Sustainable Energy Reviews, 13(6-7), (2009), 1523-1531.
85) R. Gomri, Second law comparison of single effect and double effect vapour absorption refrigeration systems, Energy Conversion and Management, 50 (5), (2009), 1279-1287.
86) S. Gong, K. G. Boulama, Parametric study of an absorption refrigeration machine using advanced exergy analysis, Energy, 76, (2014), 453-467.

87) D. Zebbar, S. Kherris, S. Zebbar, K. Mostefa, Thermodynamic optimization of an absorption heat transformer, International Journal of Refrigeration, 35 (5), (2012), 1393-1401.
88) G. Gutiérrez-Urueta, A. Huicochea, P. Rodríguez-Aumente, W. Rivera, Energy and Exergy Analysis of Water-LiBr Absorption Systems with Adiabatic Absorbers for Heating and Cooling, Energy Procedia, 57, (2014), 2676-2685.
89) P. Donnellan, E. Byrne, J. Oliveira, K. Cronin, First and second law multidimensional analysis of a triple absorption heat transformer (TAHT), Applied Energy, 113, (2014), 141-151.
90) Y. He, G. Chen, Experimental study on an absorption refrigeration system at low temperatures, International Journal of Thermal Sciences, 46, (3), (2007), 294-299.
91) Tano san
92) D. M. Maron, G. Ingel, N. Brauner, Wettability and break-up of thin films on inclined surfaces with continuous and intermittent feed, Desalination, 42, (1982), 87-96.
93) N. Brauner, D. M. Maron, Z. Harel, Wettability, Rewettability and breakdown of thin films of acqueous solutions, Desalination, 52, (1985), 295-307.
94) M. Trela, A semi-theoretical model of stability of vertical falling liquid films, Chemical Engineering Science, 49 (7), (1993), 1007-1013.
95) S. Yih, Stability of liquid flow down an inclined plane, Phyics of Fluids, 6, (1963), 321-334.
96) E. Hartley and W. Murgatroyd, Criteria for the break-up of thin liquid layers flowing isothermally over solid surfaces, International Journal of Heat and Mass Transfer, 7, (1964), 1003-1015.
97) B. Ponter, G. A. Davies, T. K. Ross, P. G. Thornley, The influence of mass transfer on liquid film breakdown, International Journal of Heat and Mass Transfer, 10, (1967), 349-359.
98) T. Hobler, J. Czajka, Minimal surface wetting (in Polish), Chemia Stosow. 2B, (1964), 145.
99) J. Mikielewicz, J. R. Moszynski, Minimum thickness of a liquid film fowing vertically down a solid surface, lnternational Journal of Heat and Mass Transfer, 19, (1976),771-776.
100) R.E. Johnson Jr., R.H.J. Dettre, Contact Angle Hysteresis. III. Study of an Idealized Heterogeneous Surface, The Journal of Physical Chemistry, 68, (1964), 1744-1749.
101) L.W. Schwartz, S. Garoff, Contact Angle Hysteresis on Heterogeneous Surfaces, Langmuir, 1, (1985), 219-230.
102) J.W. Krumpfer, T.J. McCarthy, Contact angle hysteresis: a different view and a trivial recipe for low hysteresis hydrophobic surfaces, Faraday discussions, 146, (2010), 103-111.
103) L. Gao, T.J. McCarthy, Contact Angle Hysteresis Explained, Langmuir, 22, (2006), 6234-6237.
104) J. D. Killion, S. Garimella, A Critical Reviev of models of coupled heat and mass transfer in falling-film absorption,InternationalJournal of Refrigeration, 24, (2001), 755-797.
105) J. D. Killion, S. Garimella, A Reviev of Experimental Investigationsof Absorption of Water Vapor in Liquid Films Falling overHorizontal Tubes, HVAC&RESEARCH, 2 (9), (2003), 111-136.
106) S. Jeong, S. Garimella, Falling-film and droplet mode heat and mass transfer in a horizontal tube LiBr/water absorber, International Journal of Heat and Mass Transfer, 45 (7), (2002), 1445-1458.
107) H.T. Honda, T.W. Chung, Effect of Surface Tension on Mass Transfer Devices, Mass Transfer in Multiphase Systems and its Applications, Prof. Mohamed El-Amin (Ed.), (2011), 273-299.
108) V. M. Soto Francés, J. M. Pinazo Ojer, Experimental study about heat and mass transfer during absorption of water by an aqueous lithium bromide solution, International Proceedings of the ASME-ZSITS International Thermal Science Seminar, Bled (Slovenia), 11-14 June, (2000), 535-542.
109) V. M. Soto Francés, J. M. Pinazo Ojer, Validation of a model for the absorption process of H2O(vap) by a LiBr(aq) in a horizontal tube bundle using a multi-factorial analysis, International Journal of Heat and Mass Transfer, 46, (2003), 3299-3312.
110) R.H. Wassenaar, Measured and predicted effect of flowrate and tube spacing on horizontal tube absorber performance, International Journal of Refrigeration, 19 (5), (1996), 347–355.

111)Doniec, Laminar flow of a liquid rivulet down a vertical solid surface, Canadian J. of Chemical Eng., 69, (1991), 198-202.
112)Doniec, Flow of a laminar liquid film down a vertical surface, Chemical Eng. Science, 43 (4), (1988), 847-854.
113)Doniec, Phys. Chem. Hydrodynamics, 5, (1984), 143-152.
114)S. Yamaguchi, J. Jeong, K. Saito, H. Miyauchi, M. Harada, Hybrid liquid desiccant air-conditioning system: Experiments and simulations, Applied Thermal Engineering, 31 (17–18), (2011), 3741-3747.
115)J.H. Snoeijer, B. Andreotti, A microscopic view on contact angle selection, Physics of Fluids, 20, (2008), 057101.
116)M.A. Rodríguez-Valverde, F.J. Montes Ruiz-Cabello, P.M. Gea-Jódar, H. Kamusewitz, M.A. Cabrerizo-Vílchez, A new model to estimate the Young contact angle from contact angle hysteresis measurements, Colloids and Surfaces A: Physicochemical and Engineering Aspects, 365 (1–3), (2010), 21-27.
117)X. D. Wang, X. F. Peng, B. X. Wang., Contact angle hysteresis and hysteresis tension on rough solid surface, Chinese Journal of Chemical Engineering, 12(5), (2004), 615-621.
118)Faghiri, Y. Zhang, Transport Phenomena in Multiphase Systems, Academic Press, Burlington, MA 01803,USA, (2006).
119)A.W. Adamson, A.P. Gast, Physical Chemistry of surfaces, 6th ed., John Wiley and Sons, (1997).
120)B.J. Kim, I.S. Kang, Absorption of water vapor into wavy-laminar falling film of aqueous lithium-bromide, KSME Journal, 9, (1), (1995), 115-122.
121)G. Kocamustafaogullari, I.Y. Chen, Falling film hea transfer analysis on a bank of horizontal tube evaporator, AIChE Journal, 34 (9), (1988), 1539-1549.
122)H. Daiguji, E. Hihara, T. Saito, Mechanism of absorption enhancement by surfactant. International Journal of Heat and Mass Transfer, 40(8),(1997), 1743–1752.
123)L. Hoffmann, I Greiter, A Wagner, V Weiss, G Alefeld, Experimental investigation of heat transfer in a horizontal tube falling film absorber with aqueous solutions of LiBr with and without surfactants, International Journal of Refrigeration, 19 (5), (1996), 331-341.
124)Kyung, K.E. Herold, Y.T. Kang, Experimental verification of H2O/LiBr absorber bundle performance with smooth horizontal tubes, International Journal of Refrigeration, 30 (4), (2007), 582-590.
125)M. Mittermaier, P. Schulze, F. Ziegler, A numerical model for combined heat and mass transfer in a laminar liquid falling film with simplified hydrodynamics, International Journal of Heat and Mass Transfer, 70, (2014), 990-1002.
126)N.I. Grigor'eva, V.E. Nakoryakov, Exact solution of a combined Heat- and Mass- transfer problem during film absorption, Inzhernerno-Fizicheskii Zhurnal, 33 (5), (1977), 893-898.
127)G. Grossman, Simultaneous heat and mass transfer in film absorption under laminar flow, International Journal of Heat and Mass Transfer, 26 (3), (1983), 357-371.
128)T. Meyer, F. Ziegler, Analytical solution for combined heat and mass transfer in laminar falling film absorption using first type boundary conditions at the interface, International Journal of Heat and Mass Transfer, 73, (2014), 141-151.
129)G. Grossmann, Simultaneous heat and mass transfer in absorption/desorption of gases in laminar liquid films, Proc. A.I.Ch.E. Winter and Annual Meeting, Orlando, Florida, (1982).
130)ISO/IEC guide 98-3(JCGM 100:2008), Evaluation of measurement data – Guide to the expression of uncertainty in measurement, 1st edition, September, 2008.
131)Kashiwagi, T., 1988, Basic mechanism of absorption heat and mass transfer enhancement by the Marangoni effect, Newsletter, IEA Heat Pump Center, 6, 2-6.

早稲田大学　博士（工学）学位申請　研究業績書

(List of research achievements for application of doctorate (Dr. of Engineering), Waseda University)

氏 名　Niccolo Giannetti　　印

（As of 2 月, 2016）

種 類 別 (By Type)	題名、　発表・発行掲載誌名、　発表・発行年月、　連名者（申請者含む） (theme, journal name, date & year of publication, name of authors inc. yourself)
論文 1	Thermodynamic analysis of regenerated air-cycle refrigeration in high and low pressure configuration, International Journal of Refrigeration, vol. 40 (2014), 97-110, N. Giannetti, A. Milazzo.
2	Entropy parameters for desiccant wheel design, Applied Thermal Engineering, vol. 75 (2015), 826-838, N. Giannetti, A. Rocchetti, K. Saito, S. Yamaguchi.
(3)	Irreversibility analysis of falling film absorption over a cooled horizontal tube, International Journal of Heat and Mass Transfer, vol. 88 (2015), 755-765, N. Giannetti, A. Rocchetti, K. Saito, S. Yamaguchi.
(4)	Entropy parameters for falling film absorber optimization, Applied Thermal Engineering, vol. 93 (2016), 750-762, N. Giannetti, A. Rocchetti, A. Lubis, K. Saito, S. Yamaguchi.
(5)	Thermodynamic optimization of three-thermal irreversible systems, International Journal of Heat and Technology, vol. 34, (2016) Special Issue 1, S83-S90, N. Giannetti, A. Rocchetti, K. Saito.
国際発表 (6)	Analytical study of falling film absorption on a partially wetted horizontal tube, 26th International Symposium on Transport Phenomena, September 27th - October 1st (2015) Leoben (Austria), N. Giannetti, K. Saito, S. Yamaguchi, A. Rocchetti.
(7)	Local entropy generation analysis of water vapour absorption in a LiBr-H_2O solution film, over a horizontal cooled tube, 24th IIR International Congress of Refrigeration, August 16th – 22nd (2015) Yokohama (Japan), N. Giannetti, A. Rocchetti, K. Saito, S. Yamaguchi.
8	Cascade refrigeration system with inverse Bryton cycle on the cold side, 24th IIR International Congress of Refrigeration, August 16th – 22nd (2015) Yokohama (Japan), N. Giannetti, A. Milazzo, A. Rocchetti.
(9)	Thermodynamic optimization of three-thermal irreversible systems, CLC2015 Constructal Law & Second Law Conference, May 18th - 19th (2015) Parma (Italy), N. Giannetti, A. Rocchetti, K. Saito.
発表 (10)	吸収器の水平管流下膜構成における熱と物質移動係数の解析式 (Analytical expression of heat and mass transfer coefficients on a partially wetted horizontal tube of falling film absorber), 2015 年度日本冷凍空調学会 年次大会, October 20th -23rd (2015), ジャンネッティ ニコロ, 齋藤 潔, 山口 誠一, アンデレア　ロッケッティ.
(11)	Anew model for partial wetting of inclined surfaces, 第 49 回空気調和・冷凍連合講演会講演論文集 (東京海洋大学, 東京), April 15th – 17th (2015), ジャンネッティ ニコロ, 齋藤　潔, 山口 誠一.

⑫	濡れ性を考慮した水平流下液膜式熱交換器の熱物質移動特性(Heat and mass transfer characteristics of falling film on a partially-wetted horizontal tube), 2014 年度日本冷凍空調学会 年次大会(佐賀大学, 佐賀), September 10th – 13th (2014), ジャンネッティ ニコロ, 中西 祐一, 山口 誠一, 齋藤 潔.
⑬	Semi-theoretical wettability model for falling film heat exchangers, 第 48 回空気調和・冷凍連合講演会講演論文集 (東京海洋大学, 東京), April 16th – 18th (2014), ジャンネッティ ニコロ, 齋藤　潔.
記事 ⑭	リキッドデシカント空調システム用中間冷却／加熱型接触器における流下液膜流動状態の可視化 (Visualization of Falling Film on Outer Surface of Fin-Tube Heat Exchanger), 「冷凍」10 月号第 90 巻第 1056 号 (2015), 小林　祐太，ジャンネッティ ニコロ，山口　誠一，齋藤　潔，中山　浩，宮岡　洋一.